FLUID MECHANICS RELEVANT TO RESPIRATION - FLOW WITHIN CURVED OR ELLIPTICAL TUBES AND BIFURCATING SYSTEMS

A Thesis submitted for the

Diploma of Imperial College

by

DAN EMIL OLSON, B.Sc.

Physiological Flow Studies Unit,
Department of Aeronautics,
Imperial College,
London S.W.7.

December 1971.

"The mechanics of breathing is a problem requiring on one hand the detailed knowledge of a classical anatomist and on the other hand the analytic understanding of an engineer. The anatomists have clearly presented their side of the subject and their conclusions have duly penetrated to the pages of current textbooks. It is amazing, however, to discover how superficial has been the analysis of the engineering aspects of the subject by physiologists. Perhaps it is because, to most physiologists, chemistry has seemed a more fruitful tool than physics; or more likely because the flow of air through tubes seemed too simple for serious attention or of too little practical value to medicine."

Fenn, W.O. (1951) Mechanics of Respiration. American Journal of Medicine, January, p.77.

ACKNOWLEDGEMENTS

I thank my parents, Mr. and Mrs. Robert O. Olson for instilling in their children an interest in academic achievement. And further I acknowledge my brother, Dr. David Edward Olson, and Dr. Giles Franklin Filley, for setting examples of research in science and medicine which were a primary source of motivation in these studies.

I would like to acknowledge the association of Dr. Kim Parker in the theoretical analysis presented in Chapter 2, and Dr. Tim Pedley in the theoretical analysis presented in Chapter 4. I would also like to thank Dr. Robert Schroter and Dr. Colin Caro for carefully reading, evaluating and criticising this thesis. And I am very thankful to Dr. Caro for inviting me to his Unit and for his continued interest in this work.

My deepest appreciation is to my wife, who has supported me and this research throughout, and to my sons, whose simple presence make any effort worthwhile.

CONTENTS

	Page No.
ABSTRACT	1
INTRODUCTION	3
CHAPTER 2	54
CHAPTER 3	137
CHAPTER 4	217
CHAPTER 5	252
CONCLUSION	293
APPENDIX	294
REFERENCES	304

ABSTRACT

This study is an attempt to understand some of the basic principles of the fluid mechanics within the respiratory airways. The problem of flow in this system may be defined by describing the geometry of the airways, determining the effect of elasticity of the airway walls and the effects of the pulsatility of respiration on the flow. It is concluded that the fluid is Newtonian and the flow laminar and quasi steady in a quasi-rigid tubular system of complex geometry.

Investigations are carried out on flow within six large scale models of symmetrical and asymmetrical bifurcations (which directly mimic the geometric and fluid dynamic state of the airways). The flow within the bifurcations is found to be quite complex, being an elliptical fluid dynamic problem. The gross patterns of the secondary currents can be roughly inferred from a potential flow solution which considers the curvature alone, but in general the flow properties are of a real fluid. The secondary flows rapidly develop just before the point of bifurcation and then rapidly diminish. Changing the entrance conditions, the angle of bifurcation or the curvature of bifurcation has significant effect on the secondary flows but much less effect on the primary flow/

flow. The complexity of the problem forced the investigation to be essentially empirical in nature.

Flow within curved circular tubes was studied to obtain the three dimensional velocity field as the fluid enters the curve and develops toward the steady, laminar, fully developed curved tube flow. A range of Reynolds numbers (100 to 2000) and Dean numbers (50 to 1000) appropriate to the bifurcations were studied. The results show the periodic manner by which the flow progresses toward the fully developed curved tube flow. This can be seen in the primary flow field which is initially organised as a potential flow and rapidly develops toward a viscous condition. The secondary flows also oscillate in magnitude but / only small reversals in direction are observed. The pattern of secondary flow deviates from predictions at the higher Dean numbers. The energy dissipation, kinetic energy, wall shear distribution and the position of the centre of mass flow all follow this basic periodic pattern.

Flow in straight tubes of circular cross section which progressively become elliptical in cross section is studied theoretically and experimentally. The three dimensional flow field is shown to be similar for both potential and viscous conditions. Strong secondary flows are shown to develop rapidly.

A device for measuring low speed, three dimensional, laminar flows is developed and analysed both theoretically and experimentally for its operation in air.

GENERAL INTRODUCTION

The process of respiration is carried out by forcing air through a network of tubes that convey the respiratory gases to a thin membrane of very large surface area. This membrane separates the oxygen rich, carbon dioxide poor air from the oxygen poor, carbon dioxide rich blood, allowing diffusion to occur between blood and air. This network of tubes continually increases its cross sectional area by frequent bifurcations; the sum of the area in the two daughter tubes of the bifurcation being larger than in the parent tube. This bifurcation pattern successfully accomplishes the main task of creating a large final surface area to facilitate the terminal diffusion process.

Within this system of multiple branched conduits the convection and diffusion of the flowing gas takes place in a complicated manner. The understanding of this coupled transport problem is of physiological interest and medical concern in that frequently the process of moving the respiratory gases through the airways to the terminal exchange membrane breaks down, causing disability and ultimately death.

Interest in the transport processes occurring in the airways has rapidly increased within the last decade. Whilst these transport processes have long been of basic physiological interest, motivation to investigate the physics/

physics of these phenomena has only come with the technical developments which are essential for practical application to diagnosis or medication (Macklem, 1).

The problem of air flow in the pulmonary system is unique in comparison with other biological flow problems which have so far been studied. The fluid mechanics of air flow in the lung is much simpler than the flow of blood in the major vessels (as an example) in that the air within the respiratory airways may be considered as a Newtonian fluid in quasi-steady, laminar motion within quasi-rigid conduits. The conduits are of complex geometry but have been described with relative completeness. Also the relatively easy access of investigators to the pulmonary airways (again compared, for example, with the vascular system) facilitates the possibility of physiologically assessing the fluid mechanic predictions. This provides the exciting possibility of developing a deep physical basis for understanding the mechanics of respiration.

An understanding of some of the principal fluid mechanical processes occurring during respiration is the ultimate goal. This study is limited to the inspiratory phase of respiration and applicable only to lungs of normal anatomy and quiet to moderate respiratory rates. These limitations exclude the almost infinite number of geometric aberrations occurring in disease and also the dynamic

(both/

(both geometric and elastic) changes occurring with very deep or very fast inspirations. The procedure followed toward this goal can be simply stated as follows:

1) Definition of the problem.
2) Study of flow in large scale models of biological bifurcations.
3) Development of a physical understanding of the flow properties in the scale models.
4) Study of flow in replicas of the actual biological system; and
5) Evaluating the fluid dynamic predictions from the above four procedures in physiological experimentation.

The "Definition of the Problem" is one of the most difficult aspects of this procedural routine. The first chapter will briefly outline the morphometric and physiologic studies carried out to define the process of respiratory gas flow in fluid dynamic terms. A variety of features of the respiratory airways can significantly affect the flow. The anatomy of a typical bifurcation which incorporates the geometric features pertinent to the flow is determined. Previous anatomical or physiological investigations have not been concerned with this specific information; and therefore had to be obtained before the fluid mechanic studies could commence. The pattern of the series-parallel arrangement of the airways in the pulmonary system also had to be determined. This is to elucidate the degree/

degree of geometric assymmetry of the branching system and how this system divides up the flow to each of the lungs' respiratory units. The volume flow rate of the inspired gas into each branch must be known so that predictions of the fluid mechanics parameters (mean velocity, Reynolds numbers, Dean numbers, etc.) can be made. The elasticity of the airways can also influence the internal fluid mechanics, as in the case of flow in the major arteries (Atabek, 2). The walls of the airways may respond to the local pressure and shear variations by changing their shape. Therefore measurements of elastic properties in the airways had to be conducted. Finally, the basic pattern of respiration had to be quantified. This is to say that the frequency, velocity and time course of an inspiration needed to be quantitatively evaluated.

Procedures 2 and 3 are the primary concern of this dissertation and will be considered in the third, fourth and fifth chapters. Chapter 2 is concerned with the analysis and evaluation of a velocity measuring instrument which had to be developed in order to experimentally study the low speed, highly three dimensional laminar flows considered in Chapters 3, 4 and 5. The instrument basically measures the time and direction of flight of a heated tracer of gas. The device is both experimentally and theoretically analysed/

analysed for its behaviour within the velocity ranges of interest in the model studies.

Procedure 2 was accomplished by studying the flow properties in large scale models of airway bifurcations. Each of the models incorporated the basic geometric pattern found in the human airways (as discussed in Chapter 1). Several models were used so that the angle of bifurcation and the curvature ratio (see Chapter 1) could be independently varied to encompass the variation found in the biological system. Two fluid mechanic entrance conditions were studied; a flat entering velocity profile and a parabolic entrance profile.

Equations which accurately describe the flow in bifurcations could not be developed because of the simultaneous effects of curvature, elliptical shape and a boundary layer development within the bifurcating tube. This created a severe limitation on the depth of physical understanding of the flow (procedure 3). Some degree of understanding was obtained by studying the flow in models of each of the basic geometric features which constitute a bifurcation. These were (1) a tube progressively becoming elliptical, and (2) a circular curved tube.

In Chapter 3 the fluid mechanics of flow entering a curved tube is investigated. The study concentrates on the development of the flow from two entrance conditions (a/

(a flat and a parabolic entrance velocity profile) to fully developed curved tube flow. The three dimensional flow field is determined at frequent intervals during the flow development for a wide range of laminar flows and curvatures. The results are compared to the numerous theories for fully developed curved tube flow and also to Pickett's (2a) analysis of developing curved tube flow.

Chapter 4 is concerned with a theoretical and an experimental analysis of the flow within a straight tube which is originally circular in cross section and then becomes elliptical in shape. The experimental studies were conducted on models which had a rate of change of cross sectional shape (with fixed cross sectional area) similar to that found in the airways. The theoretical studies were conducted for a low Reynolds flow and a potential flow in a tube with a slowly changing cross sectional shape. Three dimensional flow fields were predicted and measured for both potential and a viscous inlet conditions.

The study of flow within replicas of the pulmonary airways is depicted as procedure 4 and was also conducted. These models were created from casts of normal human cadavers taken shortly after death. This study therefore incorporates the more intricate or subtle geometric features of the airways and attempts to be a medium through which information produced in this dissertation can be extrapolated/

extrapolated to the living pulmonary system. This study also defines the entrance conditions into the small airways and therefore the entrance conditions into the models studied in Chapter 5. The results of this effort are also used to help quantify the effect of pulsatility on the flow within the airways, and this effect will be discussed in Chapter 1.

Procedure 5 is a heroic task in itself, and no effort has been made at present to attempt this aspect of the problem.

This thesis is primarily concerned with the studies of fluid mechanical problems and classical techniques of investigation are employed for their solution. We may therefore ask why physiology is even considered. This is because the problem is formulated within physiology and the fluid dynamic studies are focused to produce information primarily for the physiological system. This leaves us with a very complicated fluid mechanic problem, where simplifying assumptions may not be made specifically to construct mathematical solutions or to optimally demonstrate some internal flow phenomenon. This philosophy also requires that several fluid mechanical problems must be investigated simultaneously. Essentially then, the fluid mechanical study becomes subsidiary to the broader physiological problem which must be understood to appreciate the logic involved in choosing the fluid mechanical problems studied and results desired.

CHAPTER 1

Definition of the fluid mechanic problem in the human airways

This chapter is concerned with the definition of the general fluid mechanic conditions existing in the human lung during a normal inspiratory manoeuvre. Three basic features of the problem are considered:

1) What is the geometry of the tubes;
2) What influence does the oscillatory nature of respiration have on the flow; and
3) What influence do the elastic walls of the airways have on the flow.

The conclusions to these questions are relatively simple. The geometry of the conduits is in general complex, but a typical (the statical mode and median) geometric pattern for a bifurcation can be described. Further, the principal geometric parameters and their variations can also be quantified. The oscillatory nature of respiration has little effect on the flow, as does the elasticity of the airway walls. These last two conclusions seem benign, but the basic approach taken to study this problem depends strongly on these conclusions, and therefore they are considered in some detail.

In this chapter it is concluded that the basic fluid mechanics in the small airways during inspiration can be understood/

understood by studying flow in models of complex geometric bifurcations, curves and elliptical tubes which incorporate the geometric parameters found in the normal lung. The models may have rigid walls and may be studied under steady flow conditions.

A. General anatomy of the respiratory airways

The airway system in the human lung can conveniently be separated into three separate sections. The upper and central airways is the first of these sections and consists of the air passages from the mouth and nose down through the pharynx and larynx into the trachea, and finally into the large bronchi. The initial part of this system consists of a single conduit of highly complex cross section, but below the first branching point, the carina, we have a tree-like structure where each parent branch divides into two smaller daughter branches. Figure 1.1 shows the internal structure of this area. The central airways include the first two bifurcations (that is, the central airways terminate when there are four branches). These last structures are called lobar bronchi and at this point the airway enters the parenchyma of the lung; that is, they become surrounded by the lung tissue.

The next section consists of the bronchi and bronchioles which/

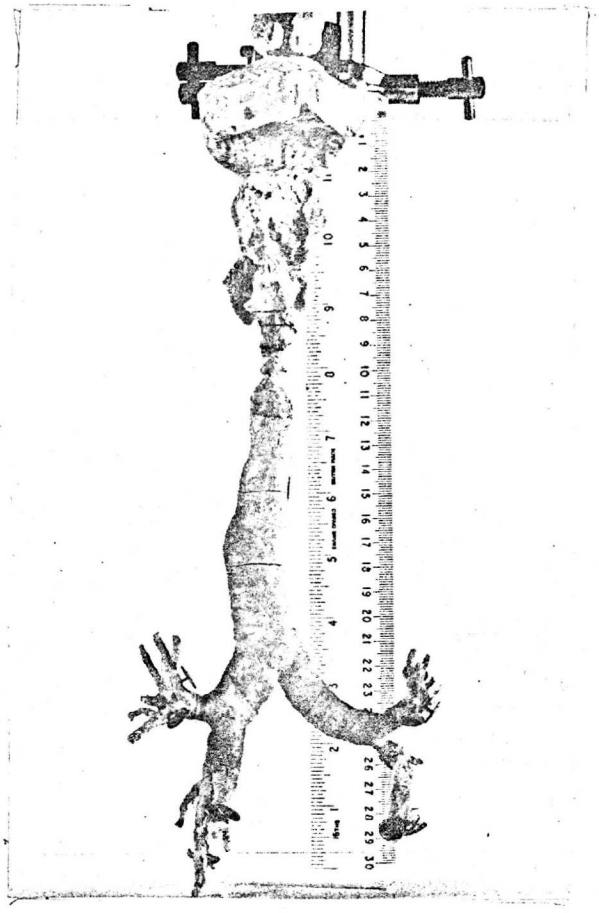
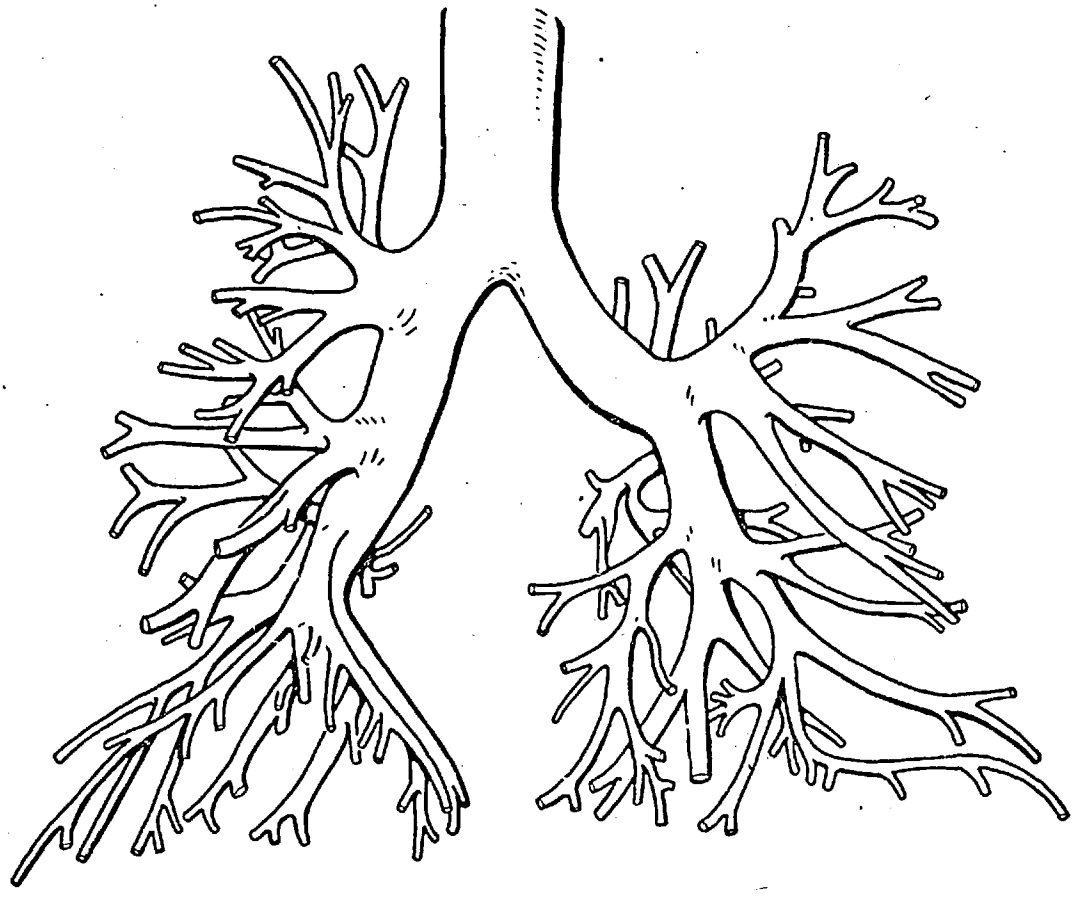


FIGURE 1.1 Silicone rubber cast of the upper and central airways. Mouth and nasal septi are at top with segmental bronchi marked with pins. Upper airways are from mouth and nose down to larynx (at 7.5 inches on scale). Central airways include trachea and first two bifurcations; ending with four lobar branches.

which continually branch in a complex but ordered pattern. This branching process is carried out, on average, thirteen times, increasing the number of tubes from four to about 45,000 (Weibel, 3; Horsfield et al, 4). The diameter of the tubes decreases, being about 1.0 cm at the lobar bronchi to about 0.05 cm at the terminal bronchi, but the total cross sectional area increases 30-fold. This part of the bronchial tree is usually defined as the middle airways. Figure 1.2 is a drawing of the branching in the larger middle airways, and Figure 1.3 shows a cast taken of the smaller middle airways.

At this point the basic system of relatively smooth circular tubes bifurcating into more smooth circular tubes changes. Now bubble-like structures start to protrude from the sides of the tube, which is now defined as a respiratory bronchiole. The basic branching pattern remains, but progressively more of these sack-like structures protrude from the conduit until the previously circular tube is unrecognisable. Figures 1.4 and 1.5 show this geometric arrangement. The sacks are the alveoli of the lung which are the surface membrane where the diffusion takes place between blood and air. There are about 300,000,000 alveoli in a normal human lung, and they comprise over 95% of the lung volume. This last section of the bronchial tree is defined as the lower (or distal) airways. Figure 1.5 shows the average geometric features of this branching pattern determined by Olson et al (5).



RECONSTRUCTION OF PREDOMINANT PATTERNS •

(after Boyden)

	GENERATION	NUMBER	DIAMETER (mm)	AREA ATTAINED (cm^2)
Bronchi (above)	5—9	137		4
Term. Bronchi	7—13	1,000	1.0	8
Term. Bronchioles	10—20	45,000	.5	88
Resp. Bronchioles	12—25	200,000	.365	210
Alv. Ducts & Sacs	15—30	14,500,000	.365	70,000
Alveoli		300,000,000		500,000

FIGURE 1.2 Artistic reconstruction of middle airways (after Bayden).



FIGURE 1.3 Cast of bronchioles; small of the middle airways. Stem branch is approximately 1.5mm in diameter. Note the sharp division (flow divider) at each branch point within structures down to .7mm in size. Also note symmetry of branches and angle of branching.

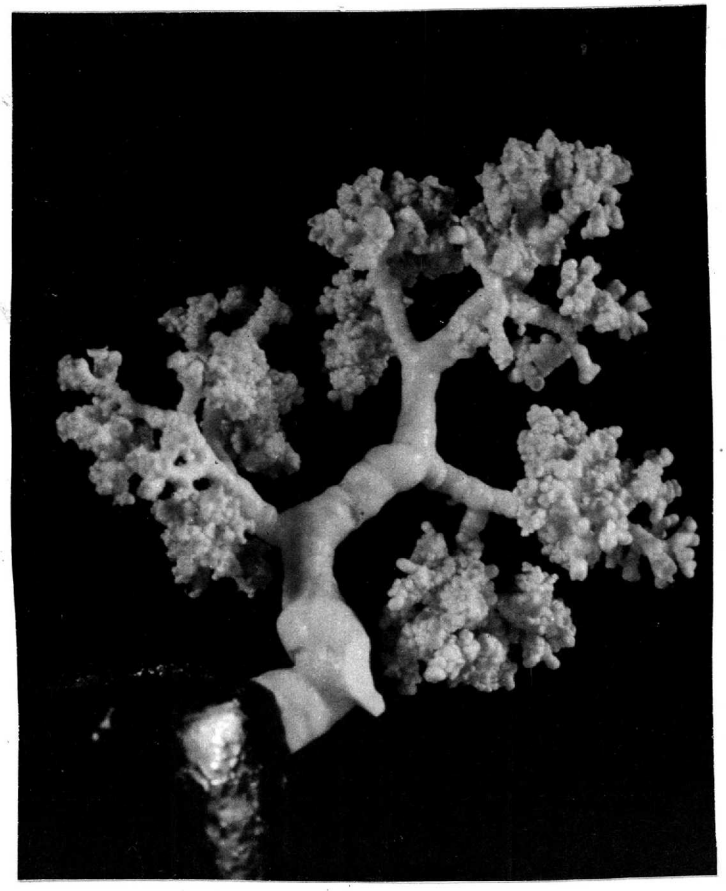
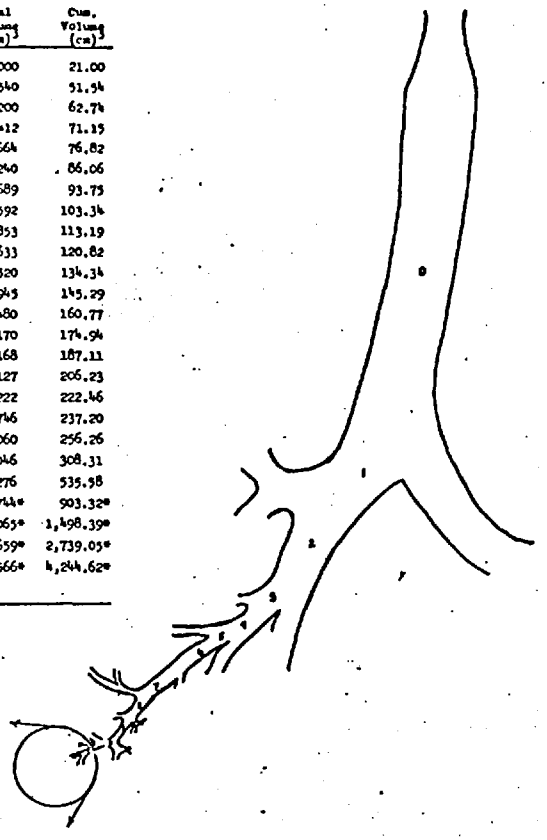


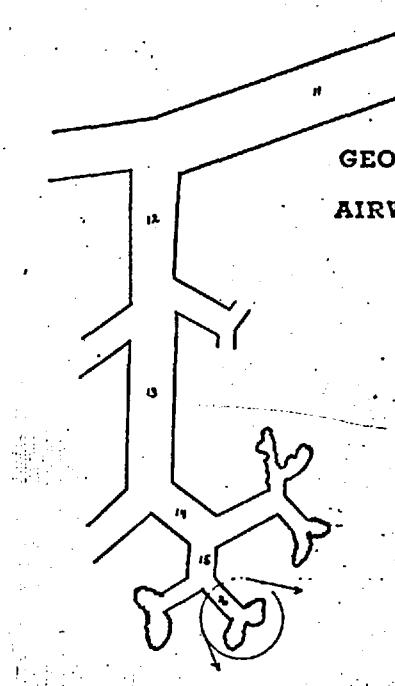
FIGURE 1.4 Cast of lower airways, showing respiratory bronchioles and alveoli.
Alveoli are small bubble shaped structures with diameter of approximately 0.35mm.

GEOMETRICAL FACTORS

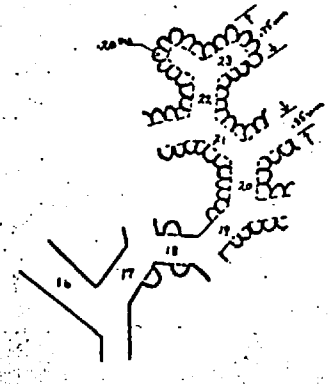
Name of Structure	Avg. Order	Number of Structures	Dia. (mm)	Length (cm)	X-Section Area (cm)^2	Volume of Tube (mm)^3	Total X-Section (cm)^2	Total Volume (cm)^3	Cum. Volume (cm)^3
Mouth & Pharynx	-	1	20.	70.	300.	21,000.	3.00	21.000	21.00
Trachea	0	1	18.	120.	254.5	30,540.	2.55	30.540	51.54
Primary Bronchi	1	2	13.	42.2	132.7	5,600.	2.65	11.200	62.74
Bronchi	2	4	9.4	30.3	69.4	2,103.	2.78	8.412	71.15
"	3	7	7.2	23.4	40.7	952.	2.85	5.664	76.82
"	4	20	5.65	18.4	25.1	462.	5.02	9.240	86.06
"	5	33	4.5	14.6	15.9	233.	5.25	7.689	93.75
"	6	88	3.6	10.7	10.2	109.	8.98	9.592	103.34
"	7	143	3.0	9.75	7.07	68.9	10.11	9.853	113.19
"	8	232	2.4	7.80	4.52	32.9	10.48	7.633	120.82
"	9	609	2.0	6.50	3.42	22.2	20.83	13.520	134.34
Bronchiole	10	986	1.63	5.30	2.09	11.1	20.61	10.945	145.29
"	11	2,580	1.33	4.32	1.39	6.00	35.86	15.480	160.77
"	12	4,180	1.10	3.57	.95	3.39	39.71	14.170	174.94
"	13	6,760	.90	2.83	.64	1.80	43.26	12.168	187.11
"	14	17,710	.74	2.51	.43	1.08	76.15	19.127	206.23
"	15	28,660	.61	1.97	.29	.566	83.11	16.222	222.46
Terminal Bronchiole	16	46,370	.50	1.62	.20	.318	92.74	14.746	237.20
Respiratory Bronchiole	17	121,400	.50	.80	.20	.157	242.80	19.060	256.26
"	18	196,400	.65	.80	.33	.265	648.12	52.046	308.31
"	19	514,200	.75	1.0	.44	.442	2262.48	227.276	535.58
Alveolar Duct	20	832,000	.35+	1.0	.11	.442	915.20	367.744*	903.32*
"	21	1,346,300	.35+	1.0	.11	.442	1480.93	595.065*	1,498.39*
"	22	3,524,600	.35+	.8	.11	.352	3877.71	1,240.659*	2,739.05*
Alveolar Sac	23	5,702,900	.35+	.6	.11	.264	6273.19	1,505.566*	4,244.62*
Alveoli	--	299,400,000	.20+	.2	.03		(645,600.)		

* Includes Volume of Tube Plus Alveolus on Tube
+ See Figure for Detailed Geometry
() Surface Area of Alveoli





GEOMETRY OF THE AVERAGE AIRWAY IN THE HUMAN LUNG



FLUID DYNAMIC FACTORS

Name of Structure	Avg. Order	Fluid Friction Surface Area (cm)^2	Fluid Friction Area to X-Section Area (Ratio)	Distance To Alveoli (cm)	Distance From Mouth (cm)	Number Alveoli Struc
Mouth & Pharynx	-	62.8	.209	381.2	70.	
Trachea	0	56.5	.222	311.2	190.	
Primary Bronchi	1	40.8	.307	191.2	232.2	
Bronchi	2	29.5	.425	149.0	262.5	
"	3	22.6	.555	118.7	285.9	
"	4	17.8	.709	95.3	304.3	
"	5	14.1	.887	76.9	318.9	
"	6	11.3	1.108	62.3	329.6	
"	7	9.42	1.332	51.57	339.4	
"	8	7.54	1.668	41.82	347.2	
"	9	6.28	1.836	34.02	353.7	
Bronchiole	10	5.12	2.450	27.52	359.0	
"	11	4.18	3.007	22.22	363.3	
"	12	3.46	3.642	17.90	366.8	
"	13	2.83	4.422	14.33	369.7	
"	14	2.32	5.395	11.50	372.2	
"	15	1.92	6.621	8.99	374.2	
Terminal Bronchiole	16	1.57	7.850	7.02	375.8	0
Respiratory Bronchiole	17	1.57	7.850	5.4	376.6	1
"	18	2.04	6.181	4.6	377.4	2
"	19	2.36	5.363	3.8	378.4	5
Alveolar Duct	20	-	-	2.8	379.4	15
"	21	-	-	1.8	380.4	15
"	22	-	-	.8	381.2	15
Alveolar Sac	23	-	-	0	387.2	20
Alveoli	--	-	-	(0)	(381.2)	

FIGURE 1.5 Geometry of average pathway from trachea to alveoli from Olson, et al (5).

B. Branching pattern and general morphology in the middle airways

The bronchi and bronchioles of the middle airways form a regular, asymmetrical bifurcating pattern where the two daughter tubes each have a smaller diameter than the parent tube, but the cross sectional area of both daughter tubes is greater than in the parent tube by about 25%. Weibel (3) was the first to systematically study the morphometry of the airways. Actually Weibel's main purpose was to evaluate the pulmonary vascular system and the proposed symmetrical branching model (Model A) of the pulmonary airway system was a by-product of the main study. The basic geometric features of Weibel's anatomical model, such as mean diameter or length of each tube, were determined from large numbers of airways and these measurements have been subsequently confirmed by several other investigators (Horsfield, 4; Davies, 5). The weak part of the anatomical model was the method by which Weibel put the tubes together to produce a branching tree.

Weibel proposed a symmetrical branching network: one where both daughter tubes are identical. This model has inconsistencies with reality. First, it implies that all pathways from mouth to alveoli must be the same; this is contrary to measurement. Second, it predicts too large a number of terminal structures. Weibel realised these deficiencies/

deficiencies, but Model A was proposed because of its simplicity. Recent investigations by Horsfield (4) and Olson (5) have attempted to model the asymmetrical bifurcation pattern in the lung. Such branching models are not unique to the respiratory airways. Horton (6), Strahler (7), Murray (8) and Woldenberg (9) have investigated the branching patterns in other systems, such as rivers and trees. It is interesting to note that these naturally occurring branching patterns have basic similarities in that a deficient binominal series (such as the Fibbonacci Series) usually describes the branching pattern.

The lung studies were carried out by making casts of the airways and then measuring all the principal dimensions for each of the 20,000 or 30,000 major branches. The difficulty comes when looking into the tree and deciding which branches are sisters to which other branches, and which branches are just distant cousins. That is, some mathematical rule must be formulated (usually on functional or teitological grounds) which determines what family any one branch belongs to. This must be done so that the dimension of any branch plucked from the tree can be statistically compared to its nearest relative.

In/

In Weibel's symmetrical system the parent branch of a bifurcation would belong to family N, while each of the daughter branches would belong to the family once removed from the parent, such as N-1. In the asymmetrical lung model (4, 5 and 9) the parent (stem) branch belongs to family N, while one daughter belongs to family N-1 and the other to family N-4. (In the Fibbonacci series the "relationship" would be N for parent and N-1 and N-2 for the two daughter tubes.)

All members of the same family have similar diameter, length and branching angle. This degree of asymmetry predicts the correct number of terminal units, gives the correct range of pathway lengths and also has the minimum range of geometric variation within a family. Figure 1.6 shows a schematic diagram of such a typical asymmetrical bifurcation. The diameter of the parent is D, while that of one daughter is 0.875D and that of the other is 0.66D. The area increase between the parent and two daughters is 25%. The branching angle of the large daughter is 25^{o}, while the branching angle of the small daughter is 45^{o}. The radius of curvature, R, is about five to six times the diameter in the big daughter and about two to four times the diameter in the small daughter tube. Figure 1.6 shows the typical arrangement of a bifurcation in the middle airways. The diameter is strongly influenced by its branching position, while the branching angles and asymmetry are/

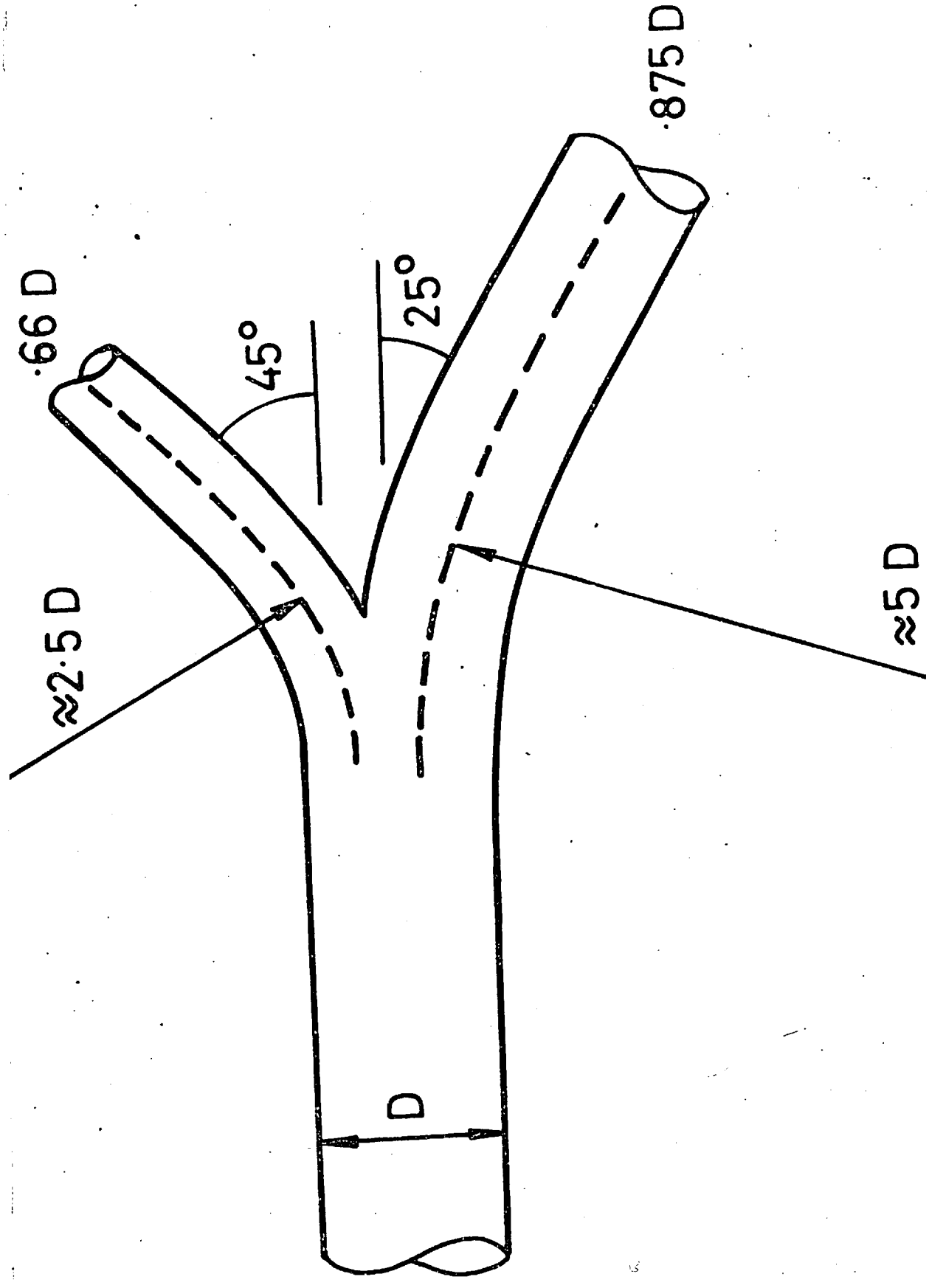


FIGURE 1.6 Most typical pattern of a bifurcation in the middle airways. Note asymmetry in diameters, curvatures and branching angle.

are weak functions of the position within the bronchial tree. The diameter, as previously mentioned, decreases as we go deeper into the lung. The total branching angle (sum of both daughter branching angles) becomes larger as we go deeper, being between 50^{o} and 90^{o} in the smaller of the middle airways. The branching pattern becomes progressively more symmetrical as we go deeper, being almost completely symmetrical in the peripheral airways.

C. Detailed morphology of a bifurcation in the middle airways

Other more detailed features of a bifurcation must also be known before we can construct a model. These features were determined by taking silicone rubber casts of approximately 500 branches in the middle airways and slicing them in a plane parallel to the axis of the bifurcation for the determination of the radius of curvature (R), bifurcation angles and wall waviness. The silicone casts were also sliced as shown in Figure 1.7 to determine the shape of lumenal cross section perpendicular to the flow. First the bronchi are most typically circular in shape. The index of elliptivity obtained for the branches was usually quite small. This shape changes near the far end of the branch. The transition between parent and daughter tubes progresses as shown in Figure 1.3. The total length of a bronchus is between 2.5 and 3.5 diameters at its origin/

origin and midpoint of length a bronchus is usually circular in section; the distal 20% of the length constitutes a transition zone in which the section changes shape in order to give rise to two daughter branches which are circular at their origin. The dividing plane of the daughter branches is termed the flow divider. The transition process is shown in Figure 1.7, where the transition zone first becomes an ellipse (b) of the same area as the circular section (a) preceding it. When the minor curvature of the ellipse approximates to the curvature of the daughter tube, the shape of the transition departs from an ellipse. It then becomes more flattened, so that its minor axis approximates to the diameters of the daughter branches and its area increases (c). The section is then indented by the margins of the flow divider (d) which finally divides into two smaller, circular branches (e).

The area normal to the flow in the transition zone changes in a uniform fashion between the area of the parent and the summed area of the daughter branches. This change in area takes place between sections (b) and (d). A plot of the increase in area through the transition is sigmoid in shape.

The geometry of the flow divider is shown in Figure 1.8, where the sharpness is shown in A where $r/d < 0.1$; this indicates that at the centre of the flow divider the leading/

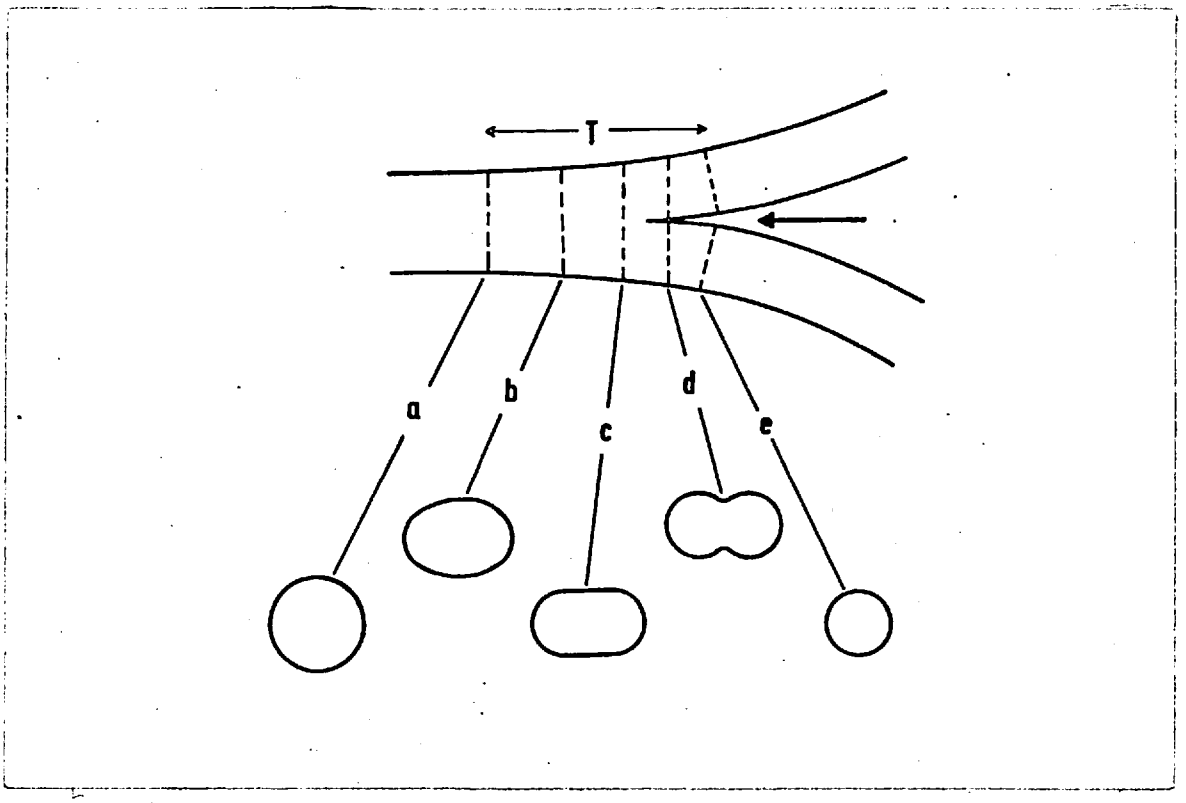


FIGURE 1.7 Typical shape of transition zone between parent and daughter in the middle airways. Sections a and e are circular while b is elliptical.

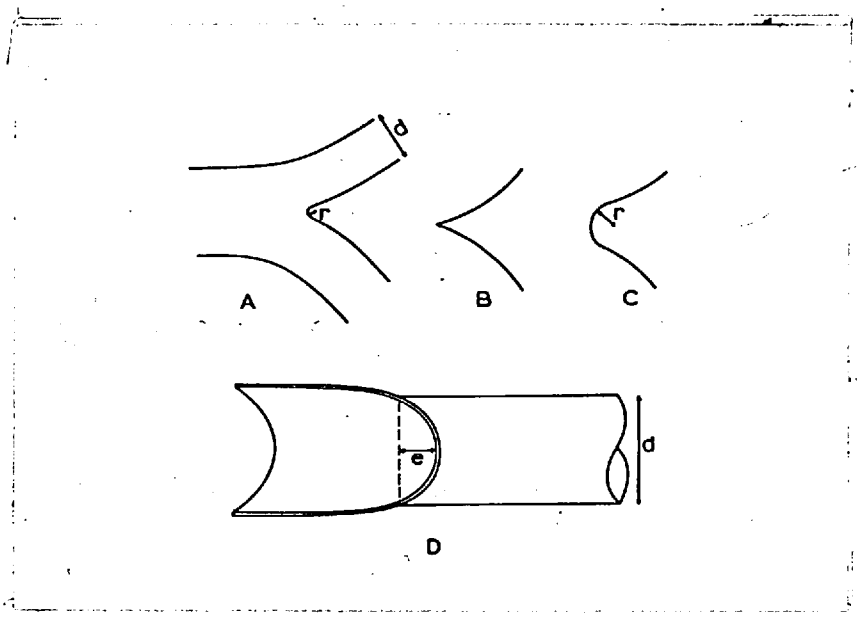


FIGURE 1.8 Geometry of the flow divider in the middle airways.

leading edge is relatively sharp. Figure 1.9 shows the leading edge of the flow divider photographed under bronchoscopy in a normal, living human lung, in order to permit comparison with the cast data. The flow divider is not really a wedge in that the leading edge is not totally perpendicular to the axis of the parent. Instead the flow divider is as shown in part D of Figure 1.8, where $e \leq d/4$.

The walls of the bronchi are relatively smooth, as can be seen in Figure 1.3. The area and perimeter of the slices depicted as (a) in Figure 1.7 were analysed and showed that, on average, the branches are not tapered, but maintain the initial diameter until the last 20% of the branch's length (the transition zone). Figure 1.9ashows repeated diameter measurements down some of the large branches in the middle airways. This figure displays the maximum waviness and tapers found in the middle airways.

This thus describes the typical geometry of a bifurcation. Basically the pattern incorporates three features. The transition zone is a circular tube becoming progressively elliptical in shape, while maintaining a constant cross sectional area. We shall discuss flow in such a tube in Chapter 4. The daughter tube is a circular curved tube with a curvature ratio R/d of between 3.5 to 7. Flow entering such curved tubes will be analysed in Chapter 3. And finally we have the flow divider and section/

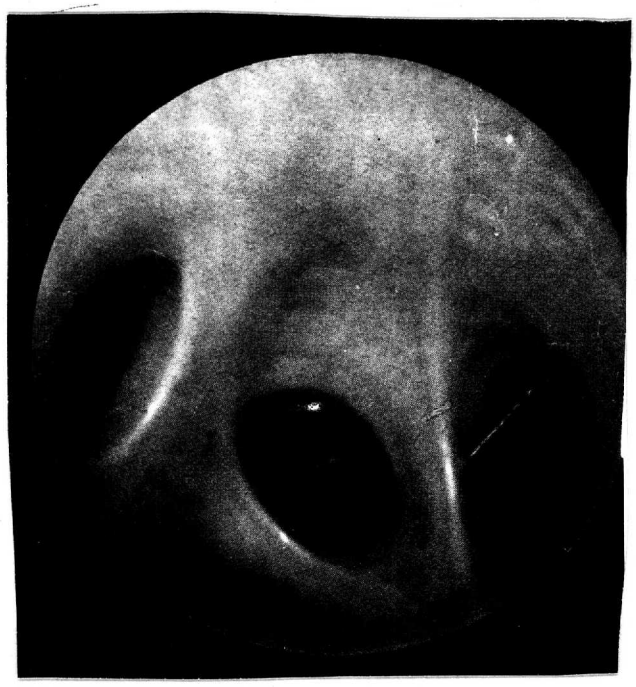


FIGURE 1.9 View down the left lower bronchus in a normal lung showing division into basal branches. Further downstream division is also seen. Note sharpness of flow divider and small waves on wall surface.

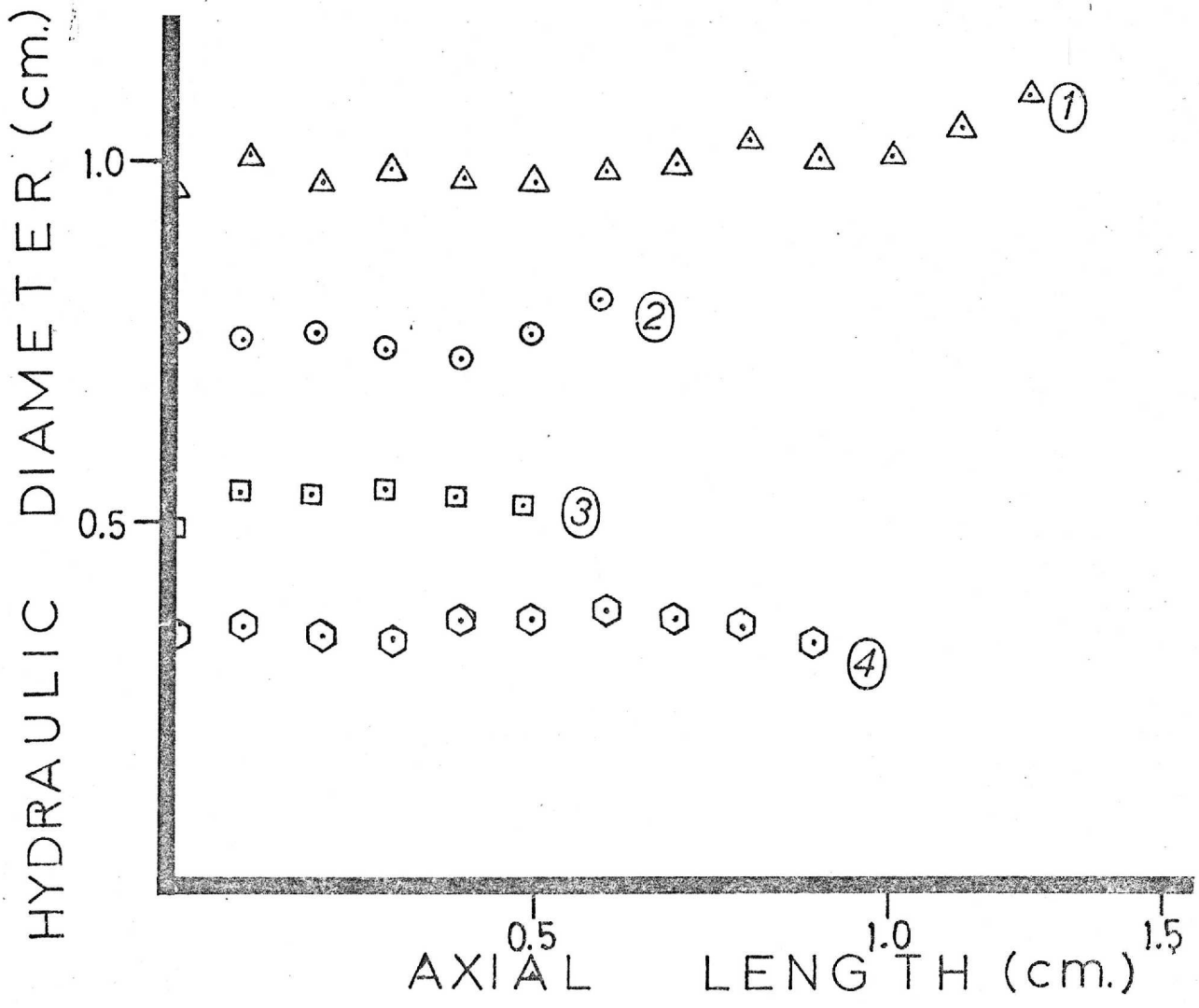


FIGURE 1.9a Repeated diameter measurements of middle airway bronchi within a left lung cast, sliced as shown in figure 1.7 Indicates wavyness of walls and uniformity of diameter. Note increase in terminal 20% of length within (1) and (2). (1) upper left sublobar; (2) upper pre segmental, (3) segmental (4) sub-segmental.

section immediately preceding the divider, where the area increases. The flow within appropriate scale models of the entire bifurcation will be analysed in Chapter 5.

D. General fluid mechanic parameters in the airways

The function in each of the three anatomical lung regions (upper-central, middle and lower airways) is quite different. The upper and central airways warm and humidify the incoming air and convey the gas to the middle airways. In the upper airways the convection patterns are very complex, due to the large geometric variations in size, shape and branching angle. This complex geometrical arrangement limits the applicability of fluid mechanic studies in simplified models. Fortunately the airways are quite large, allowing for studies in life-size replicas of the system. Such studies carried out in replicas made from casts of normal human upper and central airways have been conducted to understand the fluid mechanics in this area: Dekker (10), West (11), Olson & Horsfield (12), Olson (13), Olson & Sudlow (14), Sekihara & Olson (15).

Table 1.1 shows some typical parameters of the convective and diffusive transport processes occurring within the central (trachea to lobar) and middle (lobar bronchi to terminal bronchiole) airways. These values are for a typically quiet respiration of 500 ml/sec inspiration.

Since/

TABLE 1.1

PARAMETERS OF FLOW INDICATING ORGANIZATION OF CONVECTIVE AND DIFFUSIVE FLOW;
INSPIRATION - V = 500 ml/sec.

	Location	Order	Diameter (cm.)	Distance To Alveoli (cm)	Mean Velocity	Reynolds Number (Re)	Peclet Number (Pe)	Dean Number (K)
Central Airways	Trachea	0	1.8	31.1	250	2400	1250	-
	Primary Bronchi	1	1.3	19.1	240	1670	505	3000
	Lobar Bronchi	2	.94	14.9	229	1500	344	2300
		3	.72	11.9	224	860	262	1200
Middle Airways	Segmental Bronchi	4	.57	9.5	127	390	117	600
		5	.45		121	300	88	500
		6	.36		71	150	38	250
		7	.30		63	100	31	180
		8	.24		61	80	24	150
		9	.20		36	40	12	70
	Bronchiole	10	.16	2.8	35	30	9	60
Lower Airways		11	.13		18	12	4	50
		12	.11		16	9	3	40
		13	.09		15	7	2	30
		14	.074		8	3	1	12
		15	.061		8	2.5	0.8	10
	Terminal Bronchiole	16	.050	0.7	7	2	0.6	8

$$Pe = \frac{\text{Convective motion}}{\text{Diffusive motion}} = \frac{\bar{u}\,a}{\kappa}$$

$$Re = \frac{\text{Inertial forces}}{\text{Viscous forces}} = \frac{2a\bar{u}}{\nu}$$

The total cross sectional area of the bronchi rapidly increases with increasing orders of bronchi and therefore the mean velocity of the gas rapidly decreases, as shown in the table. The Reynolds numbers infer a possible turbulence in the trachea, even at this quiet rate of inspiration. But as we go deeper into the lung the flow becomes progressively dominated by viscosity. The range of Reynolds numbers of interest in the middle airways is from about 1000 to 10 for the inspiratory rate shown. The studies of the convective patterns in the upper and central airways show that instabilities in the flow occur down to the lobar level and then are rapidly dissipated. The studies also show that when the flow enters the middle airways the gas has been warmed to body temperature, saturated with water vapour and the axial velocity profile is flat.

The primary function of the middle airways is to convey the inspired air down to the alveoli within this system of increasing cross sectional area. The transport processes in these bronchi become quite complex, being a combination of both convective and diffusive phenomena. This type of process has been studied by Wilson & Lin (16) and Cumming (17). These investigations conclude that the convective organisation has overwhelming influence on the/

the convective-diffusive interaction, both in the middle airways and, surprisingly, also in the peripheral airways. The diffusion process in the smallest airways is markedly affected by the boundary conditions created by the convection-diffusion phenomena in the middle airways (Cumming, 18; Stibitz, 19).

Table 1.1 presents a parameter indicative of the diffusive-convective mode of transport. The Peclet number describes the relative mass movement by convection to that by diffusion. We can see from Table 1.1 that the motion is dominated by convection in the central airways and by diffusion in the lower airways. The Peclet number shown in the table disregards a radial velocity distribution and a radial diffusion process. These radial transport processes can be very important in the axial transport of diffusible material, as shown by the theories of Taylor (20), Aris (21), Lighthill (22) and Chatwin (23).

The curvature of the conduits will influence the amount of secondary flows generated. The Dean number (Dean, 24) will describe the amount of curvature present, and therefore this parameter may be used to infer the magnitude of the secondary flows present. This parameter is shown in Table 1.1 and infers that the curvature of the bifurcations in the central and middle airways produces/

produces strong effects on the secondary motions in the flow.

The process of moving respiratory gases in the peripheral or lower airways is primarily diffusive. The fluid mechanics in this part of the pulmonary tree is a viscous flow as the magnitude of the Reynolds number is of order one or less. Lew & Fung (25) and Lew (26) have recently developed theoretical arguments for the flow in these distal branches.

The first part of understanding the transport processes in the middle airways is to determine the convection patterns; this is the prime aim of this thesis. Since we ultimately wish to understand the diffusive-convective interaction, the features most important to determine are ...

the primary and secondary currents. Other features which are also important are the wall shear, so that particle deposition may be predicted, the energy dissipation and the kinetic energy. The last two features will determine the static pressure within the bronchial lumen, which in turn will predict the calibre of the vessel.

E. Properties of oscillatory flow in elastic tubes

Basically two aspects of the flow can be affected when a periodically varying pressure gradient is imposed on the fluid in an elastic tube. Inertial effects can cause the fluid motion to have phase lags with respect to the pressure gradient. Also pressure changes can be propagated down the tube as a wave whose speed and attenuation will be determined by the elastic properties of the tube wall. The shape and calibre of the elastic tube may depend upon the axial pressure gradient within it. Factors such as these have considerable effect in the vascular and other biological flow systems. This is also true for the flow of air in the pulmonary airways, in that respiration is a periodic function and the airways are elastic tubes. We shall analyse the pulsatility in this section and then the effects of elasticity in the next.

Two possible effects of the oscillatory nature of the flow must be considered:

1) The development of the oscillatory Stokes layer

in/

in relation to the geometrically constrained boundary layer; and

2) The effect of pulsatility on the secondary flows.

The first of these problems has been well studied for both fully developed and developing flow in elastic or rigid straight tubes (Womersley, 29). The basic parameter dictating the effect of the periodically imposed pressure gradient can be easily deduced. Consider a fully developed laminar flow in a straight, rigid tube, where there are no radial motions of the fluid and the velocity, u, along the tube is independent of the axial distance (z). The equation of motion in cylindrical coordinates will then be

$$\frac{\partial u}{\partial t} = -\frac{1}{\rho}\frac{\partial p}{\partial z} + \nu\left(\frac{\partial^2 u}{\partial r^2} + \frac{1}{r}\frac{\partial u}{\partial r}\right)$$

where ρ and ν are the density and kinetic viscosity respectively and the pressure gradient ($\frac{\partial p}{\partial z}$) will be independent of z. Imposing a periodic pressure gradient

$$-\frac{\partial p}{\partial z} = P e^{i 2\pi \varpi t}$$

and writing

$$u = u_1 e^{i 2\pi \varpi t}$$

and non-dimensionalising by $y = r/a$ where a is the radius of the tube, the equation of motion becomes:

$$\frac{d^2 u_1}{dy^2} + \frac{1}{y}\frac{du_1}{dy} - i\frac{(a^2 2\pi\varpi)}{\nu} u_1 = \frac{P a^2}{\mu}$$

The solution is governed by the parameter

$$\alpha^2 \equiv \frac{a^2 2\pi\varpi}{\nu}$$

which/

which is usually referred to as the Womersley parameter. This parameter α is simply the thickness of the Stokes layer $(2\nu/\omega)^{\frac{1}{2}}$ over the thickness of the hydrodynamic layer which would be present in steady flow; in this fully developed laminar case, this is simply the tube radius, a. When α is small, /the flow will be quasi-steady and the particles of fluid everywhere in the tube will respond simultaneously to the applied pressure gradient. When α is large, the motion of the laminae close to the tube wall follows the pressure gradient more closely than the laminae in the tube core which show phase lags to the imposed pressure gradient. In this case viscous effects are confined to a Stokes layer near the tube wall.

This type of flow was first investigated by Richardson & Tyler (27) and Sexl (28), but the problem was analysed in greater depth by Womersley (29). Sexl's problem was of pure oscillatory motion where no net flow occurred in a rigid circular tube.

The analysis for the unsteady fully developed flow has been extended to include a net flow component and also elastic walls by a variety of authors - Morgan & Kiely (30), Morgan & Ferrante, (31) and Atabek & Lew (32). The earlier analyses restrict the study to waves of small amplitude and large wavelength and solve for limiting values of the α parameter. Womersley, and more recently, Atabek & Lew, consider the same problem, but solve for a range/

range of α parameters and with a large range of oscillatory amplitudes and wave lengths. These results show the relatively small importance of the wall elasticity in affecting the motion of the fluid within an elastic tube which has a modulus of elasticity and Poisson ratio (see next section), radius, inertial damping and internal pressure typical of the pulmonary airways (see Figure 9.2, page 184, in McDonald (33)).

The above discussion concerns infinitely long tubes, whereas the airways are tubes of only two to three diameters in length. This series arrangement of short tubes can be thought of as a series of entrance-type flows (Pedley, 34).

A study of unsteady entrance flow in a rigid tube has been conducted by Atabek & Chang (35) for the case of a uniform velocity profile entering the tube. This time dependent velocity is composed of a constant term superimposed on a general periodic function of time. The constant component was taken to be greater than the amplitude of the periodic component, thus preventing any backflow.* Kuchar and Ostrach (36) have extended this study to include elastic

*This situation does not occur in the respiratory system, where the backflow (expiration) is equal to the forward flow (inspiration). Extrapolation of these studied to the pulmonary system is thus probably hazardous.

walled tubing. Both studies yield the velocity distribution and time dependent entrance length. Again the effect of elasticity on the internal fluid motion was small and in general the dependence on the parameter α is similar to the fully developed case. However these studies indicate the existence of an interaction between the Stokes layer and the axial growth of the viscous boundary layer. The magnitude of this interaction is, however, of second order. In general, the steady viscous boundary layer develops faster within an oscillatory flow. This results in a periodically varying entrance length whose mean length is slightly less than the entrance length for a steady flow.

The above analyses of Womersley, Atabek and Kuchar all show that when the magnitude of the α parameter becomes greater than order one, the oscillatory effects start to become significant in dictating the viscous boundary layer and gross organisation of the primary flow within the core of the tube. None of these analyses consider the aspects of a time dependent flow in a tube with secondary flows. Lyne (37) has investigated the secondary flows in a curved circular tube with a pressure gradient along the tube, varying in a sinusoidal manner with respect to time. He develops asymptotic expansions for large values of α. The magnitude of secondary flows are shown to be governed by a parameter, Re_s, similar to a

Reynolds/

Reynolds number, where

$$Re_s = \frac{\bar{u}^2 a}{R \omega \nu}$$

with R the radius of curvature of the tube. Asymptotic theories are developed for large and small values of this parameter. For large values of α (i.e. flow which is predominantly influenced by the periodicity) the direction of the steady part of the secondary flow is shown to be in the opposite sense to that predicted for steady fully developed curved flow (see Chapter 3). This result occurs for all values of Re_s and means that the centrifuging effect is not to force the fluid from the inner to outer wall, as in the steady curved flow case, but instead drives the inner (core) fluid toward the centre of curvature.

This effect becomes significant only at relatively high values of α. In Lyne's solution the directions of secondary flow showed a tendency toward the steady problem at

$$\alpha \leq 16 \quad .$$

In the previous discussion we have noted that the Womersley parameter, α, is simply the ratio of the Stokes layer to the viscous boundary layer in steady flow. To calculate α for the pulmonary system we must therefore known the magnitude of the steady viscous boundary layer at frequent locations within this rapidly branching system of tubes. Neglecting the interaction between a developing boundary layer and an oscillatory pressure gradient (this effect should be small), we can measure the developing

boundary/

boundary layers in steady flow conditions within cast replicas of the pulmonary airways and use this quantity as the length scale in predicting α. Figure 1.10 shows velocity contours taken for one of the steady flow conditions studied within a cast replica of the central and larger bronchi of the middle airways. The boundary layers are shown to be of order 0.25 x radius or smaller. Table 1.2 shows the α parameter in each segment of the typical pathway in the lung described in Figure 1.5 and calculated for quiet* and moderate* respiratory frequency and depth.

The table shows the ratio of boundary layer thickness to tube radius (δ/a) and α parameters calculated using the boundary layer as the length scale (α_δ) and using the tube radius as the length scale (α_a). The results of Table 1.2 show that the magnitude of the α parameter is usually below one and therefore periodicity in breathing probably has little effect on the flow for quiet to moderate respiration. Only in the central airways and using the tube radius as the length scale can we calculate parameters or order one at these breathing frequencies.

We/

*The quiet respiration is defined at an inspiratory volume flow rate of 500 ml/sec and a frequency of one breath each four seconds. This is the breathing pattern when the subject is at rest. Moderate respiration is defined as the respiration at a mild rate of exercise, which is 1000 ml/sec inspiratory flow at a frequency of one breath each three seconds.

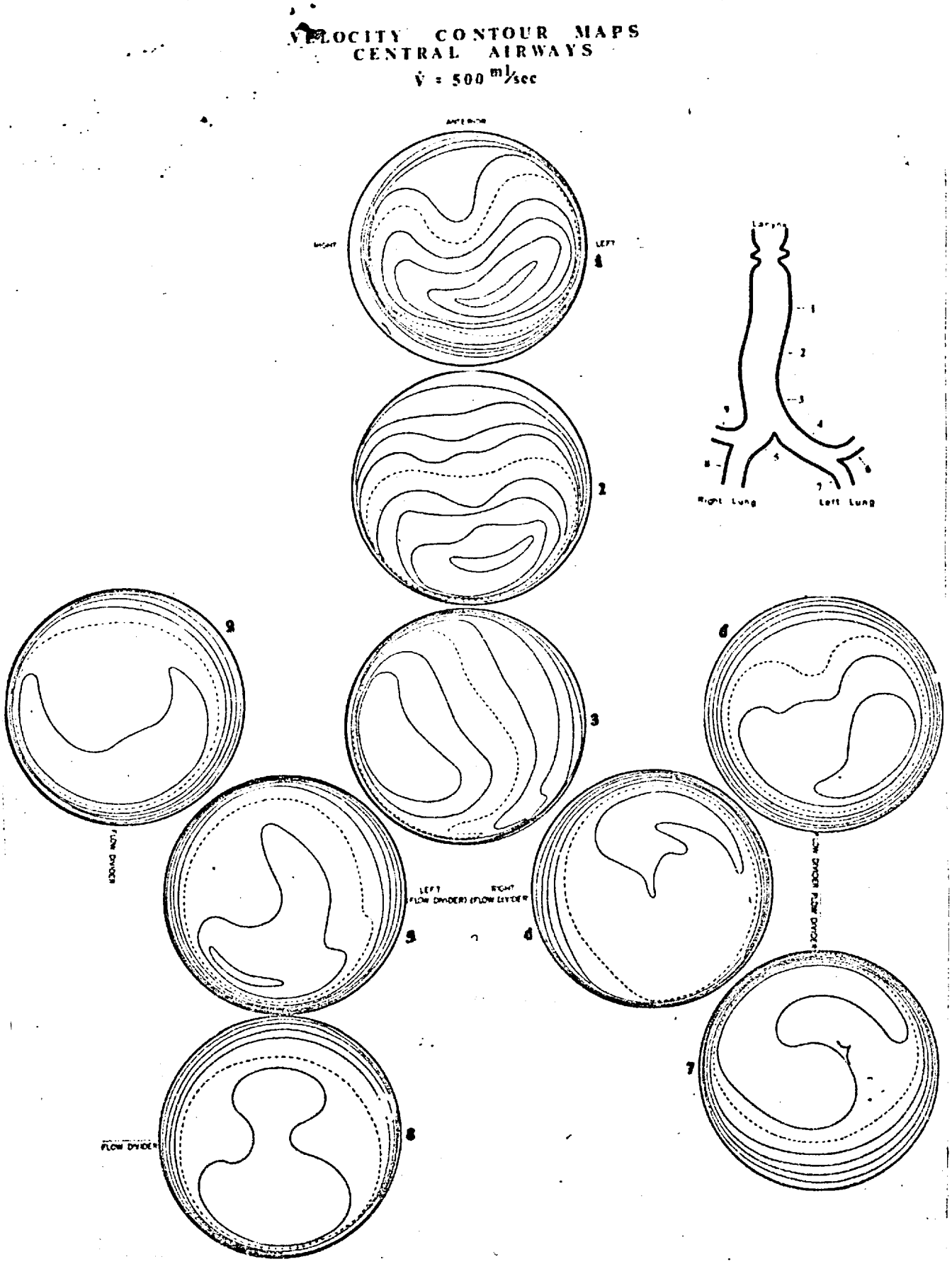


FIGURE 1.10. Velocity contours measured in a cast replica of the central airways with steady flow and a proceeding upper airways cast with appropriate sized larynx. Contours of 0.2 non-dimensional velocity, the dashed contour line is the mean velocity. Velocity typical of a resting, quiet respiration.

TABLE 1.2 WOMERSLEY PARAMETERS IN THE LUNG

Location	Order	Diameter (cm)	Resting Breathing δ/a	Resting Breathing α_s	Resting Breathing α_a	Mild Exercise Breathing δ/a	Mild Exercise Breathing α_s	Mild Exercise Breathing α_a
Trachea	0	1.8	.28	.77	2.75	.45	1.83	4.07
Primary Bronchi	1	1.3	.18	.36	1.99	.20	.59	2.94
Lobar Bronchi	2	.94	.18	.26	1.44	.18	.38	2.12
	3	.72	.24	.26	1.10	.18	.29	1.63
Segmental Bronchi	4	.57	.22	.19	.87	.17	.22	1.29
	5	.45	.25	.17	.69	.20	.20	1.02
	6	.36			.55			.81
	7	.30			.46			.68
	8	.24			.37			.54
	9	.20			.31			.45
Bronchiole	10	.16			.24			.36
	11	.13			.20			.29
	12	.11			.17			.25
	13	.09			.14			.20
	14	.074			.11			.17
	15	.061			.09			.14
Terminal Bronchiole	16	.050			.08			.11

Resting Breath - volume flow of 500ml/sec at frequency of 1 breath each 4 sec (ω = .25/sec)
Mild Exercise - volume flow of 1000ml/sec at frequency of 1 breath each 3 sec (ω = .167/sec)
α_s is Womersley Parameter based on hydrodynamic boundary layer
α_a is Womersley Parameter based on tube radius
δ is the boundary layer measured with steady flow in cast replicas of the pulmonary airways and meaned over the circumference and length of the branch.

We therefore conclude that the fluid mechanics within the bronchial tree are quasi-steady (for both primary and secondary currents) at all but the most rapid breathing conditions.

One other aspect of the periodicity must be considered: that is the pattern of breathing is not a sinusoidal function in time. Fig.1.11 shows the basic shape of the respiratory pattern measured in six young normal subjects. The feature to note is the constant inspiratory flow rate which takes up over 85% (85% to 93% in the six subjects) of the time of inspiration. Therefore we can conclude on these "physiological" grounds that the velocity during inspiration will not be continually changing as in a sinusoidal pattern.* This implies that the preceding arguments about the oscillatory nature of the flow are probably conservative, lending further support to the conclusion that respiration is a quasi-steady flow problem. Instead of an oscillatory analysis, the problem of a suddenly moving flow within a conduit is probably more appropriate to the pulmonary system. This is simply the solution of the Rayliegh layer. The conclusions of such a Rayliegh layer analysis also show that the flow within the middle airways is quasi-steady.

F./

---

*Higher frequency components of the respiratory cycle are neglected.

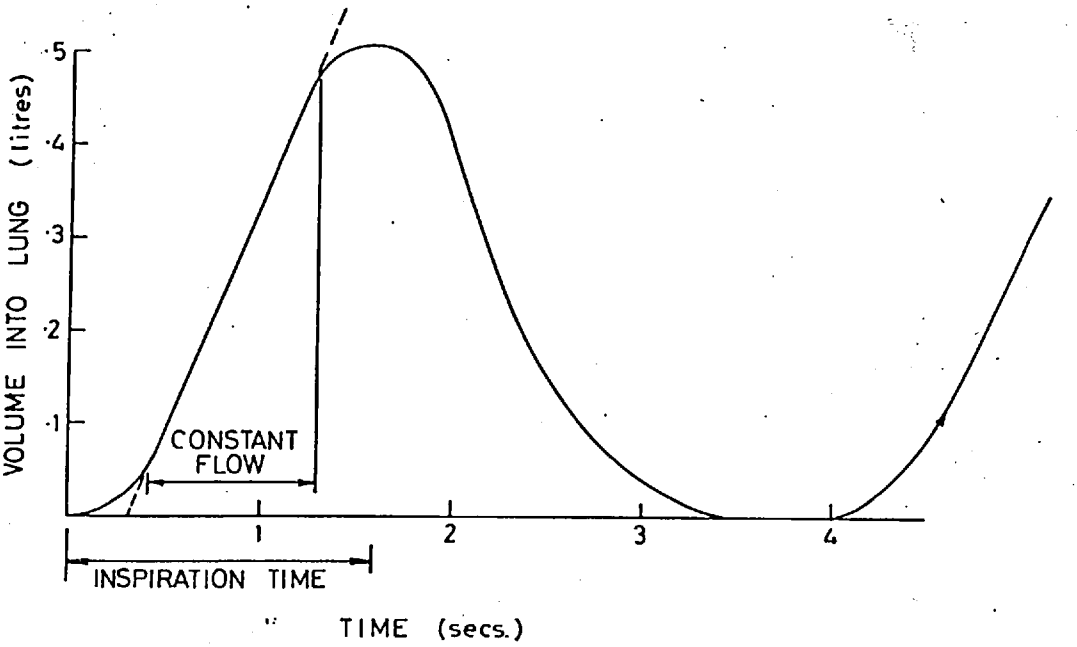


FIGURE 1.11 Pattern of quiet respiration. Note constancy of inspiratory flow.

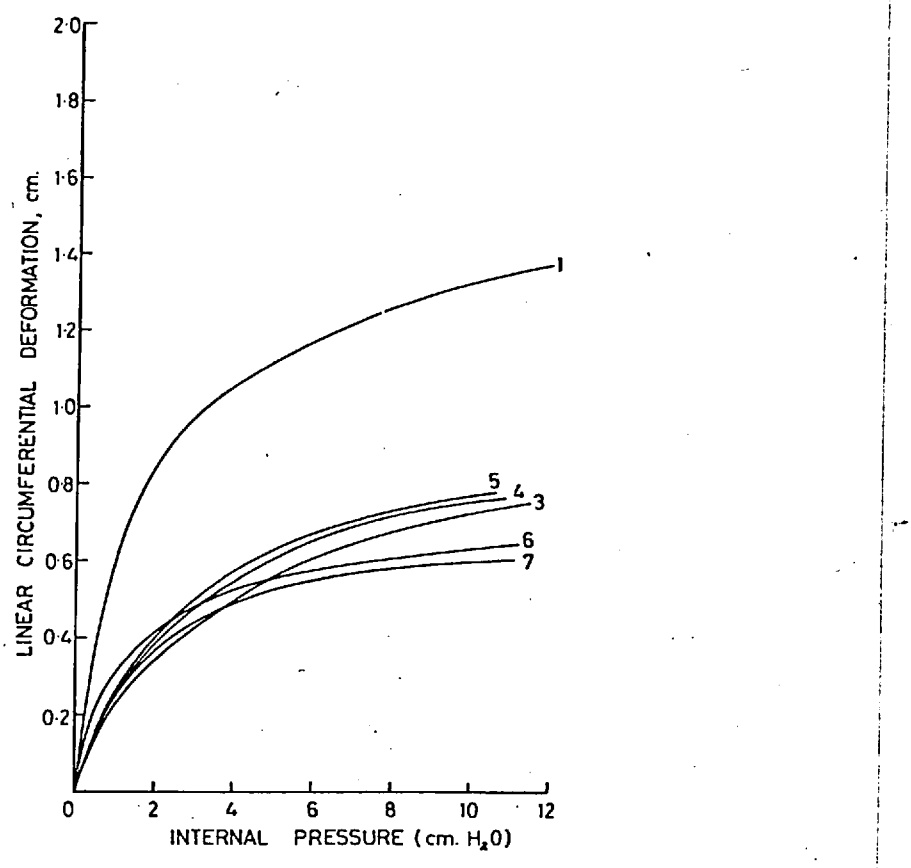


FIGURE 1.12 Linear deformation measured in bronchi removed from normal lung shortly after death. Axial deformation is very small. Numbers refer to order of branches shown in figure 1.5 Note order 1 is not within the parenchyma of the lung. Also note the similarity in tangential deformation although diameters of the tubes differ by a factor of three.

F. The elasticity of the airways and its effect on the flow

The airways in the lung are elastic structures. This is a fundamental property of the bronchial system in that respiration is basically carried out by expanding and contracting the bronchial tree and its distal alveoli. Most of the volumetric change occurs in the most distal air sacs (and highly compliant alveoli) which may expand their volume by 100%, but the bronchi and bronchioles which convey the air to the alveoli also change volume by about 5 to 10%.

The changes in calibre of the bronchi and bronchioles can be easily observed when watching respiration under fluoroscopy and this aspect of respiration has received considerable attention in the physiological and medical literature. It is quite unfortunate that most of this extensive literature cannot be used to develop an understanding of the effects of elasticity on the flow. This is primarily due to the failures of the observers to quantitate the elasticities. Instead the primary aim was to compare in vivo studies of the qualitative volumetric excursion of airways in normal and pathological conditions. Therefore the author set forth to determine the bronchial elastic characteristics which have relevance to the pattern of air flow. During the time of the study which will be discussed briefly here, two other investigations of the elastic/

elastic properties of the airways which have relevance to the internal flow have been published (Hughes, 38; Hyatt, 39) and two studies on the stress distribution in the lung have appeared (Mead, 40; West & Mathews, 41).

The bronchi change calibre during respiration for two reasons. The excursion of the chest wall (i.e. the ribs, etc.) pulls the lung at its periphery, which stretches the alveoli and bronchi within the lung parenchyma. The second reason the bronchi change shape is from the internal fluid mechanics. The alveoli which surround the bronchi are at the downstream end of the flow during inspiration and therefore have a lower pressure than the static pressure within the bronchial lumen. This creates a pressure across the bronchi wall tending to expand the bronchi during inspiration, and will be defined as the transmural pressure. The static pressure within the bronchus will depend upon the viscous dissipation and kinetic energy of the fluid (remembering that the bronchial tree has an expanding area). Assuming that the alveolar pressure remains constant, then the transmural pressure will be directly related to the static pressure within the lumen of the bronchi, which will in turn affect the calibre and shape of the bronchus. This is the basic influence that the fluid mechanics has on the elastic walls in the quasi-steady flow problem.

The expansion of the elastic tube wall will identically follow/

follow the internal axial pressure gradient only if the vessel is very compliant in the axial direction. With an axial component of elasticity the tube wall will distort into a shape which is dependent upon the transmural pressure at the chosen axial position and also dependent upon the state of walls expansion at adjacent axial positions. The distance through which an expansion of the wall at one axial point (from a point source load around the tube circumference) will affect the expansion of some up or downstream position of the tube wall can be defined as a relaxation length, r_l. This distance can be calculated from Timoshenko (42) to be

$$r_l = 0.61a$$

for a circular tube with radius a. This means that the wall of the tube will distort from pressures within the tube an axial distance of 0.5a away. Therefore if the axial pressure gradient is abruptly changing (within a distance less than 0.5 radius) we may expect significant stress concentrations resulting in complex wall configurations. The axial pressure gradient will affect the state of expansion of the vessel, but the shape of the vessel may also have significant effect on the internal flow. The simplest case, of coupling between the elastic and hydrodynamics, is steady fully developed laminar flow in an elastic tube. This was studied by Morgan (43), who showed that the tube radius decreases in size due to the axial pressure gradient. The studies of unsteady, fully developed/

developed flow in distensible tubes have already been discussed. Except for the effect of elasticity on the pressure wave movement, it was shown that the elasticity of the bronchi had little effect on fluid motion in the oscillatory condition other than that expected in the steady conditions.

Kuchar & Ostrach (44) studied the steady entrance flow problem in elastic tubing. The analysis showed that the coupling between wall and fluid mechanics results in a shortened hydrodynamic entrance length, i.e. the flow develops faster.* The elastic entrance length was of the order of a tube radius.

The airways are a rapidly branching network of tubes where a new viscous boundary layer develops at each branching point; somewhat like a series of entrance conditions. In this situation it is possible that changes in the static pressure could occur over very short axial distances creating a very complex wall configuration and coupling between the wall shape and developing viscous boundary layer. To elucidate this possibility, the static pressures within the life-size cast replica of the central and middle airways was measured.

The/

*Not to be mistaken for the similar effect of the oscillatory flow on a developing boundary layer in an elastic or rigid tube, as discussed in the previous section.

The static pressure gradient was also obtained from the large scale bifurcation model studies of Chapter 5 (see Fig. 5.12). Both cases agree approximately with the work of Kuchar & Ostrach (44) in that the axial pressures change with an axial length scale of the order of a tube radius or larger. These results suggest that the elastic bronchi will expand in a simple mode. And this state of expansion can be approximated by assuming that the tube uniformly changes its calibre in response to the mean internal pressure within any one bronchus. I shall use this assumption to develop the equation for the bronchial distortion and analysis of the pressure wave velocity within the elastic walls of the bronchi.

Assuming a circular tube with an isotropic elasticity of E, a wall thickness of h and an initial radius a where

$$\frac{h}{a} << 1$$

and letting Poisson ratio be defined as σ, the equation for the motion of the wall can be simply derived to be (Atabek, 2)

$$\frac{dr}{dP} = \frac{Eh}{r} - P(1-\sigma) - \frac{\sigma T_A}{r} \qquad (1.2)$$

where P is the transmural pressure, changes in this pressure being assumed small, and T_A is the axial stress.

We further assume an internal oscillatory flow where the wave length λ is much longer than the tube radius, a, and only small deformations of the tube walls.

We/ $a/\lambda << 1$

We take the velocity, pressure, and cross-sectional area respectively to be of the form

$$u = u(x,t) = U_o + u_1 e^{jK(x-Ct)}$$
$$p = p(x,t) = P_o + p_1 e^{jK(x-Ct)}$$
$$A = A(x,t)$$

and ignore the inertia of the wall substance. In the above equations, $K = 2\pi/\lambda$, is the wave number and C is the wave speed. U_o and P_o are the mean steady values of velocity and pressure and these quantities are assumed slowly varying with the axial distance x and also uniform across any one cross section.

We can now linearise the equation of motion for the wall and fluid and examine the real parts of the Fourier component. This gives us

$$K(U_o - C)u_1 = -\frac{1}{\rho} K p_1$$

and

$$K(U_o - C)p_1 = -\left(A/\left(\partial A/\partial p\right)\right) K u_1$$

from which we can deduce that

$$C = U \pm C_o$$

where C is the wave speed, U the mean gas velocity and C_o is the wave speed within the elastic wall. Using our thin vessel analysis, we can calculate C_o as:

$$C_o = \left\{ \frac{Eh}{2\rho a} - \frac{P_o}{2\rho}\left[1 - \sigma - \frac{\sigma T_A}{2a\rho} \right] \right\}^{1/2}$$

With Poisson's ratio, σ, set to zero

$$C_o = \left(\frac{Eh}{2\rho a} - \frac{P_o}{2\rho} \right)^{1/2} \qquad (1.3)$$

where/

where the term $P_0/2\rho$ is the initial stress (Atabek, 2) in the bronchial wall caused by the lung expansion during inspiration.

This is then the relation between the wave speed and elasticity in the circumferential direction. The distortion of the cross-section by the mean transmural pressure is of course given by equation (1.2). To calculate these equations, we must determine the magnitudes of the airway elasticity, E. This was done by removing the bronchi and large bronchioles from four normal human lungs taken immediately after death. Each of the 200 bronchial segments were then individually stretched by imposing a series of internal pressures. The change in internal volume was recorded along with the axial deformation. The bronchi have considerable amounts of muscle coating. This muscle was relaxed by bathing the whole preparation in isotonic saline. The walls of a bronchus are a composite of three stretchable fibres, cartilage, elastin and reticular fibres. Each of these fibres has a distinctly different elasticity and it is currently accepted that some of the fibres exist in a wrinkled or wavy unstressed state. Therefore some deformation must occur before these wavy fibres are straightened and start to exhibit their resistance to stretch. This gives rise to the possibility that only discrete areas of the wall take up the stress and that these stressed areas change depending upon which type of fibre/

fibre is taking the current load. To evaluate this possibility each bronchus was "branded" with a tiny hexagonal pattern and the distortion of the pattern was observed microscopically.

Several features of the elastic walls of the airways became readily apparent. The linear axial deformation is very much smaller than the circumferential deformation. This infers a highly anisotropic structure with a relatively rigid axial component. The smaller bronchi are more compliant than the larger ones. This relation is quite definite in that the linear circumferential deformation in all intra-parenchymal airways is equal. And finally the brand distortion showed, apart from the axial to circumferential anisotropicy, that the wall of the bronchi acted as a homogeneous elastic structure.

Figure 1.12 shows the linear circumferential deformation from a variety of small bronchi averaged for the four lungs studied. The orders of the bronchi refer to the Figure 1.5. It can be seen that these structures exhibit elastic characteristics similar to other biological structures. The deformation of the bronchial wall is at first large for a given increment in stress. The walls begin to act as a more rigid structure once the magnitude of stress passes a given value. Biologists normally interpret the preliminary strain as the deformation necessary to unwrinkle the tough elastic fibres. The stress experienced/

experienced by the bronchi under normal fluid mechanic conditions is always less than this "unwrinkled stress" point, and therefore the magnitude of the elasticity can be determined from the initial shape of the curves in Figure 1.12. Table 1.3 shows the Young's Modulus obtained by fitting a straight line to the first part of the stress-strain curve and using the initial cross sectional area of the bronchial wall. Using these values for Young's Modulus the radial deformation calculated using equation 1.2 is simply:

$$\frac{\Delta r}{a} = \frac{Eh}{r} \Delta P$$

where we have neglected the axial stress and prestress terms. The quantity $\frac{\Delta r}{a}$ is the percentage of radial deformation when the transmural pressure is changed by ΔP. The alveoli which surround the intra-parenchymal bronchi will be at the downstream end of the flow and therefore the transmural pressure across the bronchial wall will be equal to the viscous pressure loss occurring in the fluid moving between the bronchus and the terminal alveoli. Two recent analyses of pressure drop in the lungs (Pedley, 34; Olson, 5) are used to predict the viscous pressure loss, and thus the transmural pressure. The percentage of radial deformation exhibited by the wall when changing from a 500 ml/sec inspiration (quiet) to a 1000 ml/sec inspiration (moderate) is calculated and shown in the table. We can see that the deformations which occur when changing the flow conditions by 100% are quite small; being about

1%/

TABLE 1.3

+ Order of Bronchus	Bronchus diameter (initial)	Young's Modulus in circum direction (dynes/cm^2)	% Radial deformation ** Model 1 (%)	Model 2	Wave speed (cm/sec)	Mean Velocity (cm/sec)	Wave Speed / mean vel.	Wave length (cm)
1 *	1.3	9.1×10^4	0.55	0.23	2.13×10^3	2.4×10^2	8.9	1.53×10^3
3	0.72	12.5×10^4	1.24	0.55	2.5×10^3	2.2×10^2	11.2	1.43×10^3
4	0.57	9.1×10^4	1.10	0.25	2.13×10^3	1.27×10^2	16.8	0.81×10^3
5	0.45	6.9×10^4	1.02	0.37	1.86×10^3	1.21×10^2	15.4	0.77×10^3
6	0.36	5.0×10^4	0.85	0.20	1.57×10^3	0.71×10^2	22.1	0.45×10^3
7	0.30	4.75×10^4	0.75	0.27	1.54×10^3	0.63×10^2	24.5	0.40×10^3

* Bronchus of order 1 is not a part of the middle airways and it is not within the parenchyma of the lung.

** The % radial deformation is the deformation of the bronchus when increasing the flow from a quiet inspiration (500 cc/sec) to a moderate inspiration (1000 cc/sec). The deformation going from 0 to 1100 cc/sec inspiration rate is about 25% greater than the given values. Thus the deformations are still about 1% of initial size.

Model 1 was calculated from Pedley et al, and Model 2 from Olson et al.

\+ See table, figure 1.5

1% or less in all cases.

The wave speed in the wall (calculated from equation 1.3) and the mean velocity of the gas for a quiet inspiration are also shown in the table. The wave speed determined in this manner is 10 to 25 times faster than the mean velocity of the gas at quiet inspiration and two to five times faster than the velocity at a maximal rate of inspiration (2500 cc/sec).

We assumed a long wave length for calculation of the wave speed and radial deformation. The wave length can be calculated as $\lambda = \frac{c}{2\pi\overline{\omega}}$ and this is also shown in the table. The wave length predicted in this manner is of the order of 1000 cm while the total length of the bronchial tree is only of order 30 cm in length (see Figure 1.5). We therefore conclude that the pressure gradient will <u>not</u> move as a wave in the pulmonary system, but pressure within the bronchi will simply follow the imposed pressure oscillations almost instantaneously.

One other feature of the elasticity in lungs should be noted. It has recently become apparent that bronchial elasticities obtained by cutting up the lung and stretching the tissue in vitro does not produce similar results to bronchial elasticity measured in vivo. Hughes (38) has recently conducted such in vivo studies, which conflict with the in vitro studies of Hyatt (39). In general,

Hughes/

Hughes found a relatively similar Young's Modulus to those shown in Table 1.3, but he found no anisotropicity, nor any dependence on the elasticity with bronchial size. Hyatt's lung studies showed higher values of E but similar anisotropicity and similar elastic dependence on bronchial size as shown in the table. Hughes and Hyatt used dogs' lungs, while the data for Table 1.3 is from human lungs. Hughes' studies can be arranged to give a Young's Modulus of: $E = 11.7 (10^4)$ Dynes/cm^2 and these values were also used to determine the wave speed and wall deformation. The results are very similar to those of Table 1.3.

We can therefore conclude that the elasticity of the bronchial tree will have little effect on the flow during the inspiration manoeuvres considered in this study. Further, the bronchial dimensions will not deform more than about 1%. This deformation will take place primarily at the points of bifurcation and extend axially for about a distance of one radius.

CHAPTER 2

A pulsed wire technique for measurement of velocities and directions in steady, three-dimensional, low speed flows

This chapter will report a method for simultaneously measuring the velocity and direction of very slowly moving fluids. The technique consists of measuring the time of flight for a cloud of heat moving between two fine wires arranged in parallel. The thermal cloud is produced by electrically heating the upstream wire and sensed by the downstream wire operated as a simple resistance thermometer. The time and location of the maximum response in the sensor wire is used for velocity and direction determination. The chapter will discuss the theoretical behaviour of the probe and the results of some calibration experiments. This chapter will also serve to explain the experimental methods used when operating the pulsed wire probe* in the model flow studies of the following three chapters.

Introduction

During recent years an active interest in the understanding of flows in the human body has motivated the study of laminar motion in highly complex three-dimensional flow/

*Hot wires and wall shear probes are also used in the model studies. The methods used for these instruments and the techniques of data handling will be discussed later.

flow patterns. The available techniques for measurement of such flows, either within the body or in model studies, are inadequate for a variety of reasons. Essentially what is needed is a device which can indicate velocity and direction simultaneously with an accuracy of about 1% for low speeds (the air used in our model studies moved at velocities from 0.1 cm/sec to 100 cm/sec). Furthermore, the instrument must be small and must complete its measurement within a short time interval (to allow for the study of pulsatile flows). The use of a static pitot tube for measurement of such flows is ruled out because of the very low velocities. Hot wire anemometers, with very careful usage, can be used to measure air velocities down to about 5 cm/sec. Below these velocities the natural convection interacts with the forced convection to give ambiguous results. The hot wire can also be used to indicate the direction of the velocity. Unfortunately the ability of the hot wire to sense direction at low velocities is severely limited. Furthermore in three-dimensional flows the hot wire has an ambiguous response from a simultaneous pitch and yaw response. The use of crossed wires does not correct this problem at low speeds.

This paper describes a measuring technique which overcomes these difficulties. The measuring system is quite simple; it consists of two very thin wires positioned parallel to one another and spaced a millimetre or two apart/

apart. The upstream wire is electrically heated with a short pulse of current lasting a few microseconds. This heats the upstream (pulsed) wire to maximum temperatures of about 1000°C. The temperature of the upstream wire then decays through the combined mechanism of forced and free convection to the immediately surrounding gas, radiation to the surroundings, and conduction to the wire supports. The heat diffuses and is convected downstream changing the thermal environment of the downstream (sensor) wire in a characteristic pattern. The downstream wire is operated as a simple resistance thermometer. The time taken between the original pulse and the peak signal in the downstream wire is used to indicate the magnitude of the velocity vector. The direction of flow is sensed by revolving the downstream (sensor) wire around the pulsed wire to find the centre of the thermal wake. At very low velocities a correction has to be made on the directions in the vertical plane due to buoyancy effects. So far only a simple probe mounting is used, which requires that the probe be introduced into the flow at two perpendicular planes so as to obtain all three components of velocity (more complex probe mountings could eliminate this problem). The technique is very sensitive to velocity and direction, allowing for measurements of velocities with an accuracy of less than 0.1 cm/sec (1 cm/sec to > 100 cm/sec) and direction measurements of 2°-5° at velocities below 10 cm/sec and less than 0.5° at velocities above 10 cm/sec. The instrument is unfortunately/

unfortunately very delicate and measurement is difficult until one becomes very proficient at replacing and aligning the thin (0.0001" dia.) wires.

The technique described here is not original, it was first described by Bauer (45) for application to very high speed flows; both Sato (46) and Kovasznay (47) had previously used a somewhat similar approach. More recently, Bradbury & Castro (48) in England and Tombash (49) in the USA have been using modified versions of Bauer's original probe for use in highly turbulent flows. All of these authors have used the instrument in a velocity range where the probe works essentially by convection with thermal diffusion having secondary influence. The problem we present is just opposite to the previous efforts. We have essentially a thermal diffusion problem being influenced by convection.

Kovasznay and Sato made heated wake velocity measurements for air speeds of about 500 cm/sec. Both workers made use of a sine wave to heat the upstream wire. They would then move the downstream wire with respect to the upstream wire to detect the length of one heat wave. The air velocities and heating frequencies were kept low so that the thermal inertia of each wire did not interfere with the measurement.

Bauer used a method with two hot wire anemometers parallel to each other. He briefly analysed the response characteristics/

characteristics of his system, including the thermal inertia of the two wires, but since his velocities were very high (he wanted to measure velocities in the range of 75 metres/sec) he was able to partially dismiss the effects of thermal diffusion. Bauer used his instrument to indicate both the magnitude and direction of the flow. The principle of operation was to have two fine wires arranged in parallel on a mounting device which could allow the whole device to rotate along its axis and also to allow the upstream wire to be moved separately. The upstream wire was heated with a pulse of current, while the downstream wire was operated as a simple resistance thermometer. The time taken for the initial part of the tracer of heat to reach the second wire was measured and used to indicate the magnitude of the velocity. The direction of flow was measured by first rotating the probe about its axis and noting the yaw response on the resistance thermometer wire. Next the upstream wire was moved until the wake of the upstream wire passed over the downstream sensory wire.

Bradbury noted that the response of Bauer's probe would be very sensitive to flow direction so that in a turbulent flow most of the heat pulses would miss the downstream sensor wire. To overcome this problem, Bradbury rearranged the wires of the device so that they were perpendicular to one another. He also added a third wire to the instrument, another sensor wire, so that he had sensors on both sides of the pulsing wire. This allowed

him/

him to investigate reversed flows. Bradbury made a more detailed analysis of the response of his probe at velocities large enough so that thermal diffusion made only a small effect (about 2 metres/sec for the probe geometries he used). Bradbury's method was to determine the initial response of his sensor (resistance thermometers) wires. Without thermal diffusion or any interference of the convection by the viscous wake, the time of flight for the heated cloud of gas would correspond to the time taken between the pulse and the initial response of the down-stream sensor wire (see Figure 2.1). Without the above effects the sensor wire would indicate a discontinuity in slope at the time of flight. The response would then rise with a linear slope determined by the thermal inertia of the sensor wire (and complicated somewhat by conduction to the sensor wires supports). The thermal diffusivity would tend to eradicate this discontinuity. Both Bradbury and Castro, and Tombash, analysed this convection-diffusion problem to indicate when the effects of diffusion would have passed the sensor wire. They could then extrapolate back to zero response to indicate the time of flight. Tombash did this by digitising his response curve and analysing the shape of the curve on a computer. Bradbury & Castro simply used a convenient voltage offset to indicate a time close to the time of flight.

We use much lower velocities and therefore the effect of thermal diffusion has a very large influence on the sensor/

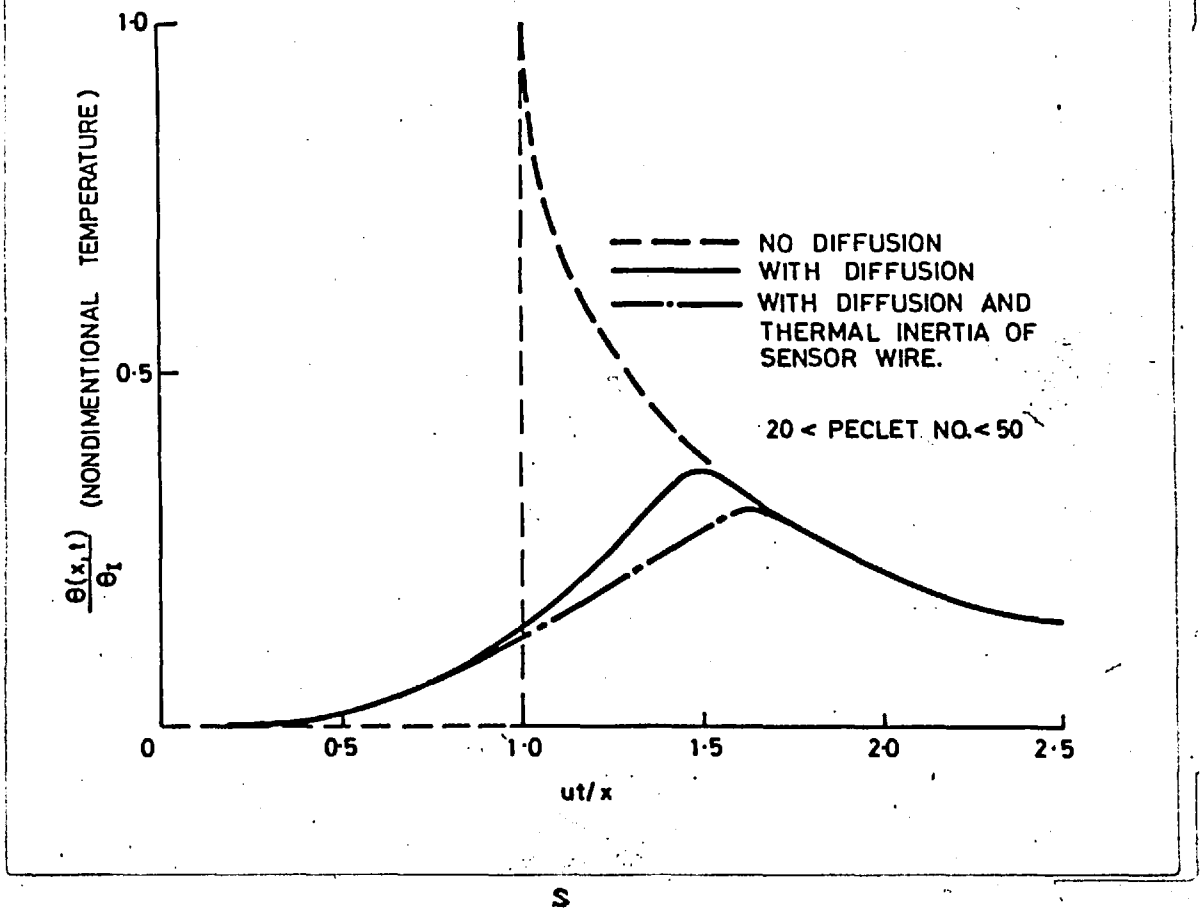


FIGURE 2.1 Response of sensor wire with conditions of differing thermal diffusion and sensor wire inertia. Solid line indicates approximate magnitude of sensor wire response with Peclet number between 20 and 50.

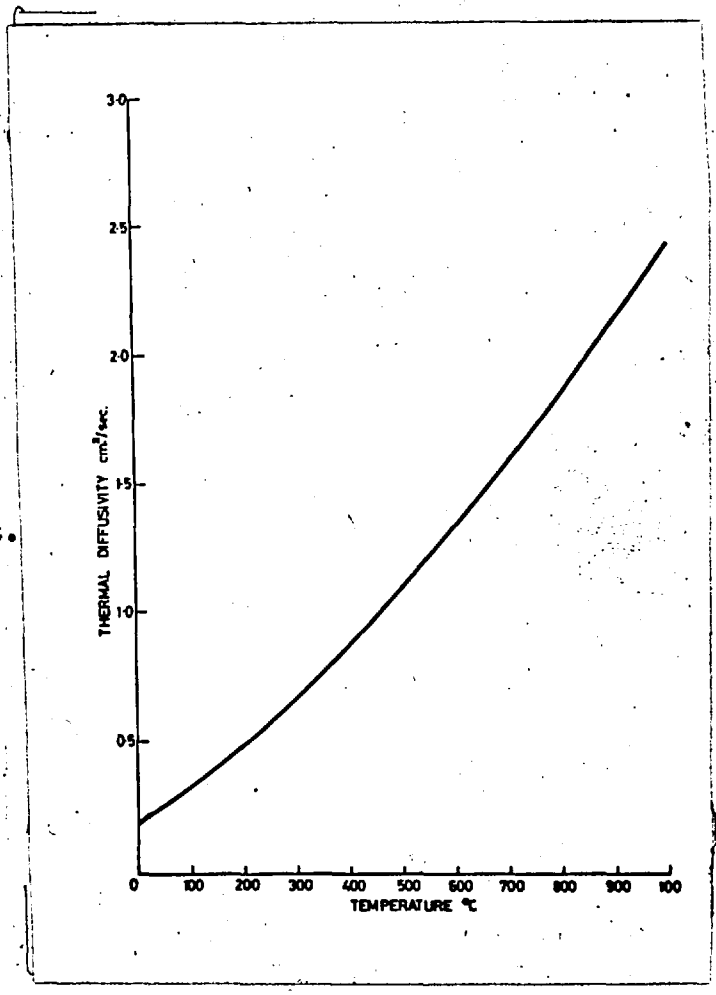


FIGURE 2.2 Thermal diffusivity of air as function of temperature. Note the five fold change over the temperature range of interest.

sensor wire response. In essence we have a thermal diffusion problem being distorted by convection. The initial response of the sensor is hopelessly insensitive to convection at lower velocities. This is in contrast to the location of maximum signal which is quite sensitive to the fluid velocity. Predicting the location of the maximum signal in the sensor wire for a messy diffusion-convection problem such as this is much more difficult than predicting the initial response. We must predict the whole shape of the thermal cloud produced by the pulsed wire, the distortion of this cloud by diffusion and the convection pattern of the viscous wake, and then the response by the sensor wire. We experimentally investigated the parameters of this problem so as to get the analysis down to a manageable complexity. The most sensitive aspects of this problem are: the temperature decay pattern of the pulsed wire (i.e. the initial shape of the thermal cloud), the convection-diffusion interaction, the variable diffusivity diffusion and the natural convection (or buoyancy) effects. The thermal inertia of either wire, the viscous wake of the pulsed wire, and the conduction of heat to the wire supports are of much less importance for the velocities considered in this study.

Analysis

In the general case the temperature of a fluid is governed by the equation:

$$\frac{\partial \theta}{\partial t} + \mathcal{U} \cdot \nabla \theta = K(\theta) \nabla^2 \theta$$

(2.1)

Two assumptions have to be made before we can attempt approximate solutions to this equation. The first assumption is that the velocity is uniform everywhere. This seems to be a good assumption considering the velocities and Reynolds numbers, based on the wire diameters, used in this study. The wake produced by the wire will be either a Stokes or an Oseen wake ($Re \approx O(10^{-2})$). Since the wires are spaced more than 1300 diameters apart, the effect of the wake on the temperature field around the sensor wire must be small. Furthermore this type of problem, i.e. a diffusion in a convection field without a boundary, is very difficult to solve. Taylor (20), Aris (21) and many subsequent authors (51, 52, 53, 54) have solved the problem of simultaneous diffusion and convection for various convection patterns with a solid boundary around the flow. This allows the assumption of almost complete diffusional mixing in the radial direction. Lighthill (22) solved a special case of the diffusion convection problem where a solid boundary was not necessary, i.e. for flow within a tube, radial diffusion was small. The solution could only be found for a parabolic velocity distribution. Chatwin (23) has recently obtained an expression valid for radial diffusions between the limits required by Lighthill's and Taylor's theories. If the velocity distribution in the wake of our pulsed wire was assumed to be an inverted parabola, the Lighthill solution to simultaneous/

simultaneous convection-diffusion might be applied. This was not attempted because of the strong influence of the thermal diffusivity (κ) which can easily overwhelm any effect contributed by the velocity distribution in the wake.

The second major assumption is that the thermal diffusivity, κ, is not a function of temperature. As can be seen in Figure 2.?, temperature has a very strong influence on κ for the air temperatures of interest (0-1000°C). Crank (55) discusses the various solutions, both closed form and iterative methods for solving the diffusion equation with a variable diffusivity. Fujita (56) creates several variable transformations to solve the diffusion equation where the diffusivity depends on temperature in special ways. These transformations are not possible with the addition of the convective terms in the diffusion equation. The only satisfactory method of handling the variable diffusivity was an empirical one. This will be discussed in the next section.

Using the above two assumptions, the equation for a line source of heat within a uniform velocity field with a constant diffusivity is:

$$\frac{\partial \theta}{\partial t} + u\frac{\partial \theta}{\partial x} = \kappa\left(\frac{\partial^2 \theta}{\partial x^2} + \frac{\partial^2 \theta}{\partial y^2}\right) \qquad (2.2)$$

The solution to such an equation can be obtained by the method of instantaneous line sources (Carslaw & Jaeger, 57, p.261) with $\phi(t)$ as an arbitrary source term, located at (x', y')

$$\theta(x, y, t) = \frac{1}{4\pi\kappa}\int_0^t \phi(t')\, e^{-r^2/4\kappa(t-t')}\, \frac{dt'}{t-t'} \qquad (2.3)$$

where $\Theta(x,y,t)$ is the temperature at the chosen point, $r^2 = [(x-Ut)^2 - x'^2] + (y-y')^2$ and $\rho c \phi(t)$ is the rate per unit time at which the source liberates heat.

Two solutions to this problem are readily available depending on $\phi(t)$. If $\phi(t)$ describes an instantaneous line source of heat equal to a strength of Q, the solution is:

$$\Theta(x,y,t) = \frac{Q}{4\pi\kappa t} e^{-r^2/4\kappa t} \qquad (2.4)$$

Also if $\phi(t)$ is a constant equal to Q', the solution is:

$$\Theta(x,y,t) = \frac{-Q'}{4\pi\kappa} Ei\left(\frac{-r^2}{4\kappa t}\right) \qquad (2.5)$$

where

$$-Ei(-x) = \int_x^\infty \frac{e^{-u}}{u} du$$

is the exponential integral. We shall see that the solution of our problem will tend toward equation (2.4) for the low Peclet number case (low velocities) and tend toward solution (2.5) at the high Peclet number case (high velocities), with moderations for thermal inertias of the measuring devices. Therefore, the precise function of the heat loss from the source (i.e. $\phi(t)$) is critical for understanding this diffusion-convection problem.

Heat loss from the pulsed wire

In general the heat balance in the pulsed wire can be written -

Heat electrically generated = heat stored in wire
+ heat lost due to the stream via forced convection and natural convection
+ heat lost to surrounding due to radiation
+ heat lost to supports via conduction.

The electrical heat generation is produced by a pulse of essentially constant voltage for a time of 22 to 150 micro seconds. These pulses are shown in Figure 2.4. The time of heating is much less than the time constant of the temperature decay of the wire. Therefore we can assume that during the time of the electrical pulse the wire is heated instantaneously and uniformly without losing any heat to the surroundings.

The temperature rise of the wire can then be described by $$\left(\frac{V}{\ell}\right)^2 \Delta t = \rho c \sigma(\theta)\, \theta$$

where $$\sigma(\theta) = \sigma_0 \left(1 + \alpha\theta + \beta\theta^2 + \gamma\theta^3 + \epsilon\theta^4\right)$$

and σ_0 is the wire resistivity at room temperature, ρ the wire density, C the specific heat of the wire, and θ the temperature increase from room temperature. V is the voltage, l the wire length and Δt is the pulse duration. Nickel was chosen as the material for the pulsed wire (for reasons to be discussed later). The coefficients α, β, γ, and ϵ are coefficients of a five power least squares fit to the σ vs. θ curve for nickel obtained from a variety of sources (58, 59, 60). The mathematical relation fits the curve of Fig. 2.3 within 1%. The high power fit is needed because nickel undergoes a magnetic transformation at about 360°C. Figure 2.5 indicates the temperature obtained by various pulses of different voltage or time duration.

At high velocities past the wire, forced convection plays a predominate role in the temperature decay of the pulsed wire. At the lower velocities considered within this/

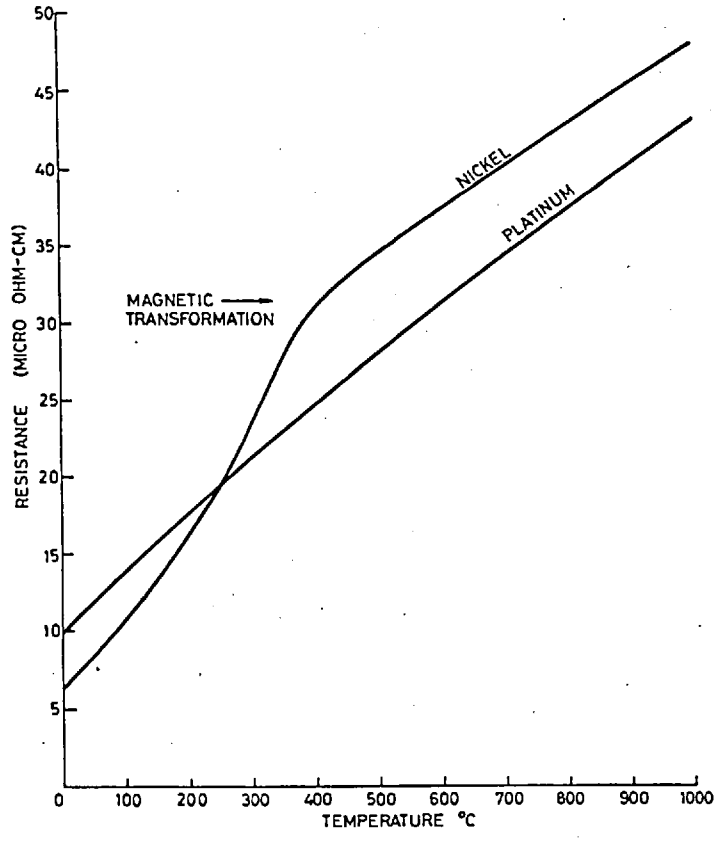


FIGURE 2.4 Voltage pulses across a nickel wire, 12.5 microns and 0.4cm in length with room temperature resistance of 3.3ohms. Note symmetry of pulse with rise and fall time of within 5 micro seconds.

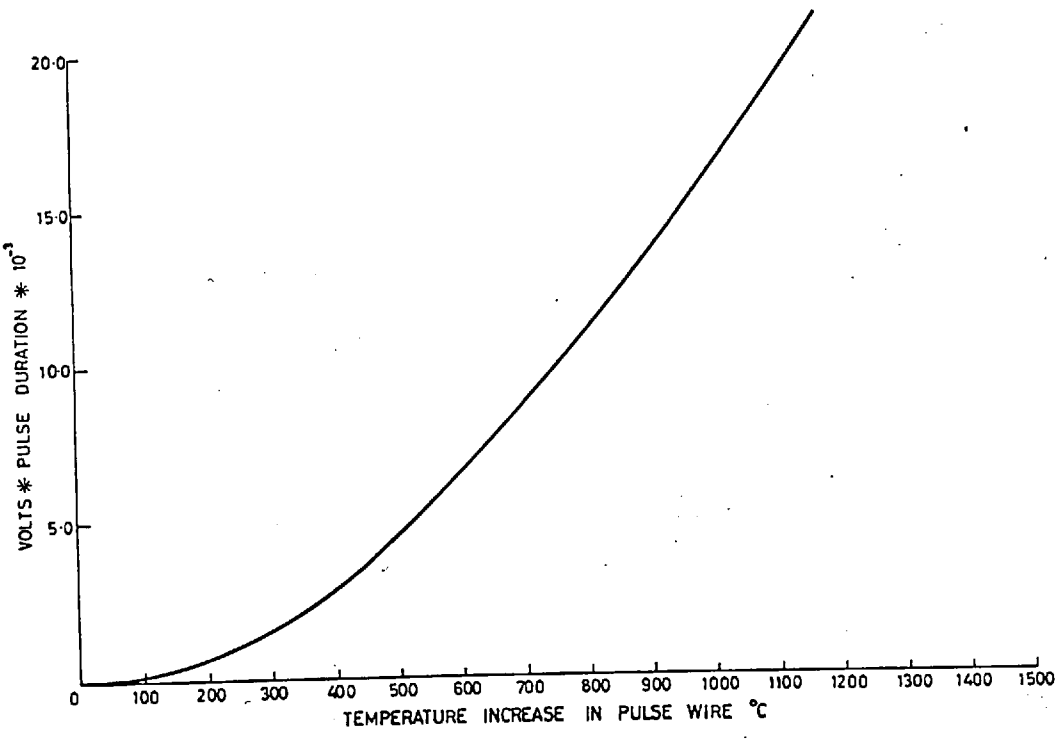


FIGURE 2.5 Temperature increase in a 12.5 micron diameter nickel wire as a function of the voltage and time duration of pulse.

this study, the heat is lost from the pulsed wire via a combination of several modes of heat transfer. We shall consider each of the modes of heat loss in more detail.

The heat lost to the wire supports by conduction has been considered by Collis & Williams (61) and analysed by Bradbury & Castro (62). These efforts show the importance of the aspect ratio (diameter/length) for conductive heat loss to the wire supports. As we have mentioned, the volumetric size of the probe is constrained so the probe may be used for internal flow problems. This constraint therefore defines the length of the pulse wire, creating a relatively low aspect ratio of about 200 to 400. A solution of the steady state convective-conductive heat loss problem will help display this dependence on aspect ratio.

If we assume that the Nusselt number is constant along the length of the wire, and that the thermal conductivities K_w and K_a are not functions of temperature (which is a poor assumption for K_a); then the <u>steady-state</u> solution to the heat loss can be obtained.

$$\frac{i^2 r_w}{A_1} = \pi K_a Nu (\theta_w - \theta_f) + K_w \frac{\pi d^2}{4} \frac{d^2\theta_w}{dx}$$

(steady electrical heating) = (forced convection losses) + (conduction losses)

We can integrate this equation and rearrange to get

$$Nu = \frac{\frac{i^2}{A}\int_0^l r_w \, dx}{\pi K_a \int_0^l (\theta_w - \theta_a)\, dx} - \frac{2K_w}{\pi K_a} \frac{\frac{\pi d^2}{4} \left.\frac{d\theta}{dx}\right|_{x=0}}{\int_0^l (\theta_w - \theta_a)\, dx}$$

where the first term in the righthand side is the Nusselt number/

number if no conduction was present. With $\alpha \nabla_0 \theta_w = \nabla_w - \nabla_0$ we can solve for the second term in equation (2.6) in terms of the Nusselt number (with no conduction) if we make the following assumptions:

1) The wire is not heated to high temperature, which is a poor assumption for the pulsed wire.
2) Aspect ratio is large ; $\ell/d >> 1$
3) $K_a/K_w >> 1$

The boundary conditions are

$$\frac{d\theta_w}{dx} = 0 \qquad \text{at } x = 0$$

$$\theta_w = 0 \qquad \text{at } x = \pm \ell/2$$

and the solution is

$$\frac{\frac{d\theta}{dx}\Big|_{\ell/2}}{\int_{-\ell/2}^{\ell/2} \theta_w \, dx} \approx \frac{-2}{\ell d} \left(\frac{K_a}{K_w}\right)^{1/2} Nu^{1/2}$$

We can rearrange equation (2.6) to give

$$Nu_m \approx Nu + C\, Nu^{1/2}$$

with

$$C = d/\ell \left(\frac{K_w}{K_a}\right)^{1/2}$$

where Nu is the Nusselt predicted assuming no conduction losses and Nu_m is a type of Nusselt number incorporating both convective and conductive heat losses. Some typical values of C are--

$$C \approx 0.10 \qquad \ell/d \cong 400$$

$$C \approx 0.20 \qquad \ell/d \cong 200$$

This infers that the correction due to conduction for wires with a constant heat source may be approximately 10% to 20% for the steady state condition with the aspect ratios (ℓ/d) appropriate for the probes used in this work. The problem/

problem using a non-steady heat source will be less affected by the conduction term than the above steady problem. A solution to the non-steady heat loss problem can be obtained from Carslaw & Jaeger, p.135 -

$$\theta = \theta_w \frac{\cosh x (\eta/K_w)^{1/2}}{\cosh \ell (\eta/K)^{1/2}} - \frac{4\theta_w}{\pi} \sum_{n=0}^{\infty} \frac{(-1)^n e^{-\eta t - \frac{K_w(2n+1)^2\pi^2 t}{4\ell^2}}}{(2n+1)\left[1 + \frac{4\eta\ell^2}{\pi^2 K_w(2n+1)^2}\right]} \cos\frac{(2n+1)}{2\ell}\pi x$$

where $\eta = \frac{Nu\,\pi d}{c\rho\varpi}$, and the second term in the equation has the conduction loss within it.

We can see that the magnitude of the terms in this series rapidly approaches zero with increasing n so we take only the first term. Within this term

$$e^{-(\eta + K_w\pi^2/4\ell^2)t}$$

we have contribution from the forced convection η and conduction $K_w\pi^2 t/4\ell^2$. Now using typical values of η, K_w, d, l, we find that the time scale for heat loss due to conduction (with the lowest aspect ratio, 200) is of order ¼ second where the time scale for loss due to convection is of order 1/80. This implies that the heat is lost predominately through convection in the initial phase after a heated pulse. Therefore we can conclude that the conductive heat losses to the supports is not significant in the transient state and becomes about 10% to 20% of the forced convection loss in the steady state. We will therefore neglect conduction for our transient problem.

The above arguments concern the <u>amount</u> of heat lost via conduction as compared to convection. An aspect of the conduction related to the above arguments and important to/

to the yaw response (see last section of this chapter) of the probe's operation, is the distance on each end of the pulsed wire which will be cooled by conduction to the wire supports. The characteristic distance of heat diffusion along a rod to an infinite sink is approximately

$$x \cong \sqrt{K_w t}$$

where K_w is the wire thermal diffusivity and t the time of diffusion. Using a time for diffusion equal to the time constant of temperature decay experimentally found (see later) in the pulse wires, we obtain

$$x \cong 0.02 \text{ cm}.$$

With the length of the pulsed wire equal to about 0.5 cm we conclude that the distance cooled by conduction at each end of the wire will be approximately 5% of the wire length.

The heat loss from the pulsed wire due to radiation can be considerable since the initial temperature of the wire is quite high. Furthermore the heat loss will depend on the temperature to the fourth power (as opposed to all the other mechanisms of heat loss which are a function of the temperature to the first power). This means that the temperature decay function of the pulsed wire, the $\theta(t)$, can be significantly altered by radiation.

Imbedding the conduction and natural convection heat losses into the forced convection term, our energy balance can now be written:

$$(\rho c \ell)\frac{d\theta}{dt} = -\frac{K_a Nu^*}{d}(\theta-\theta_a) \quad - \quad K^*(\theta^4-\theta_a^4)$$

(combined conduction, natural and forced convection) (radiation)

where Nu* is a Nusselt number corrected for conduction to the supports and natural convection, and K* contains the Stefan-Baltzman constant and emissivity for the surface of the probe wire.

If we let $\tau = \left(K_a Nu^*/\rho c d\ell\right) t$

$\delta = K^*/K_a Nu^*/d$

$\theta_a^4 \ll \theta^4$

then

$$\frac{d\theta}{d\tau} + (\theta-\theta_a) + \delta\theta^4 = 0$$

If we assume $\delta \ll 1$ we can then expand the temperature in powers of δ, $\theta = \theta_0 + \delta\theta_1 + \delta^2\theta_2 + \cdots$

Substituting for θ and separating powers of δ we have:

$$\left[\frac{d\theta}{d\tau} + \theta_0 - \theta_a\right] + \delta\left[\frac{d\theta_1}{d\tau} + \theta_1 + \theta_0^4\right] + O(\delta^2) = 0$$

Solving for θ_0

we have $$\frac{d\theta}{d\tau} + \theta_0 - \theta_a = 0$$

$$\theta_0 = \theta_a + (\theta_I - \theta_a)e^{-\tau}$$

where we have used the initial condition, at

$$\tau = 0 \qquad \theta_0 = \theta_I$$

Solving for θ_1

$$\frac{d\theta_1}{d\tau} + \theta_1 + \left[\theta_a + (\theta_I - \theta_a)e^{-\tau}\right]^4 = 0$$

with the initial condition $\theta_1(0)=0$, and using Laplace transforms the solution for θ_1 is

$$\theta_1 = \theta_a^4(e^{-\tau}-1) + 4\theta_a^3(\theta_I-\theta_a)(-\tau e^{-\tau}) + 6\theta_a^2(\theta_I-\theta_a)^2(e^{-2\tau}-e^{-\tau}) + 4\theta_a(\theta_I-\theta_a)^3\left(\frac{e^{-3\tau}}{\tau} - \frac{e^{-\tau}}{\tau}\right) + (\theta_I-\theta_a)^4\left(e^{-4\tau}/3 - e^{-\tau}/3\right)$$

Combining the zeroth and first order solution, we have

$$\Theta = \Theta_a - \delta\Theta_a^4 + e^{-\tau}\left\{\underline{(\Theta_I-\Theta_a)} + \delta\Theta_a^4 - 6\delta\Theta_a^2(\Theta_I-\Theta_a)^2 - 2\delta\Theta_a(\Theta_I-\Theta_a)^2 - \underline{\frac{\delta}{3}(\Theta_I-\Theta_a)^4} - 4\tau\delta\Theta_a^3(\Theta_I-\Theta_a)\right\} + \underline{6\delta\Theta_a^2(\Theta_I-\Theta_a)^2 e^{-2\tau}} + \underline{2\delta\Theta_a(\Theta_I-\Theta_a)^3 e^{-3\tau}} + \underline{\frac{\delta}{3}(\Theta_I-\Theta_a)^4 e^{-4\tau}} \qquad (2.7)$$

where the three underlined terms are the most important. If we take a Nusselt number appropriate for very low velocities past our heated wire and an emissivity for a corroded nickel wire, we can approximate the coefficients on each of the exponentials in the above equation. This approximation gives the order of magnitude of δ as

$$\delta = O(10^{-8})$$

which implies that the zeroth and first order expansion solution presented above is probably accurate. Using this δ the coefficients of each exponential for an initial pulsed wire temperature (Θ_I) of about 500°C are approximately

$$\Theta \cong \Theta_a + e^{-\tau}\left\{\underline{5(10^2)} - 10^{-3} - 10^{-1} - \underline{5(10^2)} - 10^{-5}\right\} + e^{-2\tau}(10^{-3}) + e^{-3\tau}(10^{-1}) + e^{-4\tau}\underline{(5(10^2))}$$

This shows that the two terms in the coefficient on $e^{-\tau}$ are about equal in magnitude at this Θ_I, but opposite in sign. The coefficient on $e^{-4\tau}$ is also of about the same magnitude but at this initial pulsed wire temperature the $e^{-4\tau}$ term will have somewhat greater influence than the other/

other terms. At temperatures above $\theta_I = 500^{o}C$ the term will dominate and below this value of θ_I (for the low convection rates chosen) the $e^{-\tau}$ will dominate. At higher convection rates the dominance of $e^{-\tau}$ will extend to somewhat higher temperatures. This brief analysis is obviously not needed to arrive at the conclusion that at high temperatures radiation will be the primary mode of heat loss and at lower temperatures convection will dominate the problem. The analysis simply allows a quantification of this obvious conclusion. This quantification is important because at higher convection rates a strong influence from radiation occurs at temperatures slightly higher than the pulsed wire's operating temperature. While at lower convection rates the influence of radiation extends down into the operating temperatures of the pulsed wire and exhibits its effect in the rate of thermal decay of the pulsed wire. The conclusions to the temperature decay of the pulsed wire are that initially the slope of a θ vs. time curve for the pulsed wire should be four times the "steady state" slope produced by the convection alone. And that a smooth transition should occur between the decay rate of $e^{-4\tau}$ to the decay rate of $e^{-\tau}$; i.e. the terms $e^{-3\tau}$, $e^{-2\tau}$, etc. This also indicates that for low convection rates the decay rate will be a function of temperature.

The heat loss to the fluid via natural convection is very difficult to analyse mathematically and very sensitive to the wire orientation with respect to the horizontal and

to/

to the direction of forced convection. Yih (63, 64) and Cebeci (65) produce mathematical analysis of the natural convective losses and the velocity field induced by these buoyancy forces with no simultaneous forced convection. The Grashof numbers based on the wire diameter and mean temperature are shown in Table 2. Yih indicates that for these Grashof numbers the natural convection from a horizontal line source is in a laminar state, creating a low heat loss and very small velocities. Assuming very low forced convection the heat loss from natural convection has been theoretically solved by Cole & Rashko (66), Kassoy (67) and Mahoney (68), assuming an Oseen wake. Hodnett (69), Collis & Williams (61, 70) and Owen & Pankhurst (71) have empirically analysed the heat loss from fine wires due to natural convection with and without the presence of forced convection. Collis & Williams indicate that the natural convection is not significant provided

$$Re > Gr^{1/3}.$$

For our system this means a velocity of greater than 5 cm/sec. For Reynolds numbers below this value the forced and free convection have an interaction which greatly depends on the orientation of the wire. Since the probe is to be used in flows with significant secondary currents, the orientation of the forced convection will vary with position within the flow field. We therefore include the natural convection heat loss with the forced convection, predicting the overall heat loss from the empirical studies already quoted.

Forced convection will be the major mode of heat loss at velocities above 5 cm/sec and at wire temperatures below about 500°C. Many investigators have analysed the problem of forced convection heat loss from wires. Theoretical work has been conducted by Cole & Roshko assuming a constant property continuum fluid. The measurements of Collis & Williams however show that the Cole & Roshko result overestimated the Nusselt number, also that the Oseen-type analysis yields only the zeroth-order term in an asymptotic expansion for Nusselt number. More recently the theory has been advanced by making matching asymptotic expansions of the flow and thermal field around an infinite wire by Kaplun (72), Lagerstrom (73) and Proudman (74). More important for our problem, where the wire temperature is quite high, Chang (75), Kassoy (67) and Aihara (76) have analysed the heat loss with variable fluid properties due to temperature. It is shown that for high temperatures the Nusselt number greatly decreases from the predictions extrapolated from low temperatures.

Many investigators have empirically studied the loss of heat from wires due to forced convection. Most important for the range of wire Reynolds numbers of interest are King (77), Hilpert (78), Collis & Williams (61), Davies & Fisher (79), Aihara (76) and Bradbury & Castro (62). The heat transfer law proposed by Collis & Williams for the wire Reynolds number range $0.02 < Re < 44$ is given by

$$Nu \left(\frac{\theta_m}{\theta_a}\right)^{-0.17} = 0.24 + 0.56\, Re^{0.45} \qquad (2.8)$$

Aihara shows that for high wire temperatures the Nusselt number predicted by this equation is too high by between 10 to 25%. The relationship predicted by equation (2.8) seems however to describe accurately the forced convection aspects of our experiments.

Figure 2.6a shows the temperature of the pulsed wire as a function of time for the indicated initial temperature and velocity of air past the wire. These temperatures were obtained by measuring the resistance in the wire as a function of time after initially being pulsed to a variety of initial temperatures. You will note that the initial slope of the decay is four times the later slope and that a smooth transition occurs between these two rates of decay. The straight line indicated as c-w is the decay rate predicted by the Collis & Williams relation for the prescribed velocities and temperature loadings. The temperature decays are shown for several other initial temperatures in Figure 2.6b with zero velocity past the wire. Figure 2.6c exhibits the temperature decays from several initial temperatures with a velocity (59 cm/sec) past the wire which is approximately mid-range for the scale of velocities for which the probe is designed to measure. It can be seen that radiation ceases to be a major contribution to heat loss with wire temperatures below 300°C. Equation (2.8) can be made to fit the measured temperature decay accurately.

The/

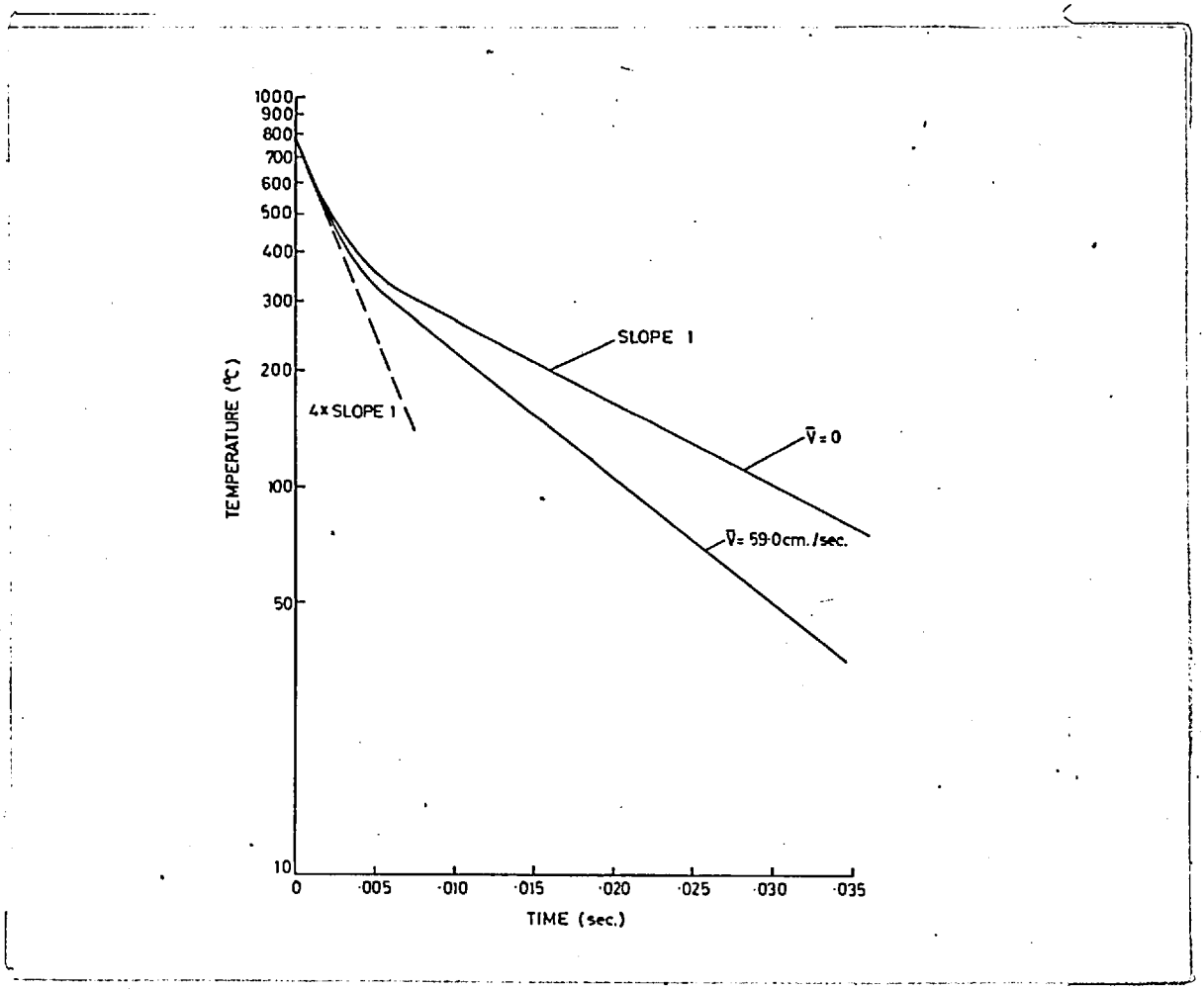


FIGURE 2.6a Measured temperature decay of pulse wire as a function of time for two velocities past the wire.

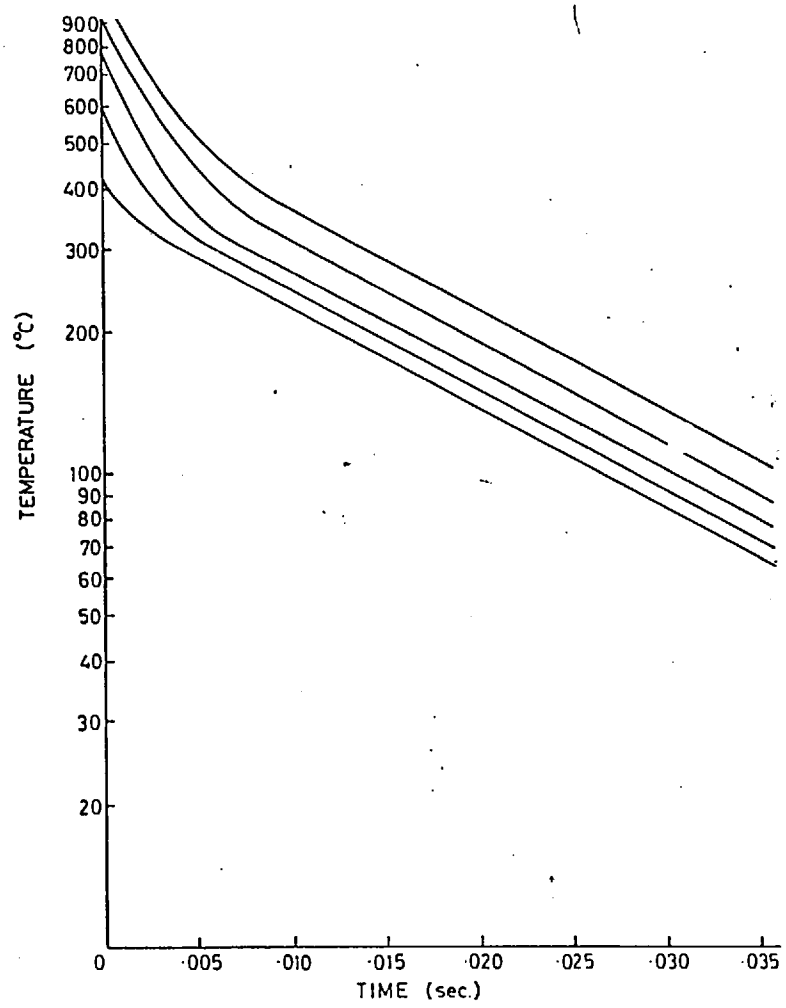
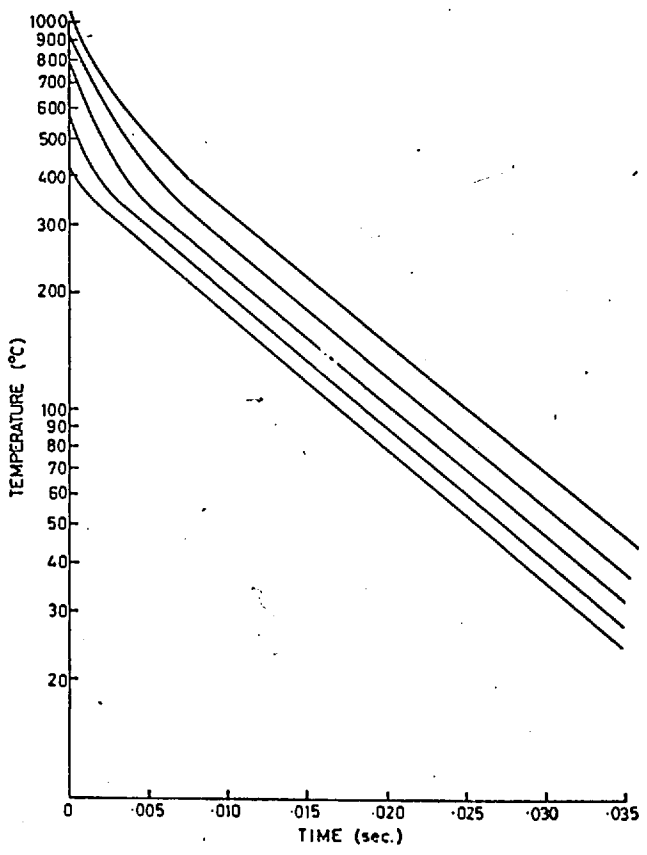


FIGURE 2.6b Measured temperature decay of wires at several initial temperatures with zero velocity past the wire.

FIGURE 2.6c Measured temperature decay of wires at several initial temperatures with velocity of 59.0 cm/sec past wire. Reynolds number based on wire diameter and viscosity at room temperature is 3.8



The use of several powers of the exponential decay will unfortunately cause difficulties in the ultimate solution of the diffusion equation (2.1). Therefore a single power exponential was fitted via a least squares method to the empirical decay rates. Figure 2.7 shows the resultant single exponential curve fitted to the measured temperature decay for a convenient initial temperature. Figure 2.8 shows the measured time constants obtained in this "fitted" manner as a function of velocity. The dashed line is the time constants predicted from Collis & Williams, equation (2.8).

We can conclude that the temperature in the pulsed wire as a function of time will be approximated by the equation

$$(\theta_w - \theta_a) = (\theta_I - \theta_a)\, e^{-t/\tau_p} \qquad (2.9)$$

where θ_I is the initial temperature and τ_p is the empirical time constant which depends on the Nusselt number and wire temperature.

The magnitude of the decay time constant is of importance for the solutions to the diffusion equation (2.1). When the velocity is low past the pulsed wire the time for the temperature decay in the pulsed wire will be about five times shorter than the time for diffusion between the pulsed and sensor wire (i.e. 0.012 sec vs. 0.060 sec). This allows the assumption of an instantaneous source for/

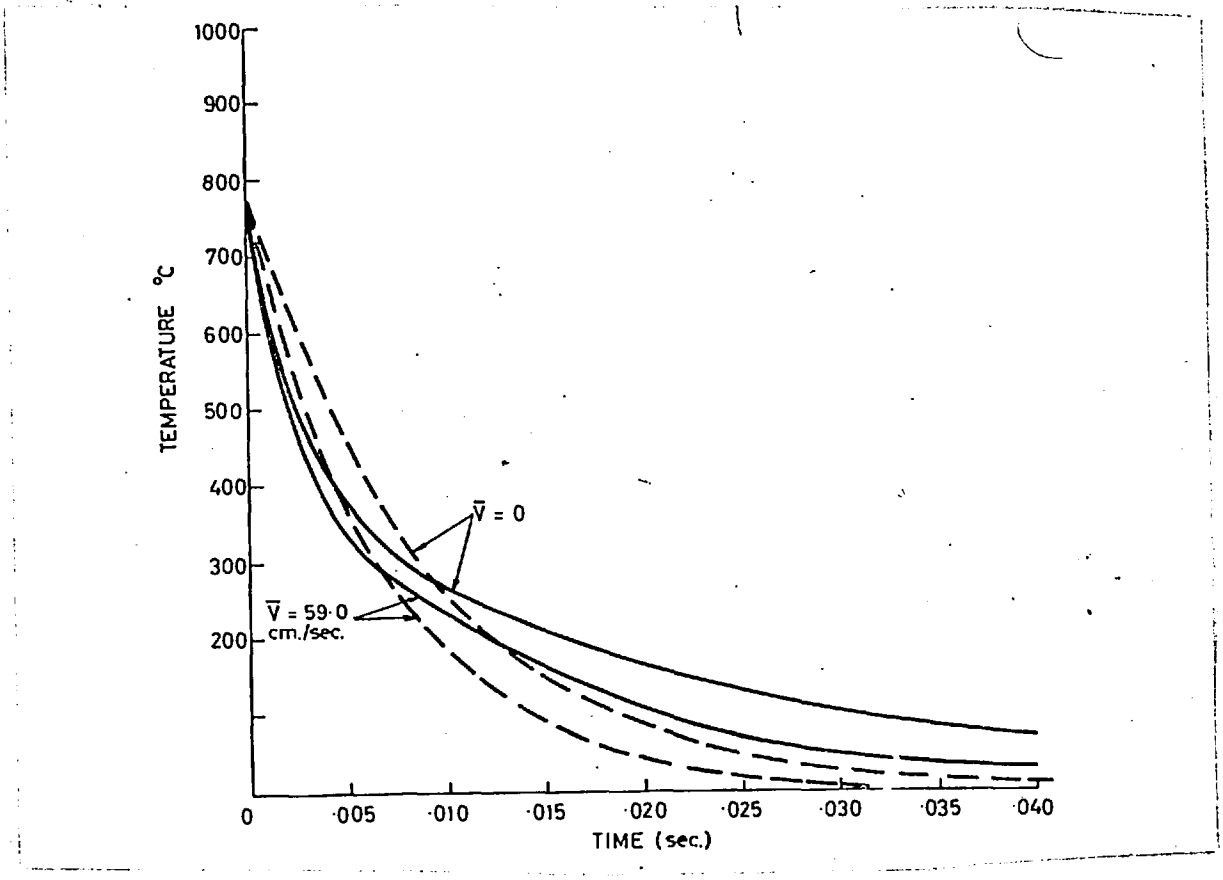


FIGURE 2.7 Single exponential equation fitted to measure temperature decay. Dashed line is fit while solid line indicates measured data. The fit for the initial temperature showed the greatest discrepancy from measurement.

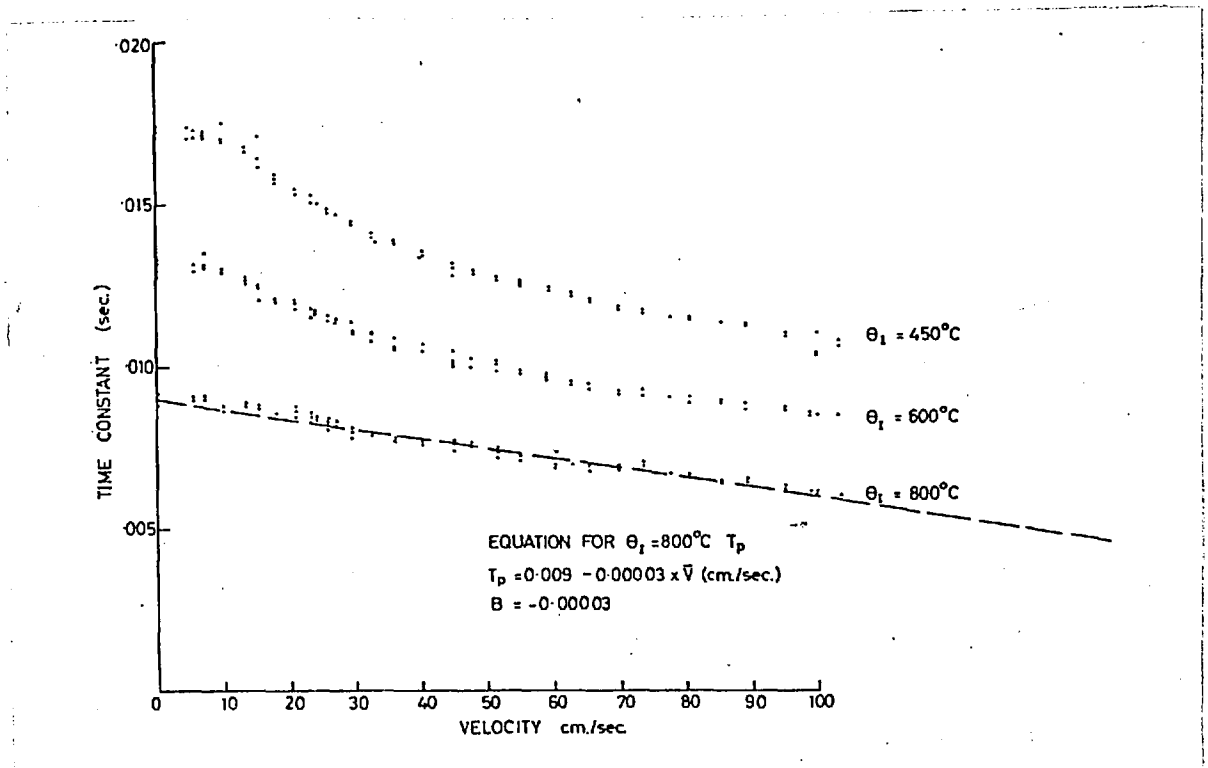


FIGURE 2.8 Time constants of a single exponential function fitted to measured temperature (via least squares method) as a function of initial temperature and velocity past the wire. Dashed line in the figure is the relation used in the theoretical solutions.

for the solution of equation (2.1) at the very lowest velocities. At high velocities the time for temperature decay of the pulsed wire is several times longer than the convection time between the two wires. Therefore the solution will tend toward a continuous heat source as the fluid velocity becomes infinitely large.

Another problem which involves the convective heat transfer between a flowing fluid and a wire is important in the operation of the pulsed wire technique. This problem involves the transient condition between the warmed fluid and the sensor wire, operated as a simple resistance thermometer. Since this problem is similar in nature to the heat loss in the pulsed wire it will be briefly treated here.

The temperature of the heated air when it reaches the sensor wire is much lower than the initial temperature of the pulsed wire. Therefore many of the difficulties involving radiation in the pulsed wire do not occur in the sensor wire. Furthermore since a much smaller wire is used the aspect ratio of the sensor wire is very high, eliminating any conductive losses to the supports. Empirical investigations were carried out with the sensor wire operated at much lower temperatures than the pulsed wire, to determine the magnitude of the transient thermal state in the sensor wire. As expected, the temperature decay is a function of e^{-t/T_s} and the Nusselt numbers derived from/

The time constant are accurately predicted by the Collis-Williams relationship./ from the time constant/can be calculated from the equation

$$T_s = \frac{\rho_s c_s d^2}{4 K_a Nu}$$

where Nu is the Nusselt number predicted by (2.8). For the wire used in the probes the T_s is of order .0005 or less. The time constant with this size wire is approximately one to two orders of magnitude smaller than the diffusion time indicated by the probe (.05 to .005). Therefore we shall neglect the transient response of the sensor wire and assume that it responds instantaneously to the temperature of the gas surrounding it.

Solution of the diffusion equation for the high and low velocity cases

Using the source term described in the previous section we can scale the diffusion equation (2.1) and solve for two cases.

Scaling equation (2.1) with the distance between the wires $L = \sqrt{x^2 + y^2}$ and the characteristic convection time, $t_c = L/U$ we obtain the dimensionless equation

$$\Theta_\tau + P\,\Theta_\xi = \Theta_{\xi\xi} + \Theta_{\eta\eta} \qquad (2.10)$$

where $\Theta \equiv (\theta - \theta_a)/\theta_a$ is the dimensionless temperature,

$\xi \equiv y/L$, $\eta \equiv x/L$ are the coordinates scaled by the distance between wires,

$\tau \equiv t/(L/U)$ is the time scaled by the convection time between wires,

$P \equiv \frac{UL}{K_a}$ is the Peclet number, i.e. the/

the ratio of diffusion time to convection time. (K_a is the thermal diffusivity of air.)

The boundary condition to be applied at the origin is that heat is supplied by the pulsed wire (per unit length) at a rate given by

$$q = \pi K_a Nu \hat{\theta}_I e^{-\tau/\tau_p}$$

where Nu is an adjusted Nusselt number derived from the empirical heat loss measurement described in the previous section, $\hat{\theta}_I$ is the dimensionless maximum temperature of the wire, and the dimensionless decay time $\tau_p \equiv \frac{T_p U}{L}$ is a function of both the voltage pulse and the velocity u.

The other boundary condition is

$$\Theta \longrightarrow 0 \quad \text{at} \quad (\eta^2 + \xi^2)^{1/2} \longrightarrow \infty$$

The solution to (2.10) is

$$\Theta(\xi, \eta, \tau) = \frac{Nu}{4} \int_0^\tau \hat{\theta}_I e^{-(\tau - \xi')/\tau_p} e^{-\frac{P}{4}\left\{\frac{(\xi - \xi')^2 + \eta^2}{\xi'}\right\}} \frac{d\xi'}{\xi'} \quad (2.11)$$

This integral can now be evaluated for two cases to give the instantaneous temperature throughout the fluid. Making our assumption that the sensor wire responds instantaneously to the temperature of the fluid around it, the measured sensor wire temperature together with its position can be related through this solution to the speed and direction of the flow.

Consider first the direction of the flow. Notice that η, the distance of the sensor wire from the axis of the flow, appears/

appears in the integral only in the term $exp\left\{\frac{-P\eta^2}{4\xi'}\right\}$. This is a positive monotonically decreasing function of $|\eta|$. Therefore, the signal should be a maximum for $\eta = 0$. That is, the direction of the flow (in the plane perpendicular to the two wires) can be determined by rotating the sensor wire about the pulsed wire until the maximum signal is obtained; i.e. the thermal wake and the viscous wake are in line. This is true except at low velocities where the buoyancy forces acting on the warmed gas as it moves from the pulsed to sensor wire cause the thermal wake to be angled upward from horizontal. We shall discuss this in more detail in the subsequent sections. We shall neglect this very low flow region ($u < 3$ cm/sec for the probes used).

Apart from maximising the signal, the most easily measured property of the sensor wire signal is the time to signal maximum. We will show that this quantity can be related to the speed of the flow. In what follows we assume that the signal has been maximised and the sensor wire is on the axis of the flow.

The time from the initiation of the pulse to the maximum temperature measured by the sensor wire located at $(\xi,\eta) = (1,0)$ is the time at which the time derivative of the temperature is zero. From equation (2.11) this is the time determined from the equation

$$\frac{\tau_p}{\tau} e^{-\frac{P}{4}\frac{(1-\tau)^2}{\tau}} = \int_0^{\tau} e^{-(\tau-\xi')/\tau_p} e^{-\frac{P}{4}\frac{(1-\xi')^2}{\xi'}} \frac{d\xi'}{\xi} \qquad (2.12)$$

This integral equation cannot be solved analytically but asymptotic solutions can be obtained for $\frac{\tau_p}{P} \ll 1$ and for $P \gg 1$.

The two parameters for expansion are picked so that the range of velocities for which the solutions hold almost join, or, for some cases, the two ranges overlap. This is important for our particular problem because we wish to predict the instrument's behaviour for Peclet number ranges from low through to high values. If we use a low and a high Peclet number as our two expanding parameters then the solutions leave an intolerably large gap where neither solution is at all useful. Further the Peclet numbers only became less than order one at velocities less than 1 cm/sec, for the particular range of wire spacings chosen. Therefore the low Peclet number expansion is not of much interest for our problem.

Solution for low velocity

As we have discussed in the previous sections, the measured τ_p, the dimensionless decay time of the pulse wire, is a small number compared to the dimensionless time to the maximum signal in the sensor wire for low velocities. We use this fact to obtain an asymptotic solution of equation (2.11).

For/

For the particular case of a delta function source (i.e. an instantaneous pulse) the temperature given by equation (2.3) has a maximum at $\tau = \frac{p}{4} \equiv \delta$ (i.e. see equation (2.4)). It is convenient, therefore, to rescale the dimensionless time in equation (2.11), letting

$$\tau = \delta\tau' \qquad \text{and} \qquad \xi = \delta\xi'$$

$$\frac{\tau_p}{\delta\tau'} e^{-\frac{(1-\delta\tau')^2}{\tau'}} = \int_0^{\tau} e^{-\frac{\delta}{\tau_p}(\tau'-\xi')} e^{-(1-\delta\xi')^2/\xi'} \frac{d\xi'}{\xi'} \quad (2.13)$$

Assuming that $\tau_p/\delta << 1$ (observe that this ratio is independent of velocity), the integrand is very small for all ξ' except $\xi' \approx \tau'$. Defining the new variable of integration,

$$\xi' = \tau' - \frac{\tau_p}{\delta}\xi''$$

we can expand the integrand in powers of τ_p/δ. The equation becomes

$$\frac{\tau_p}{\delta\tau'} e^{-\frac{(1-\delta\tau')^2}{\tau'}} = \frac{\tau_p}{\delta} \int_0^{\frac{\delta\tau'}{\tau_p}} e^{-\xi''} e^{\frac{(1-\delta\tau'+\tau_p\xi'')^2}{\tau'-\tau_p/\delta\xi''}} \frac{d\xi}{\left(\tau'-\frac{\tau_p}{\delta}\xi''\right)}$$

$$\simeq \frac{\tau_p}{\delta} \int_0^{\delta\tau'/\tau_p - \xi''} e^{\exp\left\{-\frac{1}{\tau'}(1-\delta\tau'+\tau_p\xi'')^2\left(1+\frac{\tau_p\xi''}{\delta\tau'}+\left(\frac{\tau_p\xi''}{\delta\tau'}\right)^2+\cdots\right)\right.} \times\left(\frac{1}{\tau'}\left[1+\frac{\tau_p\xi''}{\delta\tau'}+\left(\frac{\tau_p\xi''}{\delta\tau'}\right)^2+\cdots\right]\right) d\xi''$$

If we examine the exponential we find that it can be rearranged to separate the orders of $\frac{\tau_p}{\delta}$.

$$\exp\{\} = \exp\left\{-\frac{1}{\tau'}\left[(1-\delta\tau')^2 + \frac{\tau_p}{\delta}\left(2\delta(1-\delta\tau') + \frac{(1-\delta\tau')^2}{\tau'}\right)\xi'' + \left(\frac{\tau_p}{\delta}\right)^2\left(\delta^2 + \frac{2\delta}{\tau'}(1-\delta\tau') + \frac{1}{\tau'^2}(1-\delta\tau')^2\right)\xi''^2 + O\left[\left(\frac{\tau_p}{\delta}\right)^3\right]\right]\right\}$$

$$= \exp\left\{-\frac{(1-\delta\tau')^2}{\tau'} - \frac{\tau_p}{\delta}\frac{(1-\delta^2\tau'^2)}{\tau'^2} - \left(\frac{\tau_p}{\delta}\right)^2\frac{\xi''^2}{\tau'^3} + O\left[\left(\frac{\tau_p}{\delta}\right)^3\right]\right\}$$

Now substituting into equation (2.13) and expanding in $exp(\tau_p/\delta)$ and $exp(\tau_p/\delta)^2$ terms, and cancelling from both sides, we are left with

$$1 = \int_0^{\delta\tau'/\tau_p} e^{-\xi}\left[1 + \frac{\tau_p}{\delta}\left(\frac{1}{\tau'} - \frac{(1-\delta^2\tau'^2)}{\tau'^2}\right)\xi'' + \left(\frac{\tau_p}{\delta}\right)^2\left(\frac{1}{2}\frac{(1-\delta^2\tau'^2)^2}{\tau'^4} - \frac{1}{\tau'^3} + \frac{1}{\tau'^2} - \frac{(1-\delta^2\tau'^2)}{\tau'^3}\right)\xi''^2 + O\left[\left(\frac{\tau_p}{\delta}\right)^3\right]\right] d\xi''$$

With some rearranging we can evaluate this integral. We note that all terms involving $e^{-\delta\tau'/\tau_p} << \left(\frac{\tau_p}{\delta}\right)^3$. The equation now becomes

$$1 = 1 + \frac{\tau_p}{\delta}\left(\frac{\delta^2\tau'^2+\tau'-1}{\tau'^2}\right) + \left(\frac{\tau_p}{\delta}\right)^2\left[\left(\frac{\delta^2\tau'^2+\tau'-1}{\tau'^2}\right)^2 + 1 - \frac{2}{\tau'}\right] + O\left(\left(\frac{\tau_p}{\delta}\right)^3 e^{-\delta\tau'/\tau_p}\right) \quad (2.15)$$

The zeroth order solution then is $\delta^2\tau'^2 + \tau' - 1 = 0$

which has $\tau_0' = \frac{-1 + \sqrt{1+4\delta^2}}{2\delta^2}$

$$\approx 1 - \delta^2 \quad \text{for} \quad \delta << 1.$$

Solving for the first order solution we let

$$\tau' = \tau_0 + \frac{\tau_p}{\delta}\tau_1$$

where

$$\delta^2\tau_0^2 + \tau_0 - 1 = 0$$

The equation then is

$$0 = \frac{\delta^2\tau'^2+\tau'-1}{\tau'^2} + \frac{\tau_p}{\delta}\left[\left(\frac{\delta^2\tau'^2+\tau'-1}{\tau'^2}\right)^2 + \frac{\tau'-2}{\tau'^3}\right] + O\left(\frac{\tau_p}{\delta}\right)^2$$

from which a Taylor expansion around τ_0 can be written and solved for τ_1. This results in $\tau_1 = 1$

and therefore the first order solution is

$$\tau' = \tau_0 + \frac{\tau_p}{\delta}$$

Finally, recalling that

$$\tau = \delta \tau'$$

then the first order solution of τ is

$$\begin{aligned} \tau &= \delta \tau_0 + \tau_p \tau_1 \\ &= \frac{\sqrt{1+4\delta^2} - 1}{2\delta} + \tau_p \\ &= \frac{\sqrt{1 + P^2/4} - 1}{P/2} + \tau_p \end{aligned} \tag{2.16}$$

In dimensional terms, the time taken between the initial pulse and the maximum response in the sensor wire which is downstream a distance x is

$$t_{max} = \frac{2\bar{K}_a}{u}\left(\sqrt{1 + 4\left(\frac{xU}{4\bar{K}_a}\right)^2} - 1\right) + \left(T_{P_0} - Bu\right) \tag{2.17}$$

where $\bar{K}_a$ is the thermal diffusivity of air at same mean temperature and U is the velocity, T_{P_0} the time constant of the temperature decay of the pulse wire at zero velocity and $T_{P_0} - Bu$ the time constant at all velocities (see Figure 2.8 for the value of B). Because of the exponential terms which have been neglected in equation 2.15, this solution breaks down at large U when τ is of the same order as τ_p.

Solution for high velocity

The above solution breaks down when τ_p/δ becomes of order one. This means that the low velocity solution breaks down when the time of flight for heat moving between the pulsed and sensor wires by diffusion and convection approached the/

the time of the temperature decay of the pulsed wire. We can obtain another solution for equation 2.11 under the assumption that $\varepsilon^2 \equiv 4/P << 1$. With this definition of ε , equation 2.11 becomes:

$$\frac{\tau_P}{\tau} e^{-(1-\tau)^2/\varepsilon^2\tau} = \int_0^{\tau} e^{-\frac{(\tau-\xi')}{\tau_P}} e^{-(1-\xi'^2)/\varepsilon^2\xi'} \frac{d\xi'}{\xi'} \quad (2.18)$$

In the limiting case of no diffusion ($P \to \infty$), the temperature maximum occurs at the convection time, $\tau = 1$. This is because we have assumed that the sensor wire responds instantaneously to the temperature of the gas surrounding it. Bauer first analysed this problem giving the expression for the temperature field downstream of the pulsed wire as

$$\theta(x,y,t) = \frac{Nu\,\theta_I}{4}\left(\frac{\pi}{P}\right)^{1/2} e^{-\frac{P}{4}\left(\frac{y}{x}\right)^2} \left\{ \operatorname{erf}\left(\frac{P}{4}\right)^{1/2} - \operatorname{erf}\left(\frac{P}{4}\right)^{1/2}\left(1-\frac{tU}{x}\right) \right\} \quad (2.18a)$$

Bradbury, making a zeroth order asymptotic expansion, obtained an equation slightly different to Bauer's in that the shape of the temperature decay of the pulsed wire is involved:

$$\theta(x,y,t) = \frac{Nu\,\theta_I}{4}\left(\frac{\pi}{P}\right)^{1/2} e^{-\frac{P}{4}\left(\frac{y}{x}\right)^2} e^{-\frac{t-x/u}{T_P}} \frac{\left\{ \operatorname{erf}\left(\frac{P}{4}\right)^{1/2} - \operatorname{erf}\left(\frac{P}{4}\right)^{1/2}\left(1-\frac{tU}{x}\right) \right\}}{1+\operatorname{erf}\left(P/4\right)^{1/2}} \quad (2.18b)$$

The physical interpretation of these results is that when $P/4 >> 1$, the diffusion is only significant near the front of the pulse giving the error functions in Bradbury's or Bauer's equations. This function is like a step function with a rise time of $4x/U\sqrt{P}$ (for about a 90% complete rise). These/

These analyses primarily predict the initial slope of the response in the sensor wire. Bradbury and Bauer use the initial response in the sensor wire to indicate the time of flight. This indication is quite a sensitive measure of the convection velocity at very high Peclet numbers. At lower Peclet numbers (but still maintaining the relation $\frac{P}{4} > 1$) the initial response of the sensor wire becomes very blurred by diffusion and therefore not sensitive to changes in velocity. Furthermore the solutions of Bradbury and Bauer rapidly break down with decreasing Peclet numbers. As we have explained, the maximum response of the sensor wire now becomes very sensitive to the convective velocity. We therefore attempt to predict the entire shape of the response in the sensor wire so that we can find the maximum; i.e. where the time derivative is zero. Our analysis at the higher Peclet numbers differs from the previous ones in that we do not deal with the solution of the thermal field directly, $\theta(x,y,t)$, but instead with the time derivative of temperature. Furthermore, we need a solution of more than the zeroth order because the magnitude of the Peclet number is only about 50* for the maximum velocities considered in this study (500 cm/sec).

For large Peclet numbers we therefore assume that

$$\tau = 1 + \frac{\varepsilon}{\gamma} \tau'$$

---

*Calculated with a thermal diffusivity corrected for temperature and a wire spacing of 0.25 cm.

where $\varepsilon << \gamma(\varepsilon) << 1$

and γ is a presently undetermined function of ε. With these new variables equation (2.18) becomes

$$\tau_p e^{-(\tau'/\gamma)^2}\left[1+\frac{\varepsilon}{\gamma}\left(\frac{\tau'^3}{\gamma^2}-\tau'\right)+O\left(\left(\frac{\varepsilon}{\gamma}\right)^2\right)\right] = e^{-\frac{\varepsilon}{\gamma}\frac{\tau'}{\tau_p}}\int_0^{1+\frac{\varepsilon}{\gamma}\tau'} e^{-(1-\xi)/\tau_p} e^{-(1-\xi)^2/\varepsilon^2\xi}\,\frac{d\xi}{\xi}$$

We observe that the integrand is very small for all ξ except $\xi \cong 1$, and therefore define the new variable of integration

$$\xi = 1+\varepsilon\xi'$$

With this, the equation becomes

$$\tau_p e^{-(\tau'/\gamma)^2}\left[1+\frac{\varepsilon}{\gamma}\left(\frac{\tau'^3}{\gamma^2}-\tau'\right)+O\left(\left(\frac{\varepsilon}{\gamma}\right)^2\right)\right] = \varepsilon e^{-\frac{\varepsilon}{\gamma}\frac{\tau'}{\tau_p}}\int_{-1/\varepsilon}^{\tau'/\gamma} e^{-\xi'^2}\left[1+\varepsilon\left(\left(\frac{1}{\tau_p}-1\right)\xi'+\xi'^3+O(\varepsilon^3)\right)\right]d\xi$$

Evaluating the integral we obtain

$$\tau_p e^{-(\tau'/\gamma)^2}\left[1+\frac{\varepsilon}{\gamma}\left(\frac{\tau'^3}{\gamma^2}-\tau'\right)+O\left(\left(\frac{\varepsilon}{\gamma}\right)^2\right)\right] = \varepsilon e^{-\frac{\varepsilon}{\gamma}\frac{\tau'}{\tau_p}}\left\{\sqrt{\pi}-\frac{\sqrt{\pi}}{2}\operatorname{erf}\left(\frac{1}{\varepsilon}\right)-\frac{\sqrt{\pi}}{2}\operatorname{erfc}\left(\frac{\tau'}{\gamma}\right)\right.$$
$$\left.-\left(\frac{1}{\tau_p}-1\right)\frac{\varepsilon}{2}e^{-(\tau'/\gamma)^2}-\frac{\varepsilon}{2}\left[\left(\frac{\tau'}{\gamma}\right)^2+1\right]e^{-(\tau'/\gamma)^2}+O(e^{-1/\varepsilon^2})\right.$$

Expanding the error functions under the assumption that $\varepsilon << \gamma$ we obtain

$$\tau_p e^{-(\tau'/\gamma)^2}\left[1+\frac{\varepsilon}{\gamma}\left(\frac{\tau'^3}{\gamma^2}-\tau'\right)+O\left(\left(\frac{\varepsilon}{\gamma}\right)^2\right)\right] = \varepsilon e^{-\frac{\varepsilon}{\gamma}\frac{\tau'}{\tau_p}}\left\{\sqrt{\pi}-\frac{\gamma}{2\tau'}e^{-(\tau'/\gamma)^2}\right.$$
$$\left.-\frac{\varepsilon}{2}e^{-(\tau'/\gamma)^2}\left[-\frac{1}{\tau_p}+\left(\frac{\tau'}{\gamma}\right)^2\right]+O(\varepsilon^2,e^{-1/\varepsilon^2})\right\}$$

and to order $(\varepsilon/\gamma)^2$

$$\tau_p\left[1+\frac{\varepsilon}{\gamma}\left(\frac{\tau'^3}{\gamma^2}-\tau'\right)\right] = \varepsilon\sqrt{\pi}\,e^{-(\tau'/\gamma)^2}-\frac{\varepsilon\gamma}{2\tau'} \qquad (2.19)$$

The undetermined function $\gamma(\varepsilon)$ is partially determined by the requirement that the leading terms be of the same order. We chose $\gamma^2 = \left(\ln 1/\varepsilon\right)^{-1}$

This choice is convenient and is consistent with our assumption/

assumption that $\varepsilon \ll \gamma \ll 1$.

With this choice, equation (2.19) can be solved for τ', which yields to $O(\varepsilon^2\gamma^3)$

$$\tau = 1 + \frac{\varepsilon}{\gamma} + \frac{\varepsilon\gamma}{2} \ln \frac{\tau_p}{\sqrt{\pi}} - \frac{\varepsilon\gamma^2}{4} \ln^2 \frac{\tau_p}{\sqrt{\pi}} \quad . \tag{2.20}$$

This equation in dimensional terms is: $\varepsilon = \sqrt{\frac{4K}{ux}}$; $\tau_p = \frac{UT_p}{x}$

$$t_{max} = \frac{x}{u}\left\{ 1 + \sqrt{\frac{4K}{ux}} \ln\sqrt{\frac{ux}{4K}} + \frac{1}{2}\sqrt{\frac{4K}{ux}\frac{1}{\ln\sqrt{\frac{ux}{4K}}}} \ln\frac{UT_p}{x\sqrt{\pi}} - \frac{1}{4}\sqrt{\frac{4K}{ux}}\left(\ln\sqrt{\frac{ux}{4K}}\right)^{-3/2} \ln^2\frac{UT_p}{x\sqrt{\pi}} + O\left(\frac{x}{u}\frac{4K}{ux}\frac{1}{\left(\ln\frac{ux}{4K}\right)^{3/2}}\right)\right\}$$

where t_{max} is the time to maximum signal in the sensor wire.

To summarise our results then we have obtained for $\frac{\tau_p}{P} \ll 1$, or the low velocity case,

$$\tau = \frac{\sqrt{1 + P^2/4} - 1}{P^2/8} + \frac{4\tau_p}{P} \quad . \tag{2.21}$$

For $P/4 \gg 1$, or the high velocity case we have

$$\tau \cong 1 + \sqrt{\frac{4}{P\,g(P)}} + \frac{1}{2}\sqrt{\frac{4}{P}\,g(P)} \ln\frac{\tau_p}{\sqrt{\pi}} - \frac{1}{4}\sqrt{\frac{4}{P}\,g^3(P)} \ln^2\frac{\tau_p}{\sqrt{\pi}} \tag{2.22}$$

where $g(P) \equiv 1/\ln\sqrt{P/4}$

The relationship* given by equations 2.21 and 2.22 are shown in Figures 2.10a and 2.10b, along with experimental data measured for two values of Δx (the distance between pulsed and sensor wire). As can be seen the theoretical curves for the/

*We have not plotted the dimensionless solutions because the velocity appears in a complicated manner in the parameter τ_p . This makes a situation where it is virtually impossible to interpret physically useful results from a dimensionless plot.

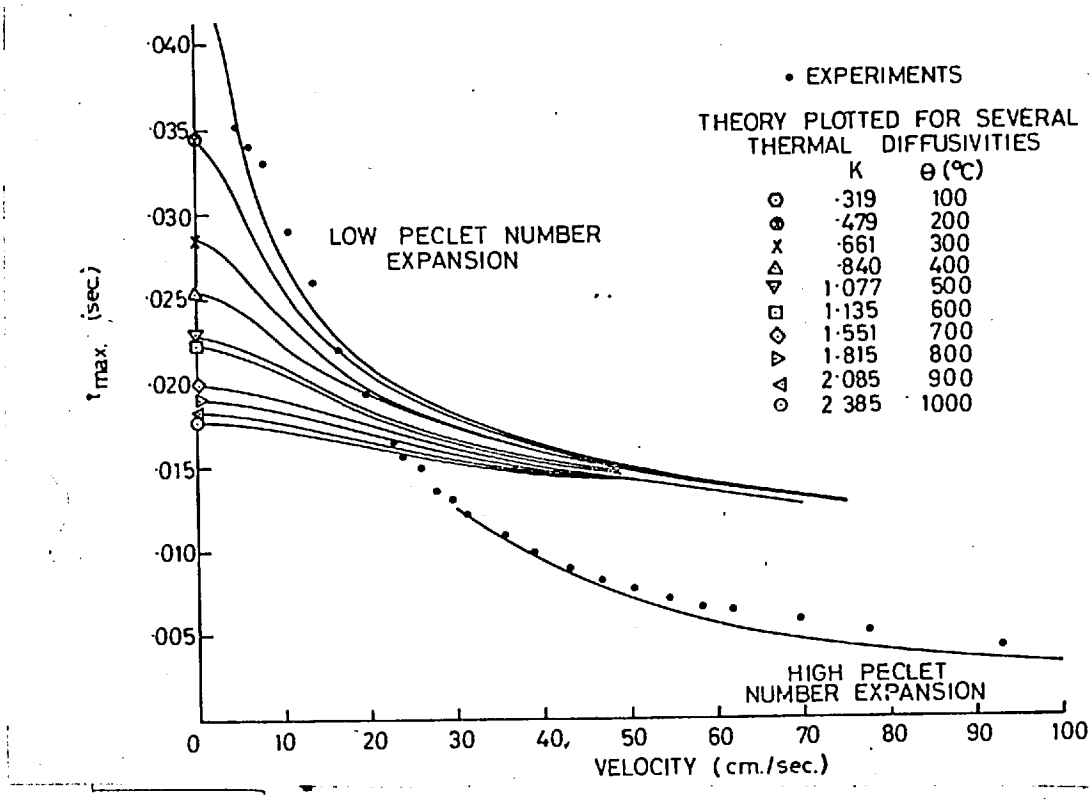


FIGURE 2.10a Theoretical predictions of behaviourof pulsed probe for both high and low velocity solutions with a wire spacing of 0.2cm. High velocity solution is shown as single line whilst low velocity solution is shown for thermal diffusivities from 100°C to 1000°C assumed to be constant. Data from probe with 0.2cm wire spacing is shown as heavy dots.

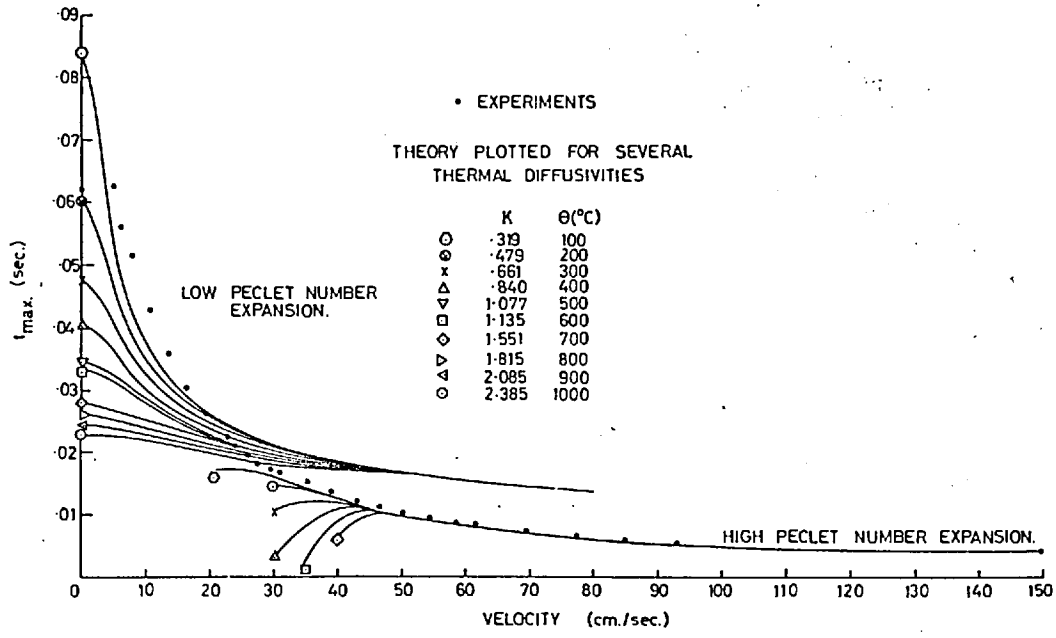


FIGURE 2.10b Same as figure 2.10a except solutions and data are for wire spacing of 0.3cm. In this case high velocity solution is also shown for several temperatures.

the high velocity corresponds closely to the experimental curve, and breaks down when the velocity decreases below 30 cm/sec. The low velocity solution is plotted as a family of curves each for a separate thermal diffusivity. None of these curves fully correspond to the data.

The fundamental limitation of the theoretical analysis for low velocities is the analytically necessary assumption of constant thermal diffusivity. Thermal diffusivity of air varies significantly with temperature, as shown in Figure 2.2 so that as the thermal pulse diffuses, it cools, decreasing the thermal diffusivity. Since we pulse to quite high temperatures, $\Theta_I \cong 800^{\circ}C$, we can expect a large change in K_a as the air cools back to room temperature. The comparisons between experiment and theory for the low velocity case is the most sensitive to a changing thermal diffusivity. This is because the time of flight is longer, giving the thermal pulse more time to diffuse and cool. This corresponds to the trend shown by the experimental data at low velocities.

We can obtain a crude estimate of the mean temperature of the gas during the flight between pulsed and sensor wire by measuring the indicated temperature in the sensor wire at the time of maximum and calculating a mean between this temperature and initial temperature of the pulsed wire. The results are shown in Figure 2.11.* Using this "mean"

*The buoyancy forces which affect the angle measurement are very sensitive to the temperature of the gas as a function of the distance between pulsed and sensor wires. Therefore a numerical solution for the temperature in the wake of the pulsed wire is presented in the section on calibration measurements. This more complex analysis is not necessary for this argument where only the mean temperature between wires is needed.

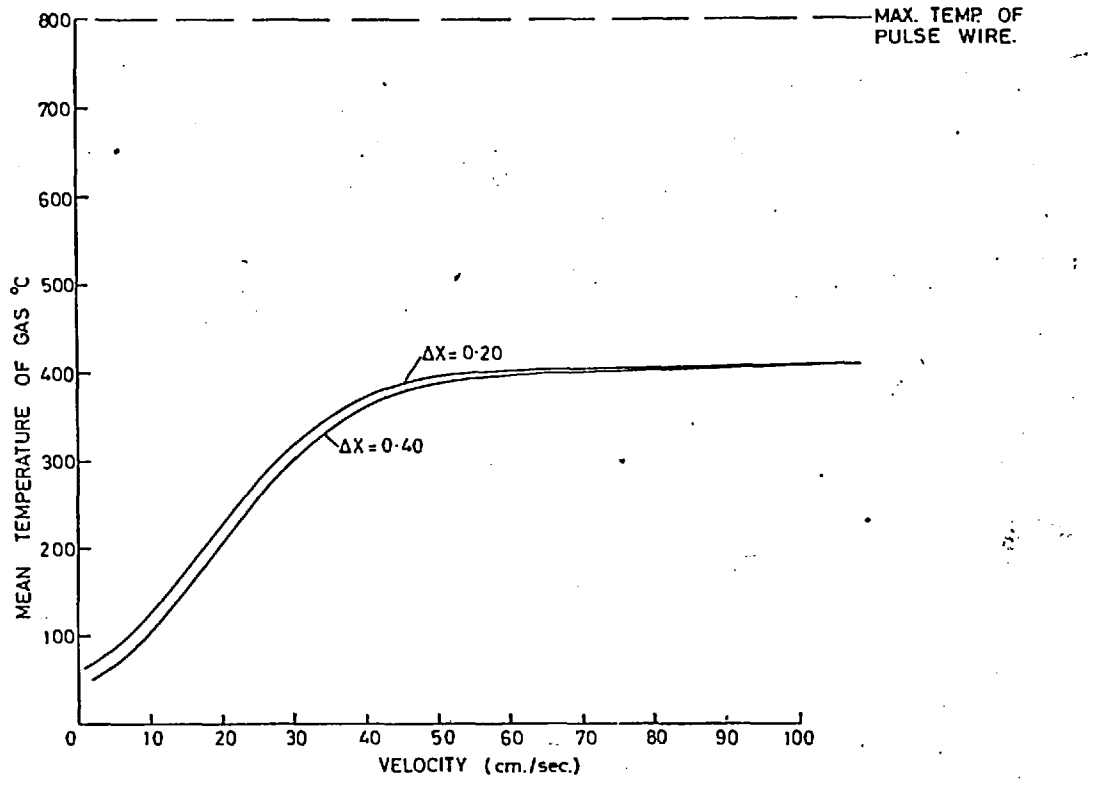


FIGURE 2.11 Mean temperature between initial temperature of pulsed wire and maximum indicated temperature of sensor. Assumed to indicate mean temperature of gas travelling between wires.

temperature to indicate the magnitude of the thermal diffusivity at each velocity, we can solve equations 2.21 and 2.22 to approximate the non-constant thermal diffusivity case. This is shown in Figure 2.12.

The important feature about Figures 2.10 and 2.12 is that it shows that there is a unique relationship between the velocity and the time of temperature maximum, measured by the sensor wire. This relationship depends only on the shape of the pulse, the geometry of the probe, and the properties of the fluid. This relationship can be measured experimentally, as shown in Figure 2.13, where the distance between pulsed and sensor wire is varied. Our theoretical analysis, particularly if the effects of variable thermal diffusivity are taken into account, accurately predicts the experimental results at all distances between the wires.

DISCUSSION

General probe configuration

The general configuration of the probe is shown in Figure 2.14a. With this configuration the average velocity and direction of the air flowing between the upstream pulsed wire and the downstream sensor wire is measured. The head of the probe is approximately cubic in shape, the length of any side being much less than the length scale of the internal flows we wish to measure. The probe sizes used in most of the calibration experiments was less than 0.5% of the diameter

of/

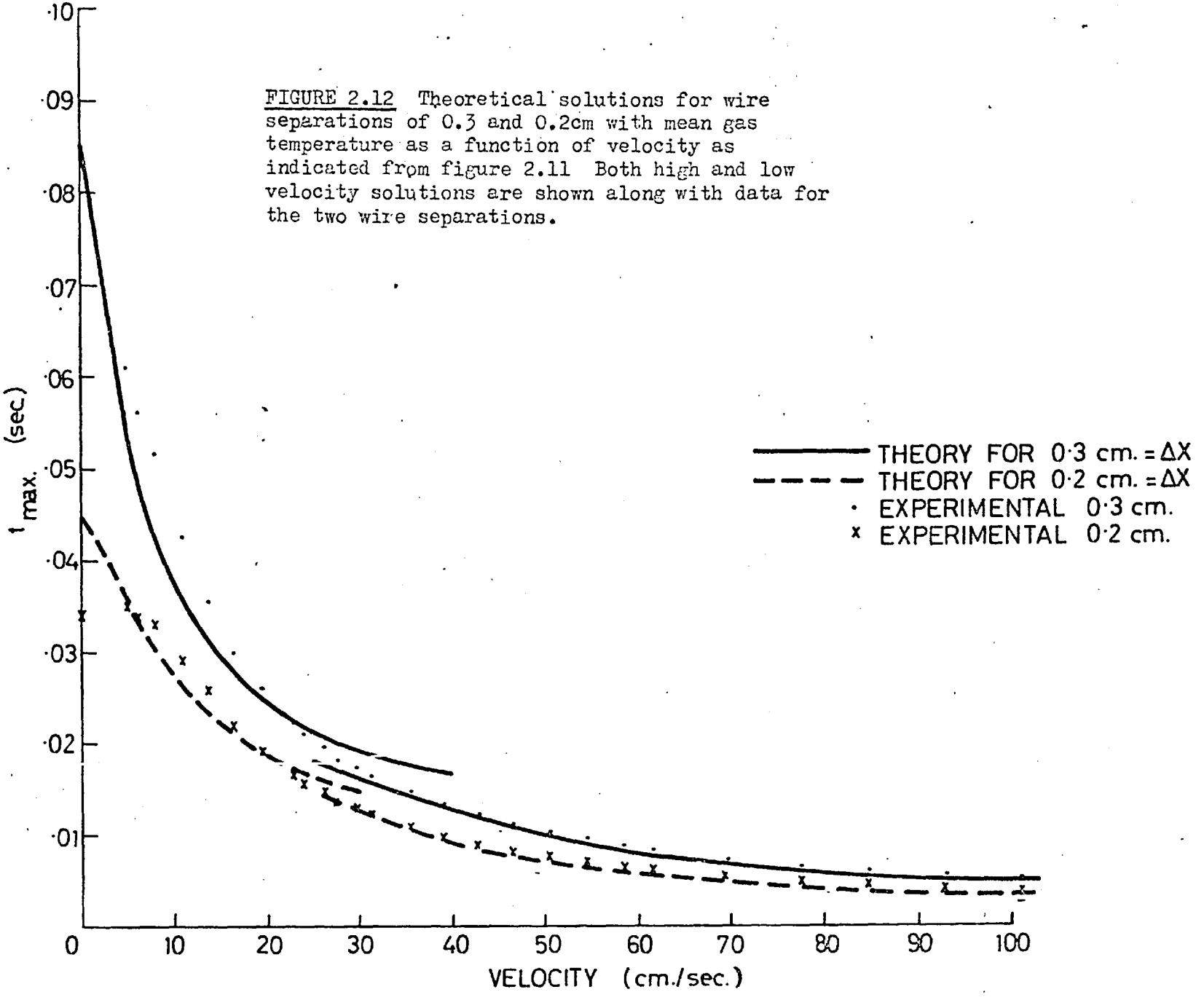


FIGURE 2.12 Theoretical solutions for wire separations of 0.3 and 0.2cm with mean gas temperature as a function of velocity as indicated from figure 2.11 Both high and low velocity solutions are shown along with data for the two wire separations.

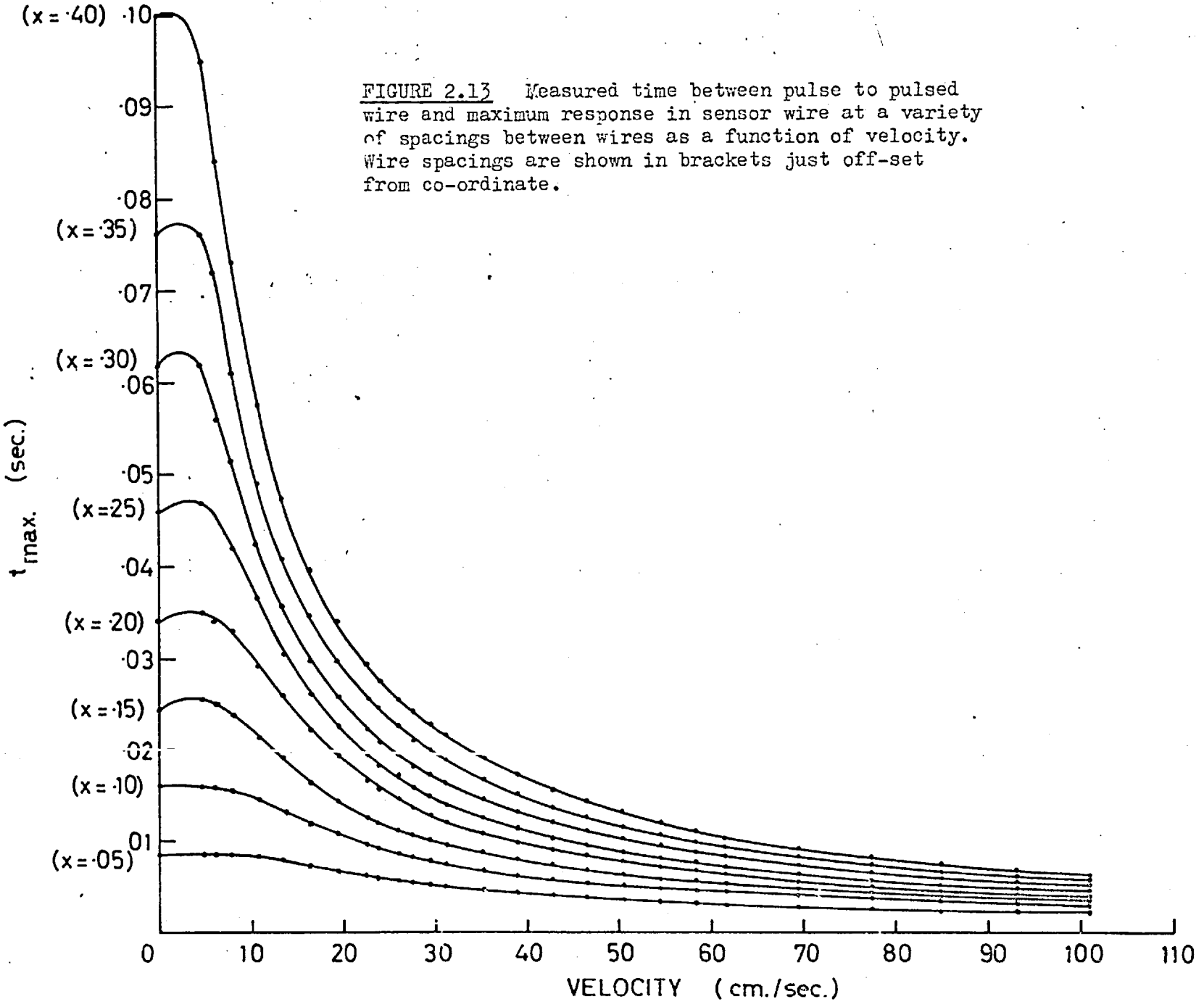


FIGURE 2.13 Measured time between pulse to pulsed wire and maximum response in sensor wire at a variety of spacings between wires as a function of velocity. Wire spacings are shown in brackets just off-set from co-ordinate.

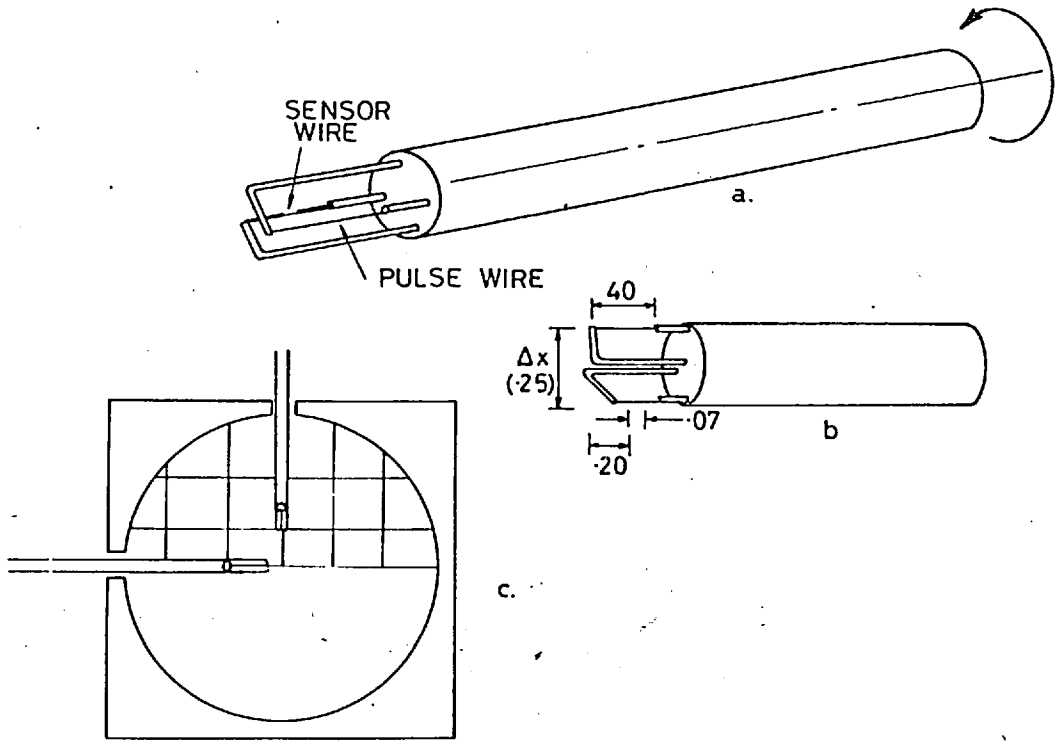


FIGURE 2.14 General configuration of pulsed probe with dimensions of probe used in studies of later chapters. Part C indicates the probe inserted from the side of a tube and traversing across the lumen in mutually perpendicular planes.

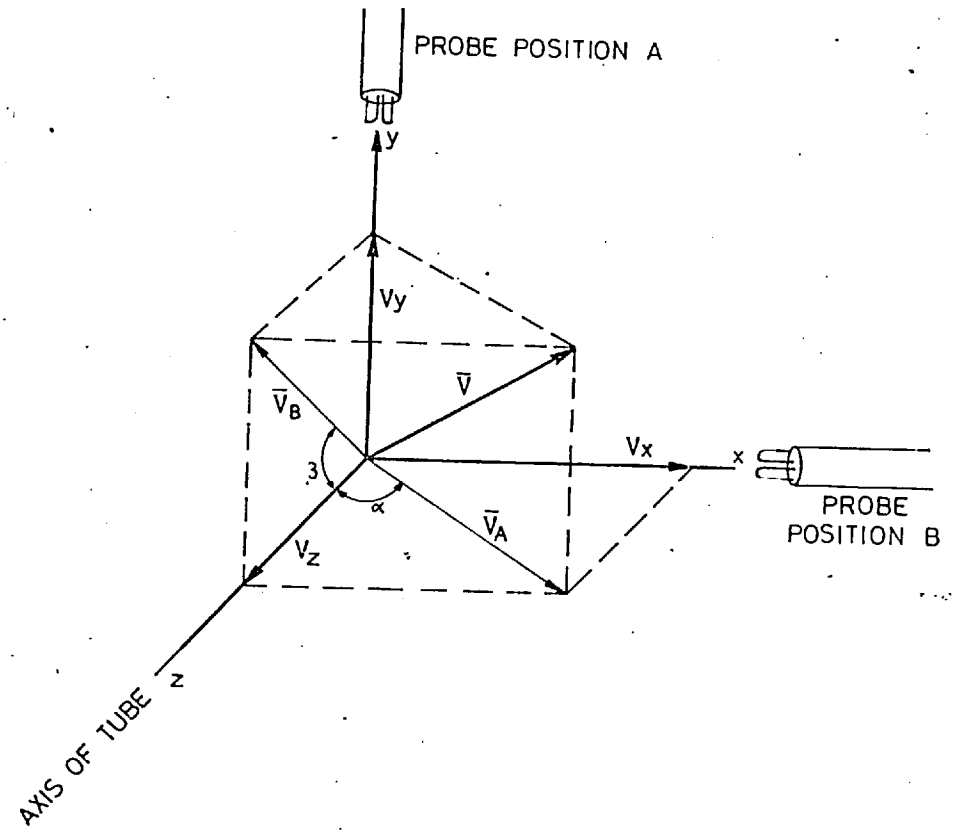


FIGURE 2.17 Probe positions and measurements taken to determine cartesian components of velocity $\bar{v}$.

of the tubes used. The cubic shape ensures that the probe can manoeuvre within the flows with the same detail as it can measure the velocity and direction. Both the pulsed wire and sensor wire rotate around the axis of the probe. Therefore the mean position for measurement never changes when the probe is rotated to find the flow direction. The length from the sensor wire to the head of the probe will limit how closely to a surface velocities can be measured. When protruding from the side of a tube (Figure 2.14c) one might be tempted to measure the flow very close to the wall from which the instrument protrudes. In such a circumstance, the pulsed wire may be within the hole through the tube wall. This can give erroneous results. The size of the wire supports must be relatively thin and placed as far laterally and downstream as possible. This is done to avoid any disturbance in the flow field between pulsed and sensor wire by the wake of the wire supports. This is a relatively minor problem because the velocity measurements are only taken after the probe has been aligned with the flow direction. Therefore the wake of the supports never directly impedes on the sensor wire. Of course if the supports are very large the diffusion of the viscous wake can be rapid enough so that the edge of the wake could envelop the sensor wire. For the size of the probes used in this study, the wire supports caused no interference in the flow patterns.

The/

The length of the pulsed wire is much longer than the sensor wire. This is done so that pulses in a flow with a yaw angle of up to 75^{o} will be intercepted on the entire length of the sensor wire. Also the pulse which is intercepted by the sensor wire at this yaw will not be distorted by end effects in the pulsed wire (such as conduction to the supports or the wake of the support). The amount of electronic noise picked up by the wire is directly proportional to the length of the wires. Finally the length of the sensor wire, along with the separation between wires, will define the smallest scale to which the flow can be described. Therefore the probe was produced with the shortest possible sensor wire which could repeatably be constructed. The pulsed wire length was then inferred from the spacing between the wires and the maximum yaw expected.

The material used for the pulsed wire must not oxidise at the high temperatures at which the pulsed wire is operated. Nickel or platinum is therefore well suited for the pulsed wire. Platinum was found unsuitable because of the difficulty in etching the wire in areas close to its supports. Often the supports were corroded. Nickel is slightly more difficult to attach and align, but did not need to be etched.

Platinum was used for the sensor wire because it could be etched over a very short distance (approximately 0.05 cm to 0.1 cm) and therefore created a very short sensing length. Furthermore/

Furthermore, the sensing length could be repeatably positioned at the projected centre of the pulsed wire. The size of the sensor wire (2.5 microns) disallows the use of any non-etched wire, therefore only platinum was used. It should be noted that great care must be taken when attaching and etching this wire. If etching is accomplished by an acid jet the force of the jet will easily break the wire. A delicate talent for making this wire is rapidly cultured with repeated failures.

The diameter of the sensor is important in that this wire must be able to respond thermally to a surrounding gas temperature within a time much shorter than the time of flight between wires. The time constant for such a wire as previously discussed can be given by

$$T_s = \frac{\rho c d^2}{4 K_a Nu}$$

where the wire materials are: the density ρ; the heat capacity, c; the diameter, d, and K_a is the air thermal conductivity. Using the wire materials for platinum, a mean K_a and Nu given by equation 2.8 is

$$T_s \cong 0.0003 \text{ sec.}$$

Since the times we measure are of order ten milliseconds or greater, the convection time constant is about three per cent or less of the measured signal. At Reynolds numbers based on the sensor wire diameters considered in this study (about 10^{-2} to 10^{-1}) the relation to the Nusselt number is approximately linear (as in an Oseen wake). The time constant,

T_{sensor}/

T_{sensor}, calculated by the above equation, then becomes approximately linearly related to the diameter. If the time constant for the sensor wire, T_s, was of the same order or larger than the time to maximum signal, t_{max}, then the measured t_{max} would become less sensitive to the velocity. Also the analytical evaluation of the probe's response would be much harder. For this reason, very small wires are preferable for the sensing element, even though the probe becomes very fragile and difficult to build. The diameter of 2.5 microns for the sensor wire is a compromise, in that 2.5 microns is the largest diameter which gives a maximum signal delay of two per cent.

The diameter of the pulsed wire is less stringently determined. Again a compromise must be made for a variety of considerations, each of about equal importance. The larger the diameter of the pulsed wire, the more current will be needed to heat the wire to the prescribed temperature. A large diameter wire will resist the thermal stress developed in the wire when pulsed. With pulses of about 1000°C, initial temperature, the thermal stresses are very large, causing breakage in a 12 micron wire after only a few pulses. At initial temperatures of 500°C to 800°C, the life of the wire is much longer but the sudden thermal expansion and contraction of the pulsed wire can cause a vibration in the probe, creating an anomalous response in the sensor wire or breaking the fragile sensor wire.

The/

The temperature decay of the pulsed wire is faster with a smaller wire. This creates a more sharply peaked thermal cloud moving between wires and ultimately a more sharply peaked response in the sensor wire. Therefore it is easier to determine the position of maximum signal in the sensor wire. A small diameter pulse wire will have a larger aspect ratio and therefore lose less heat via conduction to the wire supports. The conduction to the supports is not a desirable condition because it may cause large end effects in the pulsed wire. This means that flows with large yaws cannot be measured (i.e. the sensor wire will receive a temperature signal derived from the end effects of the pulsed wire at larger yaw angles). The aspect ratio also affects the direction indication. The direction is determined by sending a train of pulses through the pulse wire, rotating the wires around the axis of the probe until the centre position of the thermal wake is found. This operation depends on the principle that each pulse identically heats the air surrounding the pulsed wire. If conduction to the supports is significant, then the frequency of the train of pulses would have to be determined by the heat capacity and heat dissipation of the supports. Furthermore the physical connection between pulse wires and support would have to be similar for each pulse wire in order to maintain the same conduction pathway. Also the configuration of the support itself would have to be similar for each probe. It is therefore desirable to create the/

the largest aspect ratio (or the smallest diameter) possible to decrease the conduction to the supports. It is also desirable that the viscous wake of the pulsed wire be laminar. This gives a more sharply defined thermal wake, which in turn allows a more accurately defined direction.

The diameter of the pulsed wire used for operation in the velocity ranging from 1 cm/sec to 100 cm/sec was 12.5 microns. This seemed to be a good compromise between the wire life and accuracy and ease of operation. The thermal vibration problem was largely negated by soldering the pulse wire in a slightly slack position. Then, under a microscope, we carefully kinked the wire close to each support, so that the resulting wire was straight and in parallel to the sensor wire. This gave a pulse wire with a long life, but the position of the pulse wire had to be repeatedly checked during operation.

The distance between the pulse and sensor wires is the single most important parameter of the configuration. This parameter will define the convection time x/u and the Peclet number $\frac{ux}{\kappa}$. As can be seen in the theoretical evaluation of the probes response, the wire spacing will determine the shape of the t_{max} to velocity curve. By considering the range of velocities to be measured, the spacing can be adjusted to give the maximum change in t_{max} for a given change in velocity. The amplitude of the signal in the sensor wire will/

will decrease with increasing spacing. This is because the two wires are in parallel and would not be true if the wires were perpendicular to one another, as in the probes of Bradbury & Castro. The spacing of the wires will be influenced by the amount of noise existing in the sensor signal so that a good signal to noise ratio can be obtained. Finally the sensitivity to direction will also depend on the wire spacing. The effect of wire spacing will be analysed in the calibration experiments.

General operation

The general principle for operation of the probe in internal, laminar flows is shown in Figure 2.14c. To measure the three components of velocity at any one point the probe must be inserted in two mutually perpendicular positions. The time to maximum and direction is measured for each probe position. The probe can be used on either horizontal or vertical planes, but corrections to the indicated direction caused by buoyancy effects must be made when operating the probe in the horizontal plane with velocities less than about 10 cm/sec. The wires are set parallel to the axis of the tube and all directions indicated relative to this. The signal in the pulse wire is used to initiate the sweep of an oscilloscope displaying the response in the sensor wire. Several such displays are shown in Figure 2.15, which shows that/

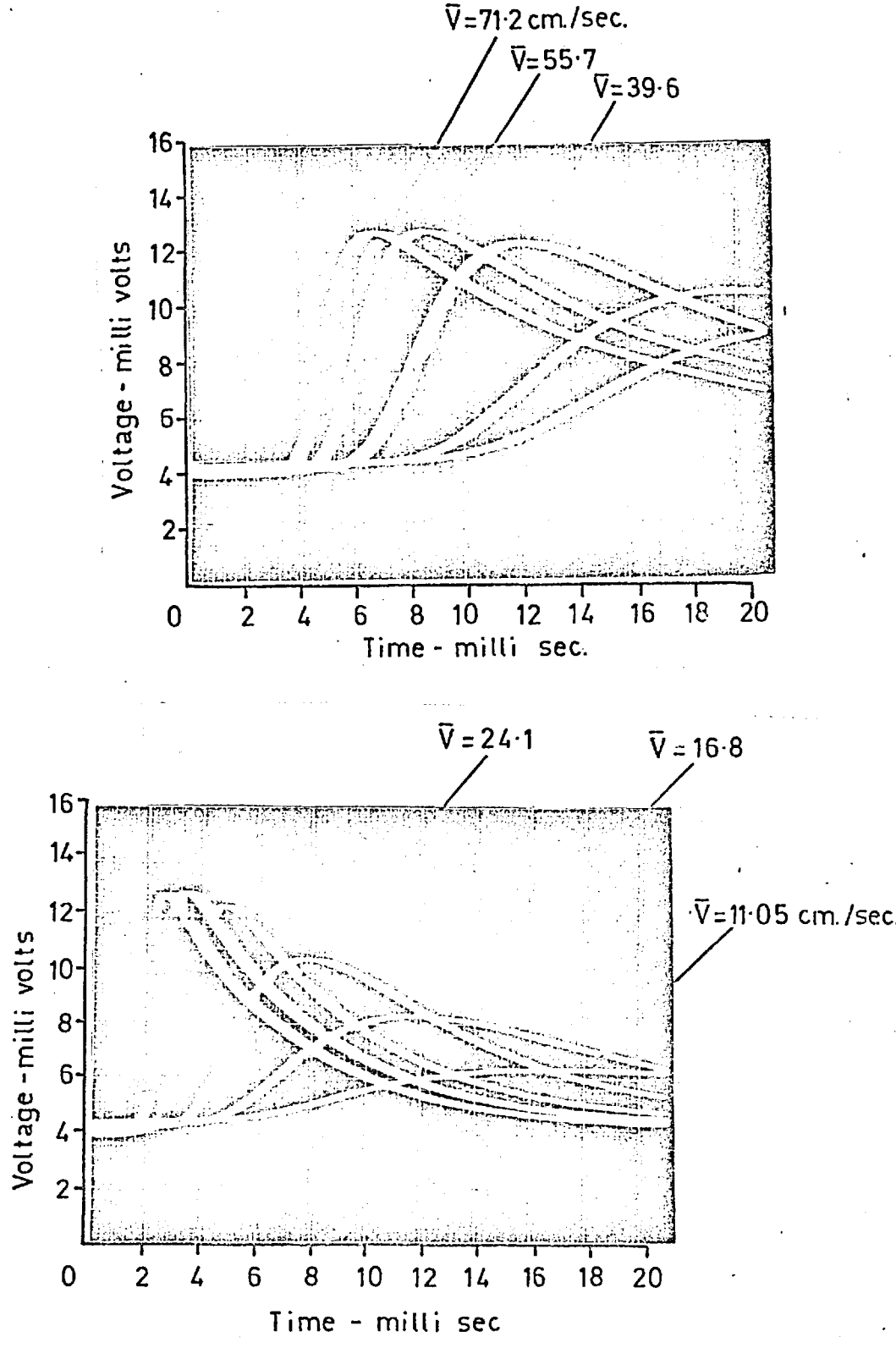
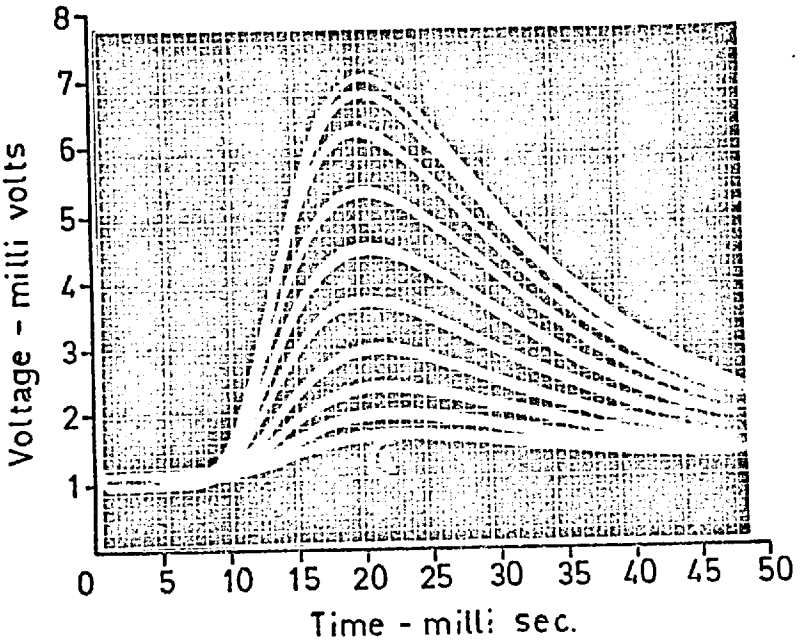


FIGURE 2.15 Oscilloscope display of signal in sensor wire at a variety of gas velocities between wires. Sweep is initiated with heating pulse in pulsed wire.

that as the velocity changes the position of the maximum signal changes as does the amplitude. The wires are then rotated about the axis of the probe, while creating a train of pulses. The change in amplitude of the sensor signal is noted; a typical example is shown in Figure 2.16. The largest amplitude indicates the centre of the thermal wake and hence direction of flow if the buoyancy forces are not significant. The probe is then aligned on the direction of flow and the time to maximum measured. This measurement is presently being made directly from the oscilloscope. The sensor wire signal is first amplified with a low noise amplifier. The time sweep for the oscilloscope is delayed until just before the maximum and then swept through at a fast rate. We therefore only look at a greatly enlarged portion of the sensor signal around the maximum response. We simply measure the distance to the maximum peak of the signal from the scope. Using the two directions and time to maximum we then correct for any buoyancy effect in the direction indication and yaw effect in the velocity magnitude indication (t_{max}). In practice the buoyancy correction is seldom made. This correction is only applied when measuring very low flows with the probe on the horizontal. Usually when measuring low flows we rotate our models so that the probe is always vertical. The yaw correction will be discussed further in the calibration experiments. The accuracy of the indicated velocity and direction is determined by the noise in the sensor signal and repeatability of the pulse. In general an accuracy of about/



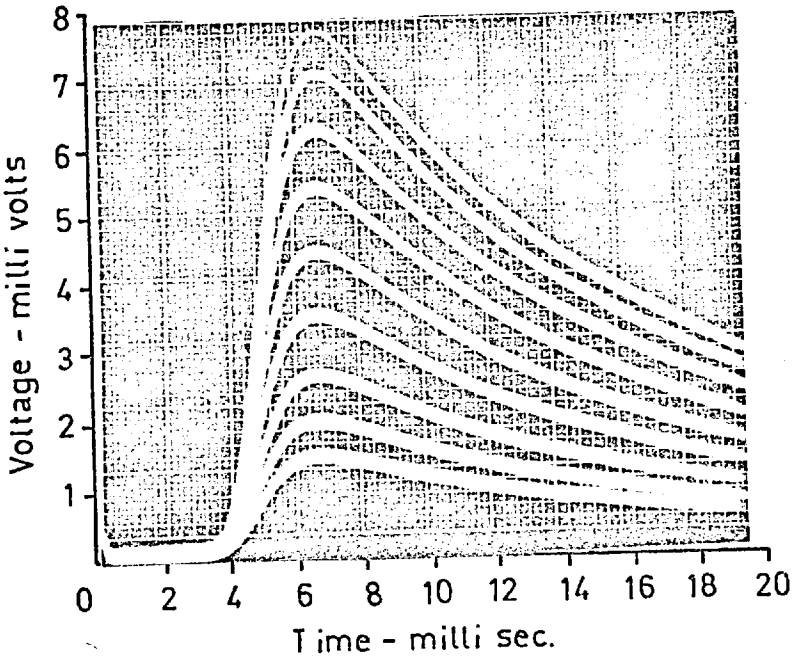


FIGURE 2.16 Oscilloscope display of signal in sensor wire at indicated angles offset from signal with maximum amplitude. The signals shown are from the probe rotated both in a clockwise and counterwise direction at the indicated angle.
Note symmetry of thermal wake.

about 0.1 mm/sec can be obtained for velocity magnitude measurements and an accuracy of about 0.5° or less for direction (this depends on the velocity).

Figure 2.17 shows the two positions A, B, of the probe. In position A the probe is rotated by angle α into the plane made by V and V_A and the magnitude of V_A along with α measured. Likewise the probe in position B is rotated by angle β into the plane defined by V and V_B and the magnitude of V_B and β measured. Experiments on the yaw response of the probe show that V_A is related to V by $V_A = V(\cos\beta)^{2/3}$ and $V_B = V(\cos\alpha)^{2/3}$

Using these relations V is then calculated and V_y, V_x, V_z obtained by

$$V_y = V_B \sin\beta$$
$$V_x = V_A \sin\alpha$$
$$V_z = V_A \cos\alpha$$

where V_z is the primary velocity and V_y and V_x are the secondary velocity.

In practice each point is not determined by two separate measurements. Instead the probe is traversed in a hexagonal pattern, as shown in Figure 2.14c, and the angles α, or β (along with V_A and V_B) measured at frequent intervals along each traverse. Then a Fourier analysis is used to extrapolate the data from each plane to every point within the flow. The points where the hexagonal pattern cross are the only positions where two actual measurements occur. If we deem an accuracy of 2% to be acceptable, then the equations can be/

be simplified for flows with angles of 10% or less. The equation then becomes

$$V_y = V \sin \beta$$
$$V_x = V \sin \alpha$$
$$V_z = V \cos \alpha$$

and

$$V_A \cong V \cong V_B$$

Within most internal flows studied, this is the case, and experimentally the magnitude of V_A and V_B are the same. With this low angle condition only one measurement needs to be taken. The three components of velocity found by vectorial summation. This assumption of low angle was not made for any of the calibration experiments or subsequent experiments.

One last feature about the general operation of the probe should be noted: unlike hot wire anemometers the pulsing probe need not be frequently calibrated. A series of calibrations for different separation distances between the wire and different pulse intensities were done. If the size of both pulse and sensor wire are always the same and the same pulse intensity is always used, then the only parameter which can change the relation between t_{max} and velocity is the wire separation distance. Therefore instead of calibrating the probe in a known flow, as one would need with a hot wire, the separation distance between pulse and sensor wire need only be measured (using a microscope). If it were not for this feature, the use of this extremely delicate device would be very limiting. That is, one would have to build the probe, calibrate/

calibrate in a known flow, and use it before it broke. If a calibration was required with each wire repair then the progress of data taking would be very slow indeed.

Circuitry for pulse and sensor wire

The general purpose of the circuitry for the pulsed wire is to create a symmetrical square pulse of a desired voltage and time duration. The circuitry was designed to give a voltage pulse which could be varied continuously from 0 to 12 volts across a 3 ohm resistor and the time duration varied in multiple increments from 22 microseconds to 50 milliseconds. By increasing the voltage or time duration, a hotter pulse is created. Figure 2.19a shows pulses of differing time duration across a 3.3 ohm nickel pulse wire (12.5 u diameter and 0.4 cm in length). The rise and decay times of the voltage pulse are of the order of one microsecond. Since the time scale of thermal decay in the pulse wire is of the order of 10 milliseconds, then any pulse duration shorter than about a millisecond will not interfere with the thermal decay of the wire. Usually a pulse of 12 volts and 70 microseconds was used so that the initial temperature of the pulse wire was about 800°C. This gives a large enough response in the sensor wire so that the signal to noise ratio is large. Further, the pulse created in this manner is cool enough to allow a long pulse wire life and also to minimise perturbations in the direction indication due to buoyancy. The most

important/

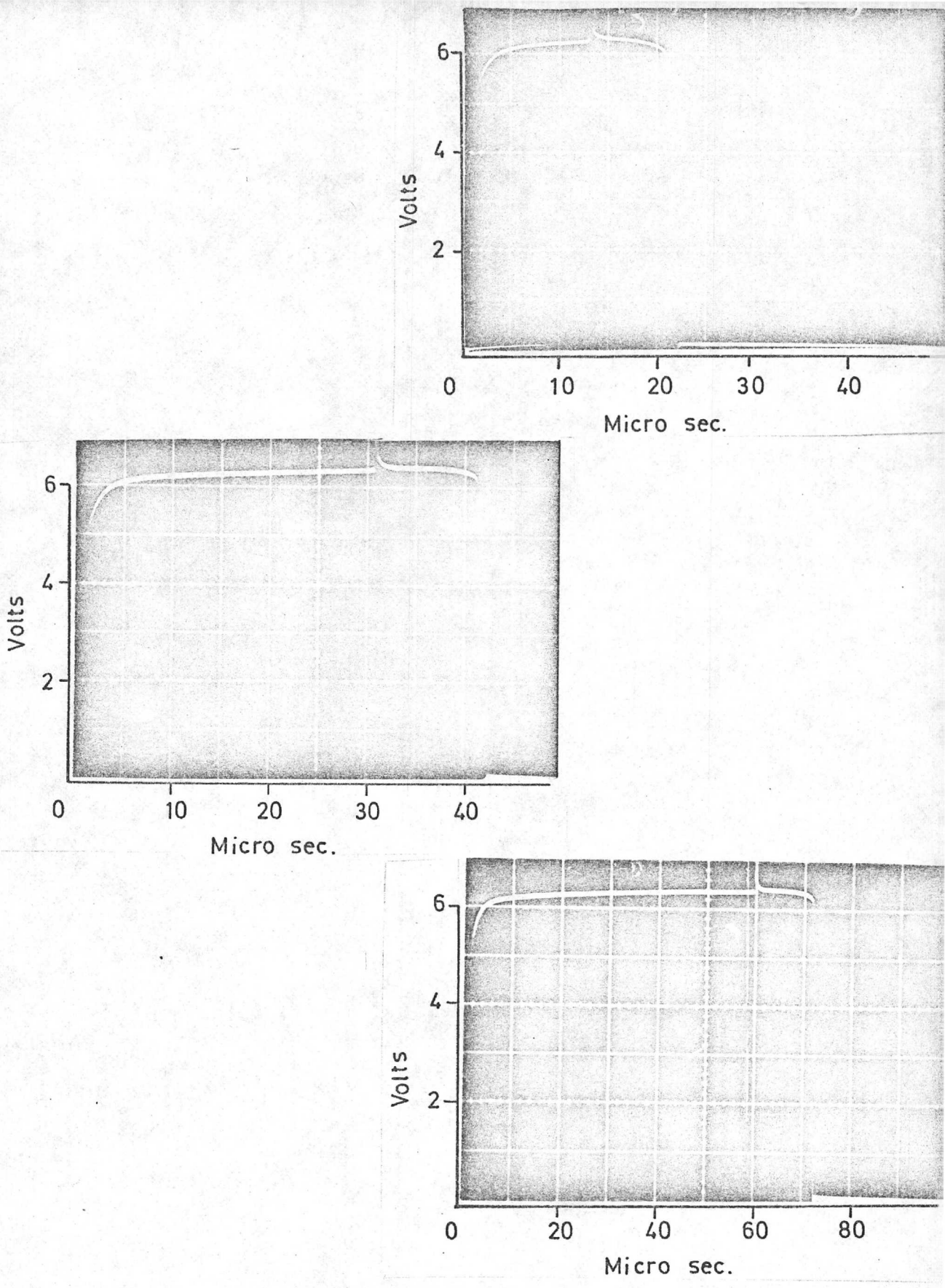

6
4
2
Volts
0
10
20
30
40
Micro sec.
6
4
2
Volts
0
10
20
30
40
Micro sec.
6
4
2
Volts
0
20
40
60
80
Micro sec.

FIGURE 2.19a

important aspect of the pulse is that it be accurately repeatable.

The circuitry developed was patterned after Bradbury & Castro with some modifications. The power source was simply a large bank of capacitors which were charged between pulses. This gave a repeatable voltage pulse as long as enough time was given between pulses for the capacitors to charge (about 0.1 seconds). The pulse generator allows either a single pulse or a train of pulses to be produced at a variety of frequencies. The single pulse operation is useful in determining the gross direction of the flow, whereas the pulse train is used for the finer direction measurement. All of the circuitry electrically floated in that there was no internal ground to the probe. This was done to create very fast rise and decay times for the pulse. To eliminate any ground loops or inductive electronic noise, all the equipment was screened and the screening mutually grounded.

The sensor wire circuitry was very simple, consisting of a simple bridge powered by a battery and a low noise amplifier, as shown in Figure 2.19. The sensor wire is operated as a simple resistance thermometer by supplying it with current from a 9-volt battery. The circuitry ensured a constant voltage across the sensor wire. In principle the current through the sensor wire should be as high as possible for the maximum signal in the sensor wire. In practice when the/

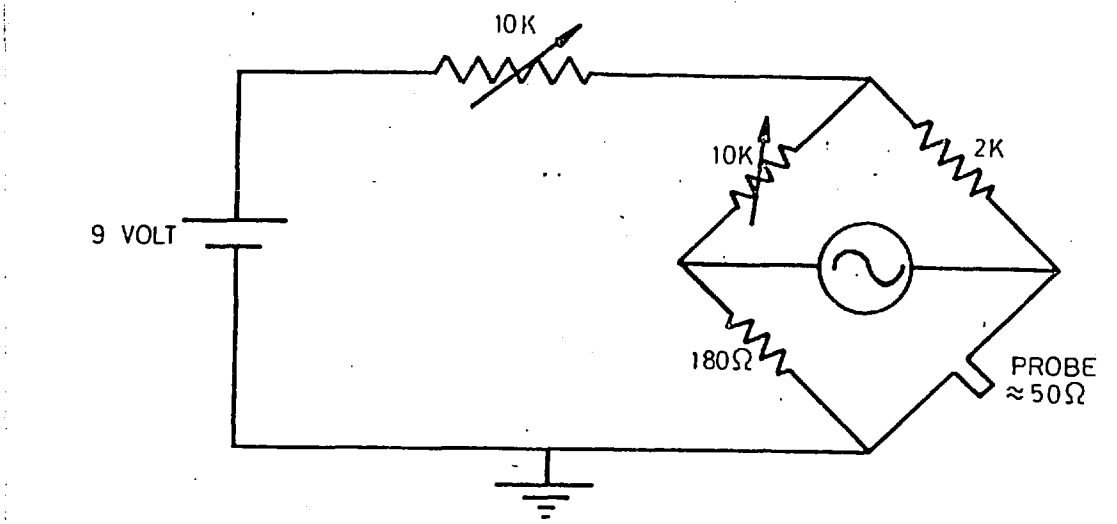


FIGURE 2.19b Sensor wire circuitry.

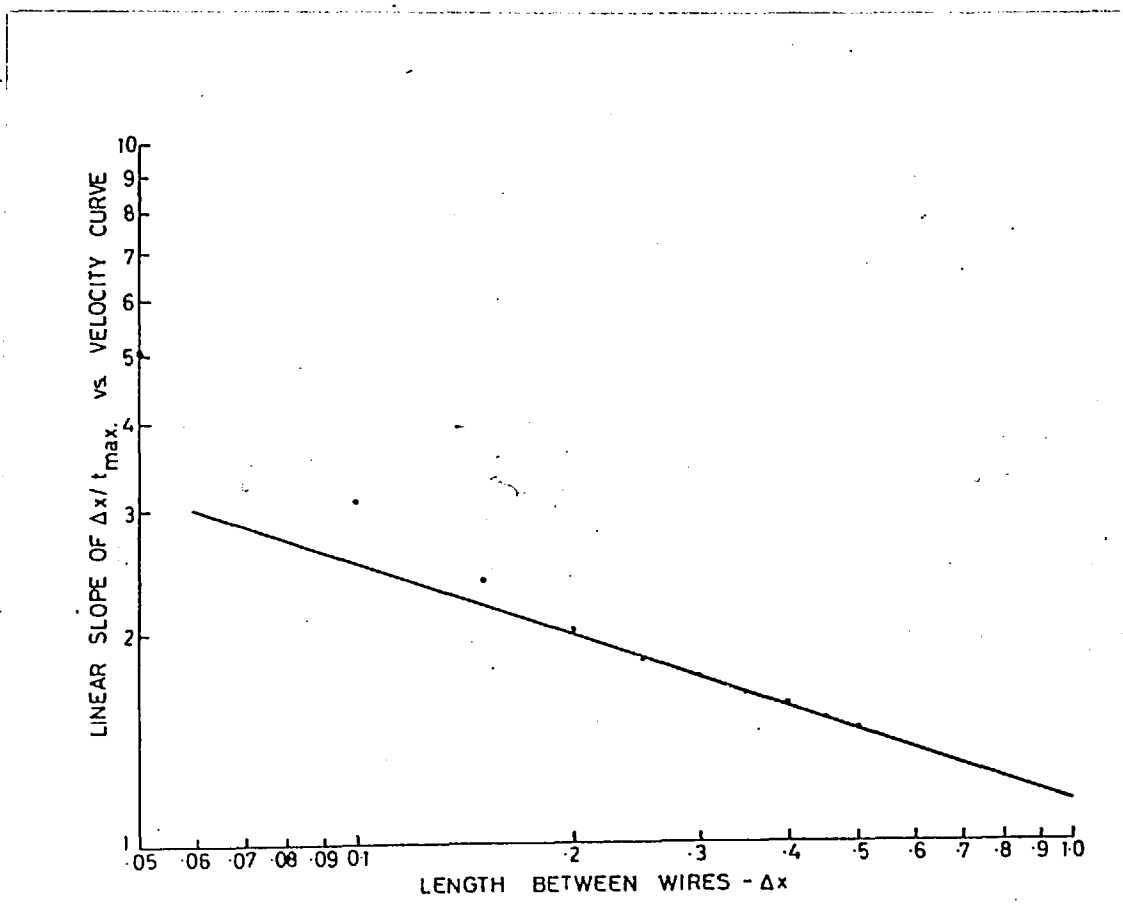


FIGURE 2.23 Linear slope of the least squares fits shown in figure 2.22 as a function of separation distance. Note that for wire separation spacing greater than 0.2cm the slopes in figure 2.22 are related by -0.333.

the temperature of the sensor wire becomes high enough, the sensor wire starts to act as a hot wire anemometer. The velocities we studied are steady, but nevertheless the signal from the sensor wire when acting as a hot wire anemometer sometimes fluctuated with an amplitude of about 10-20 micro volts. This is probably due to small changes in the temperature of the gas (even though great care was taken to remove any velocity fluctuations and to isolate the system thermally). To eliminate these fluctuations the current through the sensor wire was reduced so that the degree of anemometering was small. This slightly reduces the amplitude of the sensor wire response. Electronic noise can be a problem in the sensor wire circuitry. The sensor wire readily picks up noise inductively from the pulsed wire because the two wires and their supports are arranged in parallel loops. To diminish this problem, all the circuitry, both sensor and pulse, was screened and the screening mutually grounded. This reduced the noise to the order of 5-10 microvolts. A low noise amplifier was used for the sensor wire signal. The amplifier also allowed the filtering of noise signals which had frequencies outside the range of the frequency of the signal measured. In practice these precautions allowed a noise level of about 10-15 microvolts with the lowest signal of about 20 millivolts (at 0-3 cm/sec). With this noise level measurements of the magnitude and direction of the flow can be made to an accuracy of 0.1 cm/sec and about 0.5 to 0.1 degrees.

The/

The output of the low noise amplifier was displayed on an oscilloscope. The sweep of the scope was delayed and the time base expanded so that only the vicinity of the maximum signal in the sensor wire was shown. The time to maximum signal was measured directly from the oscilloscope. An alternative approach would be to differentiate the sensor signal and indicate the time to maximum by starting an electronic clock with the pulse to the pulsed wire and stopping when the differential of the sensor wire signal becomes zero. Since a display of a series of sensor signals must be present to determine the direction, it was convenient to use this display simply to measure the magnitude of the velocity, and no attempt was made to further automate the procedure.

Calibration experiments

Experiments were carried out in two calibration rigs to further study the properties of the pulsed probe. The features investigated were the separation between pulse and sensor wire, the direction sensitivity, the buoyancy effect on direction, and the yaw response of the probe.

The calibration rigs were developed to produce steady, isothermal, laminar flow, which was parallel to the axis of the tube. It is actually surprisingly difficult to develop a flow repeatedly accurate to less than 0.1 cm/sec and parallel to the axis of the tube by less than 0.1^{o}. One rig consisted/

consisted of a 1.5" entrance bell which was fed from a centrifugal pump through a series of heat exchanges and pleniums. The pleniums had large volumes, which dampened any fluctuations caused by the pump. The volume flow to the bell was measured by special rotameters. The bell was fed from a large plenium containing screening and flow straighteners just proximal to the bell. This eliminated the condition where any random vortex occurring in the entrance plenium could be concentrated as the flow was forced into the mouth of the bell. The flow straighteners were positioned to be parallel to the axis of the bell and to the downstream outrun. This outrun is needed because the system is run by very low pressures; therefore fluctuation in the environment distal to the outrun can affect the flow at the bell. The bell was calibrated by taking velocity profiles, using both the pulsed probe or a hot wire anemometer, at four planes within the mouth of the bell, each $\pi/4$ degrees apart. Ten different volume flow rates were measured. The profiles were then integrated and the calibration of the pulsing probe and hot wire were adjusted until the integrated velocity profiles matched the volume flow rates indicated by the rotameter within 0.5%. Both the presence of the probe and the temperature of the gas were compensated for. Simultaneous to this, the second rig was also calibrated. This rig consisted of a long straight 2" tube fitted with a similar entrance bell (2"), plenium, flow straighteners and thermally insulated. The tube was over 100 diameters in length/

length, had polished inner walls, and was straightened by cold rolling to one mil in ten feet. Velocity profiles at plane each $\pi/4$ degrees were also taken in this rig and the integrated volume flow rates compared to the rotameter indication. The profiles in the entrance bell were of course very flat, whereas those in the long tube were parabolic [redacted]. The profiles in the calibration bell and subsequent outrun were compared to profiles by Nikuradse (80) and analysis by Langhaar (81) and Schiller (82); very favourable comparisons were obtained.

The theoretical analysis, previously discussed, concludes that at any velocity past the probe the indication used for measuring velocity (the time to maximum sensor signal) is a function of two non-dimensional groupings; the Peclet number (which is the Reynolds number multiplied by the Prandtl number) and the temperature decay of the pulse wire,

$$\tau = f(P, \tau_p)$$

where

$$\tau = t_{max}/(u/x)$$

$$P = ux/K(\theta)$$

$$\tau_p = t_p(\theta, u)/(x/u)$$

Theoretically, the data for the parameters x and t_p should be collapsed by these non-dimensional groupings. Figure 2.13 displays the dimension association between t_{max} and U with a variety of x, holding t_p constant. It is however not convenient to use the above dimensionless parameter, because all these groupings contain u, the quantity we seek experimentally. This/

This creates a severe limitation in elucidating each parameter's influence.

Another major difficulty may possibly be in the dependence of the thermal diffusivity, K_a, on temperature. We can partially get around this difficulty.

If we analyse the temperature of a moving line as a function of time with an instantaneous source, then

$$\frac{\Theta(t)}{\Theta_I} = \frac{1}{4\pi K t} e^{-((x-x_0)^2+(y-y_0)^2)/4tK}$$

If the coordinates move with the line the equation can be approximated as:

$$\frac{\Theta(t)}{\Theta_I} \cong \frac{1}{4\pi K t}$$

which infers that the temperature is an inverse function of K_a and t. If we approximate the thermal diffusivity as a linear function of Θ then $K_a = K_I \frac{\Theta(t)-\Theta_I}{\Theta_I} + K_{\Theta_I}$ and if $\Theta(t) >> \Theta_I$ and $K_a >> K_{\Theta_I}$ then

$$\frac{\Theta(t)}{\Theta_I} = \left[\frac{1}{4\pi K t}\right]^{1/2} \qquad (2.25)$$

With a constant source of heat the temperature is a function of the exponential integral as we have previously mentioned, equation (2.5). Expanding the integral with a t_{max} appropriate for the higher velocities measured, we find that the temperature of the gas surrounding the sensor wire at t_{max} does not change much with changing velocity. Therefore we can grossly predict that the temperature around the sensor wire at t_{max} should increase with decreasing t_{max} (or increasing velocity) until a maximum is reached and then further decrease in t_{max} (increase in U)will have little change in this/

this gas temperature at t_{max}. Essentially what this says is that at low velocities the thermal decay of the pulse wire is short compared to the time of flight and the pulse approximates an instantaneous source. Since no more heat is then being supplied to the gas, the temperature of the thermal cloud convecting toward the sensor wire is being dissipated by diffusion. And the temperature of the cloud depends on how long diffusion has taken place. At higher velocities the pulse wire thermal decay is long compared to the time of flight so that the heat supplied to the gas approaches a constant source. In this condition the temperature of the thermal cloud is determined by the amount supplied by the source minus diffusion losses. As the convection time decreases the effect of diffusion becomes less and the temperature at t_{max} (there is of course no maximum in the sensor signal for a truly constant source) is less affected by changing velocity. A complete solution for the temperature of the gas (as opposed to the rate of change of temperature which was analysed) would be very difficult. As was discussed previously, the solutions by Bradbury or Bauer are not applicable because of the low velocities, and therefore low Peclet numbers, involved in our study.

A numerical solution was conducted using a computer program, TIGER V, kindly supplied by the General Electric Company, San Jose, California. The results were compared to the temperatures measured in the sensor wire at t_{max}, but agreement/

agreement between calculated and measured was only fair. Figure 2.20 shows the indicated maximum temperatures measured at progressive distances from the pulse wire for three velocities. This figure infers that the temperature of the gas rapidly decays from the wire temperature of 800°C to about 100°C at about 100 diameters downstream of the pulse wire. The average temperature of the gas between pulse and sensor wire is of course

$$\bar{\theta}(u,x) = \frac{\int_0^x \theta(x)\,dx}{\int_0^x dx}$$

Graphically evaluating the integral, the mean temperature as a function of U and x can be obtained and the results have the same trend as those shown in Figure 2.11. This empirically derived function shows that equation 2.25 (or the numerical solution) expresses the general trend of the mean temperature of the gas correctly.

Two other features of the problem could affect our effort to non-dimensionalise the experimental data. These are the thermal inertia of the sensor wire and the effect of the wake. Both these features have been assumed negligible in the analysis, and therefore are not included in the theoretical non-dimensional parameters. The thermal inertia could delay the indicated maximum signals as shown in Figure 2.1. Not only would the signal be delayed, but the maximum signal would decrease in amplitude. The amplitude of the sensor wire signal for a probe with a separation distance of

0.29/

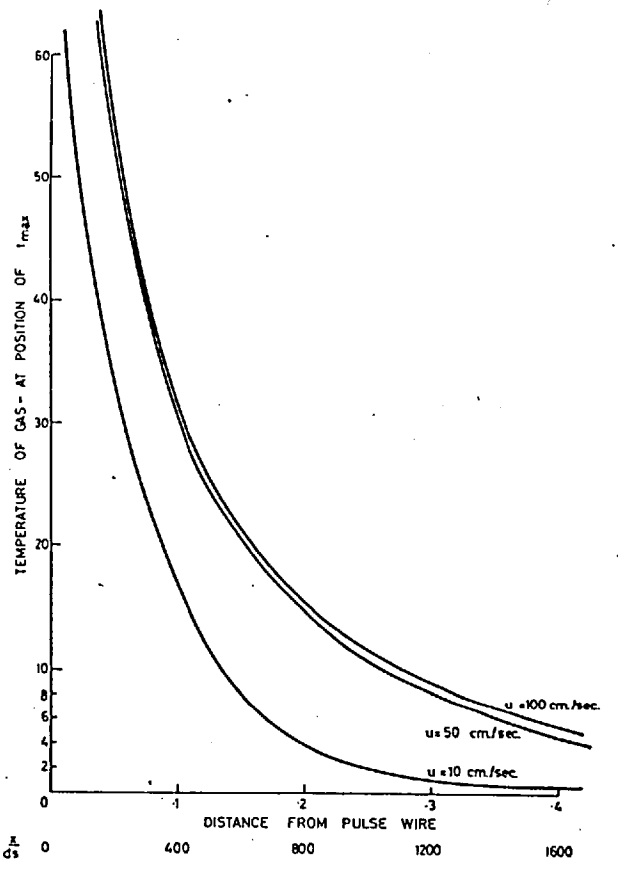


FIGURE 2.20 Maximum temparatures measured by the sensor wire as a function of distance between wires and velocity.

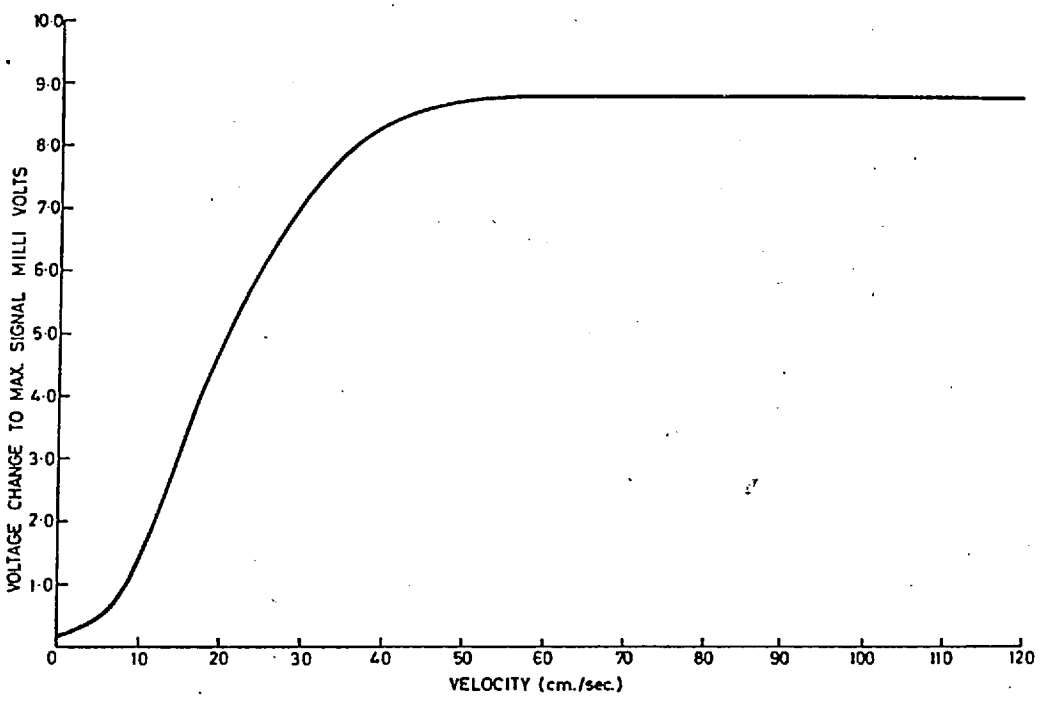


FIGURE 2.21 Maximum signal in sensor wire with wire separation of 0.290cm. This separation is typical for the probes used in chapters 3 - 5. The signal amplitude gives an indication of how much electronic noise can be tolerated in the system. Note the amplitude of the signal does not decrease between velocities of 60 and 120cm/sec.

0.29 cm and an initial temperature of the pulse wire of 800°C is shown in Figure 2.21. No decrease in amplitude is measured for velocities up to 200 cm/sec. Therefore, for the velocity range of 0 to 1 meter/sec, both the theoretical and empirical results indicate that the sensor wire thermal inertia is significant.

The wake may cause an effect which is not accounted for by the nondimensional parameters τ, P and τ_p. No simple empirical measurement is solely influenced by the wake. Therefore only the theoretical results (Schlichting, 83) applied for distances of over (say) 500 diameters downstream of a laminar Oseen wake can be put forth to infer the negligible influence of the wake.

The buoyancy forces at low velocities may also affect the relation between τ, P and τ_p.

In conclusion, we can see that the nondimensional parameters put forth by our theoretical analysis will not completely collapse the experimental calibration data. We can introduce a variable thermal diffusivity determined from the empirical temperature field which accounts for some of the discrepancy, but other effects from the wake and buoyancy forces cannot be accounted for well.

An empirical collapse of the data was however accomplished. If the data is plotted as $\Delta x / t_{max}$ vs. u, as shown in Figure/

Figure 2.22, the curves can be represented by a straight line for velocities over 10 cm/sec.* The slope of each of the curves in Figure 2.22 is a function of the separation distance as shown in Figure 2.23. For separation distances greater than 0.2 cm, this relation is best fit by the equation $\Delta x^{-1/3}$.** Figure 2.24 shows the relationship between the quantity $\frac{\Delta x}{t_{max}} * \Delta x^{-1/3}$ vs. velocity. The best fit linear equation is shown as the solid line in the figure and the relation is

$$V = 0.3672 + 1.0008 \left(\frac{\Delta x}{t_{max}}\right) \Delta x^{-1/3}$$

From which we see that the relation is almost the line of identity. No theoretical justification seems to be available for this observation (the wake would influence the results by $\Delta x^{-1/2}$), and therefore we consider this result fortuituous. For velocities below 10 cm/sec, the data for a range of separation distances from 0.2 to 0.5 cm could be collapsed with the equation

$$V = 31.026 - 143.96 \left(\frac{t_{max}}{\Delta x}\right) .$$

Again a quadratic relation provided a slightly better fit to the/

---

*The data can be fitted with a slightly lower error by using a quadratic.

**Powers of Δx^n from n = -1 to n = +1 were fitted to the calibration data for Δx between 0.2 and 0.5 cm. The fit giving the least error occurred at n = -0.332.

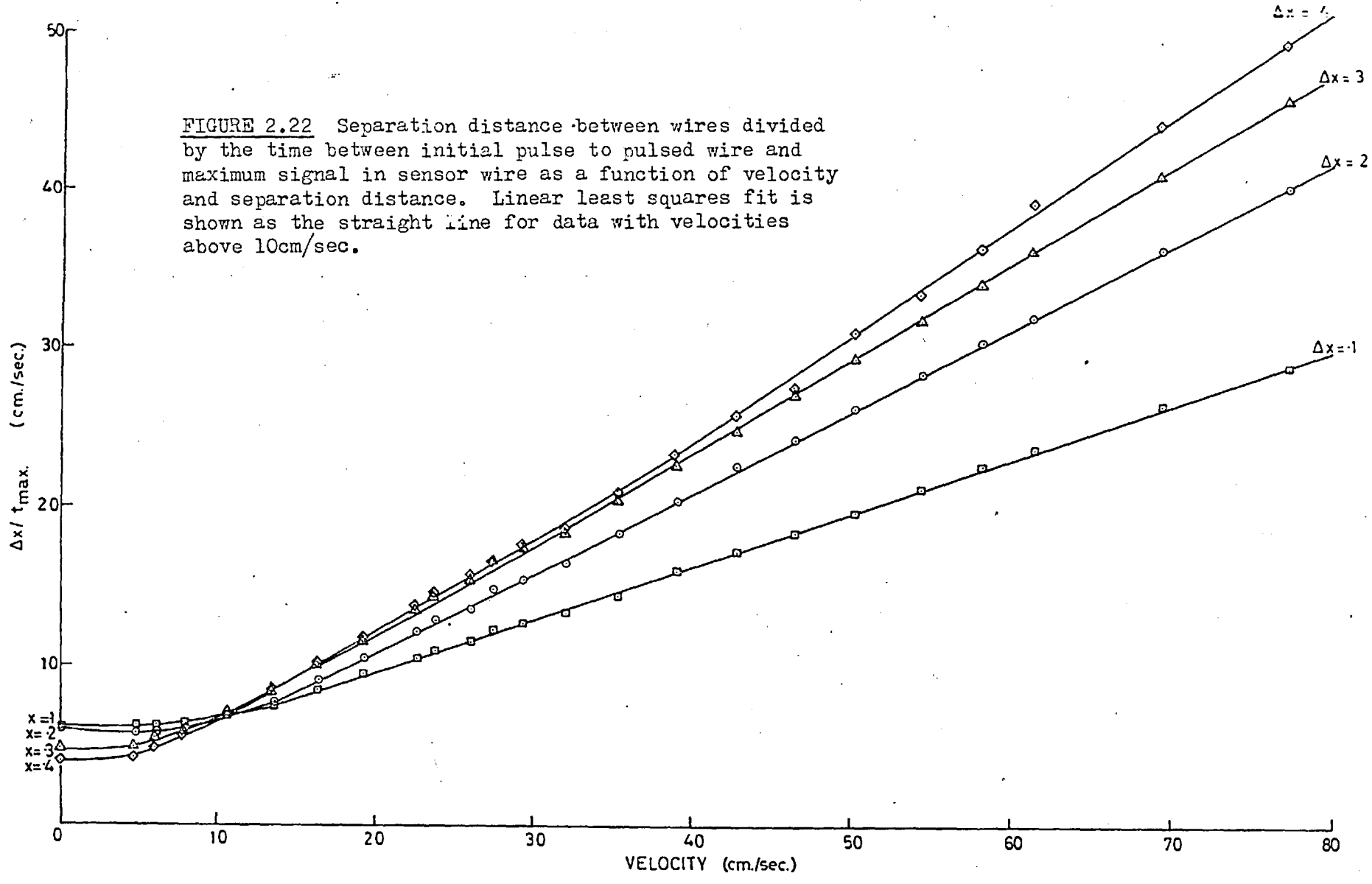


FIGURE 2.22 Separation distance between wires divided by the time between initial pulse to pulsed wire and maximum signal in sensor wire as a function of velocity and separation distance. Linear least squares fit is shown as the straight line for data with velocities above 10cm/sec.

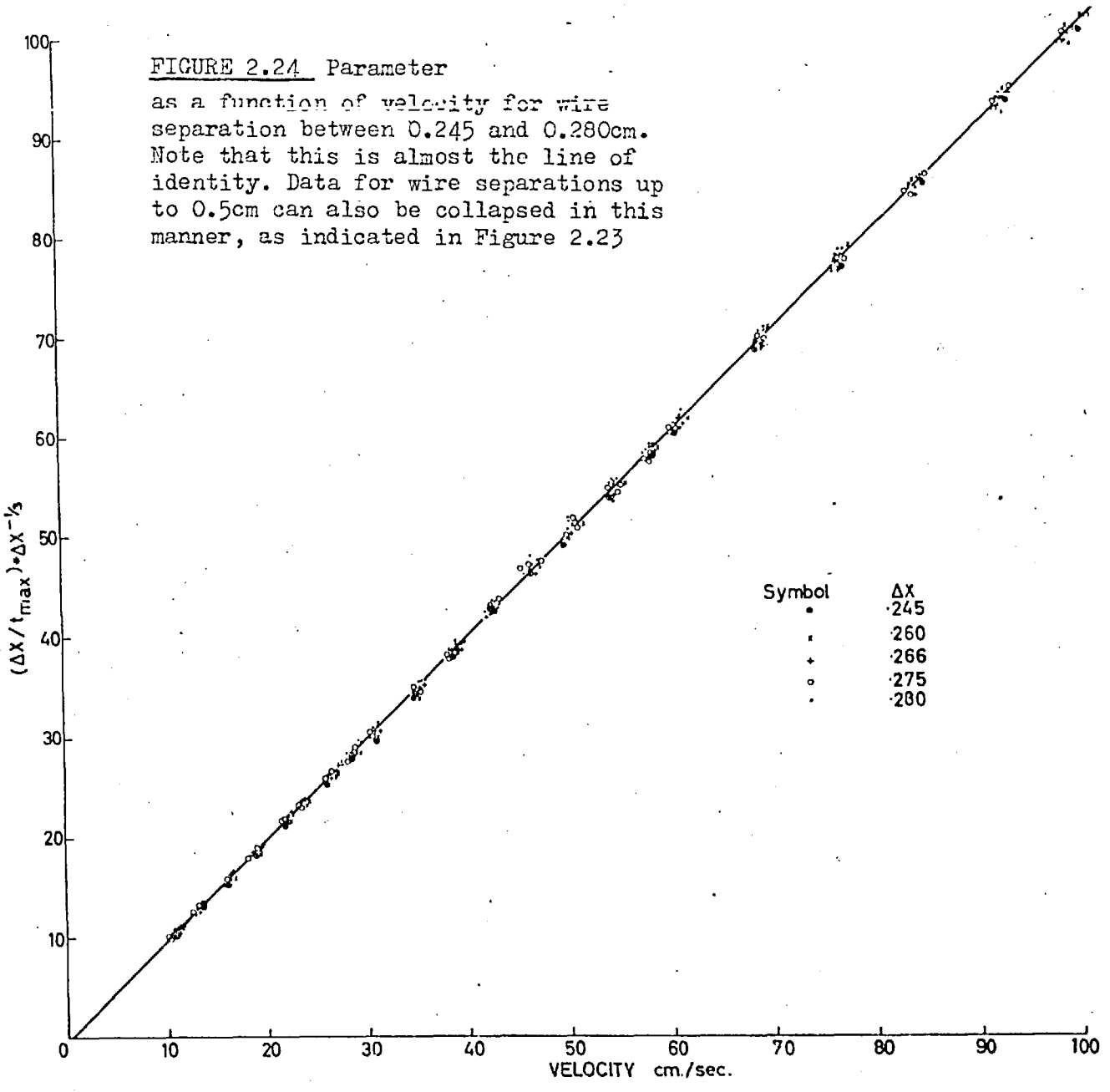


FIGURE 2.24 Parameter as a function of velocity for wire separation between 0.245 and 0.280cm. Note that this is almost the line of identity. Data for wire separations up to 0.5cm can also be collapsed in this manner, as indicated in Figure 2.23

the data, but the linear relation is sufficient to provide an accuracy of 0.3 cm/sec.

These observations have greatly simplified the calibration procedure, in that a calibration is not needed for every separation distance.

The shape of the t_{max} vs. velocity curve is associated with the error of measurement and also indicates the minimum velocity which can be measured. The measurement of the time to the maximum signal becomes less accurate as the signal decreases in amplitude. It is convenient that the slope of the t_{max} vs. velocity curve increases at about the same velocities where the accuracy of measuring the t_{max} decreases. These offsetting features result in an accuracy of velocity measurement of about 0.1 cm/sec for all velocities above the minimum measurable velocity. Figure 2.13 shows that the t_{max} for low velocities becomes ambiguous (i.e. the curve humps over and therefore has two solutions for t_{max} at low velocities). The lowest measurable velocity is a sensitive function of the separation distance. At a separation distance of 0.5 cm the minimum measurable velocity is about 1 cm/sec, and at separations of 0.25 to 0.30 cm the minimum measurable velocity is about 2.5 cm/sec.

The empirical evaluation of the parameters x and t_p indicate several features of operation. First with a constant t_p (always using the same pulse voltage and duration) the only parameter/

parameter which determines the relation between t_{max} and velocity is the separation distance, Δx. Therefore frequent calibration of the pulsed probe is not necessary as long as Δx is known. This is a great advantage over hot wire anemometry, especially when measuring low velocities. It should be pointed out that for accuracy in velocity measurement of approximately 0.1 cm/sec, the separation distance must be determined within 0.01 cm, which usually means measuring Δx with a microscope. Also the probe must be operated and handled such that Δx does not change. Therefore frequent calibrations are simply replaced by frequent measurement of Δx. A second feature of Δx is that it can be set to give a maximum accuracy over a given velocity range. Also Δx can be set to measure very slowly moving air.

Direction measurement

The direction of the velocity is found by determining the centre of the thermal wake. The accuracy of direction indication will therefore depend on the width of the wake. The half-width of the thermal wake will be of order

$$\delta = O\left(2\sqrt{\frac{K_a x}{v}}\right)$$

which means that as we increase the velocity or decrease Δx, the wake will become smaller. The influence of K_a as a function of the temperature will have the effect of increasing the width of the wake at high velocities and smaller Δx. Figure 2.25 shows the width of the thermal wake at three typical/

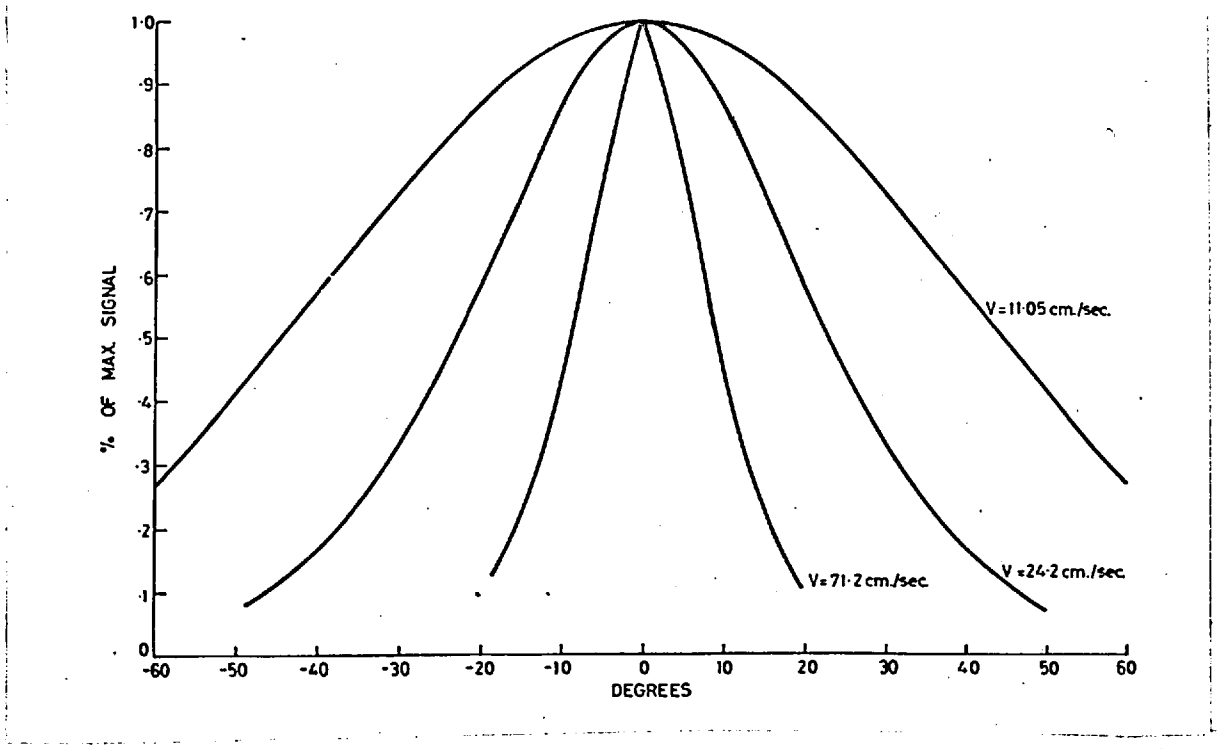


FIGURE 2.25 Thermal wake indicated by relative amplitude in the maximum signal of the sensor.

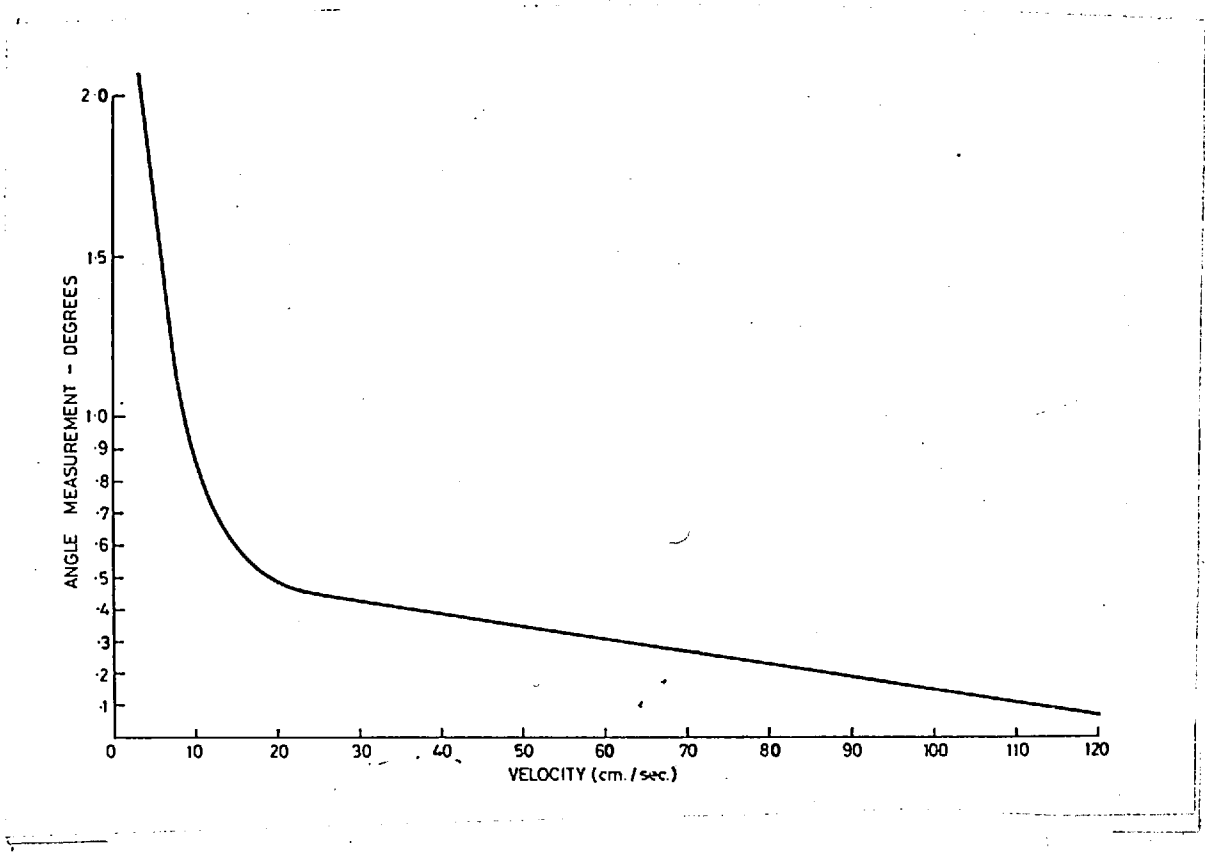


FIGURE 2.26 Repeatability in direction indication with probe operated in the entrance bell calibration rig as a function of velocity.

typical velocities. Two methods can be used for direction indication. With Peclet numbers above 10 (velocities over 20 cm/sec for the probe shown) the maximum signal can be determined by rotating the probe until a maximum is found. This procedure gives an accuracy better than 0.5^{o}. For Peclet numbers below 10 the symmetry of the thermal wake can be used to simplify the direction indicator procedure. With these low velocities the procedure is to revolve the probe to 5^{o} (say) on each side of the maximum. As the figure shows, the slope increases with increasing distance from the centre of the wake. Therefore a set angle on each side of the centre of the wake can be easily determined. Using this procedure an accuracy of below 2^{o} can be achieved at 5 cm/sec and below 1^{o} at 10 cm/sec. Figure 2.26 shows the repeatability of the direction indication as a function of velocity.

When the probe is operated on the horizontal the buoyancy forces will tend to give an erroneous direction indication at low velocities. This natural convection problem is very difficult to analyse theoretically. Yih (63) conducted an analysis for a line source of heat predicting the resultant heat loss and buoyant velocity patterns. If we use the empirically determined temperature at the centre of the thermal cloud (Figure 2.20) and moving coordinates then we can approximate a line source of heat with decaying temperature. If we could determine a time constant for development/

development of the buoyancy velocities then we might be able to analytically approximate the solution. Without this we can grossly estimate the effect of buoyancy by neglecting the transient effects and following Yih, attempt to approximate the amount of upward velocity at distances downstream of the pulse wire of 100, 200 and 300 diameters. After 300 diameters the temperature is too low to introduce significant buoyancy effects. We can conclude several general features from this gross calculation. First, with an initial pulse wire temperature of 800°C or less, the buoyancy velocity pattern downstream from the pulse wire will probably be laminar. Second, the amount of the upward movement will be a function of the Archimedes number; which is simply

$$A = \text{Grashof number}/(\text{Reynolds number})^2$$
$$= g\frac{D}{\nu^2}\frac{\Delta\gamma'}{\gamma_0}$$

where γ_0 is the density at room temperature and $\Delta\gamma'$ is the density change resulting from the increased temperature. D is the width of the thermal cloud with a mean temperature such that $\frac{\theta-\theta_0}{\theta_0}$ gives the resulting $\frac{\Delta\gamma'}{\gamma_0}$. The Reynolds number and Grashof number are both calculated using D as the length scale. Clearly D is a function of the thermal diffusion and can be measured by the width of the sensor wire signal at a given x. We then wish to determine D as a function of $\Delta\theta$ or $\Delta\gamma'$. Since only the very lowest velocities are invalid, we approximate the pulse wire as an instantaneous source. With this we can solve for $\theta(t,x)$ as in equation 2.4 and/

and obtain $\frac{d\theta}{dx}$. After a bit of algebra the relation between $\Delta\Theta$ and D is:

$$\frac{\Delta\theta}{\theta_0} = \frac{D\,Nu}{8\pi K^2 t^2}\left[ut - \frac{2K}{u}\left[\left(\frac{tu^2}{2K}+1\right)^2 - 1\right]^{1/2}\right] e^{-\frac{u^2 t}{4K} - \left(1+\frac{K}{u^2 t}\right)\left(\left(\frac{tu^2}{2K}+1\right)^2-1\right)}$$

where t is the t_{max} measured at a given x with velocity u, mean thermal diffusivity K_a and $\Delta\Theta$ is the maximum temperature change measured in the sensor wire. We can then determine A at distances downstream from the pulse wire of 100, 200 and 300 diameters. Using the calculated A at each position we can grossly approximate the upward displacement of the centre of the thermal cloud from Yih's calculations. Using the Grashof and Reynolds numbers based on the initial temperature and diameter of the pulsed wire, a distortion of 1^{o} in the direction measured occurs at an Archimedes number of about $4 * 10^{-3}$. Further, the effect of the buoyancy forces will not be a strong function of the separation distance. What this means is that most of the buoyancy effect takes place within 300 diameters downstream of the pulsed wire and therefore for distances of separation larger than 300 diameters the distortion will be similar. The calculation also indicates that the distortion will be approximately a linear function of velocity until small velocities (about 2 cm/sec) are reached. The maximum signal at zero velocity is, of course, directly above the pulse wire, or in other words, the angle of distortion is 90^{o}. Figure 2.27 shows the empirical angle of distortion caused by buoyancy in the entrance/

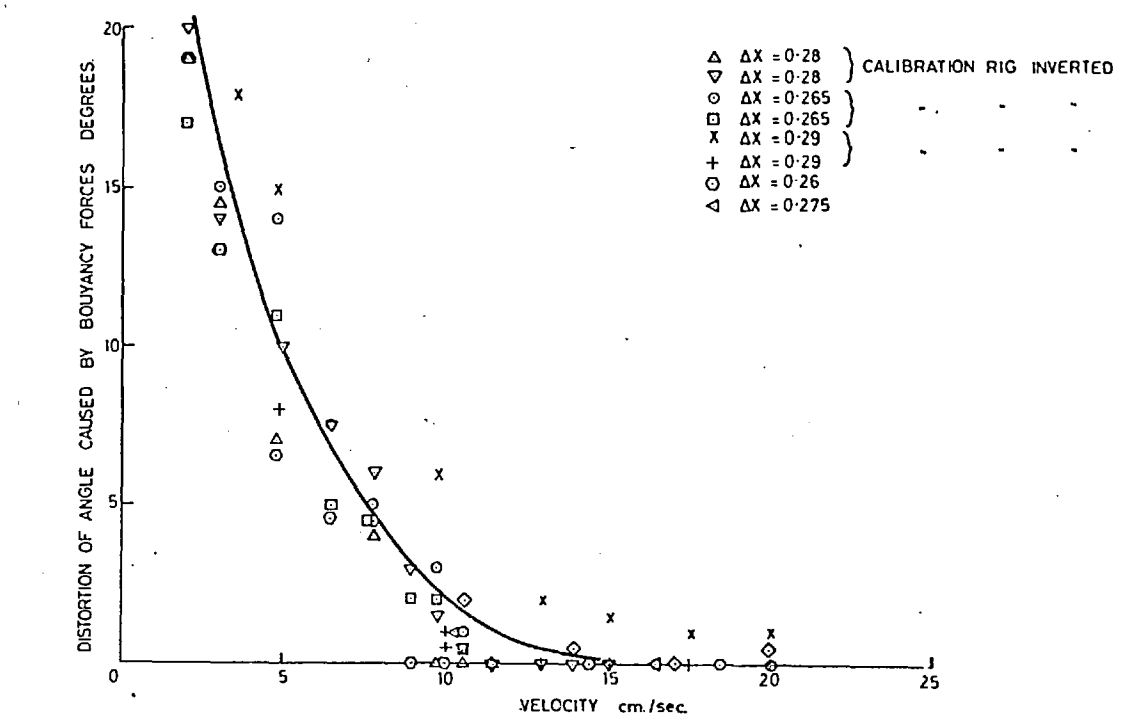


FIGURE 2.27 Measured angle distortion due to bouyancy forces at low velocities.

entrance bell calibration rig. The calculated distortion is also indicated. It is easily noted that the data is quite scattered. This can result from improper alignment of pulsed to sensor wire, or from velocities in the calibration rig not being parallel to the axis of the rig. The latter of these reasons seems to be most important. This is indicated by the unequal distortions measured when the calibration rig is used in the upright or inverted position. The improper alignment of the flow to the axis of the rig seemed to be a function of very small thermal differences of the air in the plenium before entering the calibration rig.

When the probe is operated on a vertical plane, the buoyancy forces, of course, do not affect the direction. The buoyancy forces do, however, create an effective yaw response in the vertical probe with very low velocities (<3 cm/sec). This yaw effect tends to give an indicated magnitude of velocity less than the real velocity.

Yaw response

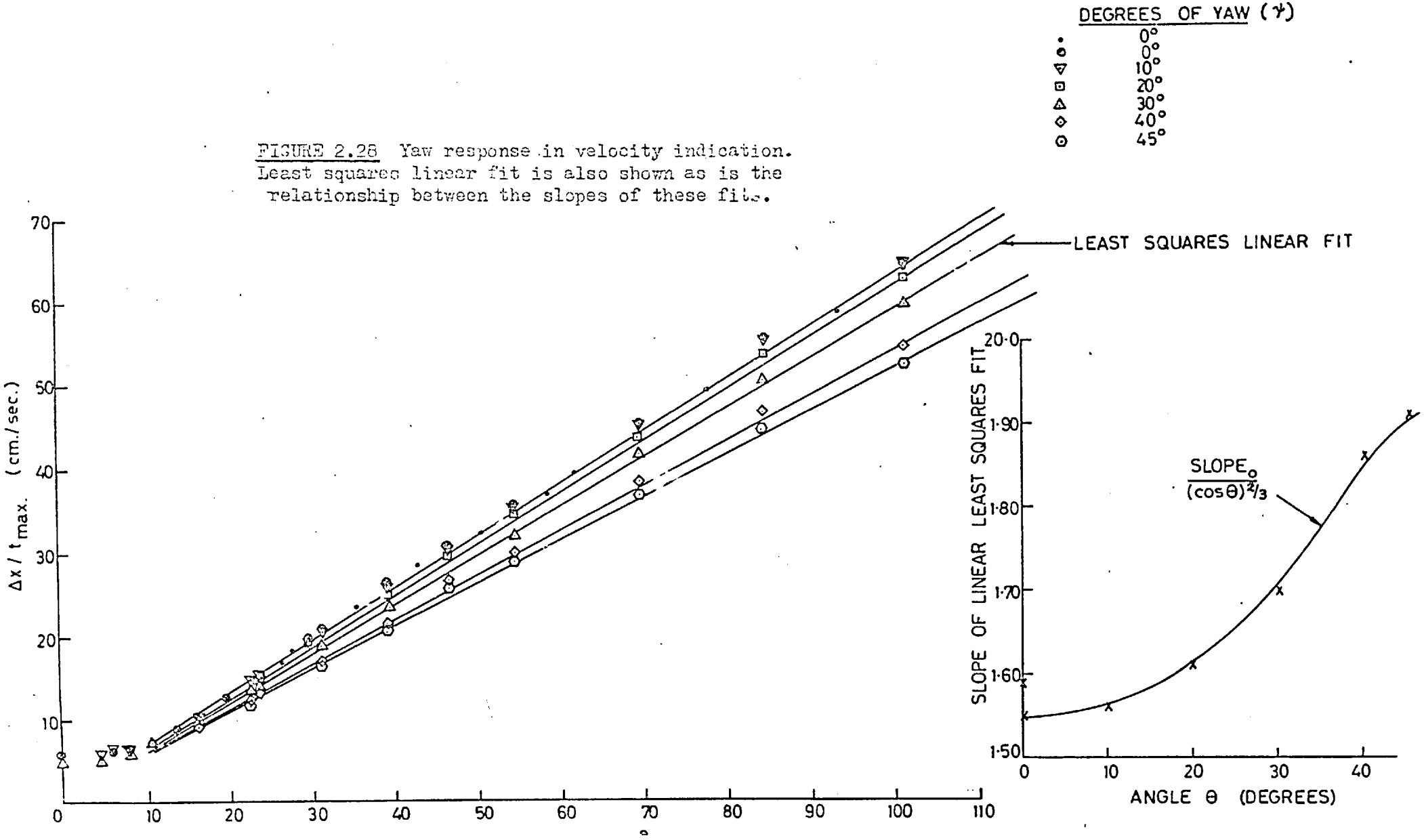
The operation of measuring a three dimensional flow field is to align the probe in one plane of the velocity vector, as shown in Figure 2.17. This usually involves measuring a flow with a yaw on the pulsed wire. The indication used for measuring the magnitude of velocity is the perturbation caused by the convection on to the thermal diffusion. No matter what/

what the convection pattern is, the diffusion problem is always the same, i.e. the length scale of the diffusion is simply the perpendicular distance between wires (separation distance). Therefore all that is changing in the problem with the introduction of a yaw is the length scale of convection by $x \cos\psi$. Figure 2.28 shows the response of the probe which has been yawed by the indicated angle. It can be concluded that the effect of yaw on the probe is simply to change the effective separation distance. Again the data can be collapsed by the parameter $\Delta x^{-1/3}$ which in this case is $(\Delta x \cos\psi)^{-1/3}$. The relationship relating velocity to t_{max} is thus

$$V = A + B \frac{\Delta x \cos\psi}{t_{max}} (\Delta x \cos\psi)^{-1/3}$$

This relationship holds until the yaw angle, ψ, becomes large enough so that the sensor wire either intercepts a signal distorted by the supports of the pulse wire, or the thermal pulse misses the sensor completely. For the probes produced in this study the minimum yaw was about 70°.

FIGURE 2.28 Yaw response in velocity indication. Least squares linear fit is also shown as is the relationship between the slopes of these fits.



CHAPTER 3

Primary and secondary flow of fluid in the entrance of a curved circular pipe

Summary

The flow entering a circular curved tube was experimentally investigated using the pulsed probe described in the previous chapter, along with hot wire anemometers. The primary and secondary velocities were determined for Reynolds numbers ranging from 150 to 1500 and Dean numbers from 45 to 800. The total kinetic energy, viscous energy dissipation and wall shear were determined from the velocity distributions. The results are compared to several of the numerous theoretical studies reported in the literature.

Introduction

The character of fluid motion in a bend has been well studied for the case of laminar fully developed curved flow and for turbulent flow entering a bend (Zanker & Brock, 84). In general the fully developed curved flow organises itself in response to the centrifugal force arising from the curvature. A pressure gradient is set up across the tube to balance the centrifugal force with the highest pressure at the outer wall of the curvature. In the/

the case of a circular curved pipe lying in a horizontal plane, the fluid near the top and bottom walls of the tube is moving more slowly than the fluid in the centre plane due to viscosity and therefore requires a smaller pressure gradient to balance the local centrifugal force. Consequently a secondary current results where the fluid in the boundary layer near the upper or lower walls is forced toward the centre of curvature, while the fluid in the core of the tube moves outward (Schlichting, 83). This pattern of a twin pair of helices was first theoretically explained by Thompson (85). The condition of fully developed curved flow only exists after the fluid has traversed what Hawthorne (86) terms the "bend transition region". Within this transition region the secondary currents undergo an oscillatory development experimentally described by Squire (87). The pattern of development depends strongly on the upstream velocity profile, the regime of the flow, the curvature and the Reynolds number. Pickett (2a) and Squire & Winter (95) have formulated theoretical arguments for the hydrodynamic laminar entrance flow in a curved pipe. Theoretical arguments have also appeared for fully developed laminar curved flow (Akiyama & Cheng, 88; Barva, 89; Pickett, 2a; Dean & Hurst, 90; Ito, 91; McConalogue & Srivastava, 92; Mori & Nakayama, 93) which conflict in the predicted secondary flow patterns at high Dean numbers. No experimental data/

data is, however, available for the entrance case with laminar flow at medium or high Dean numbers, nor is data available which accurately displays the secondary currents in either the entrance or fully developed cases.

A. Flow in the inlet region of a curved circular pipe

Theoretical considerations

In the majority of engineering situations, bends are generally in the region of 90 to 180° and therefore fully developed curved flow does not occur. Also the flow in such pipe fittings is almost always turbulent. Heat exchangers differ from this general case in that they may contain a coil of tubing where a region of fully developed flow exists (93). The theoretical work carried out primarily concerns itself with fully developed laminar curved tube flow, whereas experimental work conducted within the entry region of a curve concerns itself with turbulent flow (Rowe, 94). The application to engineering situations often requires the knowledge of the increase in resistance due to curvature whereas the application we seek requires a knowledge of the velocity distribution.

Theoretical consideration of flow in the inlet region of a curved pipe was first undertaken by Squire & Winter (95). They reasoned that at the inlet of a bend the inertial forces will predominate over the viscous forces/

forces. Thus in this initial stage of curvature the centrifugal forces will act on the velocity distribution within the inviscid core flow generating a component of vorticity in the direction of the flow, consequently a secondary velocity field is set up. Squire & Winter used the assumption of an inviscid, incompressible, steady, laminar flow to develop a simple equation relating the streamwise component of vorticity, ξ, to the angular (θ) distance from the start of the curve, and to Ω, the upstream vorticity component in the plane of the bend and perpendicular to the main flow:

$$\xi = -2\theta\Omega$$

A major difficulty in applying this equation is that the position of the primary streamlines must be known. A potential flow analysis can be conducted to find these streamlines in the initial region of the bend. If the assumption is made that the secondary flow will not distort the primary flow, then such an inviscid analysis requires the solution of a Poisson equation for a secondary flow stream function. Since the secondary velocities are linear in θ, the distortion of the flow will be proportional to $\left(\frac{R}{a}\theta\right)\theta$ where the constant of proportionality depends on the inlet velocity profile. Detra (96) found that for an inlet condition of fully developed turbulent flow into a curved pipe ($a/R = 1/27.4$), the region of linear increase in vorticity extended through 21°. Both Squire and Rowe considered/

considered a bend angle of 30° to be the extent of the linear region found in their experiments with similar curvatures and entrance conditions. For different curvatures the equation

$$\theta_L = \gamma\sqrt{\frac{a}{R}}$$

could be applied where γ is about 125° for the above experiments, but could vary by a factor of two depending upon the inlet velocity distribution.

These analyses, however, depend upon the upstream velocity distribution. If the incoming flow was without vorticity/

vorticity no secondary currents would be predicted from these inertial arguments. This shows how dependent the development of secondary currents is on the upstream velocity distribution.

Pickett obtained theoretical solutions using the opposite arguments; he attempted to isolate the effects of viscosity in determining the three dimensional velocity field at the inlet of a pipe. Pickett's assumptions require that no vorticity be present within the incoming flow. This is, however, not an unreasonable requirement if the curved tube is fed by an entrance bell creating a flat velocity profile at the entrance to the curve. Essentially Pickett's method was similar to the method used by Atkinson & Goldstein (99) for the flow development into a straight circular pipe, but with the additional feature of a curvature being present. Pickett expanded the boundary layer equations in powers of $Re^{-1/2}\frac{a}{R}$ (where a is the radius of the tube, R the radius of curvature of the centre line, and Re the Reynolds number). He also obtained a solution for the velocity distribution in the inviscid core of the pipe. He numerically evaluated the coefficients in the resulting equations for the primary, tangential and radial components of velocity for one curvature and Reynolds number and for the special case of a flat entrance profile (Re $\cong$ 9000, R/a = 0.05). The solution/

solution unfortunately breaks down rapidly for the curvatures of interest in this study. The solution only holds within a length from the entrance of the curve which is of the same order as the length in which the Atkinson-Goldstein solution holds for entrance flow into a straight tube. For curvatures of $R/a \leq 3/1$ the solution breaks down even more rapidly. This means that for the curves and Reynolds numbers studied in this chapter, Pickett's solution is applicable only for the first 4° of the bend, or less.

I evaluated the coefficients on the expansion parameters required in Pickett's equations for the velocity components to compare with one of the sets of experimental data later to be presented. For this I chose the case of Reynolds (1030) and curvature ($a/R = 1/16$) which allow the application of Pickett's solution over the maximum axial distance (4°). Predictions concerning the primary velocity distribution, the relative strength of the tangential component of velocity in the boundary layer, the viscous energy dissipation can be thus extracted from Pickett's solution and compared to the experimental data; this will be done within the discussion section.

Experimental studies

The first studies toward understanding the three dimensional flow field within a bend were conducted by Eustrice/

Eustrice (101) who introduced streams of coloured dyes into glass bends of various curvatures and bend angles from about 20° to 360°. Eustrice demonstrated the existence and general shape of the intricate and beautiful* three dimensional laminar flow field within the bends. Accurate description and quantitation of the three dimensional field from the reported two dimensional drawings is, however, difficult.

Most of the experimental studies carried out measuring the velocity field of the flow within the bend transition region of a circular curved pipe have dealt with turbulent fully-developed flow as the inlet condition to the bend. These studies are primarily concerned with evaluating the inertial development of the secondary currents. Detra, Eichenberger and Hawthorne measured the total pressure field only. Squire (87) went further by inferring the gross directions of the secondary currents based upon changes in the measured total pressure distribution supplemented by apparent** direction measurements on the axis of the bend and near the upper and lower/

---

*The patterns must have been indeed a beautiful kaleidoscope of colour since Eustrice used streaks of six different vivid colours which all remained distinct while twisting among one another.

**Squire states that he attempted yaw measurements but these measurements were not completely successful.

lower walls of the tube. Squire interpreted the results of his measurements in a 180° pipe bend with R/d = 12 and feed with fully developed turbulent flow to imply that the secondary flow in the transition region is oscillatory, with the oscillations being damped out as the flow in the curve becomes fully developed. He produced diagrams which imply that the direction of the secondary flow is at first similar to the fully developed curved flow situation and then reverses direction at an angle into the bend of 90°. The secondary currents again change within the next 30°, approaching fully developed curved flow at 120° within the bend. Figure 3.1 is a reproduction of the indicated direction of the secondary currents by Squire.

Squire's attempts to measure the secondary velocities directly were, however, unsuccessful. Rowe extended the experimental measurements of Squire by obtaining the component of secondary velocity in the plane of a 180° bend with the same experimental conditions as Squire. From the measured changes in the primary velocity, between each 30° station within a bend, along with the measured component of the secondary velocity, he produced complex secondary current patterns. These patterns always maintain the general direction of the fully developed flow currents but with areas of smaller scale vortices embedded

in/

FIG. 2.4 STAGNATION PRESSURE IN A 180° PIPE BEND (AFTER SQUIRE)

Figure 3.1

in the general pattern but opposite in direction. These twin vortices first appear near the inside of the bend. Rowe attributed these reversals to the drift of the streamwise vorticity predicted by the Squire & Winter analysis. This vorticity is produced within the first 20° to 40° of the bend at the upper and lower regions of tube where the velocity gradient is perpendicular to the plane of the bend. The vorticity is conveyed by the secondary flow toward the inner wall. The secondary flow in Rowe's measurements was slower at the inner wall (this is contrary to the results of this chapter), allowing the vortex filaments to drift closer together and form a twin vortex roll-up. This concentrated area of vorticity is then apparently propelled toward the outer wall by the secondary current in the plane of the bend.

Rowe's primary velocities were, however, similar to Squire's and showed the same trends. Both investigators found that at about a 45° bend angle the measured pressure contours appear most distorted from their initial position, and that after 120° little change in the contours were noted (i.e. the fully developed condition was reached). The magnitude of the secondary flows in Rowe's experiments showed a linear increase from the inlet of the bend to the first measured position (30°) and thereafter decreased in magnitude until at about 90° the total secondary flow reached a steady value. Rowe also made calculations (94b) using an inviscid analysis, combined/

combined with Squire & Winter's results, and the boundary condition of a fully developed turbulent profile at the bend inlet. The measurements and calculations showed reasonable agreement.

Two investigations have studied flow in the transition region of a bend with entrance profiles other than fully developed turbulent flow. Eichenberger (98) artificially produced a velocity profile for entrance into the bend which was linear in a plane perpendicular to the axis of the bend. The period of oscillations occurring in the total pressure field as the flow moves around the bend was less than that found for a fully developed turbulent inlet. Bansod & Bradshaw (100) studied the flow in an S-shaped duct with a flat entrance condition. If we consider the first curve of the bend as the inlet to a curved tube (assuming that the upstream influence of downstream conditions is small) then we can compare their results to those of Rowe. The curvature of Bansod's section (R/a =7) was, however, much smaller than Rowe's configuration. Bansod found contours of total pressure which were similar to those of Rowe and Squire in shape. He also measured yaw in the tangential direction from which he could interpret the direction of the secondary currents. The direction of these currents was similar to those measured by Rowe within the boundary layer, but were opposite in direction just outside it. Bansod could only/

only measure tangential components of velocity, not radial, so his observations are not inconsistent with the other studies. The tangential component of velocity is probably a good indication of the total secondary flow within the boundary layer, but not within the core where the general direction of secondary flow is probably parallel to the plane of the bend.

The above mentioned theoretical and experimental studies have the most direct relevance to the work reported in this thesis. Many other experimental investigations have been reported, primarily concerned with the measurement of pressure loss within the transition region of a bend. These studies are well reviewed by Zanker & Brock and by Hawthorne. In general these studies show wide variation in the measurements of energy dissipation.

B. Fully developed flow in a curve

Two basic approaches are used for solving the flow field within a curve for the fully developed laminar case. A perturbation method is applicable for flows with a low Dean number. The perturbation parameter is a/R which must be small. Dean (102) expanded the Navier-Stokes equation as a power series in this parameter and gave solutions as far as the fourth power. He showed by dynamical similarity that the flow depends on a single non-dimensional/

non-dimensional grouping

$$K = Re\,(a/R)^{1/2}$$

where Re is the Reynolds number, a the radius of the circular tube and R the radius of curvature of the centre line, and this non-dimensional parameter is now known as the Dean number. Dean showed that his analysis was reasonably reliable for values of K up to 17. Cuming (103) extended the same method to curved pipes which are elliptical in section and showed that the aspect ratio of the pipe has considerable effect on the intensity of the secondary flow. Dean & Hurst investigated the flow with Dean numbers of order one, in order to describe the secondary flow pattern. They predicted a simple pattern of secondary flow in that the direction of the secondary velocity in the core area of the tube was parallel to the plane of the bend and toward the outer wall. McConalogue & Srivastava used a Fourier-series to connect the fluid elements within the plane of cross section and then numerically solved the resulting coupled non-linear equations. The numerical solution was obtainable up to Dean numbers of 102.9. They produced patterns of secondary flow which, like those of Dean and Hurst, were directed approximately parallel to the plane of the bend in the core. The secondary flow patterns near the upper and lower walls were shown to move in an approximately tangential direction. The centre of the secondary vortex moves outward as the

Dean/

Dean number increases (as does the position of maximum axial velocity). Also the thickness of the tangential boundary layer decreases.

The other approach to the problem is to use a boundary layer analysis which may be expected to hold for high Dean numbers. Adler (104) was the first to do this. He experimentally examined the axial velocity field for fully developed laminar and turbulent flow in curved tubes with larger curvatures. He found that the velocity field was arranged with a boundary layer near the wall; the layer being thin at the outer edge of curvature and progressively becoming thicker on the wall in the tangential direction toward the inner wall of curvature. Adler then solved the boundary layer equations to predict the resistance to flow in a curve. Barva (89) used the same assumptions as Adler for the analysis of the velocity field and obtained reasonable agreement with experiment at Dean numbers of order 100. Pickett and Mori & Nakayama (93) have used similar boundary analyses for a laminar flow while Ito (91) has produced an analysis based on a Pohnhausen approximation to obtain solutions which have seemingly better agreement with experimental data. Recently, Akiyama & Cheng (88) have obtained a finite-difference solution using what they termed a "boundary vorticity method" which gives good agreement with the velocity distribution found by Adler. These theories can be/

be grouped into two classes. Barva and Pickett predict separation occurring near the inner wall of curvature, while the others do not. This prediction of separation comes about when solving the boundary layer equations (and matching to the core solution) in a step-like progression starting at the outer wall. The solution blows up at about 63° from the axis at the inner wall in Barva's calculation. He predicts that the secondary velocities are separating at this point and that a large swirl in the secondary pattern would exist there. Pickett's solution predicts that the separation is caused by distorted distribution of the axial velocity but notes that the boundary layer approximations break down at such a position of separation. The solution of Mori & Nakayama (which is most comparable to Barva's and Pickett's solutions) and the solution by Ito do not show this phenomenon occurring.

Experimental techniques*

Two circular curved tubes were constructed from blocks of Perspex. The tubes were constructed by machining two half sections along the prescribed curvature with a semi-circular cutter; this ensured that the cross-section of the model remained circular. The inside surface was polished/

*The experimental methods used in all the flow studies throughout this thesis are similar and therefore these methods will not be discussed elsewhere.

polished and slots (or holes) were milled into the model to give access to the probes. The tube diameter was 1.5 inches and two radii of curvature were used, 12 inches and 3.5 inches, resulting in curvature ratios of 1/16 and 1/4.66. Figure 3.2 shows one half-section of the model with a radius of curvature of 12 inches. Each curve extended through a bend angle of 270° but only the first 180° was used for measurement. We therefore assumed that end effects were negligible within the test section. The slots not in use were filled or taped over completely. The slot in use was filled (or taped) over partially, allowing only enough space for the probe to protrude through.

The model was not extended past 270° so as to avoid introducing a helical curvature in the model. Such helical curvatures can affect the secondary velocity field, as analysed by Pickett. The resultant test section is relatively short, limiting the ability to ascertain when the fully developed flow condition is reached. Fully developed flow was determined by two methods. The first was simply to find the angular position within the bend where the velocity field does not change between measured stations (see Figure 3.14 as an example). An alternative method was to determine the secondary flux across a plane within the cross section (in particular the vertical diameter)/

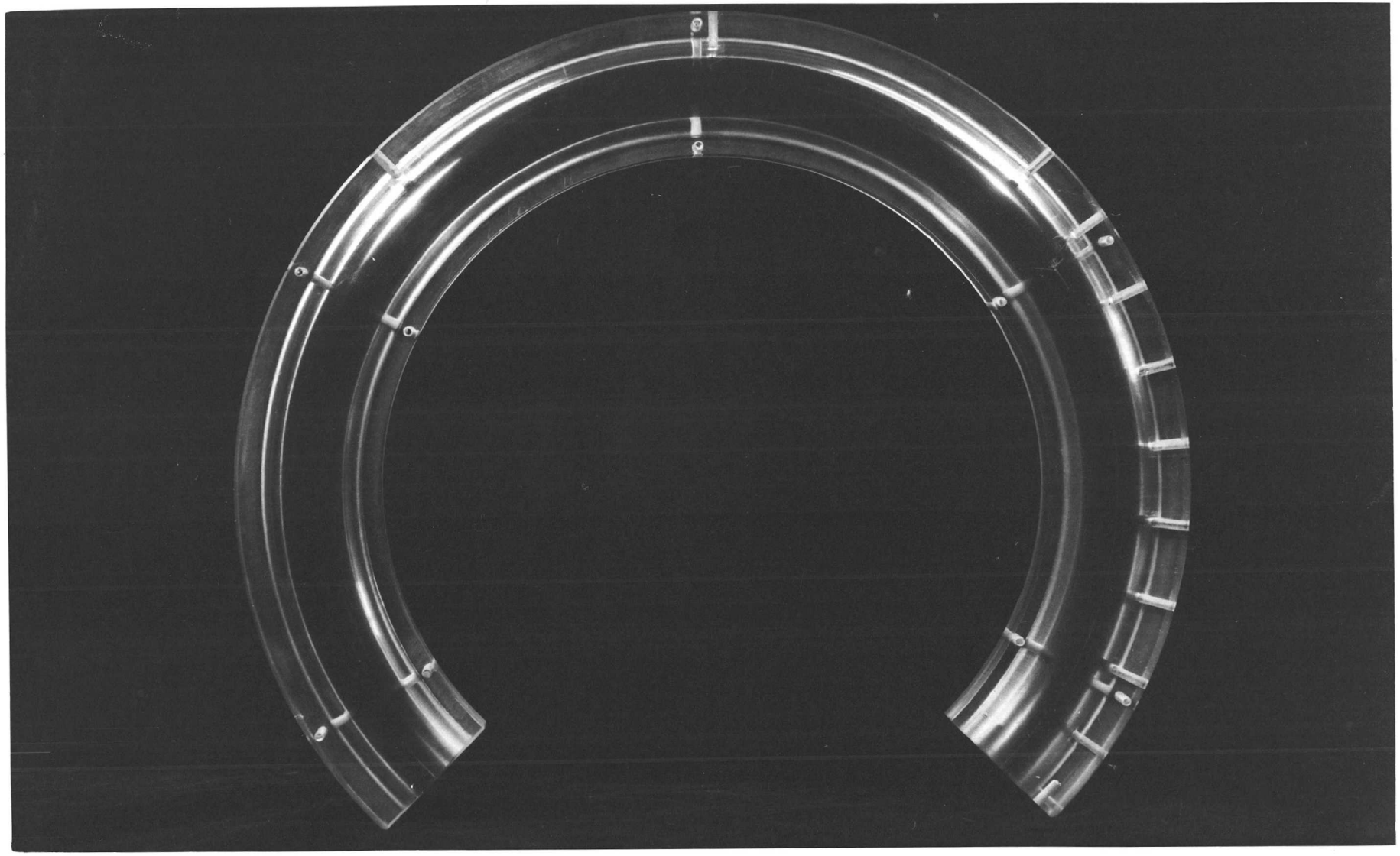


FIGURE 3.2 Curved tube model with a/R = 1/16

diameter) of the tube and perpendicular to the plane of the bend. When the net secondary flux was zero, and remained zero, the condition of fully developed flow was reached.

Two entrance profiles, flat and parabolic, were used for each model; the flat entrance profile was produced by an entrance bell feeding directly into the model.* The flow was screened and straightened immediately prior to the bell. The profiles produced at the mouth of the bell were measured with a straight outrun of 30 cm attached to the bell and the results of these measurements are shown as the first of the series of profiles in Figure 3.5 to 3.14. The direction of the velocities within the mouth of the bell was also measured and shown to be parallel to the axis of the tube within $\pm 0.5^{o}$. A parabolic velocity profile was produced by a straight, thermally isolated tube of over 100 diameters in length. The velocity profiles were within 1% of a parabolic distribution and the direction of flow was parallel to the axis within $\pm 0.5^{o}$. It should be noted that thermally isolating the system is quite important. A temperature difference of about 5^{o} between the air within the long tube and the tube walls causes buoyancy effects which become progressively larger as the flow moves down the tube. This results in a skewed axial velocity field along with a component of secondary/

*A distance of 0.5 diameters existed between the mouth of the bell and the 0^{o} position in the model.

secondary velocity of about 5% of the total velocity. Since the vorticity produced in the curve is related to the upstream vorticity, this buoyancy effect thus disturbs the velocity field within the test section. The magnitude of this thermal effect will change as the environmental temperature changes and therefore the measurements in the test section will vary from day to day. Curvature of the upstream entrance tube will also cause similar effects.

The volume flow into the system was delivered from an axial fan (a Hoover vacuum cleaner) through a volume plenum and heat exchanger. This ensured a constant flowrate and avoided any rapid thermal fluctuations in the gas. The volume flow rate was measured by rotameters, accurate to 1%. The temperature of the gas was constantly monitored and the rotameter reading corrected for temperature.

Measurements were carried out using the pulsed probe as was discussed in Chapter 2, along with specially constructed hot wire anemometers. The operation and calibration of the pulsed probe has already been discussed. The hot wires were used primarily to determine the velocity gradients near the walls, although velocity profiles were also taken with this instrument. The hot wire probes, like the pulsed probe, were calibrated within an entrance bell (see Chapter 2). Pitch and yaw calibrations were also carried out on the hot wire probes but/

but these calibrations were much less frequent than a simple velocity calibration which was run before and after each experiment. The pulsed probe is limited in its ability to measure velocities close to a surface. For the pulsed probes used in this thesis, velocities could only be measured at distances of 0.1 cm from the wall of the tube ($\approx$ 0.93 nondimensional radius in the curved tube models). The hot wire probes were used to extend the velocity measurements to locations very near the wall ($\approx$0.99 nondimensional radii), and thus wall correction calibrations were also carried out.

Multiple wall calibrations must be carried out when measuring low velocities ($<$5 cm/sec) near a wall. This is because the natural convection currents, which are important at these velocities, will be distorted by the presence of the wall. Wall calibrations were conducted for three wall orientations: vertical, horizontal and above the probe, and horizontal and below the probe. Again these calibrations were conducted at much less frequent intervals than the simple velocity calibrations. A wall correction factor was obtained for the three wall orientations at progressive distances between the hot wire probe and wall and for a variety of velocities. These calibrations were carried out within a long straight tube with parabolic velocity profiles. The hot wires used in this study were able to give adequate velocity measurement only/

only down to velocities of about 5 cm/sec. Fortunately when the velocities become this low, the viscous boundary layer is so large that the pulsed probe protrudes well into the viscous boundary layer, giving adequate description of the velocity gradient at the wall. Pitch or yaw corrections were made on the hot wire measurements. The magnitude of these corrections was ascertained by the direction indications from the pulsed probe measurements and extrapolated to the positions where the hot wire measurements were taken.

Most of the studies were carried out by protruding the probes from the side of the models. The probes used thus sensed the velocity directly off the end of the probe's shaft. The presence of the probe shaft can affect the velocity field. This effect was studied in the entrance bell by orienting the hot wires both along the axis of the tube and perpendicular to the axis (protruding from the side). The change in magnitude of the indicated velocity was simply related to the amount of blockage which the probe shaft presented (approximately 3% at maximum). Distortions of the three dimensional velocity field were more difficult to ascertain. These distortions were assumed negligible. The measurements of the velocity field indicate a symmetrical distribution which seems to validate the assumption that the probe caused little distortion.

Figure/

Figure 3.3 shows the manipulating device used for most of the measurements. The micro manipulator was used to position the probe (note: only the vertical manipulator is shown) in the vertical and horizontal directions. The swing arm on the protractor shown in the figure was used to indicate the direction of the velocity. The device was machined so that its base was parallel to the zero angle reading of the protractor, and this base was aligned perpendicular to the axis of the tube. The probe was clamped into the device and the orientation of the wires were set perpendicular to the base of the manipulator by a microscope. The whole procedure gave repeatable alignments of the pulsed and sensor wire parallel to the axis of the tube to within 0.5^{o}. The figure also shows the small curve model used and the entrance bell with flow straighteners and plenum. Measurements were taken by traversing the probe within five planes parallel to the axis of the bend (a horizontal orientation in Figure 3.3) and five planes perpendicular to the axis of the bend. Seven of such traverses are shown in Figure 3.4. Velocity measurements were taken at each millimetre increment and direction indications at each two millimetres. The direction indications were interpolated to each millimetre, thus giving an indication of the velocity at approximately each 0.05 increment of the nondimensional radius.

In all, 350 measurements were taken at each station within the tube. This relatively large number of measurements/

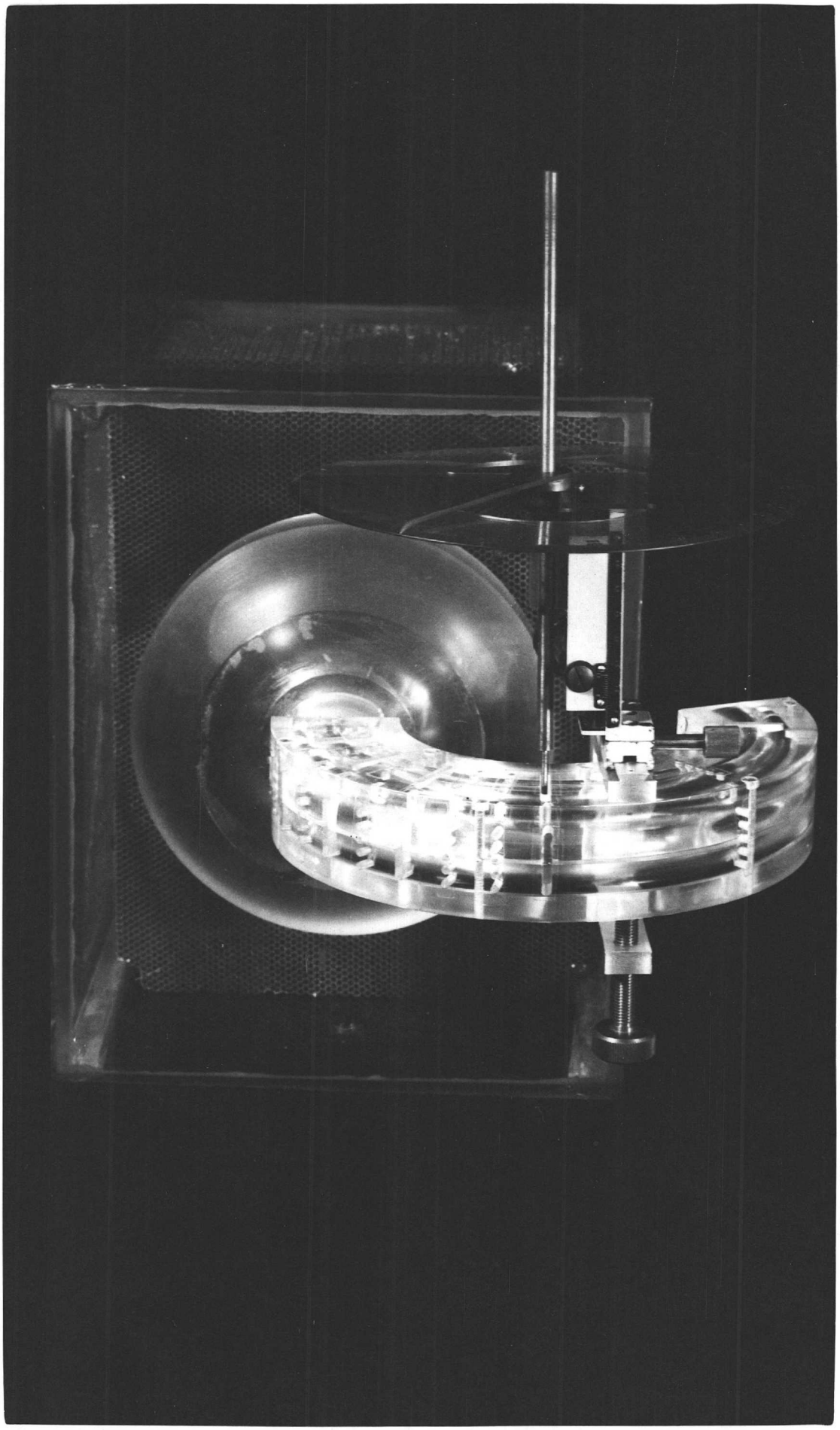


FIGURE 3.3 Small curve model, entrance bell flow straighteners and manipulating device used. Traverses of the probe were conducted in both vertical and horizontal planes. Protractor was used to indicate directions.

TYPICAL DATA SET

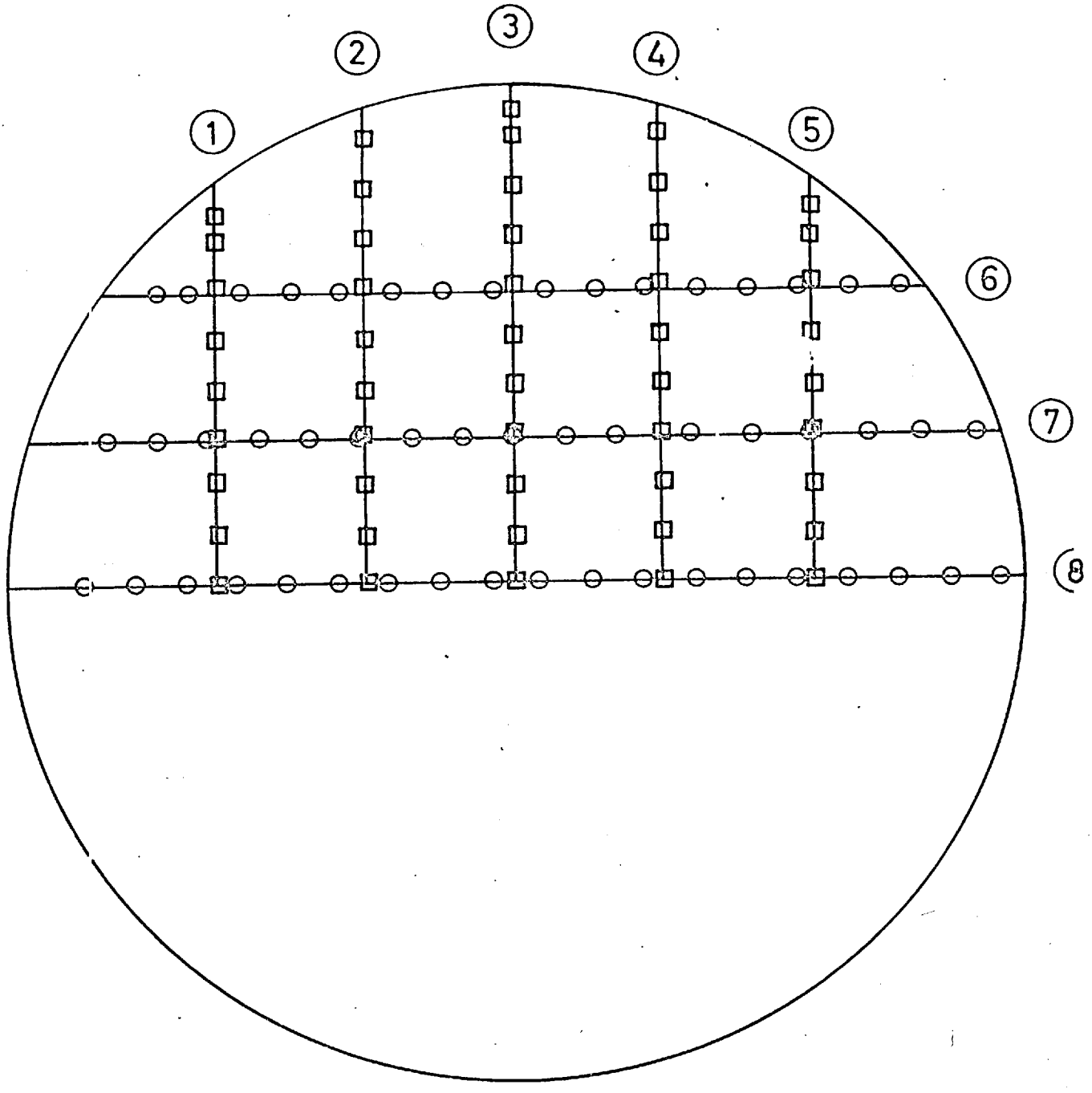


FIGURE 3.4 Eight of the ten traverses used for measurement indicating the typical location of data.

measurements was required to describe the intricate secondary flow field. Hot wire velocity profiles were taken at only two planes; parallel and perpendicular to the axis of the bend. Measurements were taken at millimetre increments within the core and at more frequent increments near the walls.

Methods of data handling

The velocity profiles from both the pulsed probe and hot wire probe were analysed to obtain the integrated volume flow rate (the zeroth moment), the first through third moment of the velocity distribution, the energy dissipation and the total kinetic energy. This analysis was carried out numerically on the CDC 6600 computer facility at Imperial College. Each profile was first interpolated using a five power Lagrangen method to obtain velocities at each position of 0.05 nondimensional radius (r). The end points of the profiles were interpolated with progressively smaller powers of a polynominal reaching a linear interpolation between the last measured velocity and the wall. The resulting pulsed probe profiles were handled differently than the hot wire profile. For the pulsed probe an interpolation of each angle (measured parallel or perpendicular to the plane of the bend) measurement was conducted in a radial direction by fitting a four term Fourier series via a least squares method to the data. This interpolation was carried out

at/

at each 0.05r. The angles measured on the planes 1 through 5 are shown in Figure 3.4, where thus interpolated to planes 6-10. This angle is the yaw which the probe encounters when used in planes 6-10, and therefore is the yaw correction needed for velocity determination. This correction, $(\cos\psi)^{2/3}$, is usually small since the maximum angles measured within the boundary layer in any one profile are usually less than about 30° ($(\cos 30^{\circ})^{2/3} = 0.908$), and the direction angles within the core flow are usually less than 10° (correction = 0.990). The velocity field, corrected for yaw, is thus obtained and is displayed directly from the data while the calculations of the moments, energy dissipation and total kinetic energy are done with a set of Fourier equations fitted to the velocity distribution. The velocity distributions obtained suggest that a four term Fourier equation will adequately describe the contours, i.e.

$$V(r,\theta) = A + B\cos\theta + C\sin\theta + D\cos 2\theta \quad ..$$

The total velocity and each Cartesian component were thus fitted with this four term Fourier series via a least squares method. The solution for the Fourier coefficient is not straight forward, because the number of data points along the outer circumferences are more numerous than along the inner circumferences, i.e. 22 fitted points at r = 0.95 to 12 points at r = 0.6). This situation creates an algebraically messy problem. Within the centre of the tube from r = 0 to r = 0.25 the fit is of course exact/

exact, because there are only four data points.

The direction of the total secondary velocity was obtained by interpolation of each measured component of the secondary velocity with a procedure similar to that used for yaw correction. In this case, however, the expected changes in direction, especially if separation phenomena are present, may occur within smaller circumferential lengths. This requires that a higher order Fourier series be used. Unfortunately it was found that when the number of terms in the Fourier series approached the number of data points being fit, instabilities in the equations occur. This is due to the fact that the direction of the total secondary velocity can vary considerably with small changes in either of the secondary velocity components, provided that both components are near zero. This difficulty limited the ability to describe the pattern of secondary flow in detail. Work is continuing on this aspect of the study.

Results

Table 3.1 shows the Reynolds and Dean numbers at which the experiments were carried out. These flow rates and curvatures were chosen so that each Reynolds number had two similar Dean number conditions and also vice versa: each Dean number had two similar Reynolds number conditions, as/

TABLE 3.1

REYNOLDS NUMBERS AND DEAN NUMBERS

OF EXPERIMENTS

Reynolds Number Re	Dean Number K	Curvature Ratio a/R
1634	756	1/4.66
1630	407	1/16
1031	476	1/4.66
1029	257	1/16
540	250	1/4.66
539	135	1/16
301	139	1/4.66
300	75	1/16
180	83	1/4.66
180	45	1/16

as can be seen in the Table. Each of the ten flow conditions was studied with the two entrance profiles (flat and parabolic). The flow within the curve with a flat inlet profile develops in a more complex manner than flow with a parabolic inlet. Therefore measurements were taken at more frequent intervals for the flow entry condition. Measurements were taken within the entrance pipe at the start of the bend, and at each 10^{o} of bend angle up to 90^{o} for the flat inlet; and at each 30^{o} for the parabolic. After 90^{o} the changes in the velocity field are much less rapid. Therefore measurements were taken at each 45^{o} position after 90^{o}, i.e. 135^{o} and 180^{o}. It was assumed from the work of Squire and Rowe that fully developed flow would have been reached before 180^{o} and therefore no systematic attempt was made to study the velocity distribution after 180^{o} of the bend. In all, 380 velocity distributions were determined, which makes the presentation of the results in this study very difficult. Clearly 380 polar contours of primary and secondary velocity distributions are unpresentable. Further, the interaction between the viscous effects and inertial effects causes an intricate development of the flow, disallowing gross generalisations to be made. The presentation of the basic ideas of this study can best be served by displaying one total analysis of the flow (all velocity components and directions) at a fully developed state. This allows comparison with the theories for/

for fully developed flow. In addition to this, the linear velocity profiles in the plane of the bend at each measured position are presented. This adequately displays the viscous-inertial interaction. Finally the secondary profiles are shown at less frequent angular intervals than the primary velocity profile and are shown for seven of the ten traverses measured within each station. This gives information as to the magnitude and pattern of the secondary velocities as a function of Reynolds number, Dean number, bend angle and entrance condition. As was shown in the previous sections of this chapter, all of these dimensionless parameters are required for an adequate description of developing curved tube flow.

Figures 3.5 to 3.14 display the measured primary velocity profiles in the plane of the bend, for the ten Reynolds and Dean number conditions measured. In general the pattern of development of the primary velocity distribution has similar trends for all Reynolds numbers measured with a similar entrance condition.

For a flat distribution of velocity at the inlet, an initial velocity skew is present at the inner wall of curvature, as would be the case in an ideal flow devoid of vorticity at the inlet. Further, this skew is present at the onset of the curve and slightly upstream, inferring that the fluid mechanics at the start of the bend must be described/

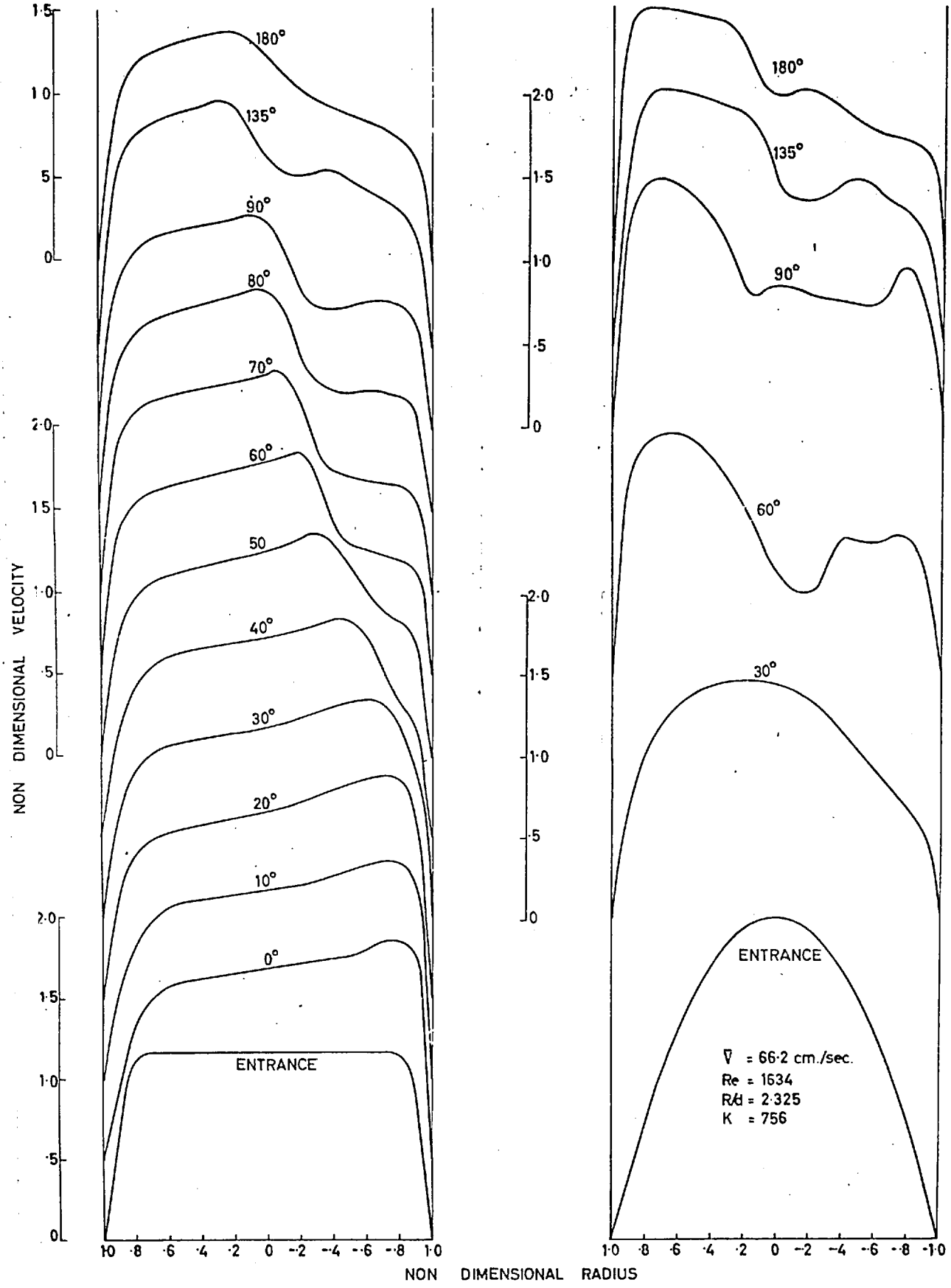


FIGURE 3.5 Velocity profiles in the plane of the bend at the indicated positions of bend angle.

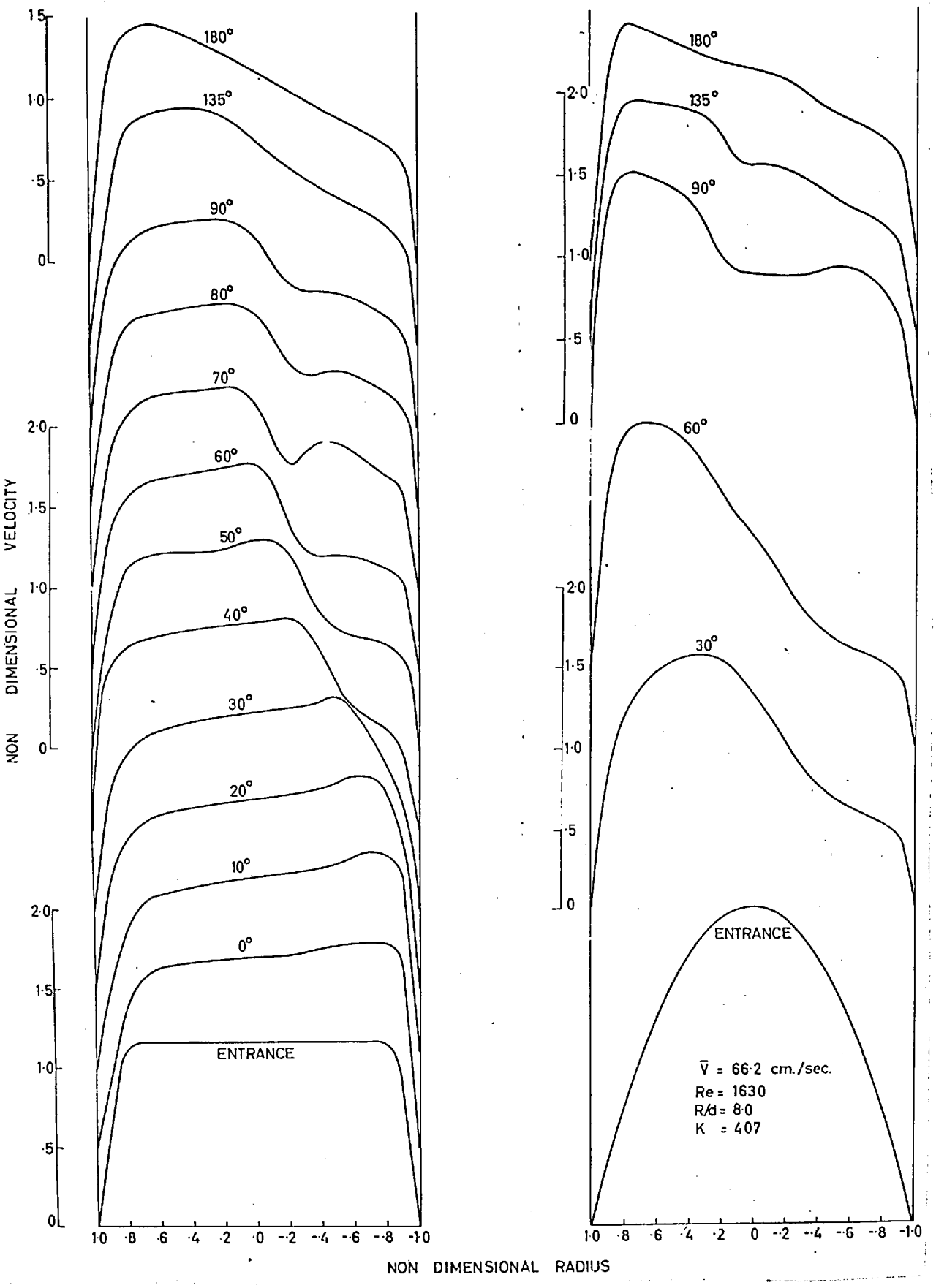


FIGURE 3.6 Velocity profiles in the plane of the bend at the indicated positions of bend angle.

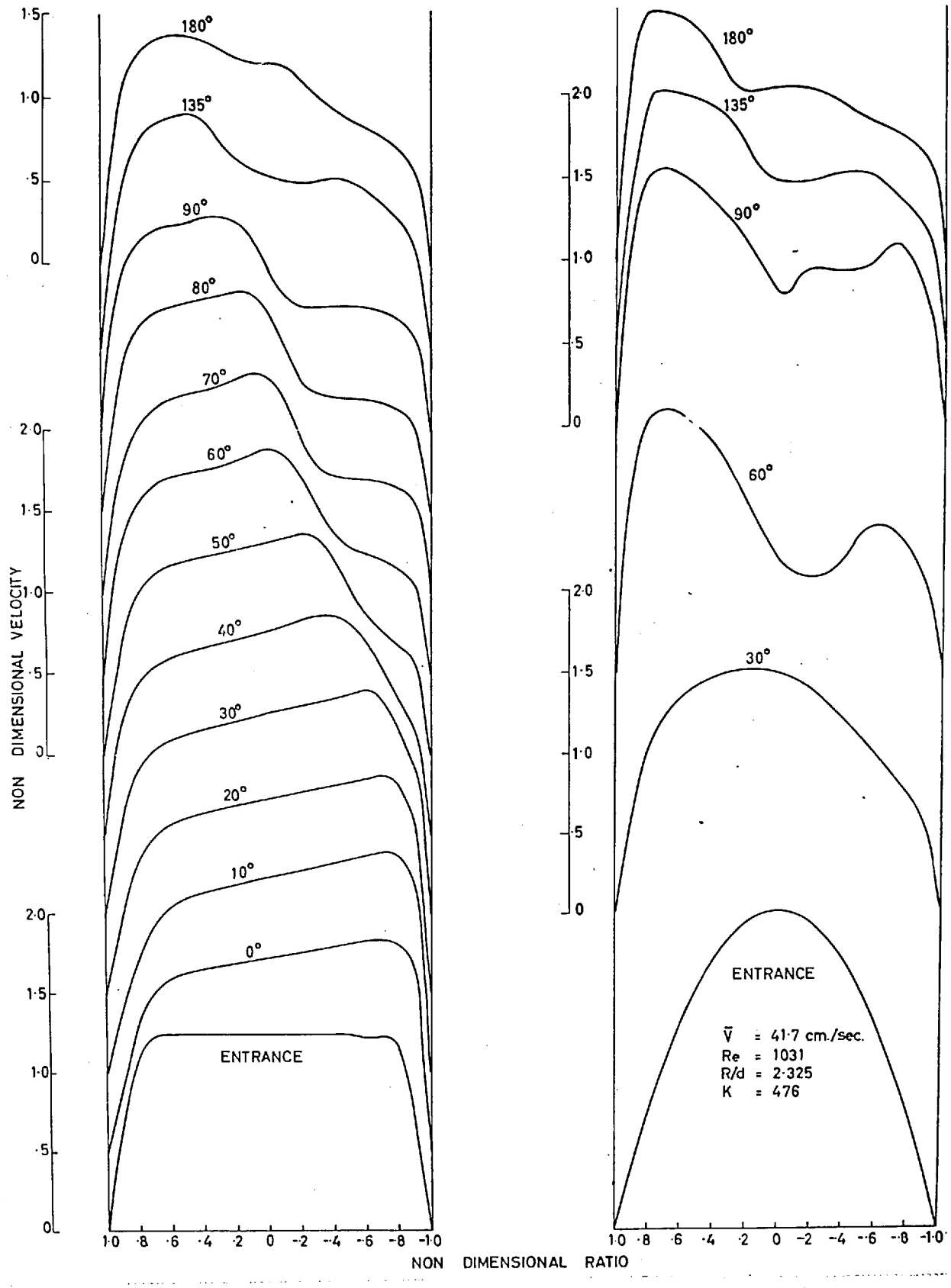


FIGURE 3.7 Velocity profiles in the plane of the bend at the indicated positions of bend angle.

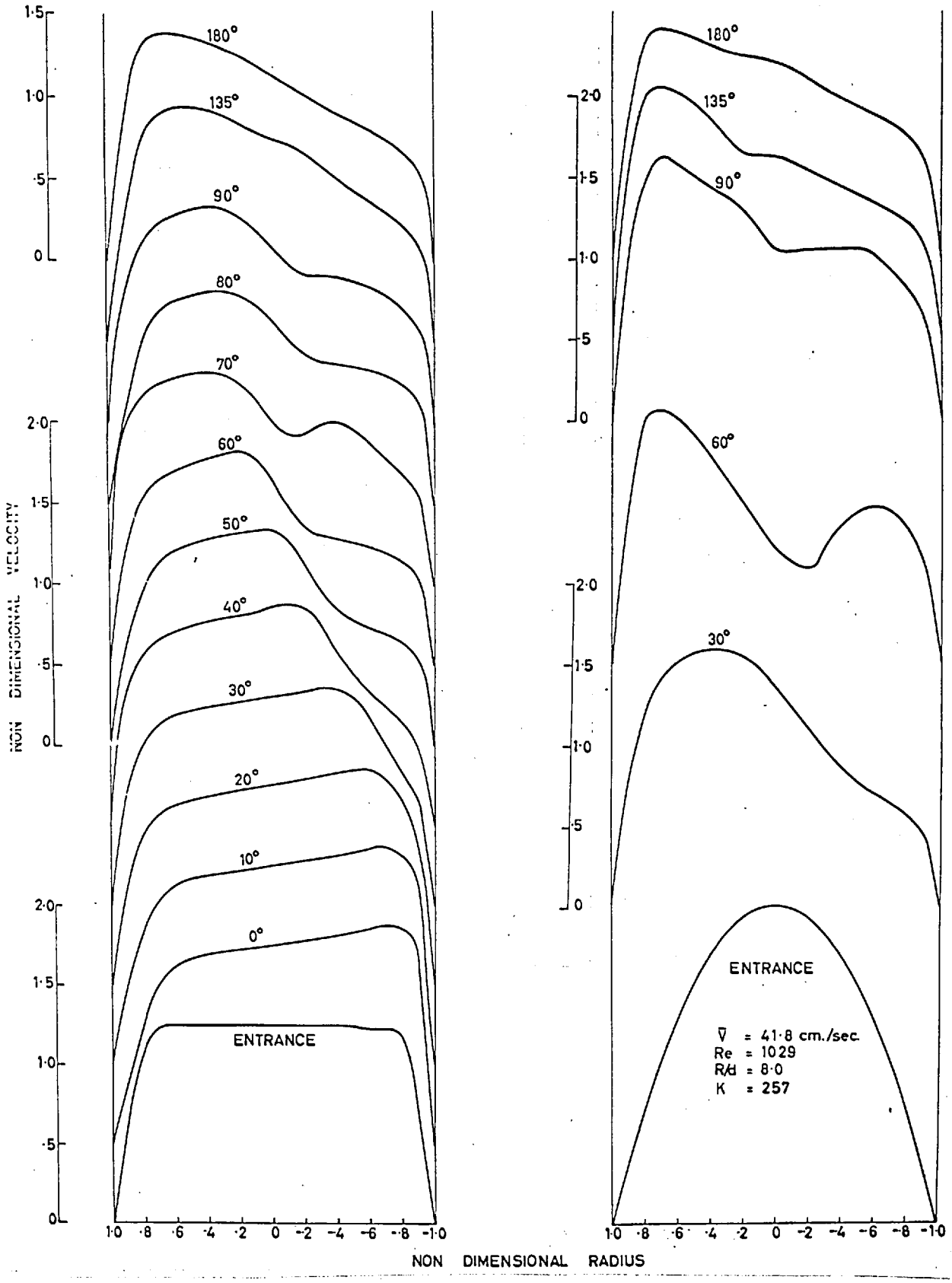


FIGURE 3.8 Velocity profiles in the plane of the bend at the indicated positions of bend angle.

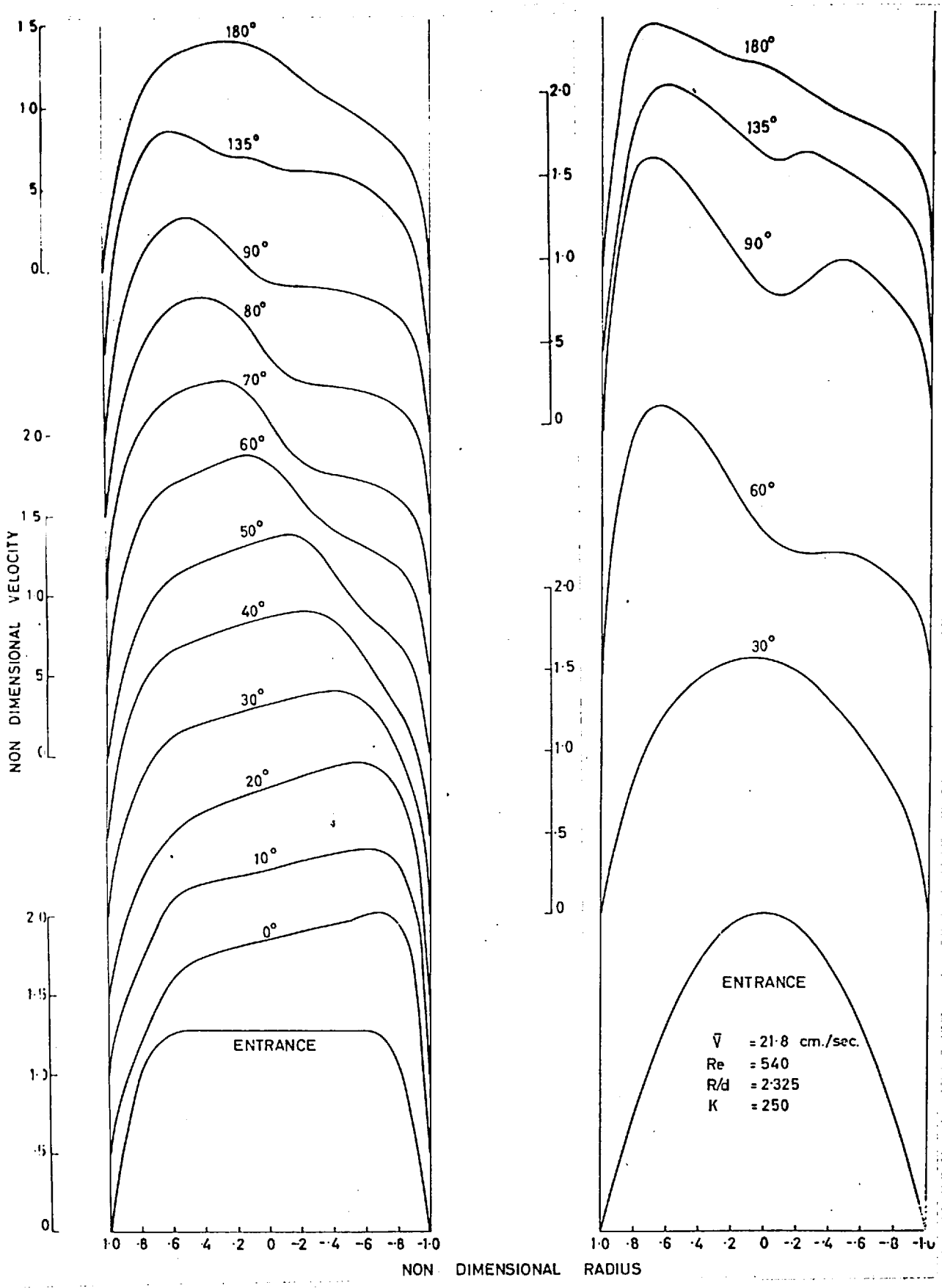


FIGURE 3.9 Velocity profiles in the plane of the bend at the indicated positions of bend angle.

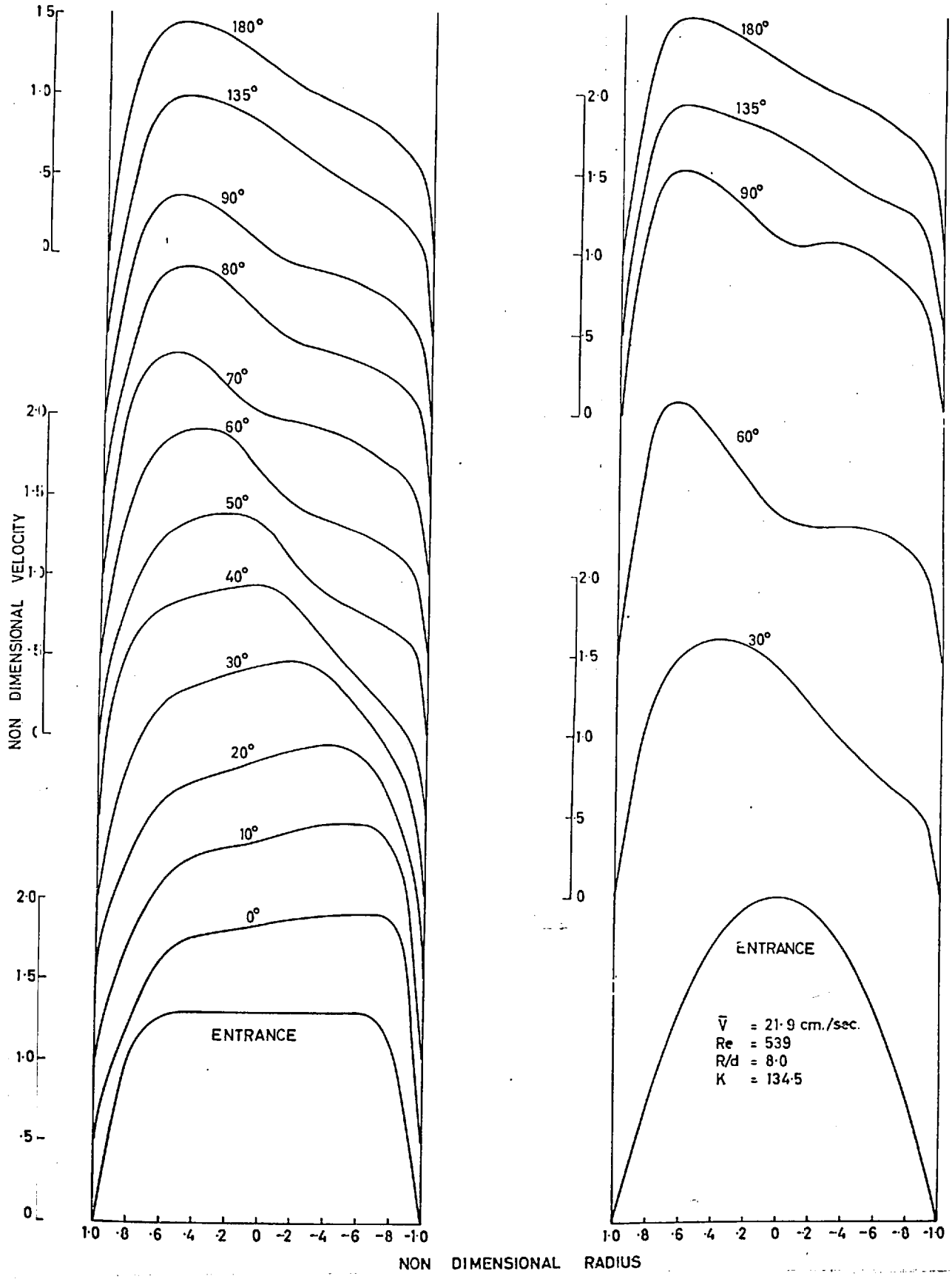


FIGURE 3.10 Velocity profiles in the plane of the bend at the indicated positions of bend angle.

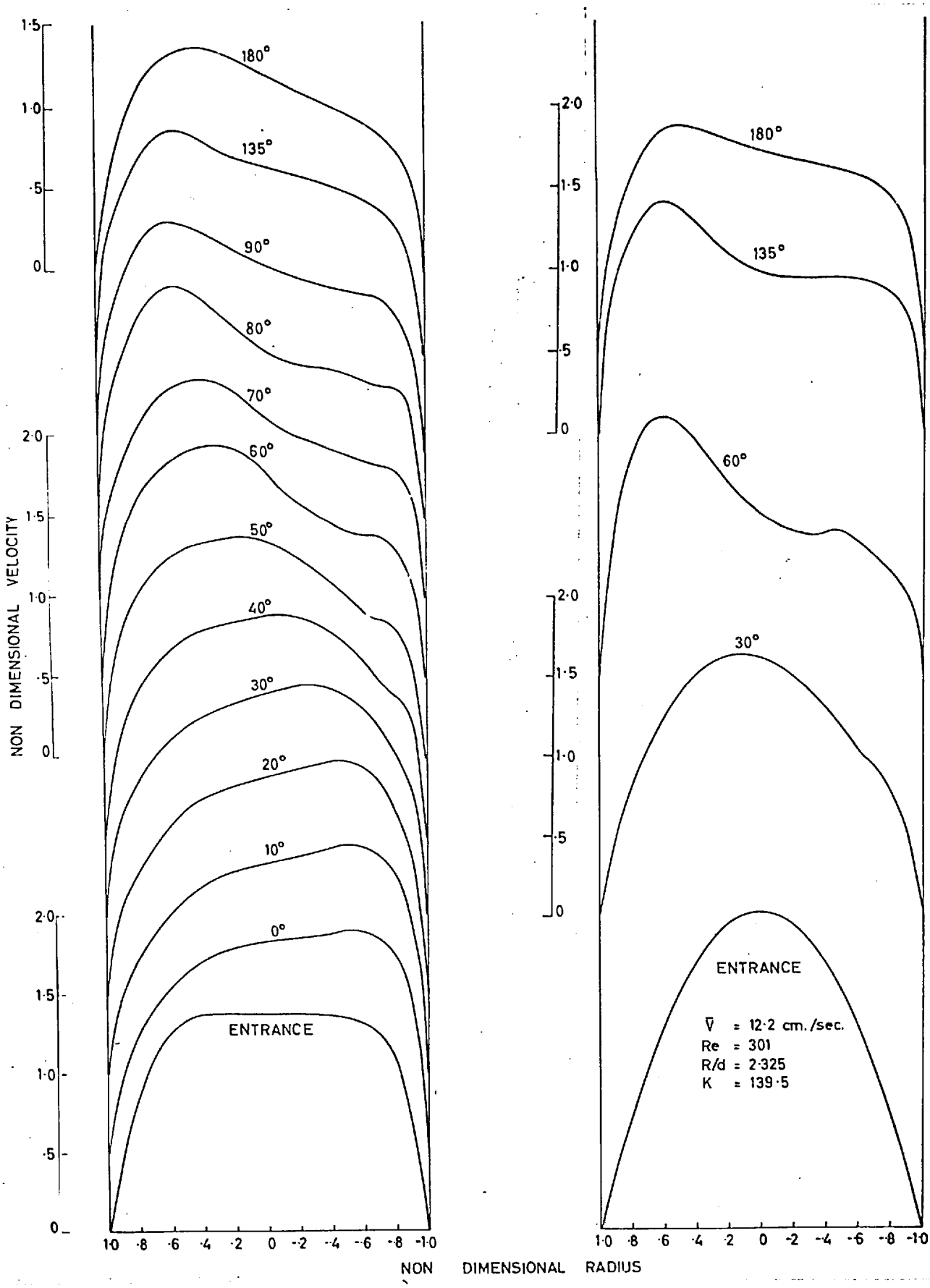


FIGURE 3.11 Velocity profiles in the plane of the bend at the indicated positions of bend angle.

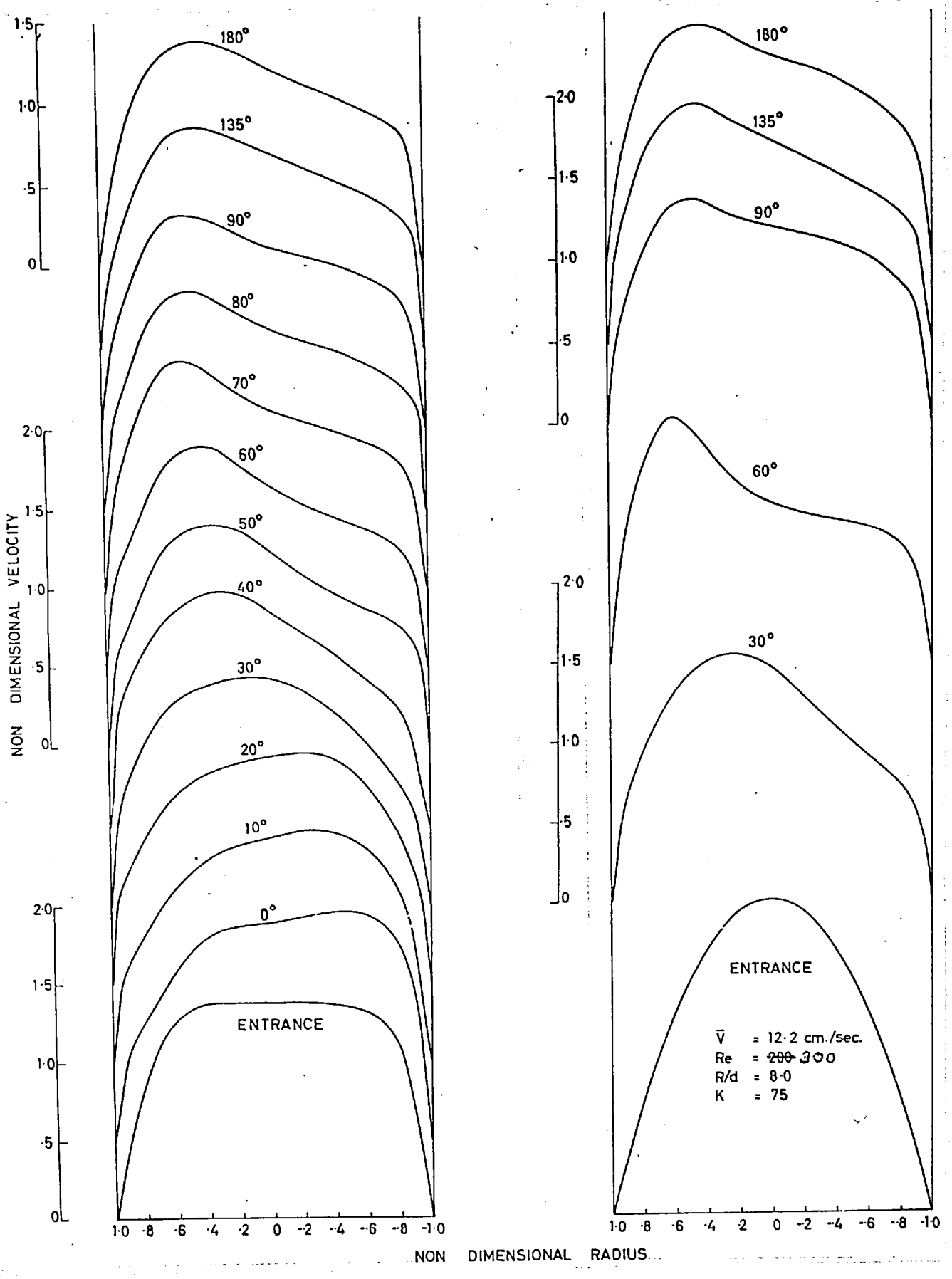


FIGURE 3.12 Velocity profiles in the plane of the bend at the indicated positions of bend angle.

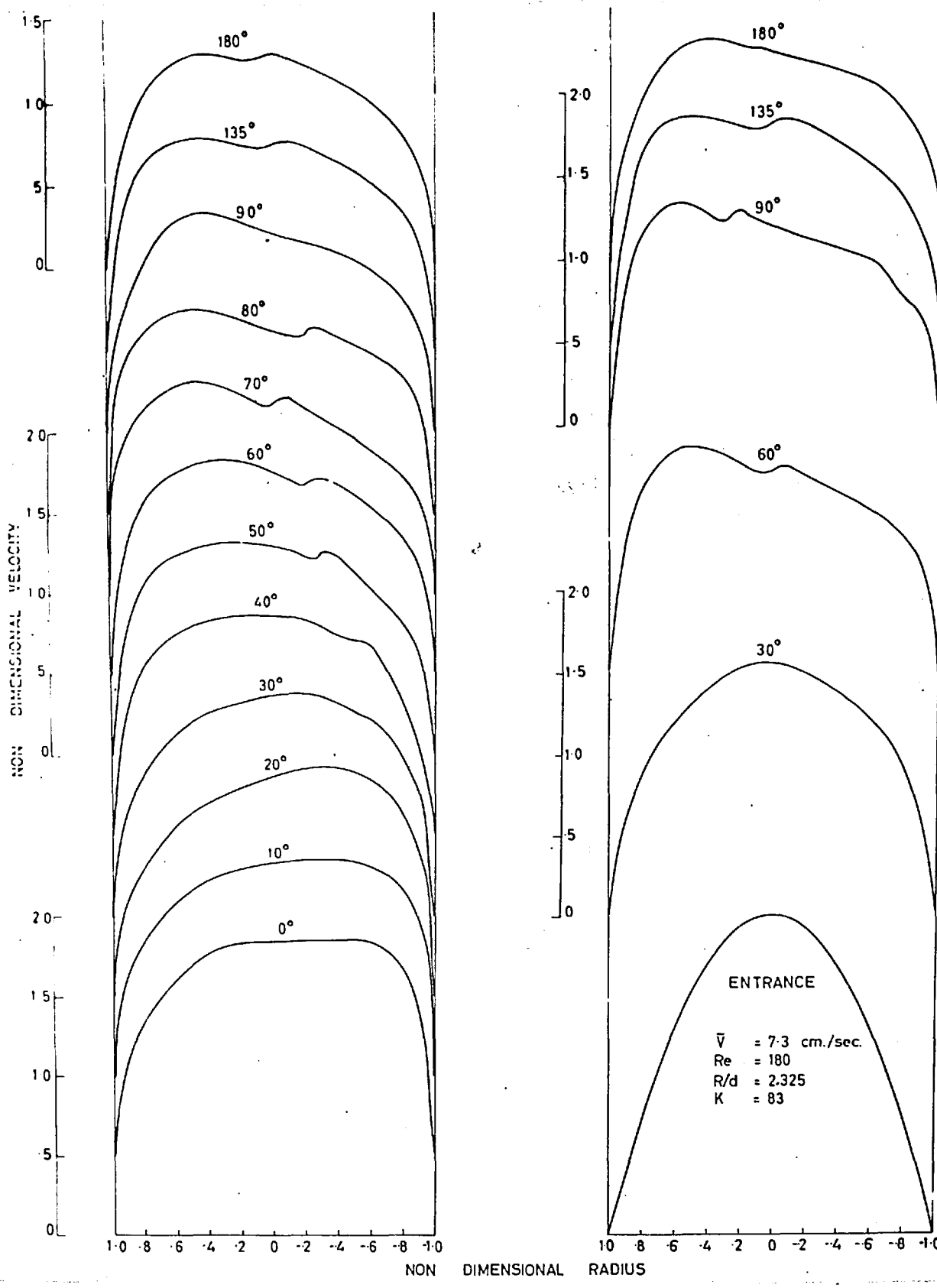


FIGURE 3.13 Velocity profiles in the plane of the bend at the indicated positions of bend angle.

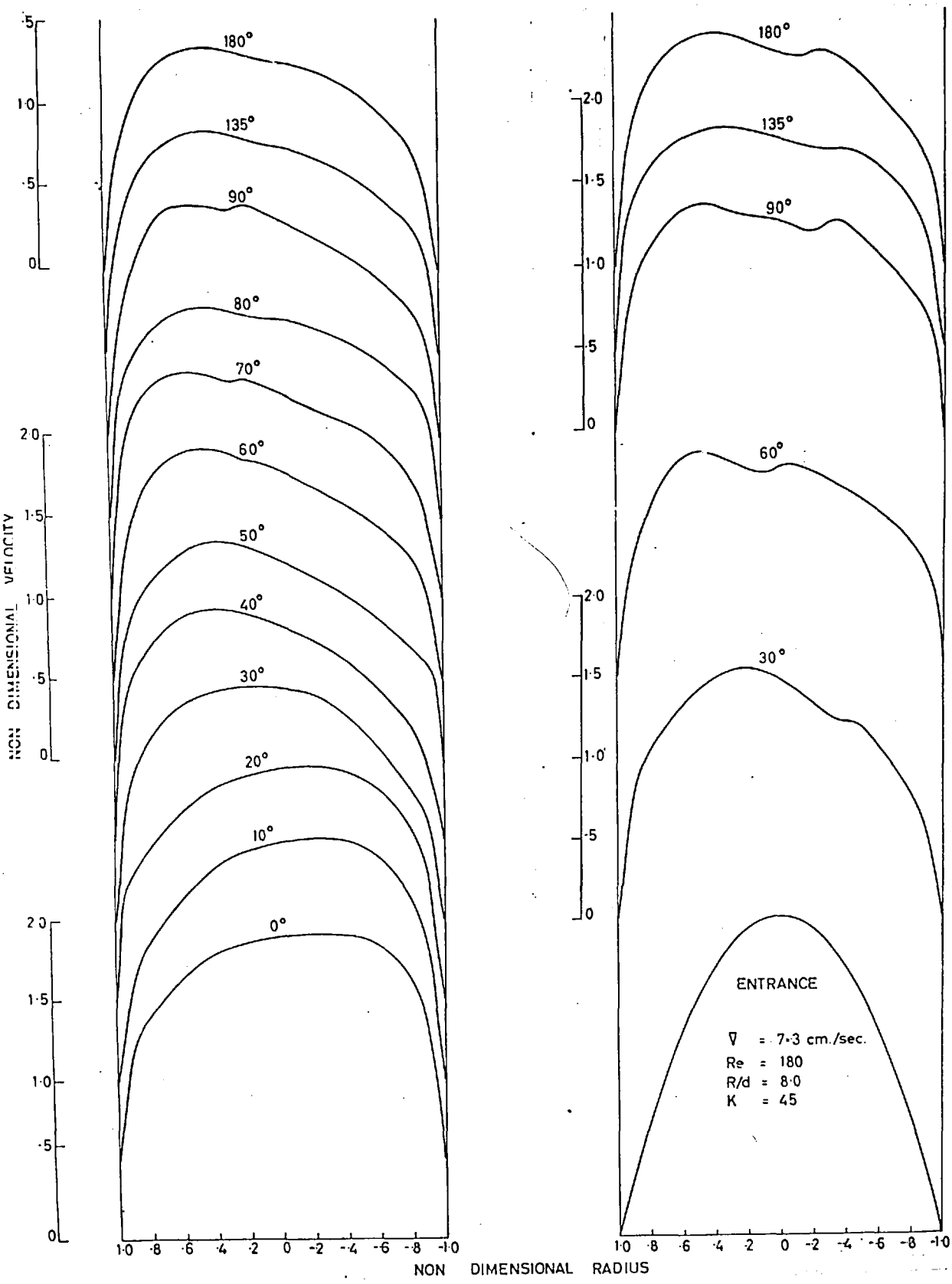


FIGURE 3.14 Velocity profiles in the plane of the bend at the indicated positions of bend angle.

described by equations which are elliptical in nature. The magnitude of the skew is related to the curvature. The development proceeds by a further increase in the potential skew within the first 20° to 30° of the bend. The total secondary flow is growing approximately linearly in magnitude, being maximum at about a 60° bend angle. The influence of the secondary currents in distorting the primary velocity distribution first becomes apparent at about 30° to 40°, depending on the Reynolds number. At this point the fluid with higher velocity is being pushed outward from the centre of curvature and is replaced at the inner wall by the slower moving fluid from the vicinity of the upper and lower walls of the tube. This causes a sharp decrease in the velocity field at the position of the inner wall. Between 40° and 90° of the bend angle, for the higher Reynolds numbers, the effect of the secondary currents "overshoots" - pulling the higher velocity fluid from the vicinity of the outer wall around toward the inner wall, creating a double humped appearance in the profiles (or a wing-like shape in the velocity contours). Beyond 90° the development of the flow within the core slows due to a rapid decrease in secondary flow within the core. The development within the boundary layer (which is now much thicker) at the upper and lower walls continues, and the high velocity fluid pulled from the outer wall is now more strongly affected by viscosity as it moves toward the inner wall of curvature/

curvature. This process continues between 90° and 180° of bend angle where the flow approximates to the fully developed condition.

With a parabolic entrance profile, the higher velocity fluid deviates directly toward the outer wall of curvature. In this case the influence of the flow on the downstream velocity profiles is much less than for the flat entrance condition. Again the magnitude of secondary flow increases in an approximately linear manner within the first 60° of the bend. The effect of the secondary currents "overshooting" is more pronounced because the velocities on the outer walls (which are being pulled in a tangential direction by the secondary currents from outer to inner wall before viscosity can reduce the velocity) are higher than the comparable velocities in the flat entrance condition. After 90° the development proceeds in similar manner to the flat entrance condition for the lower Dean numbers.

The secondary flows produced in the curve with a parabolic entrance become greater in magnitude than those produced from a flat entrance condition. This fits well with Squire and Winter's equation relating the secondary flows to the upstream vorticity. The patterns are also more intricate with a parabolic input and the length required to reach the fully developed state is longer.

The/

The magnitude of the Reynolds number and Dean number (curvature) have strong effects on moderating the general pattern of flow development within the curve. This can easily be seen by comparing the figures. The most striking feature (besides the thickened boundary layer) of the development with lower Reynolds numbers is that this expression of secondary flow "overshoot" is absent. The secondary flows are relatively stronger at lower Reynolds numbers but the viscous boundary layer grows more rapidly disallowing the secondary currents to carry high velocity fluid elements from the outer to inner wall without being affected by viscosity. The dissimilarity in curved flow development between the parabolic and flat inlet conditions became much less at the lower Reynolds numbers; the two inlet conditions giving approximately the same development pattern at the lowest Reynolds and Dean numbers measured. It can be easily seen that the Dean number is the unifying parameter only for fully developed curved flow. In the bend transition region the curvature, Reynolds number and the entrance conditions all must be present to satisfy similarity.

The primary flow development for the condition of a parabolic inlet profile or for the condition of low Reynolds number can be classified as a simple damped oscillation. The flat inlet condition at higher Reynolds number can also be classified in this manner after the initial 30° to 50° of the bend. In general the flow developed/

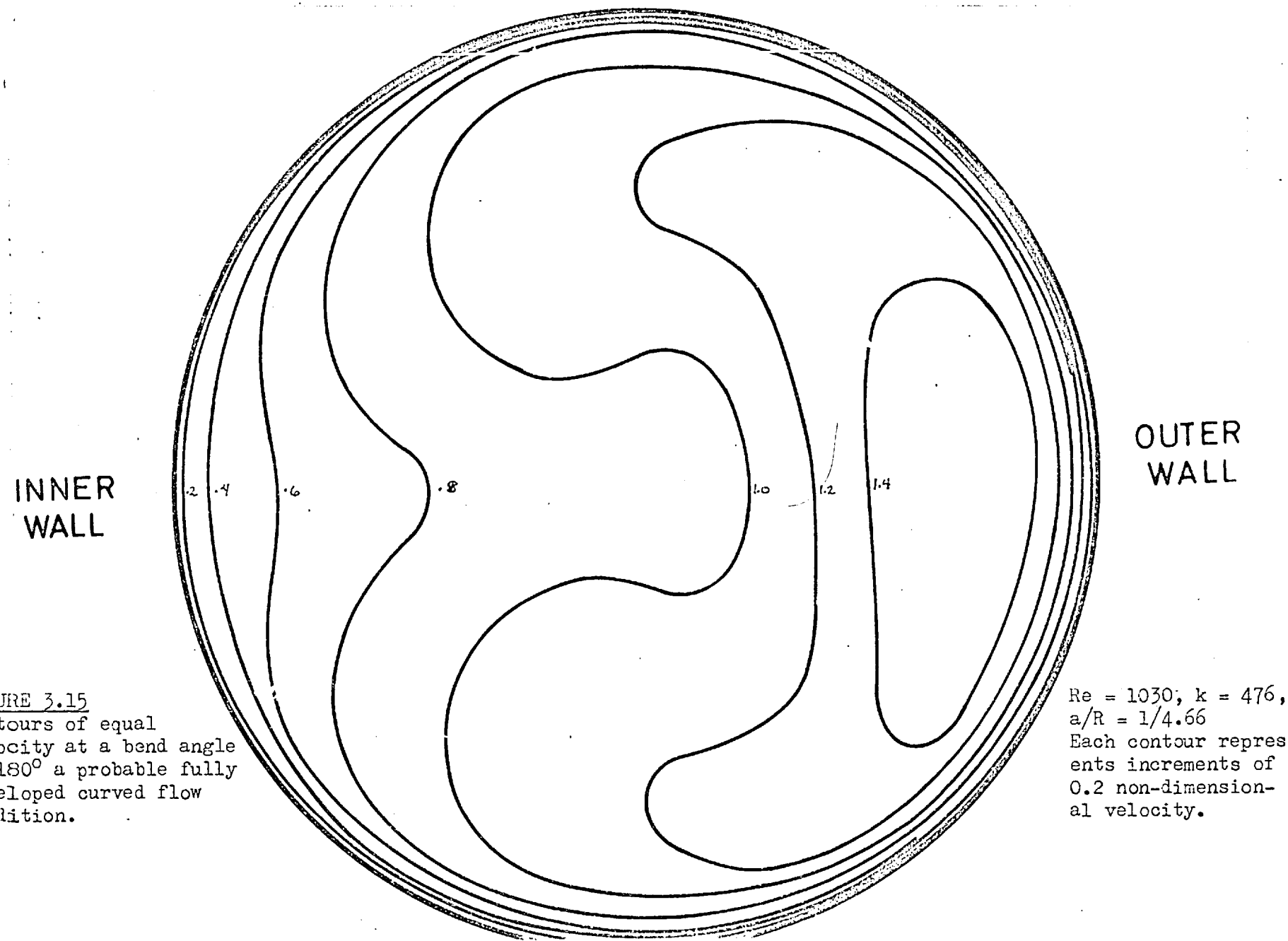
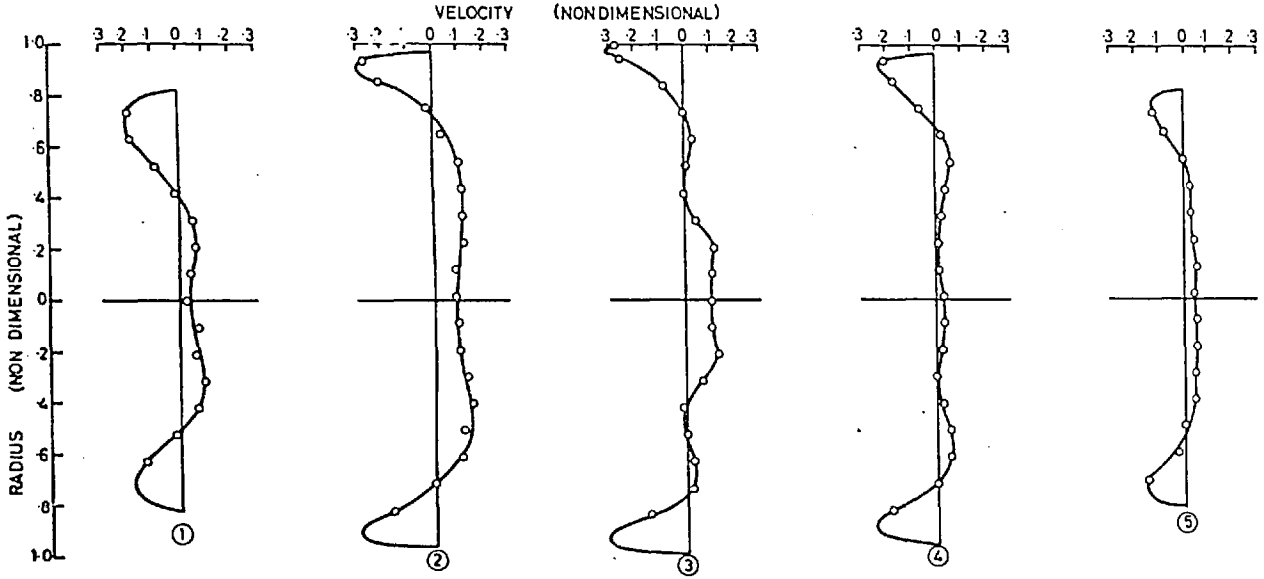


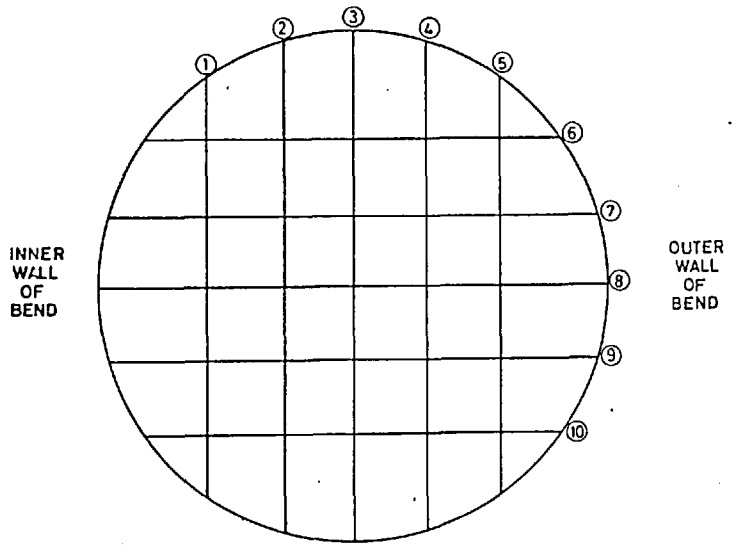
FIGURE 3.15
Contours of equal velocity at a bend angle of 180° a probable fully developed curved flow condition.

Re = 1030, k = 476, a/R = 1/4.66
Each contour represents increments of 0.2 non-dimensional velocity.



SECONDARY FLOW IN A BENT PIPE R/d = 2·33

PARABOLIC ENTRY INTO BEND; BEND ANGLE = 180°
(FULLY DEVELOPED CURVED FLOW)



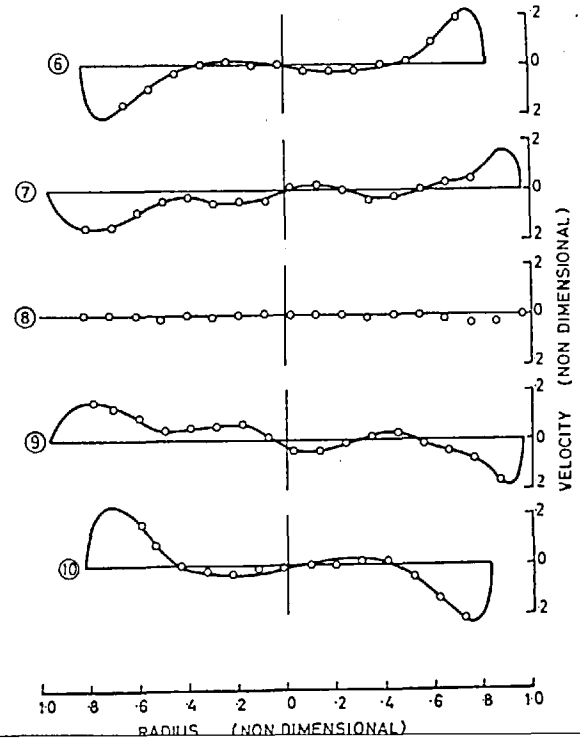


FIGURE 3.16 Cartesian components of secondary velocity.

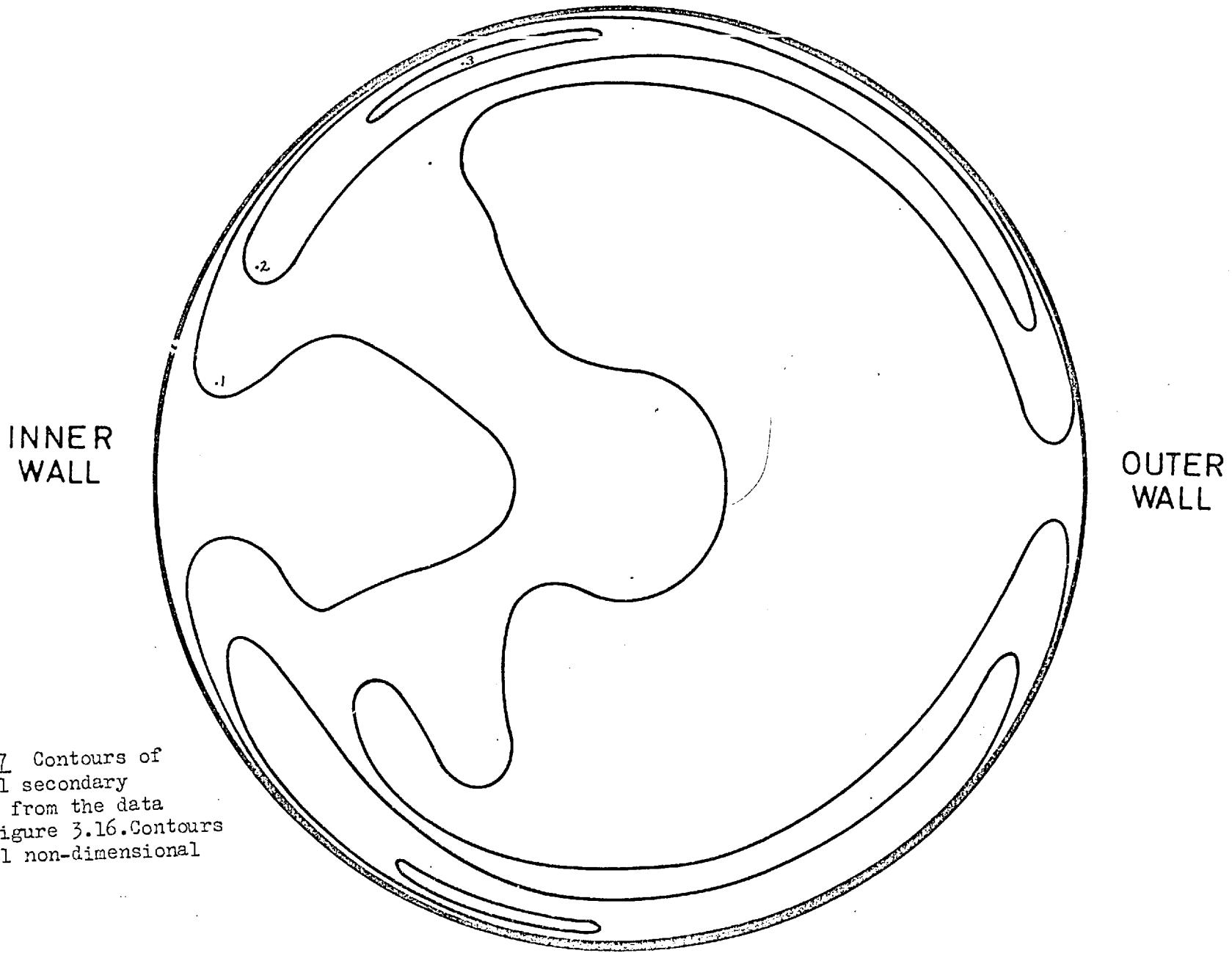


FIGURE 3.17 Contours of equal total secondary velocities from the data shown in figure 3.16. Contours at each 0.1 non-dimensional velocity.

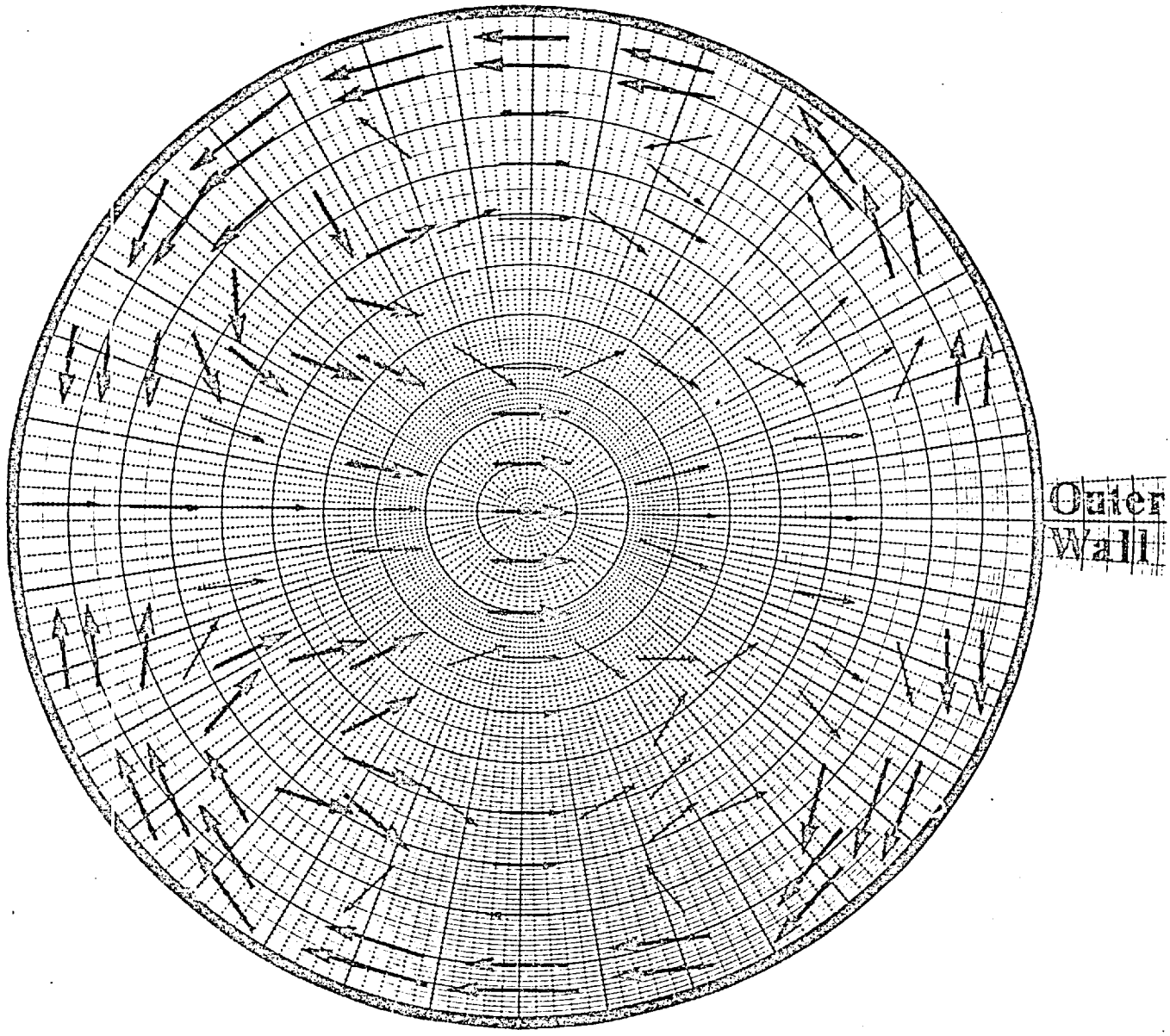


FIGURE 3.18 Directions of secondary velocities. Magnitude of velocities is indicated by length and thickness of arrows. Note vorticies at positions of 50° and 120° from the plane of the bend measured from the outer wall.

developed at a slower rate than measured by Squire or Rowe, but the sequence of primary and secondary (with exceptions) flow development measured in this thesis is generally similar to the previous work for the experiments run at lower Dean numbers.

Comparison of primary and secondary velocities at 180^{o} in a bend (the fully developed condition)

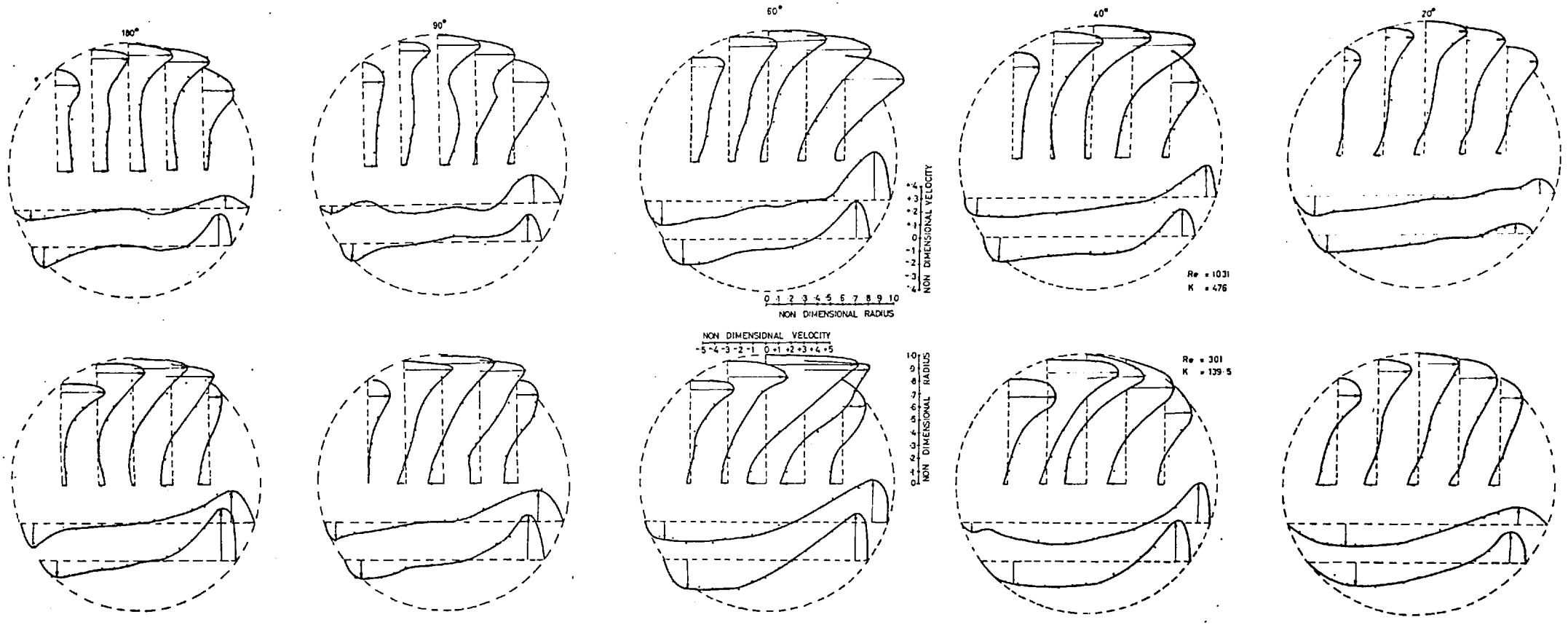
Figures 3.15 to 3.18 display the distribution of primary and secondary velocities measured at 180^{o} of bend angle for a parabolic entrance condition $a/R = 1/4.66$, a Reynolds number of 1030 and a Dean number of 476. The contours of primary velocity are similar to the measurements of Adler, Rowe and Squire, where the areas of high velocity extend from the outer wall circumferentially towards the inner wall of curvature at the higher Dean numbers. At lower Dean numbers the primary velocity distribution loses this wing-like shape and the point of highest velocity is found in closer proximity to the centre line. The primary velocity contours at 180^{o} for Dean numbers below 100 are very similar to those calculated by McConologue & Srivastava. Figure 3.16 shows the ten profiles of secondary velocity. These profiles are very nearly symmetrical with respect to the plane of the bend, approximately justifying the previous assumption that the presence of the measuring probes did not disturb the flow pattern. These profiles are similar in pattern to those found/

found by Rowe, but show a higher magnitude of secondary velocity. The transverse boundary layer indicated by the measurements is of approximately the same configuration as that calculated by Rowe and Adler, but the thickness is somewhat greater than predicted by these theories. The maximum secondary velocity is approximately 40% of the primary, and the position of this maximum is at about 0.08a from the wall. Figure 3.17 shows the contours of equal total secondary velocities, showing that the secondary velocity reaches a maximum at about 60^{o} above and below the axis of the bend at the inner wall. Figure 3.18 depicts the directions (and giving indication of the magnitude of the vector as shown) of the secondary flow. The figure displays the basic simple pattern of secondary flow moving the fluid from inner to outer wall in the core of the flow, with a direction approximately parallel to the plane of the bend and then returning to the inner wall in a tangential direction near the upper and lower walls. This pattern predominates in all of the secondary currents at a 180^{o} bend angle with Dean numbers below 500.

For the fully developed flow at Dean numbers above 300 (as in the example of Figure 3.18) a smaller scale circulation becomes superimposed on the general pattern. This is shown by four secondary vortices at positions of 50^{o} and 120^{o} from the plane of bend measured from the outer wall. These reversals are shown in Figure 3.18 as eddies/

eddies in a clockwise direction below the axis of the bend and counter-clockwise above. The vortex at 50° is simply the centre of the general circulation pattern which has moved from a position at the vertical axis of the tube (90° from outer wall) toward the outer wall. This movement of the centre of circulation is a function of the Dean number and is evident at all the Dean numbers studied in this thesis. The position of this centre of circulation agrees well with predictions by McConalogue & Srivastava for the experiments with Dean numbers up to 100. The vortex at 120° is less notable. This eddy is present only at the higher Dean numbers and may be due to either a local separation of the tangential boundary layer, as predicted by Baura and Pickett, or could be a residual of the flow development which has not dissipated. This aspect of the flow could not be further elucidated with the present apparatus.

Figures 3.19 to 3.22 depict some of the secondary velocity profiles within the bend transition region. These diagrams display the basic features of the secondary flow development found in all of the experiments. The general pattern of secondary flow is similar to the pattern described by Squire, and shown in Figure 3.1. Several features of the secondary flow in my experiments (more viscous flow) are not typical of either Squire's or Rowe's measurements. In general the secondary velocities/



SECONDARY VELOCITIES FOR FLOW ENTERING A CURVE (FLAT ENTRANCE PROFILE)

FIGURE 3.19 Profiles of cartesian components of secondary velocity within the first 180° of a curved tube. No secondary velocities detectable at 0° bend angle.

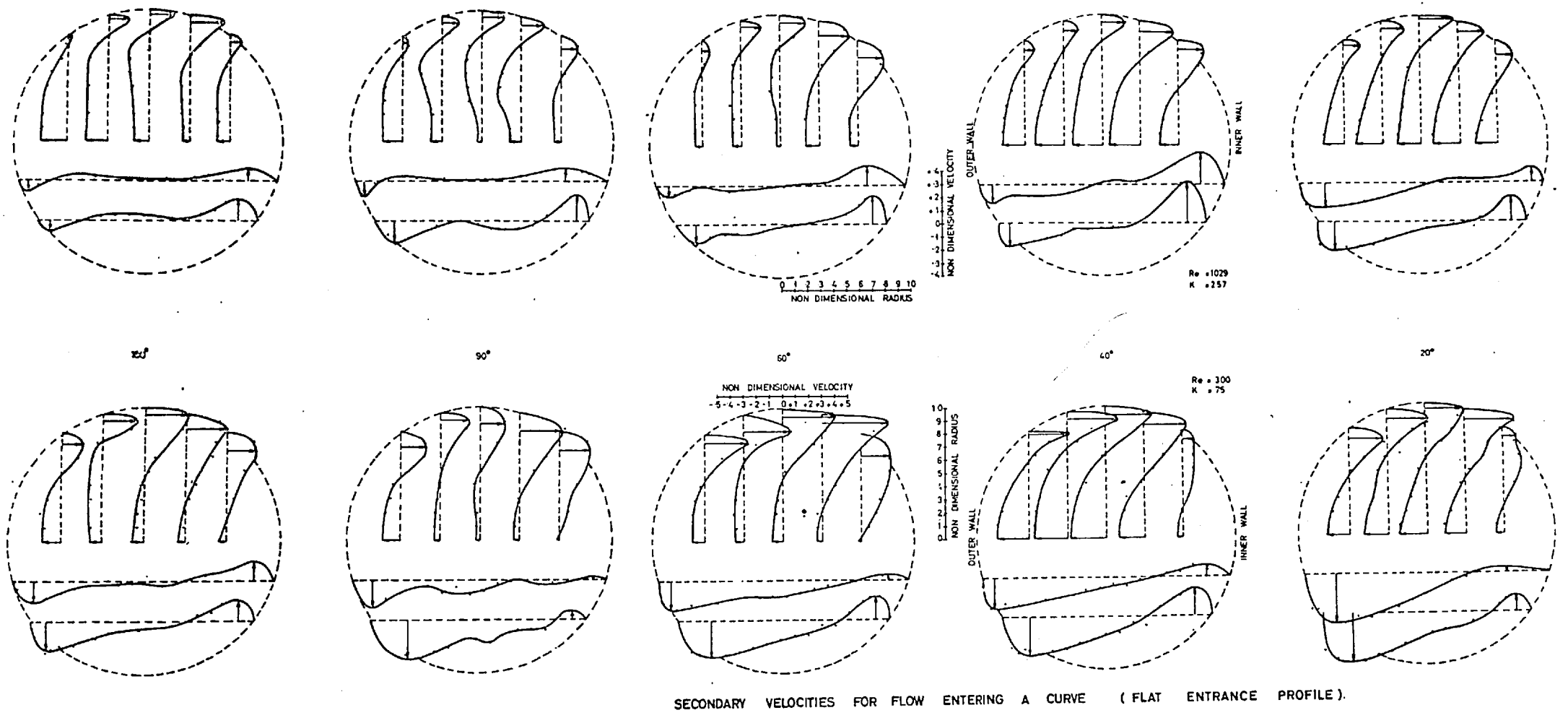


FIGURE 3.20 Profiles of cartesian components of secondary velocity within the first 180° of a curved tube. No secondary velocities detectable at 0° bend angle.

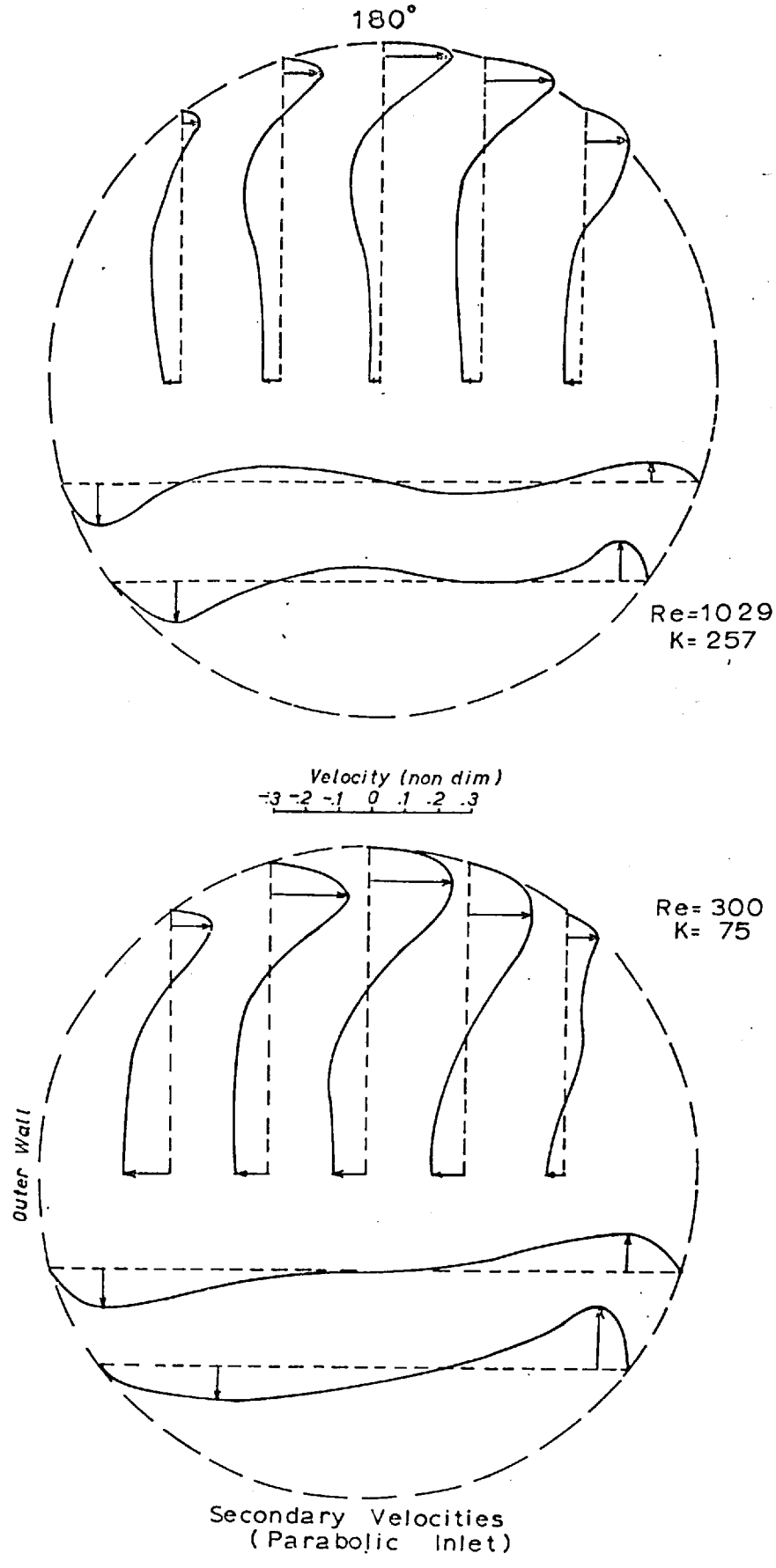


FIGURE 3.21 Profiles of cartesian components of secondary velocity at 180° of bend angle with lower Dean numbers. These profiles show the fully developed curved flow patterns of secondary currents.

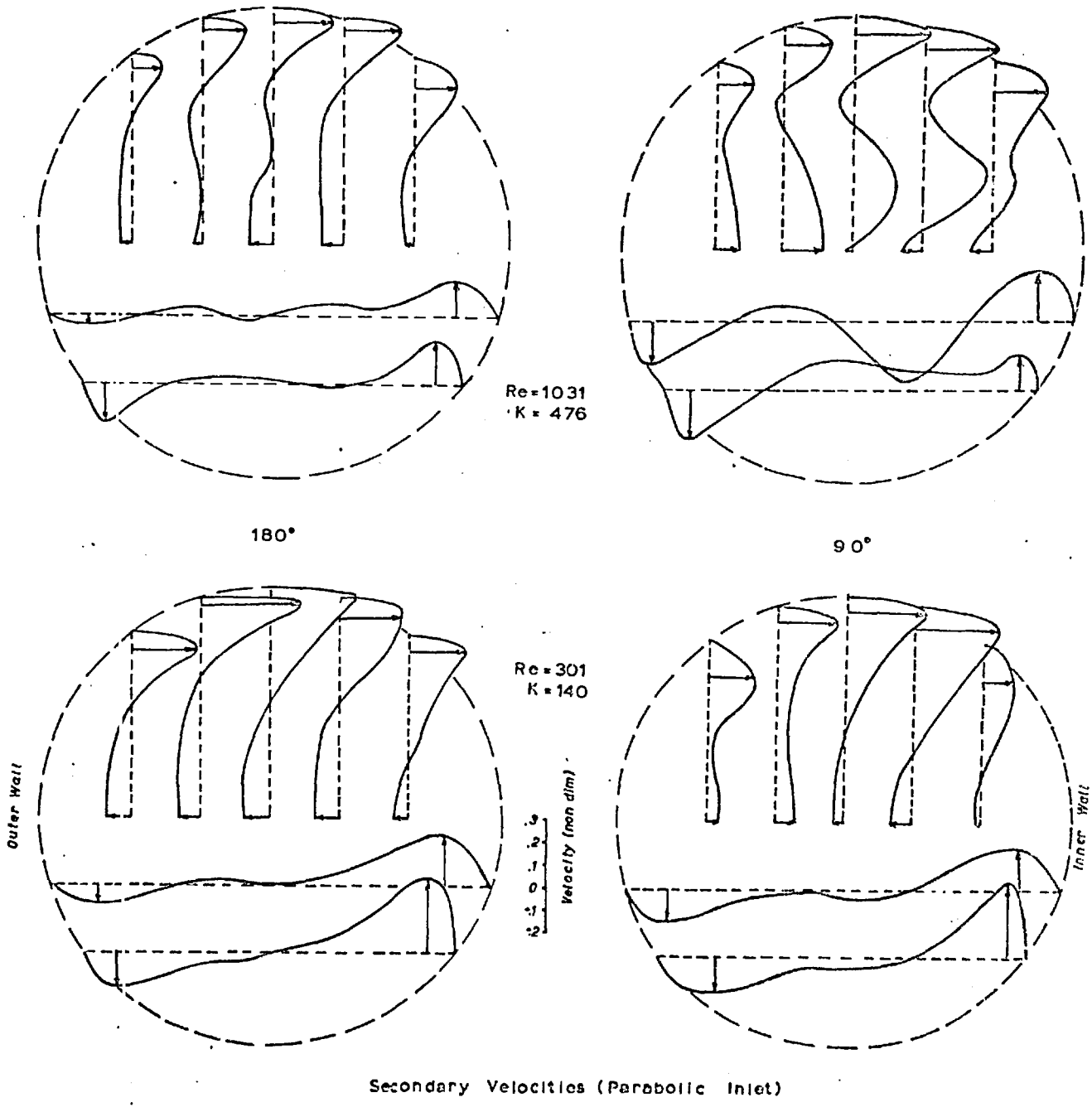


FIGURE 3.22 Profiles of cartesian components of secondary velocity in experiments with high Dean numbers. Note the complex secondary current patterns at the 90° bend angle position.

velocities increase in a linear manner until a bend angle of about 40° is reached. This can be best seen by comparing the centre line velocity to the maximum velocity in the tangential boundary layer. After about 50° the secondary velocity in the plane of the bend rapidly decreases, becoming negative (toward the centre of curvature) near the outer walls at the medium Dean numbers and negative at all points across the tube for the experiments at Dean numbers about 500. The tangential boundary layer grows rapidly up to a bend angle of 60° and thereafter remains constant or decreases slightly. The thickness of this boundary layer is of course dependent on the Reynolds number, being approximately 0.25a for the flow at Reynolds numbers of 300 or below.

A prominent feature of the secondary flow measured in the first 90° of bend angle is that continuity does not hold for the secondary flow in a plane perpendicular to the axis of the tube. This results from the net axial circulation being generated by changes in the distribution of primary velocity. Only in the fully developed flow condition do all the secondary velocity profiles preserve continuity.

A second prominant feature is the complexity of the pattern of secondary flow with the higher Dean numbers for bend angles between 90° and 180°. This condition is only/

only prominent with the parabolic entry profile. The reasons for the existence of such regions of vorticity which is opposite in sign to the vorticity produced in the initial 40° of the bend is complex. This probably results from the strong tangential component of secondary flow which creates the winged shape of the primary velocity contours shown in Figure 3.15 and referred to as overshoot. The velocity profiles along the vertical plane will have an "M-shaped" appearance after 60° to 90°. Therefore the vorticity of the primary velocity along the vertical plane in the core of the tube is in the opposite direction to that in the boundary layer. The effect of curvature is that the vortex lines are advected in a plane parallel to the plane of the bend, creating an axial component of vorticity (the Squire and Winter argument). In the boundary layer the resultant axial component of vorticity creates the secondary flow pattern which predominates in the first 40° of the bend. The advection of the vortex lines in the core of the tube (where the vorticity is now opposite in sign) creates local areas of secondary currents which are opposite in direction to the secondary currents created within the boundary layer. When the curvature is high and the entering flow contains vorticity the axial vorticity developed in the first 40° to 60° will be relatively strong (see 60° position in Figure 3.16), causing an exaggerated condition of/

of negative vorticity development downstream from the linear region. This results in local reversals of the secondary flow pattern followed by a possible total reversal of the secondary flow within the core of the tube (only). The production of "positive" axial vorticity (positive defined as in the sense of the vorticity produced in the inlet region) continues but the net axial vorticity is now the summation of the "positive" and "negative" vorticity produced. The steady state condition of "positive" and "negative" vorticity production is reached between 135 and 270° of the bend where the net vorticity is constant. It is expected that the production of "positive" and "negative" axial vorticity within a bend will proceed as in Fig.3.23.

Separation from the inner wall of the bend could cause the complicated patterns seen in Figure 3.18. This separation is not expected with the curvatures used in this study. This is deduced from the experiments of Joy (106) in bent channels. Further, the primary flow patterns do not suggest separation occurring at the inner wall.

The magnitude of the maximum secondary velocity in the tangential boundary layer indicates the direction of the total velocity (the direction is of course the measured quantity, but this is not displayed in the figures). At this point in the tangential boundary layer the direction of/

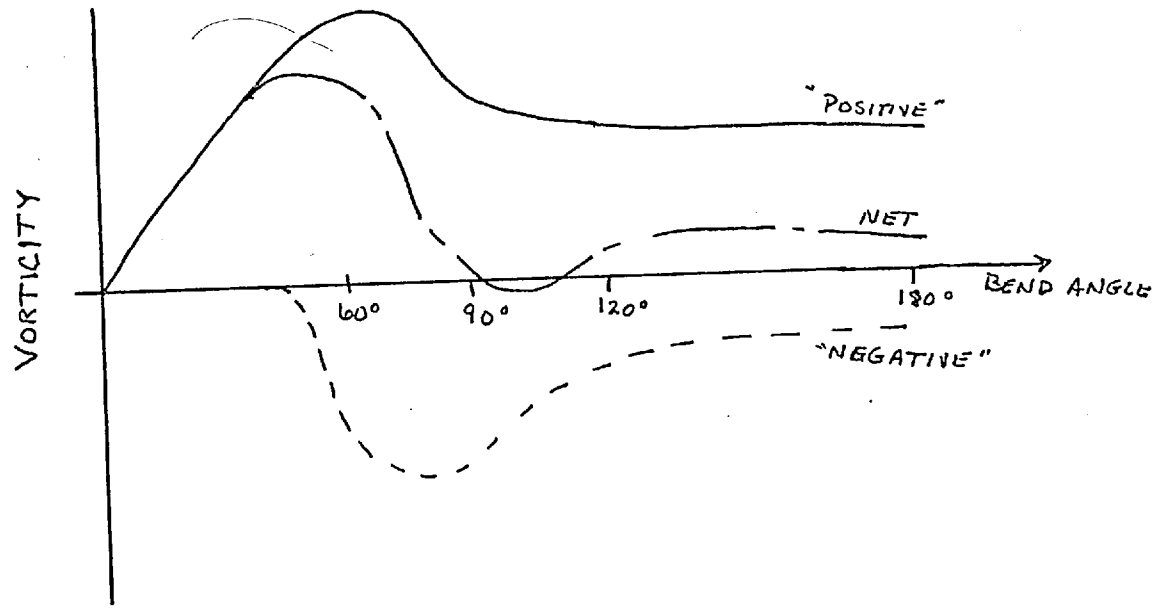


FIGURE 3.23 Expected production of "positive" and "negative" axial vorticity as a function of bend angle.

of the total velocity can be obtained from the ratio of the secondary to primary velocities. The direction obtained in this manner was found to be equal to the direction of the limiting streamline against the wall (at least as close to the wall as could be measured). Table 3.2 depicts the direction of the limiting streamline on the wall at the vertical axis of the tube. The experimental results of Rowe and Bansod, along with theoretical calculations from Pickett's analysis, are also shown.

The secondary velocity profiles also show that the magnitude of secondary velocities increases relative to the primary velocity as Reynolds number decreases and curvature increases within the bend transition region. At the higher Reynolds numbers or lower curvatures (Re = 1030, a/R = 1/16) the maximum secondary velocity is 0.25 nondimensional velocity at a bend angle of 20^{o} and at 0.05r from the wall on the vertical axis. For lower Reynolds numbers and higher curvatures (Re = 300 , a/R = 1/4.66) the maximum secondary velocity is 0.72 non-dimensional velocity at bend angle of 60^{o} and 0.08r from the wall on the vertical axis. These values are higher than have been measured in turbulent flows but seem to give similar limiting streamline directions to those observed by Eustrice. The position of maximum secondary flow is a function of the inlet condition and Reynolds number. For a parabolic entrance the largest secondary velocities/

TABLE 3.2

ANGLE BETWEEN LIMITING STREAMLINE AND AXIAL DIRECTION OF TUBE AT THE VERTICAL AXIS

Bend Angle	Re = 1030 a/R = 1/16	Re = 1030 a/R = 1/4.66	Re = 300 a/R = 1/16	Re = 300 a/R = 1/4.66	Theory of Pickett	Taken From Rowe Re = 2.36 * 10^5 a/R = 1/24	Taken From Bansod Re = 5 * 10^2 a/R = 1/47
0.5					0		
1.0					-15°		
2.0					-50°		
20	-34°	-21.5°	-45°	-45°			
22.5							-8°
30						-18°	
40	-13°	-31.5°	-25°	-40°			
60	-14°	-29°	-28°	-42°		- 9°	
90	- 5°	-29.5°	-10°	-38°			
			(-18.5°)	(-12.5°)		-12°	
120						-12°	
150						-12°	
180	-10°	-31.5°	-27°	-40°			
	(-13.5°)	(-24.5°)	(-23°)	(-26°)		-12°	

L E G E N D

FLAT ENTRANCE PROFILE FOR

Data at Re = 1030 and 300, Picketts theory Re = 1030 and Bansod measurements

( ) indicates Parabolic entrance profile

Rowe's data with fully developed turbulent entrance

negative sign indicates direction toward centre of curvature.

velocities occur between the upper or lower wall and the inner wall, at a position of 100 to 120° from the horizontal measured from the outer wall. For a flat entrance condition the position of maximum secondary velocity occurs at approximately 30° from the outer wall at a bend angle of 20°. This position of maximum secondary velocity shifts tangentially toward the inner wall as the flow progresses around the bend.

Comparison of the results with other experimental studies and theoretical predictions

Two major differences are apparent when comparing the results of this thesis and previous experimental work in the bend transition region. Viscosity plays a much greater role in my results than the previous studies; all carried out with turbulent flow (either fully developed or developing) as the inlet condition. This can easily be seen when comparing the thickness of the tangential boundary layer; being 0.08r to 0.15r in my results, as compared to values of less than 0.05r in the results of Rowe. The second major discrepancy is that the development of curved flow takes place at a slower rate in my experiments than in the previous experiments. This is similar in nature to comparing the development of laminar to turbulent flow in the entrance of a long straight pipe. Essentially the low Reynolds number flow will develop more secondary flows in the bend transition region, primarily from/

from the thicker boundary layers. This caused a more severe overshoot of the secondary currents in the initial part of the bend resulting in a more complex pattern of secondary currents downstream. Eventually the flow (both primary and secondary) will of course be typified by the Dean number (assuming that the incoming turbulent flow is now below the critical Reynolds number for the curvature). The delay in development to the condition of laminar fully-developed curved flow comes when dissipating the complex patterns of secondary currents, resulting from the overshoot.

Theoretical predictions made for fully developed laminar flow at Dean numbers up to approximately 500 fit the data well for the velocity distributions at 180° in the bend. For Dean numbers higher than 500 the experiments indicate that fully developed curved flow has not developed by 180° of bend angle. The separation of the secondary boundary layer predicted by Barva and Pickett was not observed at Dean numbers below 300 but tendencies toward separation seemed to occur at higher Dean numbers.

The theoretical predictions by Squire and Winter seem to explain the initial flow development for a parabolic velocity inlet. The flat entrance profile also seemed to generate the axial vorticity in a linear manner. This is a bit bewildering, since essentially the incoming flow was devoid of vorticity except in the very thin/

thin boundary layer and therefore the Squire and Winter result would predict no development of streamwise vorticity in the core.

Pickett's solution for the first 4° of bend angle may give some insight into the vorticity production within the curve with a flat inlet profile. The coefficients in Pickett's solution were evaluated for the condition

$$Re = 1030$$
$$a/R = 1/16$$

The axial velocity component calculated from Pickett's solution show a slightly higher velocity toward the inner wall. This predicted skew was, however, smaller than the skew shown in Figure 3.5. The magnitude of tangential velocity predicted from Pickett is at first very small but rapidly increases as the bend angle becomes about 3°. This can be seen by the large deflection in the limiting streamline predicted by Pickett and shown in Table 3.2. The measured component of tangential velocity at 10° was not as large as predicted.

After the initial linear rise in secondary flows the magnitude and pattern of secondary flow oscillates at a frequency in general agreement to that predicted by Hawthorne. This occurs between 40° and 180° of the bend angle, depending strongly on curvature, Reynolds number and entrance conditions. No theoretical predictions describe the complex sequence of patterns through which the/

the secondary flow develops in this region. This situation imposes a severe limitation on our understanding of the flow within the lung, our primary goal. The bifurcation described as typical of the airways in Chapter 1 creates a curvature which extends to angles of 35^{o} to 45^{o}. The pattern of secondary flow at the end of curvature may then be typical of this oscillatory region of a curved tube. And therefore, existing theoretical predictions for the secondary flows due to curvature will not adequately describe the convective mixing occurring as the air is propelled through the bronchus.

Velocity gradient at the tube wall

The shear against the wall of biological vessels may be important in the transport of diffusible materials (Caro, 105) or particle deposition. Therefore measurements were taken of the velocities near the wall by hot wires corrected for yaw, as explained in the methods section. It should be made clear that these measurements may not be true indications of the wall shear. What was measured was the velocity at distances of about 0.01r from the wall and outward. This is well within the boundary layers encountered in this study. Therefore extrapolation of the velocity gradient to the wall seems to be a good indication of wall shear. Figure 3.24 and 3.25 show the velocity gradients measured on the horizontal and vertical axis of the/

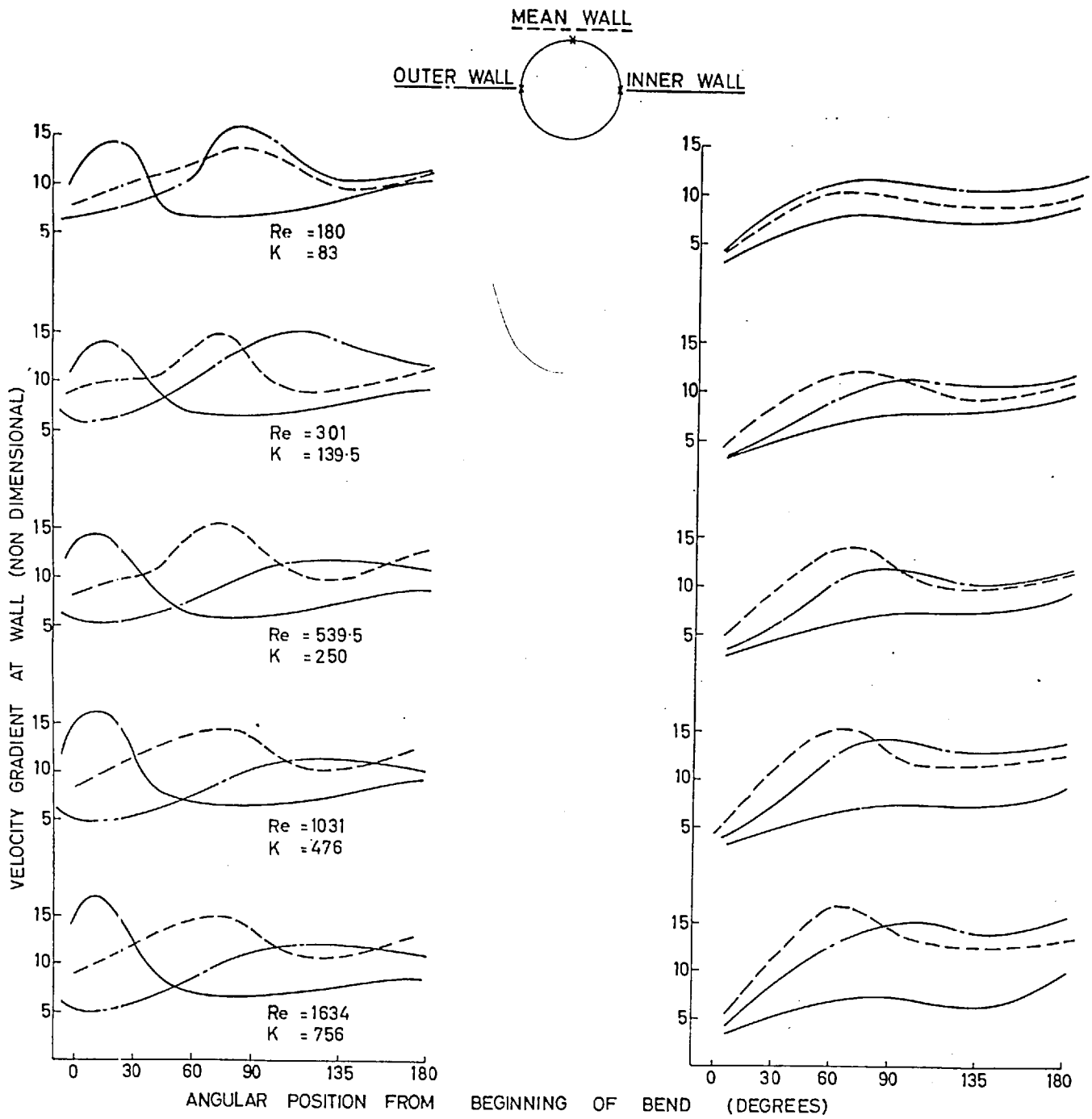


FIGURE 3.24 Velocity gradient at inner, outer and "mean" walls of curvature as measured by hot wires with wall corrections. Measurements in curve with flat entrance velocity profile is on left. Measurements with parabolic entrance profile are on right.

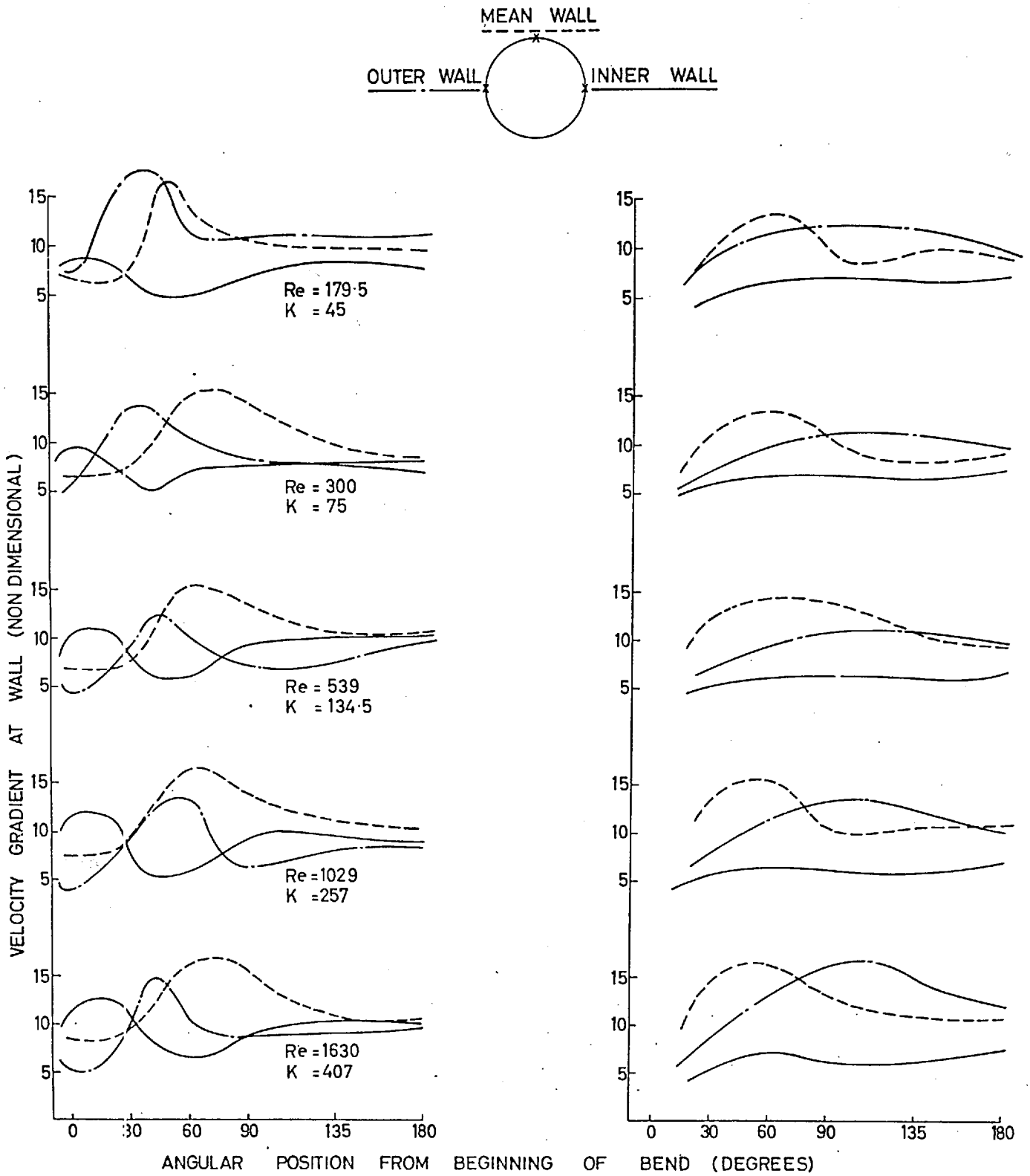


FIGURE 3.25 Velocity gradient at inner, outer and "mean" walls of curvature as measured by hot wires with wall corrections. Measurements in curve with flat entrance velocity profile is on left. Measurements with parabolic entrance profile are on right.

the curved tube for the ten experimental flow condition and the two entrance conditions. The "wall shear" indicated by the experiments shows a characteristic distribution at each bend angle for each of the two entry conditions, being only a weak function of Reynolds number or curvature. This at first seems to contradict our previous observation concerning the velocity distribution in that for slower flow the boundary layer grew more rapidly. But although the measurements of the boundary thickness indicated a thicker layer at slow flows, the nondimensional velocity gradient, well into the boundary layer, near to the wall, was measured to be constant. Careful checks were made to evaluate possible errors from improper wall calibrations or yaw corrections, but no such error was obvious. An interesting feature of the wall shear distribution is shown for the flat inlet condition, in that the distribution of shear between mean and outer wall seems to be a function of curvature alone. For the large curve the high wall shear is originally at the inner wall, which is consistent with the initial potential flow velocity skew observed. As the bend angle increases, the shear moves tangentially to the mean wall and finally at bend angles of about 120° the shear is highest at the outer wall. This movement of the gradient is in opposite sense to the secondary velocity near the wall and does not correlate well with the position of maximum secondary flow in the tangential boundary layer. In the model of higher curvature/

curvature the shear on the outer seems to lead the mean wall shear.

The parabolic inlet condition shows a more gradual fluctuation with bend angle but the "shear" distribution at bend angles up to approximately 60^{o} does not seem to be consistent with the expected shear from the core velocity distributions. The shear is, of course, lower as the flow enters the tube, in a parabolic velocity profile. Therefore rapid development in secondary flow at the mean wall may initially account for the increase in shear on the vertical axis. This is, of course, where we expect the vorticity to be first developed from the arguments of Squire and Winter.

Moments of velocity distribution

Table 3.3 displays the calculated moments from the velocity distributions measured. The first moment is the position of mass flow, and therefore indicates the net secondary flows occurring as the fluid moves around the bend. Figure 3.26 shows the positions of mass flow as a function of bend angle for four Dean numbers and two inlet conditions. This figure simply summarises what the secondary velocity profiles showed. At the inlet to the curve for a flat entrance profile, there is a net shift in mass toward the centre of curvature, followed at about 20^{o} by a net shift outward, which overshoots the final steady/

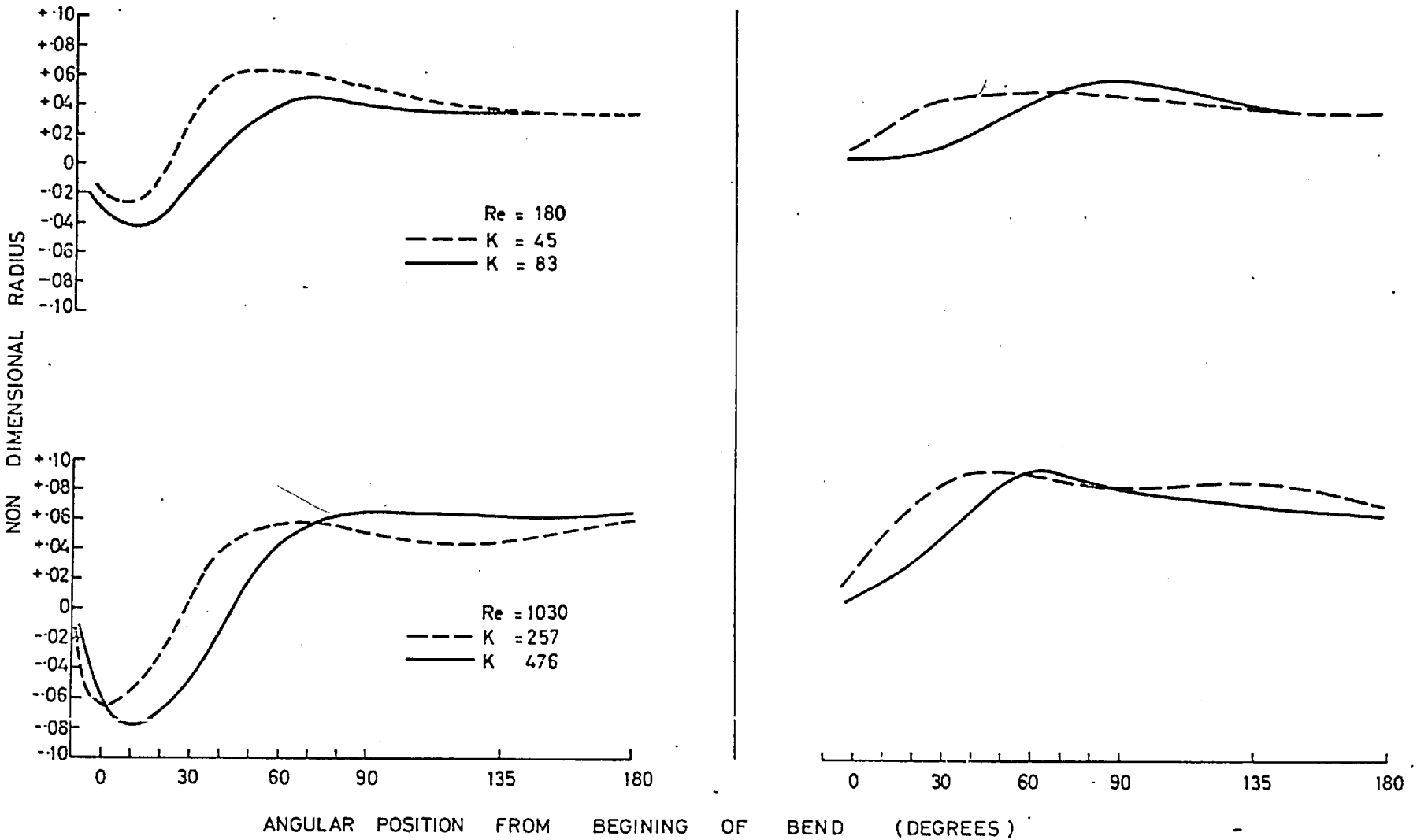


FIGURE 3.26 Positions of the centre of mass as a function of bend angle. Measurements with flat entrance velocity profile are on left-hand side, measurements with parabolic entrance velocity profile are on right.

steady state position of mass flow. For the parabolic condition, the centre of mass flow simply progresses toward the outer wall of curvature.

The second moment indicates the spread of the velocity distribution and is simply the standard deviation of a statistical three-dimensional distribution. For a parabolic profile the second moment is $0.577r$ and for a totally flat velocity distribution the second moment would be equal to $0.707r$. The third moment is a measure of the skewness of the velocity distribution and would be zero for an axisymmetrical flow. These higher moments are calculated to facilitate the quantitative comparison of flow in bifurcations to flow in curves.

Energy dissipation

The rate of energy lost through viscous dissipation was calculated from the measured velocity distributions. This was done by calculating the dissipation function* with the total velocity at any point in the cross section of the tube being represented by a four term Fourier series fitted to the measured distribution, as was discussed in the section on data handling. Essentially the calculation consists simply of summing the square of the velocity gradients in the radial and tangential direction with the assumption that the velocity gradient in the axial direction is small. This assumption seems well founded when/

* Ref 99, page 99 equation (28).

when comparing the measured axial velocity gradient to the measured radial or tangential gradients. Difficulties may arise in predicting the rate of energy loss if the length scale of the numerical summation technique is larger than the length scale of the velocity gradients, especially in the radial direction, when obtaining the velocity gradients within the viscous boundary layer. Figure 3.27 shows the results of such calculations. As in the case of the wall shear and first moments, the experiments for each inlet condition show a characteristic distribution with respect to bend angle alone.

These calculations for the rate of energy dissipation can be compared to predictions upon increased drag obtained from Pickett's theoretical solution for the first few degrees of the curve with a flat inlet profile. If the tube was straight one would expect the rate of energy dissipation to decrease rapidly downstream of the entrance to the tube, as predicted by the Atkinson-Goldstein result. With a curvature present, Pickett's solution predicts that the drag will increase relative to the drag in a straight pipe, and that the discrepancy between curved and straight tubes will be a function of curvature. For curvatures present in the experimental models the drag as a function of distance along the curved tube would be predicted from Pickett's solution to be approximately constant for the first few degrees. This does not/

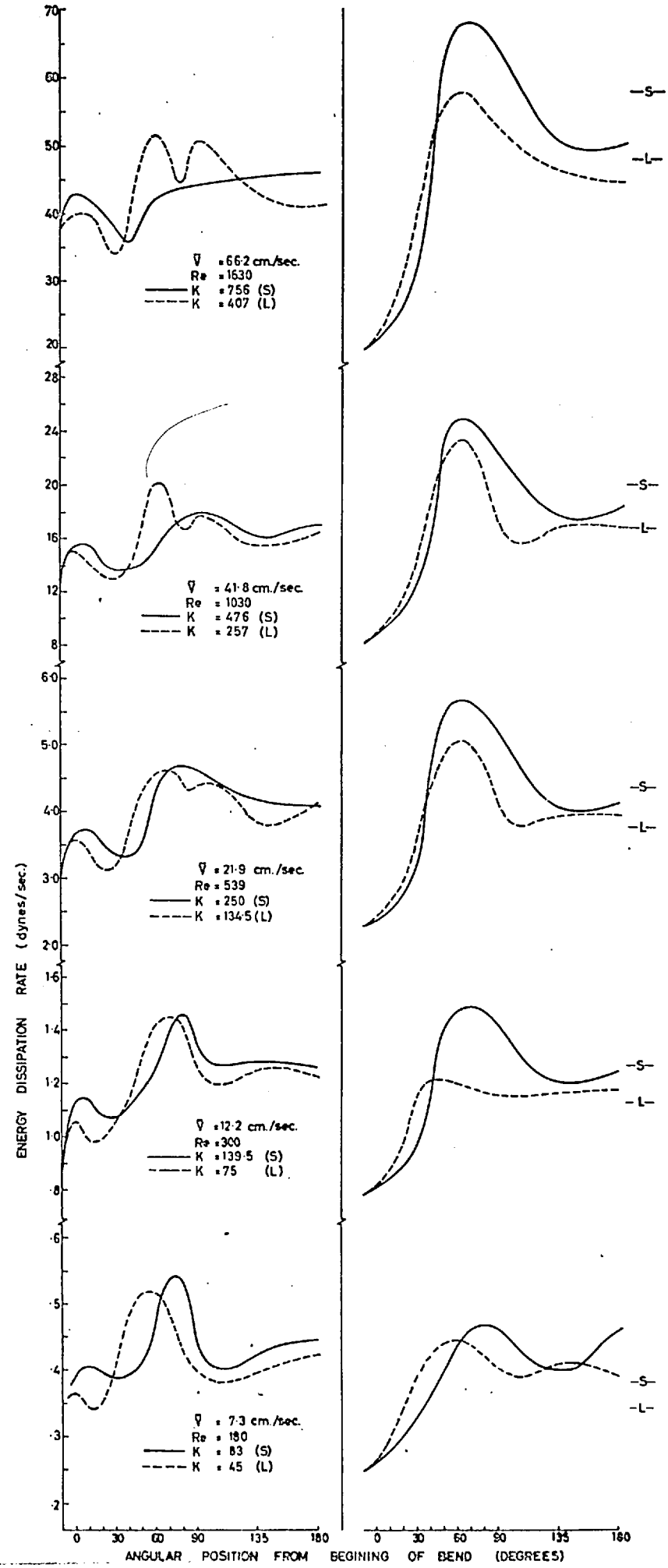


FIGURE 3.27 Energy dissipation rate as a function of bend angles. Flat inlet velocity profile data is on left; parabolic inlet is on right. See text for definition of -s- and -L-.

not compare well with the experiments which indicate that the viscous dissipation is rapidly increasing. This prediction does, however, show the trend for the viscous dissipation within the initial region of the curve not to decrease as would be expected at the entrance to a long straight tube, and that this dissipation will be a function of curvature (as can be seen in the figure) in the region of the curve.

The indication of -s- and -L- at the right of the figure is the energy dissipation calculated for fully developed curved flow from the data of White and Ito and the theoretical predictions of Ito for the friction factor, for the small and large curvature models used in this study. As can be seen, only fair comparisons are made between this friction factor at the energy dissipation rate calculated from the velocity distributions measured at 180^{o} bend angle. It is interesting to note that these calculations predict a large fluctuation in energy dissipation as the flow moves around the bend, possibly indicating why the results of pressure drop in bends have such scatter (Zanker & Brock).

Kinetic energy

The total kinetic energy was calculated from the distributions of total velocity. This was done to predict the mean static pressure from the energy dissipation/

dissipation and the changes in average kinetic energy. The mean velocity of the models does not change in the axial direction but a change in average kinetic can come about from a change in the velocity distribution. Table 3.2 shows the kinetic energy factor defined as

$$\beta = \frac{\iint v^3(r,\theta)\, r\,dr\,d\theta}{\iint v(r,\theta)\, r\,dr\,d\theta}$$

This, of course, gives

$$\text{kinetic energy} = \beta * \tfrac{1}{2} \rho \bar{V}^2$$

and therefore changes in β express percentage changes in kinetic energy. The changes in kinetic energy for the curved tube models are small compared to the energy dissipation rate.

Conclusion

I have attempted to describe the three-dimensional velocity field for laminar flow entering a bend and developing to the fully developed curved flow condition for a range of Reynolds and Dean numbers. The experiments were arranged to compare the flow development from two inlet velocity distributions which differ in their content of vorticity. The measurements have been compared to theoretical predictions for the initial development and for fully developed curved flow. The measurements are in qualitative agreement with the theories of Pickett and Squire/

Squire & Winter in the initial region of the bend where the secondary currents increase in magnitude at a linear rate. The measurements show partial arguments with the velocity distribution predicted by Pickett for a flat inlet velocity profile. At 180° bend angle the measurements are in good agreement with the theories of fully developed curved flow at Dean numbers below 500; above this value the flow is probably not fully developed at a bend angle of 180°. Between the linear inlet region and the fully developed condition the experiments show complex secondary flow patterns. At Dean numbers below 300 the general directions of the secondary flow are similar to those found by Squire and Rowe. And the qualitative arguments concerning the drift of the developing streamwise vorticity put forth by Rowe to explain the patterns of secondary currents may possibly be applicable. At Dean numbers greater than 300 the patterns of secondary currents are much more complex and show large areas of axial vorticity which is opposite in sign to the axial vorticity generated in the linear region of the bend. At present no argument is put forth to explain the development of this vorticity.

The rate of energy dissipation calculated from the total velocity field was shown to have a characteristic pattern with respect to the position of the flow within the bend. This calculation showed fair comparison with theory/

theory within the initial region of the bend and fair comparison with the measurements and theory for the fully developed condition to the calculations at 180° of the bend.

Finally the velocity gradient at the wall was measured and shown to have a characteristic pattern which strongly depends on the inlet velocity profile. This measured wall velocity gradient within the bend transition region does not have a similar tangential distribution to that within the fully developed curved case.

TABLE 3.3

MOMENTS AND KINETIC ENERGY FACTOR
FOR FLOW ENTERING A CURVED TUBE

Position	Moments of Velocity Distribution First	Second	Third	Kinetic Energy Factor	Reynolds Number	Average Velocity (cm/sec)	Dean Number	a/R
Flat Inlet Profile	0	.658	0	1.237	1634	66.2	756	1/4.66
0 Degree	-.069	.653	.019	1.295				
10(Bend Angle)	-.070	.654	.021	1.282				
20	-.060	.658	.023	1.254				
30	-.048	.655	.019	1.248				
40	-.010	.649	.011	1.271				
50	.017	.653	.011	1.256				
60	.041	.654	.023	1.289				
70	.053	.658	.027	1.290				
80	.052	.659	.027	1.298				
90	.044	.662	.027	1.281				
135	.055	.661	.026	1.261				
180	.049	.668	.021	1.204				
Parabolic Inlet Profile	.000	.578	.003	1.976				
30 Degree	.042	.631	.030	1.443				
60	.084	.694	.043	1.380				
90	.085	.688	.035	1.311				
135	.089	.664	.036	1.317				
180	.105	.666	.041	1.312				
Flat Inlet Profile	.000	.658	.000	1.237	1630	66.2	407	1/16
0 Degree	.049	.620	.015	1.297				
10	.060	.650	.019	1.309				
20	.037	.653	.018	1.266				

40	.068	.650	.019	1.299				
50	.044	.659	.029	1.297				
60	.062	.656	.036	1.366				
70	.042	.664	.030	1.281				
80	.037	.666	.023	1.242				
90	.049	.670	.028	1.252				
135	.054	.653	.033	1.332				
180	.071	.658	.032	1.309				
Parabolic Inlet Profile	.000	.578	.003	1.976				
30	.096	.645	.040	1.443				
60	.071	.687	.032	1.315				
90	.093	.673	.027	1.301				
135	.094	.660	.031	1.314				
180	.077	.661	.026	1.286				
Flat Inlet Profile	-.003	.642	.001	1.333	1031	41.7	476	1/4.66
0 Degree	-.066	.645	.020	1.333				
10	-.082	.644	.024	1.351				
20	-.061	.647	.021	1.307				
30	-.051	.646	.020	1.304				
40	-.006	.646	.010	1.289				
50	.024	.645	.017	1.318				
60	.050	.648	.021	1.338				
70	.048	.654	.030	1.346				
80	.066	.657	.029	1.353				
90	.060	.663	.038	1.347				
135	.050	.659	.028	1.286				
180	.061	.663	.016	1.245				
Parabolic Inlet Profile	.015	.575	.010	2.053				
30	.038	.621	.035	1.561				
60	.106	.685	.047	1.446				
90	.071	.682	.030	1.323				
135	.076	.662	.023	1.298				
180								
Flat Inlet Profile	-.003	.642	.001	1.333	1029	41.8	257	1/16
0 Degree	-.068	.641	.020	1.371				
10	-.057	.642	.018	1.349				
20	-.033	.643	.017	1.322				
30	.013	.640	.008	1.326				
40	.053	.642	.020	1.349				
50	.037	.650	.027	1.352				
60	.051	.654	.040	1.410				

90	.045	.656	.023	1.288				
135	.046	.653	.027	1.315				
180	.064	.657	.031	1.313				
Parabolic Inlet Profile	.015	.575	.010	2.053				
30	.085	.639	.041	1.464				
60	.077	.685	.032	1.361				
90	.082	.657	.023	1.321				
135	.091	.656	.031	1.351				
180	.061	.656	.029	1.311				
Flat Inlet Profile	-.008	.634	.001	1.383	540	21.8	250	1/4.66
0 Degree	-.045	.632	.015	1.425				
10	-.074	.637	.022	1.379				
20	-.073	.636	.024	1.387				
30	-.038	.637	.016	1.341				
40	.001	.637	.005	1.339				
50	.014	.647	.008	1.288				
60	.036	.645	.019	1.358				
70	.057	.660	.025	1.340				
80	.053	.662	.025	1.335				
90	.044	.659	.035	1.361				
135	.035	.648	.029	1.371				
180	.029	.654	.015	1.267				
Parabolic Inlet Profile	-.013	.576	.008	2.074				
30	.012	.613	.026	1.620				
60	.116	.666	.035	1.503				
90	.090	.668	.024	1.391				
135	.062	.650	.025	1.335				
180	.071	.635	.030	1.312				
Flat Inlet Profile	-.008	.634	.001	1.383	539	21.9	135	1/16
0 Degree	-.064	.633	.018	1.402				
10	-.064	.630	.018	1.425				
20	-.040	.631	.013	1.389				
30	.005	.631	.008	1.391				
40	.066	.635	.023	1.401				
50	.045	.649	.023	1.353				
60	.063	.652	.042	1.404				
70	.064	.656	.040	1.380				
80	.049	.658	.026	1.315				
90	.052	.657	.030	1.334				
135	.049	.647	.030	1.356				
180	.060	.651	.027	1.334				

Profile	-.013	.576	.008	2.074				
30	.072	.632	.038	1.483				
60	.084	.666	.027	1.408				
90	.067	.651	.021	1.341				
135	.074	.644	.027	1.391				
180	.064	.647	.029	1.380				
Flat Inlet Profile	-.017	.628	.006	1.410	301	12.2	140	1/4.66
0 Degree	-.057	.637	.024	1.370				
10	-.067	.638	.028	1.373				
20	-.051	.635	.025	1.375				
30	-.034	.638	.021	1.339				
40	-.004	.638	.010	1.330				
50	.027	.645	.019	1.296				
60	.042	.647	.021	1.313				
70	.038	.660	.020	1.249				
80	.060	.662	.024	1.266				
90	.048	.656	.034	1.324				
135	.043	.653	.025	1.285				
180	.031	.656	.012	1.242				
Parabolic Inlet Profile	.011	.590	.004	1.877				
30	.015	.614	.022	1.577				
60	.089	.654	.033	1.410				
90	.051	.664	.022	1.277				
135	.026	.647	.018	1.302				
180	.030	.654	.023	1.255				
Flat Inlet Profile	-.017	.628	.006	1.410	300	12.2	75	1/16
0 Degree	-.056	.627	.022	1.446				
10	-.038	.627	.017	1.423				
20	-.008	.630	.010	1.382				
30	.036	.630	.021	1.413				
40	.055	.635	.026	1.397				
50	.032	.650	.026	1.292				
60	.037	.649	.033	1.344				
70	.043	.646	.029	1.360				
80	.022	.659	.023	1.249				
90	.024	.653	.017	1.268				
135	.011	.654	.020	1.247				
180	.019	.649	.021	1.292				
Parabolic Inlet Profile	.011	.590	.004	1.877				
30	.038	.636	.034	1.409				

90	.030	.646	.016	1.302				
135	.047	.645	.025	1.335				
180	.030	.643	.023	1.340				
Flat Inlet Profile					180	7.3	83	1/4.66
0 Degree	-.038	.638	.018	1.344				
10	-.031	.642	.018	1.312				
20	-.043	.637	.018	1.338				
30	-.015	.642	.011	1.289				
40	.023	.638	.012	1.330				
50	.028	.645	.011	1.284				
60	.023	.642	.013	1.322				
70	.057	.661	.020	1.208				
80	.040	.664	.014	1.178				
90	.028	.646	.020	1.305				
135	.030	.647	.015	1.290				
180	.016	.653	.013	1.231				
Parabolic Inlet Profile								
30	.004	.624	.006	1.432				
60	.038	.649	.019	1.293				
90	.052	.646	.022	1.327				
135	.036	.638	.014	1.350				
180	.021	.657	.018	1.207				
Flat Inlet Profile					180	7.3	45	1/16
0 Degree	-.024	.632	.015	1.381				
10	-.034	.625	.013	1.438				
20	-.007	.631	.008	1.374				
30	.035	.629	.018	1.409				
40	.074	.639	.028	1.372				
50	.051	.656	.021	1.264				
60	.056	.644	.027	1.329				
70	.061	.640	.017	1.349				
80	.026	.657	.015	1.214				
90	.042	.637	.024	1.378				
135	.030	.651	.024	1.269				
180	.041	.644	.020	1.303				
Parabolic Inlet Profile								
30	.045	.628	.022	1.430				
60	.038	.645	.022	1.315				
90	.036	.643	.013	1.308				
135	.031	.647	.012	1.274				
180	.041	.639	.015	1.342				

L E G E N D

+ Indicates outward from centre of curvature.

For definition of Kinetic Energy Factor see text.

Bend Angle is angular position from inlet of curved tube.

Entrance condition shown at 0.5 diameters upstream from start of curvature.

CHAPTER 4

Flow within a straight tube which progressively changes cross section from circular to elliptical

In this chapter we shall study the flow within models of the transition zone of a bronchus, as defined in Chapter One. This zone has a changing cross section with respect to axial distance. Originally the tube is circular, and progressively becomes elliptical in shape while maintaining a constant cross sectional area. We have noted in Chapter 3 that the development of streamwise vorticity within the bend transition zone of a curved tube depends strongly upon the amount (and distribution) of vorticity present in the flow entering the curve. This chapter describes the flow entering the curvature of a bifurcation.

The study of flow within a developing elliptical tube is conducted in this chapter by finding solutions to a potential flow condition and a low Reynolds condition for a tube which slowly develops an elliptical shape. Neither of the conditions for the theoretical solution strictly applies to the flow conditions of interest in the models. Instead the condition of potential flow and the condition of highly viscous flow will be the bounds of the conditions of interest. We shall show that the secondary velocity patterns are similar for each of the theoretical/

theoretical solutions, and we therefore assume that an interpolation of the predictions made for the bounding conditions will explain the experimental data. The experimental part of this chapter considers laminar flow into the developing ellipse at Reynolds numbers from 300 to 2200, with two entrance conditions: a flat and a parabolic velocity distribution at entrance. The model used for the experiments in this chapter is similar to the transition zone (the region defined between a and c in Figure 1.7) in the large scale model bifurcations. The rate at which the cross section of the models used in these studies develop an elliptical shape with axial distance is identical to that found in the models in the following chapter*, but unlike the bifurcations, the models in this chapter carry on developing an elliptical shape long after the region used for measurement. Figure 4.1 shows the model used and a scale drawing of the major and minor axis. The length of the major axis is defined by a curvature of the outer wall of the bifurcation (see Chapter 1). This curvature was set at the value of five times the radius in the model, which is initially circular. We define the initial radius of the tube as a_o and the coordinate/

*This is strictly true for only three of the five bifurcating models. Two of the symmetric bifurcations have elliptical regions which develop ellipticity at a slower rate than the model of this chapter, and the one asymmetric model has a transition zone which is not truly elliptical in cross section but rather egg-shaped.

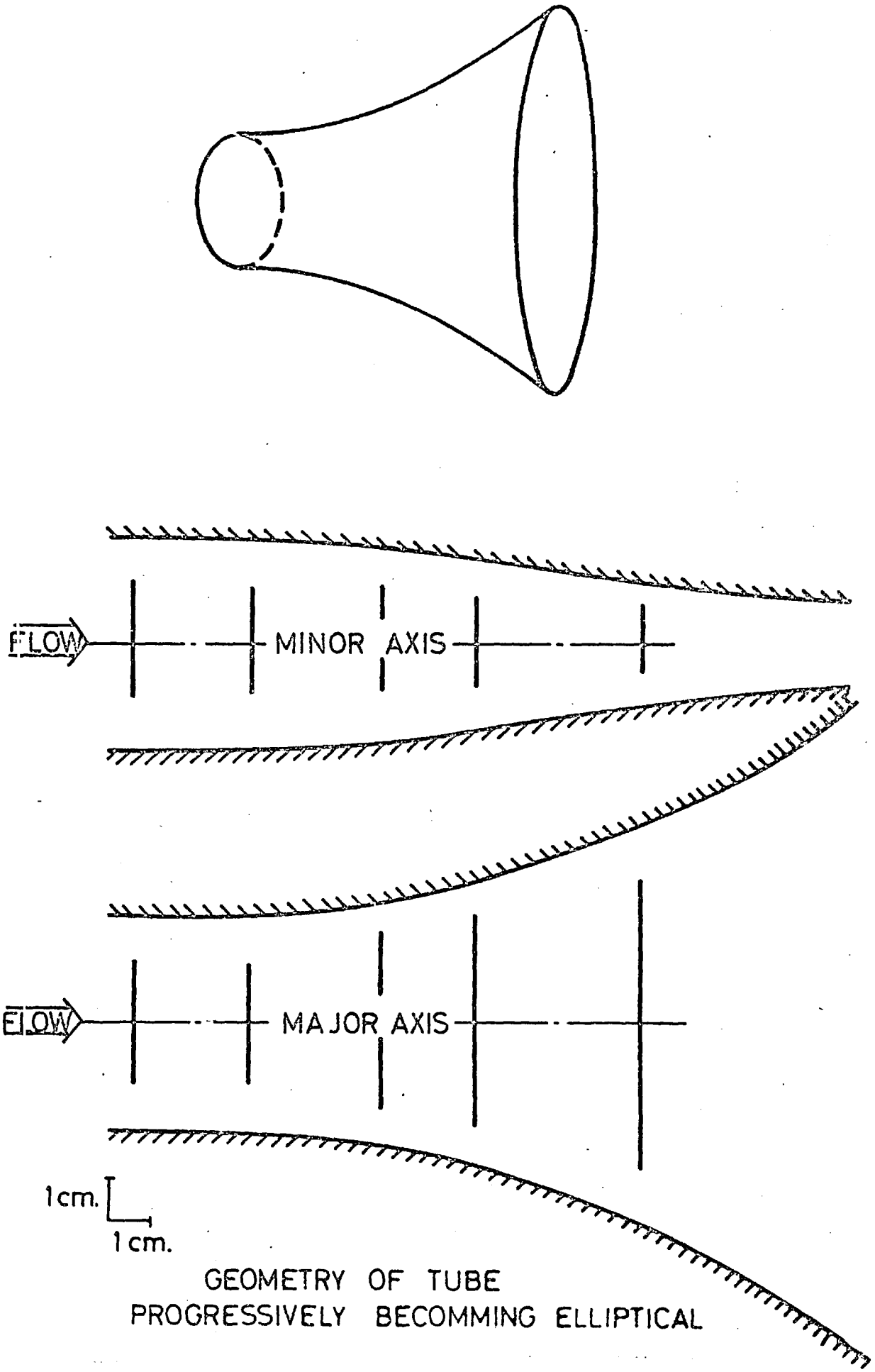


FIGURE 4.1 Model of tube which changes ellipticity with axial distance. Minor and major axis shows the changes in dimension of each axis in the model used for experimentation.

coordinate system where $\hat{x}$ is the axial dimension, $\hat{y}$ is along the major axis and $\hat{z}$ along the minor axis. We further define $\hat{a},\hat{b}$ as the major and minor dimensional axis at the axial position, and use the notation $\hat{}$ to indicate dimensional quantities. The parameter, ℓ, is a characteristic axial distance within which a significant change of cross sectional shape will take place and we require that

$$\epsilon \equiv a_0/\ell << 1 \quad .$$

Therefore the function $\hat{a}(\hat{x})$ and $\hat{b}(\hat{x})$ are arbitrary, but must be slowly varying with $\hat{x}$.

Nondimensionalising with respect to the radial and axial length scales, we obtain

$$x = \hat{x}/\ell \quad , \quad y = \hat{y}/a_0 \quad , \quad z = \hat{z}/a_0$$

and $$a(x) = \hat{a}/a_0 \quad , \quad b(x) = \hat{b}/a_0$$

where the latter quantities are the nondimensional lengths of the major and minor axis, which are a function of axial distance, x, alone. For the particular case of the models used in the experiments, the major axis is defined by $\epsilon = 1/2 \quad \ell = 2a_0$

$$a(x) = 6 - [25 - (2x)^2]^{1/2}$$

and the minor axis is defined so that the cross sectional area remains constant;

$$a(x)\, b(x) = \text{CONSTANT}$$

and

$$b(x) = \frac{1}{6 - [25 - (2x)^2]^{1/2}}$$

Therefore/

Therefore the rate of change of the axis for the experimental model is:

$$\frac{da(x)}{dx} = \frac{4x}{\left[25-(2x)^2\right]^{1/2}}$$

and

$$\frac{db(x)}{dx} = \frac{-4x}{\left[6-\left[25-(2x)^2\right]^{1/2}\right]^2\left[25-(2x)^2\right]^{1/2}}$$

which means that the major axis will be expanding and the minor axis contracting at a rate which at low values of x will be small, but as x approaches 5/2 the rate of change of the elliptical section becomes infinite.

We shall only be concerned with the regions of slowly varying cross section. This region is shown in Fig.4.1 as the four heavy lines, marking the locations where experimental studies are carried out.

Potential flow solution for a flat entrance profile entering a tube progressively becoming elliptical

The boundary of the ellipse is defined as

$$\frac{\hat{y}^2}{\hat{a}^2} + \frac{\hat{z}^2}{\hat{b}^2} - 1 \equiv \hat{F}(\hat{y},\hat{z},\hat{x}) = 0 \qquad (4.1)$$

At the entrance to the system the tube is circular with radius a_o and the velocity is everywhere uniform with magnitude U_o. We neglect the effect of the boundary layer and seek a solution in the form

$$\underset{\sim}{u} = U_o\left[\underset{\sim}{i}\, U(\hat{x}) + \nabla\phi\right] \qquad (4.2)$$

where ϕ is the potential function, i.e.

$$u = U_o + \phi_{\hat{x}} \quad ; \quad v = \phi_{\hat{y}} \quad ; \quad w = \phi_{\hat{z}}$$

where/

where (u,v,w) are the velocity components in the (x,y,z) directions and subscripts $(\hat{x},\hat{y},\hat{z})$ denote partial differentiation with respect to $(\hat{x},\hat{y},\hat{z})$ respectively.

Continuity requires

$$\nabla \cdot \underset{\sim}{u} = 0$$

which for the form of the velocity in equation (4.2) becomes

$$\frac{dU}{d\hat{x}} + \nabla^2\phi = 0$$

The boundary condition is that on F = 0

$$\underset{\sim}{u} \cdot \nabla F = 0$$

which becomes

$$(U + \phi_{\hat{x}})F_{\hat{x}} + \phi_{\hat{y}} F_{\hat{y}} + \phi_{\hat{z}} F_{\hat{z}} = 0$$

and

$$F_{\hat{x}} = -2\left\{\frac{\hat{y}^2}{\hat{a}^3}\frac{d\hat{a}}{d\hat{x}} + \frac{\hat{z}^2}{\hat{b}^3}\frac{d\hat{b}}{d\hat{x}}\right\}$$

$$F_{\hat{y}} = 2\,\hat{y}/\hat{a}^2$$

$$F_{\hat{z}} = 2\,\hat{z}/\hat{b}^2$$

Using the nondimensional notation from above, the continuity equation becomes

$$\epsilon\frac{dU(x)}{dx} + \phi_{yy} + \phi_{zz} + \epsilon^2\phi_{xx} = 0 \qquad (4.3)$$

and the boundary condition becomes

$$\epsilon(U(x) + \epsilon\phi_x)F_x + \phi_y F_y + \phi_z F_z = 0 \qquad (4.4)$$

We now expand the potential function in powers of ϵ such that

$$\phi = \epsilon\phi_1 + \epsilon^2\phi_2 + \epsilon^3\phi_3 + \cdots$$

Equation/

Equation (4.3) then becomes

$$\sum_n \left[\epsilon^n (\phi_n)_{yy} + \epsilon^n (\phi_n)_{zz} + \epsilon^{n+2} (\phi_n)_{xx} \right] = -\epsilon \frac{dU(x)}{dx}$$

and equation (4.4) becomes

$$F_y \sum_n \epsilon^n (\phi_n)_y + F_z \sum_n \epsilon^n (\phi_n)_z + \epsilon F_x \left(U(x) + \sum_n \epsilon^{n+2} (\phi_n)_x \right) = 0$$

Collecting like powers of ϵ the equation for the first order is

$$\phi_{1yy} + \phi_{1zz} = -\frac{dU(x)}{dx}$$

with the boundary condition that on F = 0

$$\frac{y}{a^2} \phi_{1y} + \frac{z}{b^2} \phi_{1z} = U \left(\frac{y^2}{a^3} \frac{da}{dx} + \frac{z^2}{b^3} \frac{db}{dx} \right) .$$

The solution to these equations is

$$\phi_1 = \frac{U}{2a} y^2 \frac{da}{dx} + \frac{U}{2b} z^2 \frac{db}{dx}$$

which satisfies the boundary conditions for all values of F.

The velocity components of the first order solution are thus

$$v_1 = \phi_{1y} = \frac{U}{a} y \frac{da}{dx} \qquad (4.5)$$

$$w_1 = \phi_{1z} = \frac{U}{b} z \frac{db}{dx} \qquad (4.6)$$

The solution for the second order is simply

$$\phi_2 = 0$$

Solutions for the third order become much more difficult. Since/

Since we only wish to characterise the flow by obtaining the general direction and approximate magnitude of the secondary currents, we include only the first and second order solution in our general solution.

For a numerical example of equations (4.5) and (4.6), we choose an axial length of 1.625 diameters from the origin of the tube with a(x) and b(x) taken from the experimental model at that location; the equations become:

$$v_1 = +0.551\, y/a$$

$$w_1 = -0.251\, z/b$$

The velocities and directions for this example are shown in Figure 4.2a.

Low Reynolds number solution for flow in a tube which slowly changes its ellipticity

An asymptotic series solution for laminar flow with low Reynolds numbers within a tube which slowly changes its ellipticity is obtained in powers of ϵ. The assumptions made for this solution are that at each axial position there is a quasi-parallel fully developed flow in response to a uniform axial pressure gradient. This assumption is equivalent to neglecting terms in the equations of order ϵ while retaining those of order $1/Re$ and/

and the solution therefore holds for Reynolds numbers of order ϵ^{-1}. In practice though, as $\epsilon \to 0$ (very slow axial variation in tube shape) the theory will hold only when Reynolds numbers are not too large so that the assumption of a fully developed condition at each axial position is not violated. The zeroth and first order solutions are obtained; the zeroth order being Poiseuille flow when the tube is circular. The details of this analysis can be found in the appendix.

The solution for the zeroth and first order expansions of the primary velocity u is:

$$u_0 = \frac{2a^2b^2}{a^2+b^2}\left(1 - \frac{y^2}{a^2} - \frac{z^2}{b^2}\right) \tag{4.7}$$

$$u_1 = \left(1 - \frac{y^2}{a^2} - \frac{z^2}{b^2}\right)\left(\alpha_1 + \alpha_2 \frac{y^2}{a^2} + \alpha_3 \frac{z^2}{b^2} + \alpha_4 \frac{y^4}{a^4} + \alpha_5 \frac{y^2z^2}{a^2b^2} + \alpha_6 \frac{z^4}{b^4}\right) \tag{4.8}$$

where the α_n's are defined in the appendix. And the first order solution for the secondary velocities are:

$$v_1 = \frac{a^2b\,(3a^2+b^2)\left(b\frac{da}{dx} - a\frac{db}{dx}\right)}{2(a^2+b^2)} \frac{y}{a}\left(1 - \frac{y^2}{a^2} - \frac{z^2}{b^2}\right) \tag{4.9}$$

$$w_1 = \frac{-ab^2\,(a^2+3b^2)\left(b\frac{da}{dx} - a\frac{db}{dx}\right)}{2(a^2+b^2)} \frac{z}{b}\left(1 - \frac{y^2}{a^2} - \frac{z^2}{b^2}\right) \tag{4.10}$$

These equations are not applicable to a tube which arbitrarily changes its ellipticity (of course any change must/

must be slow); that is, the solution could only be found for a particular function of a and b. This relation is

$$\frac{(a.b)^3}{a^2+b^2} = \text{constant}$$

This relation approximately holds in this experimental model for the first two diameters.

We choose the same location within the experimental model for a numerical evaluation of equations (4.9) and (4.10) as for the case of the potential flow solution. Equations (4.9) and (4.10) become

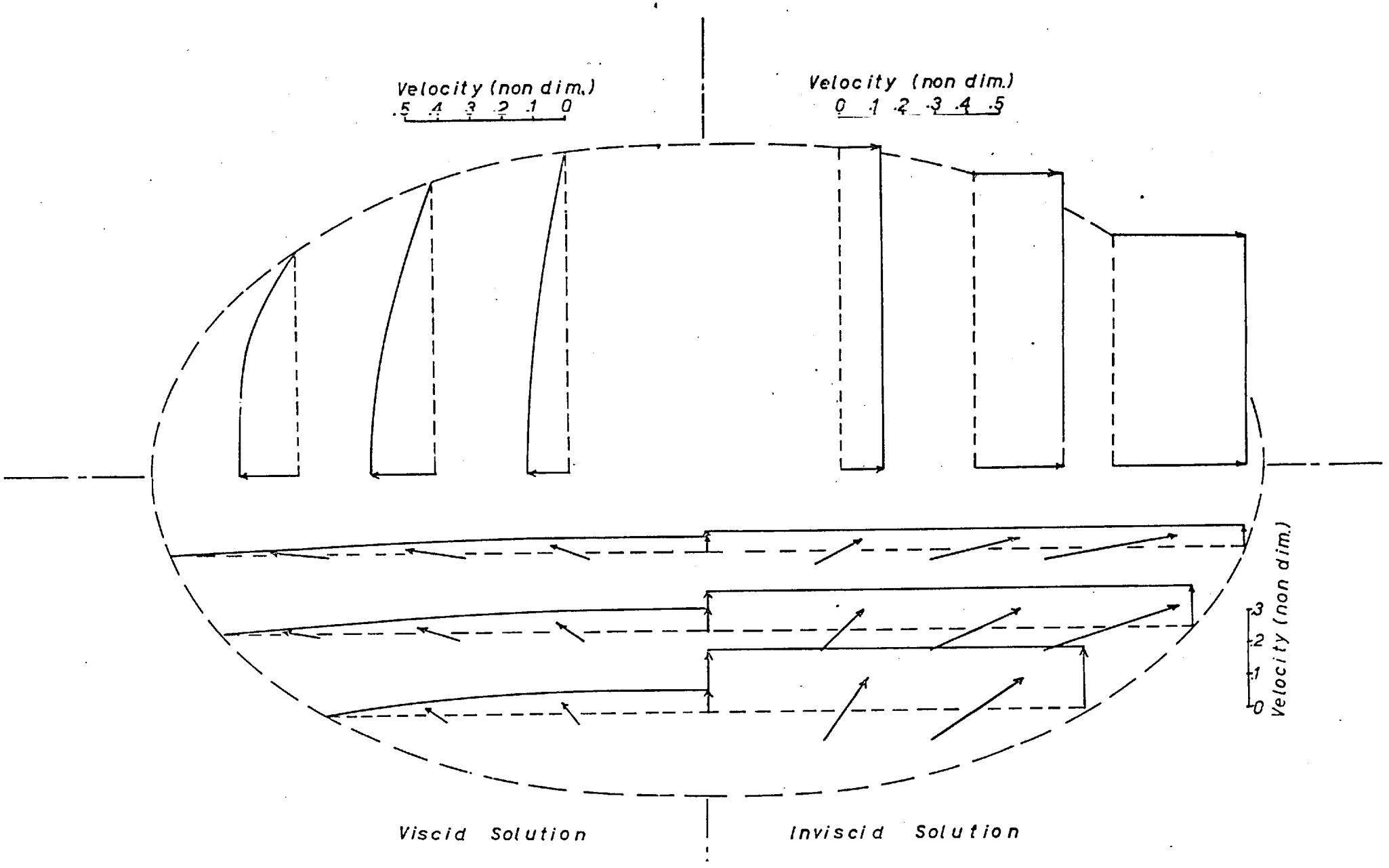
$$v_1 = +0.543\ y/a\ (1 - y^2/a^2 - z^2/b^2)$$

$$w_1 = -0.193\ z/b\ (1 - y^2/a^2 - z^2/b^2)$$

where the velocities are scaled to the mean velocity; these examples are shown in Figure 4.2b.

Discussion of theoretical results

Figure 4.2 displays the magnitude of the two Cartesian components of the secondary velocity with respect to the mean velocity. The figure also indicates the direction and magnitude of the total secondary velocity. In general the potential flow solution predicts higher secondary velocities, especially close to the walls, than the viscous flow solution. The directions of the secondary velocity for both cases are, however, quite similar. The z component (parallel to minor axis) of the secondary velocity/



FIGURES 4.2a and b. Cartesian components of secondary velocities as predicted by viscid and inviscid expansion solutions.

velocity is always negative, while the y component (parallel to major axis) is always positive. Thus the streamlines are not closed. This is because the secondary motion is set up as a response to the change in shape of the tube. For the potential flow the changing shape of the tube is the only influence in developing the secondary velocities. This can be seen from equations (4.5) and (4.6) which indicate that contours of equal total secondary velocities are concentric ellipses. The secondary velocities predicted for the viscous condition are influenced by the change in shape and the consequent variation in the basic flow; i.e. the zeroth order solution of primary velocity given by equation (4.7). This latter influence is the reason why the y component of secondary flow decreases after approximately the 0.5a position along the major axis (as opposed to the potential flow condition).

It should be carefully noted that the potential flow solution contains no effects of the boundary layer. This may be a good approximation if the boundary layer is very thin, but the results of the potential flow analysis must be suspect for locations near to the walls. Therefore comparisons between the potential and viscous flow conditions near the walls will not be made.

Examination of the viscous solutions for the primary

flow/

flow (combination of equations (4.7) and (4.8) indicates another general feature of the flow. These equations indicate that the velocity gradient at the wall on the major axis will be less than that on the minor axis; the ratio of these gradients being simply the ratio of the two axes.

The conclusions to our theoretical arguments about flow in tubes becoming progressively elliptical may be intuitively obvious. The secondary currents are simply resulting from the minor axis encroaching on the flow, while simultaneously the major axis is expanding. Thus the pattern of secondary currents could be thought of as resulting from a force parallel to the minor axis pushing the fluid toward the centre, while a force parallel to the major axis pulls the fluid away from the centre. The wall shear results also seem reasonable when compared to the predictions of shear in tubes with divergent or convergent walls.

We shall use the theoretical results of this section to compare with the experimental results of the following section.

Experimental techniques

The experimental techniques used in this chapter are similar/

similar to those discussed in Chapters 2 and 3 and only the modifications of technique unique to the experiments in the elliptical models will be discussed.

The three dimensional velocity field was determined at five axial positions within the model. The model is shown in Figure 4.1 and the axial planes where measurements were taken are indicated as the heavy lines within the tube, perpendicular to the axis. These planes of measurement are located at 0.5, 1.125, 1.625 and 2.375 diameters downstream from the circular origin of the model. The model extended axially an additional 1.5 diameters from the last measured position, continually changing its ellipticity in the same manner as in the test section. Measurements taken near the outlet end of the model did not suggest separation of the flow from the walls at the major axis. Such separation can cause upstream effects on the wall shear and on the symmetry of the mass flow. This latter influence comes as a result of separation occurring at only one wall.

From these observations we have assumed that the flow within the test section is not influenced by downstream conditions. The model ended at an axial distance of approximately four diameters and discharged into the atmosphere.

The velocity field was determined at five Reynolds numbers, each with a parabolic and flat entrance profile. The/

The Reynolds numbers, based on the diameter of the initial circular section, are shown in Table 4.1. All the flow regimes were laminar. Initial studies showed that the velocity field was very symmetrical within the test section. Therefore only one 90^{o} quadrant of the tube was measured; the other three quadrants assumed to be symmetrical. At each axial station, eight traverses of the probe were made, at positions of 0, 0.25, 0.5 and 0.75 nondimensional positions parallel to both the major and minor axes. Such traverses are shown in Figures 4.9 and 4.10.

Velocity gradients at the walls of the major and minor axis were measured with hot wires in the same manner as for the curved tube studies. The data obtained was handled in similar manner to that of Chapter 3. One important difference between the data analysis on the circular curved tubes is that all interpolations and integrations were carried out upon lines of concentric ellipses, not circles as in Chapter 3. This was done simply by introducing a weighting factor which adjusted the length of the radius at each point around the circumference of the ellipse.

The moments of the velocity field (zeroth through third), energy dissipation rate, and total kinetic energy were calculated. The first moment, indicating the location of the centre of mass flow, was forced to zero by our assumption/

TABLE 4.1

Reynolds Number of Experiments carried out on Model which progressively changes ellipticity (Based on radius of circular section)

Mean Velocity (cm/sec)	Reynolds Numbers
66.1	2164 (Laminar)
49.3	1617
23.5	770
13.8	453
10.4	341

assumption of symmetry in the velocity field.

Results

The same type of displays are used for the experimental results in the elliptical model as was used for the experimental results in the curved tube models.

Figures 4.3 to 4.8 show the primary velocity profiles for three of the five flow conditions along the major and minor axes for the flat entrance profile (Figs. 4.3 to 4.5) and the parabolic entrance profile (Figs. 4.5 - 4.8). The abscissa is now the dimensional radius. The diagrams for the flat velocity profile entrance condition show the effect that the changing elliptical shape has on development of the boundary layers. The boundary layer thickness along the major axis grows much more rapidly than within a circular straight tube ($\delta \propto Re^{-1/2}$), but this change in growth is not uniform with respect to axial length. The boundary layer on the wall at the major axis at first shows little effect from the changing ellipticity, but at a distance of about one diameter into the model, the boundary layer suddenly increases its growth rate on the major axis. This situation is opposed to the change in boundary layer growth on the convergent, minor axis. Here the boundary layer becomes thinner at an almost linear rate, starting from an axial location just downstream from the circular origin of the model.

The/

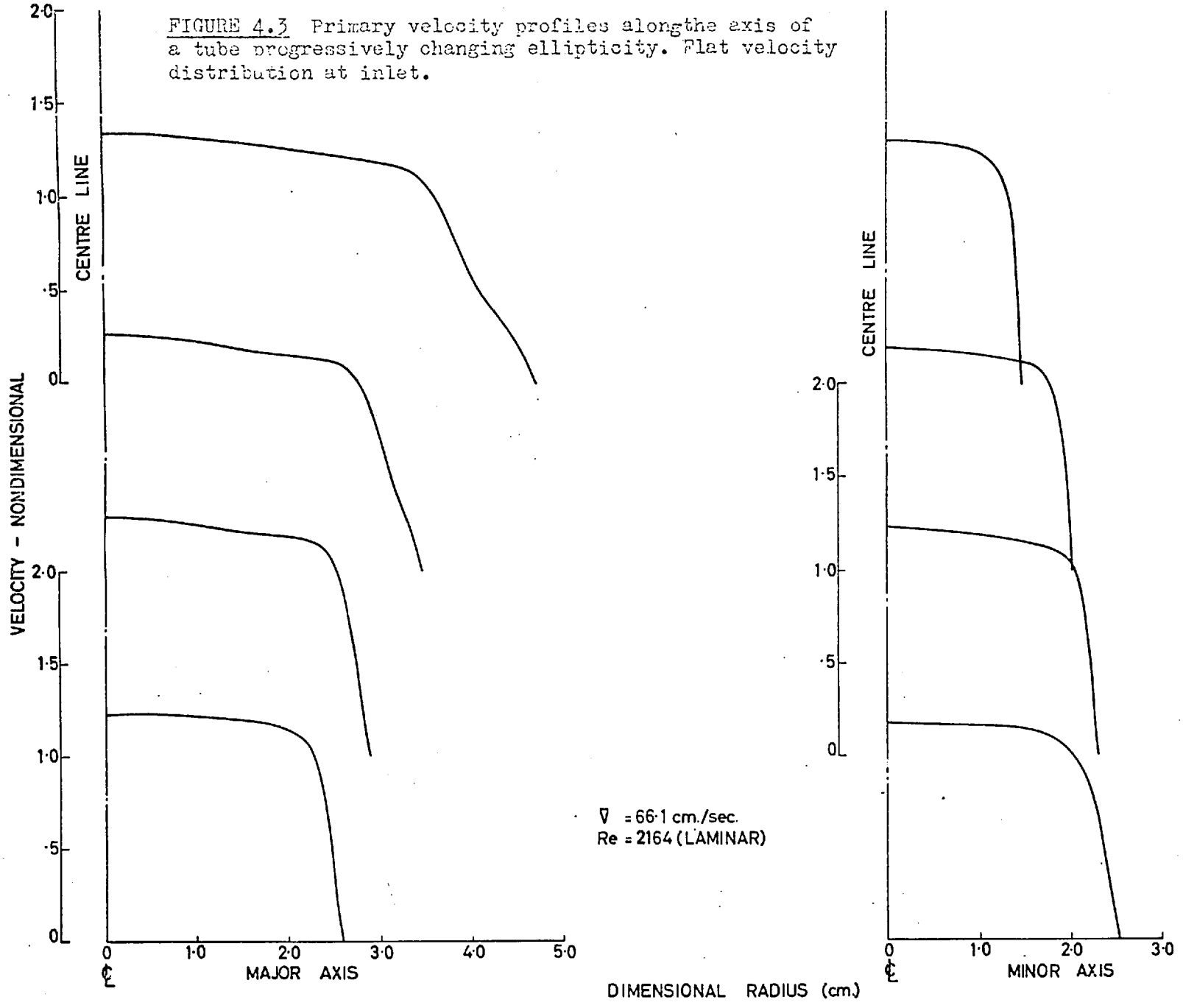


FIGURE 4.3 Primary velocity profiles alongthe axis of a tube progressively changing ellipticity. Flat velocity distribution at inlet.

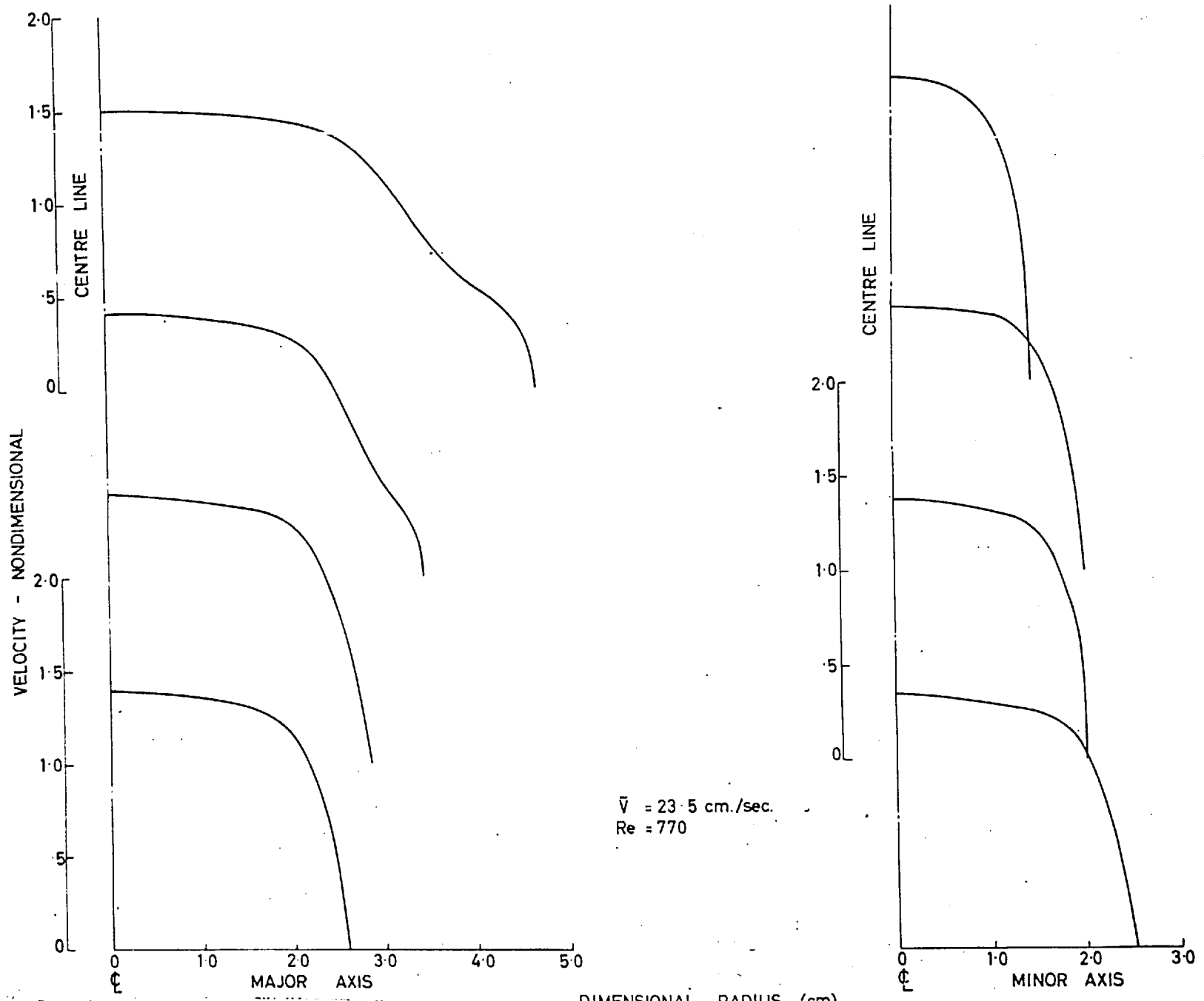


FIGURE 4.4 Primary velocity profiles along the axis of a tube progressively changing ellipticity. Flat velocity

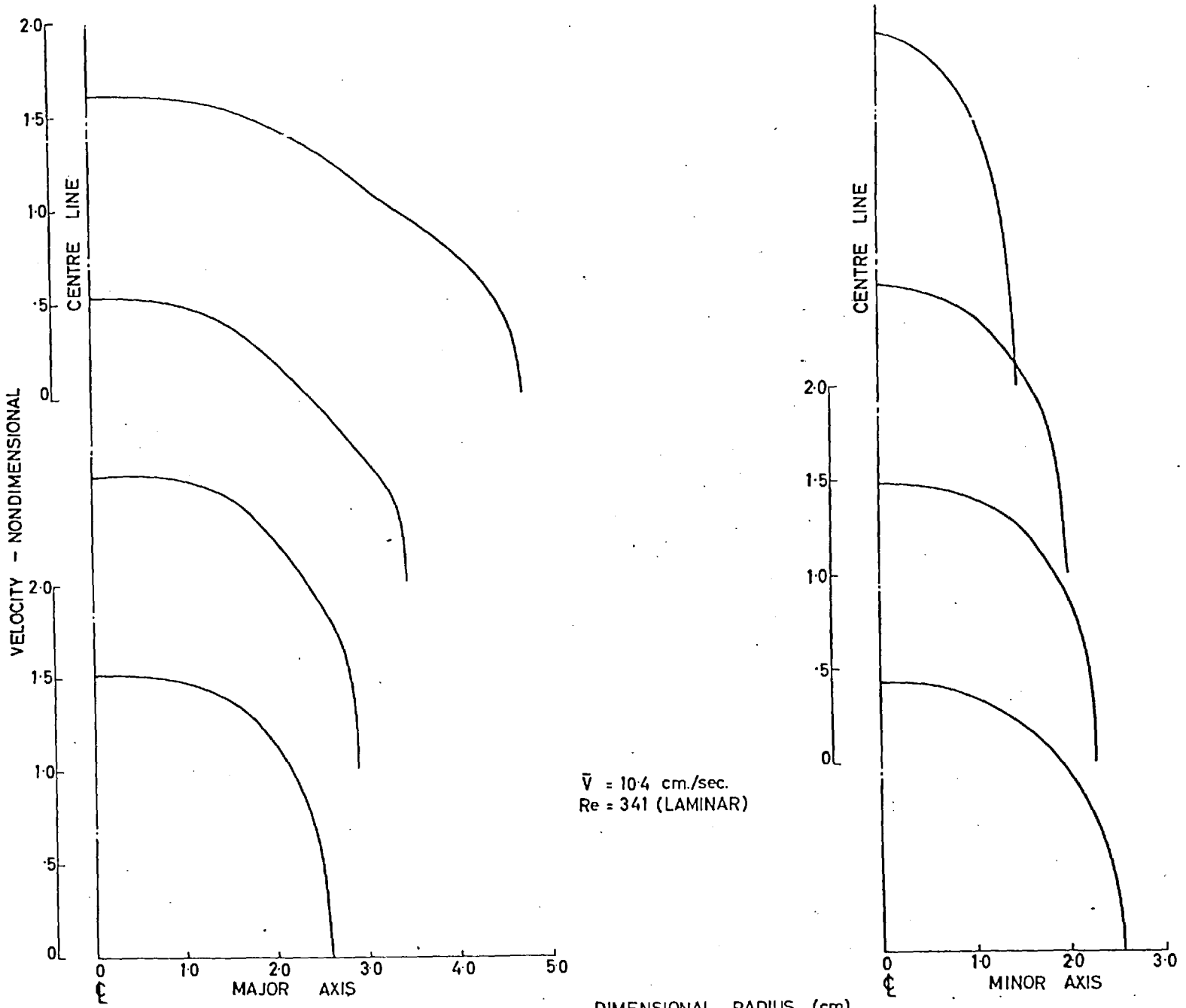


FIGURE 4.5 Primary velocity profiles along the axis of a tube progressively changing ellipticity. Flat velocit

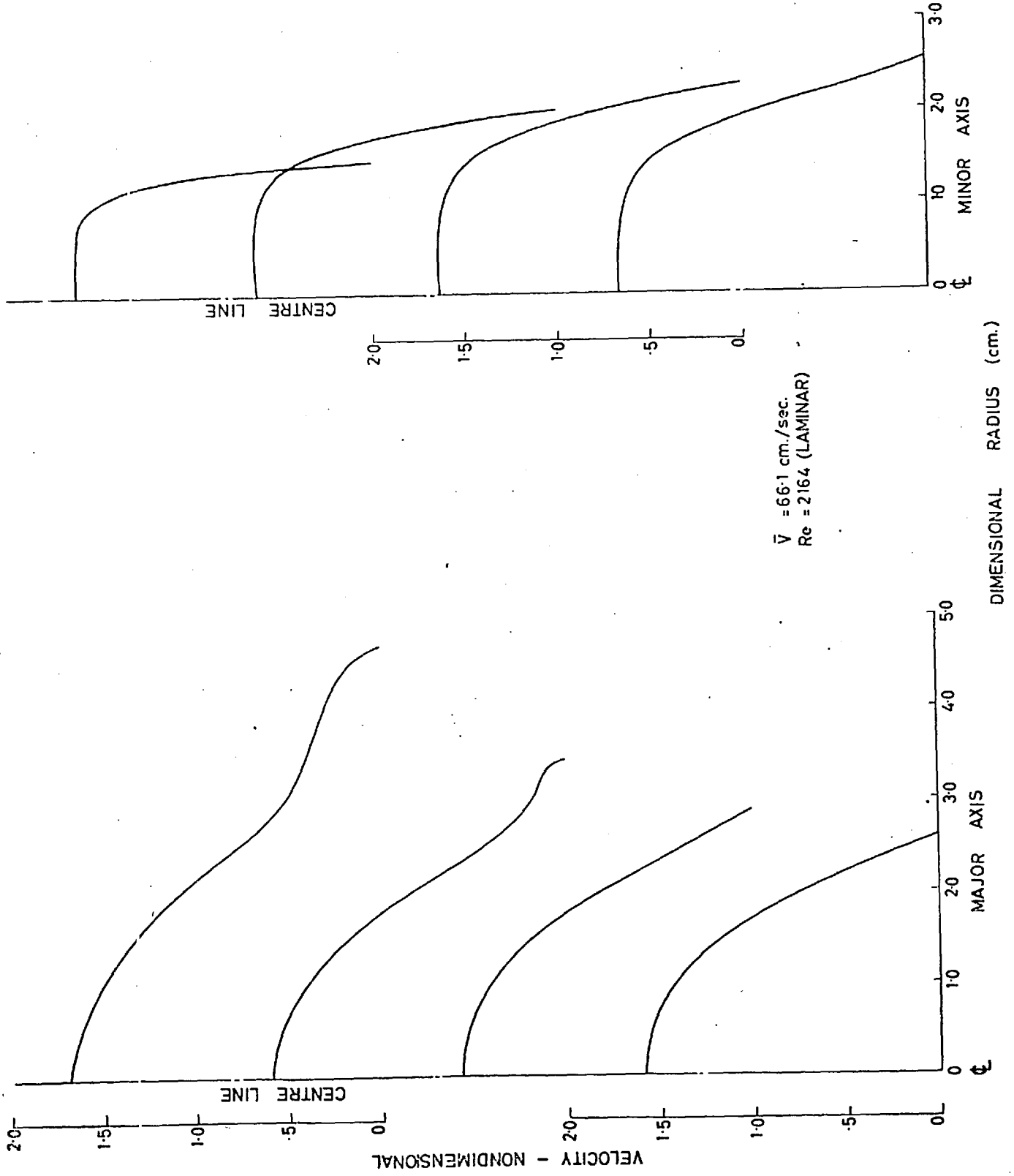


FIGURE 4.6 Primary velocity profiles along axis of tube progressively changing ellipticity. Parabolic velocity distribution at inlet.

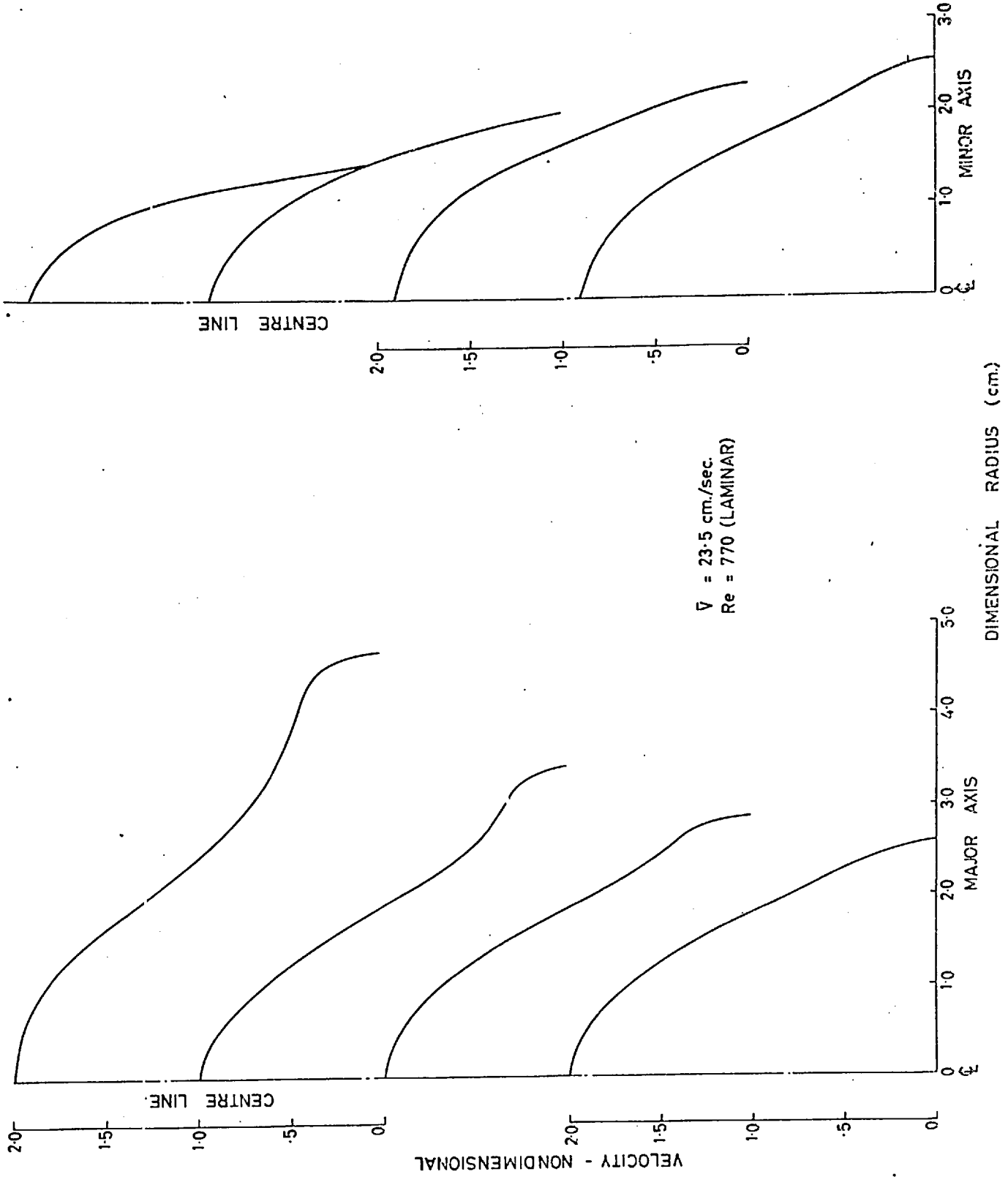


FIGURE 4.7 Primary velocity profiles along axis of tube progressively changing ellipticity. Parabolic velocity distribution at inlet.

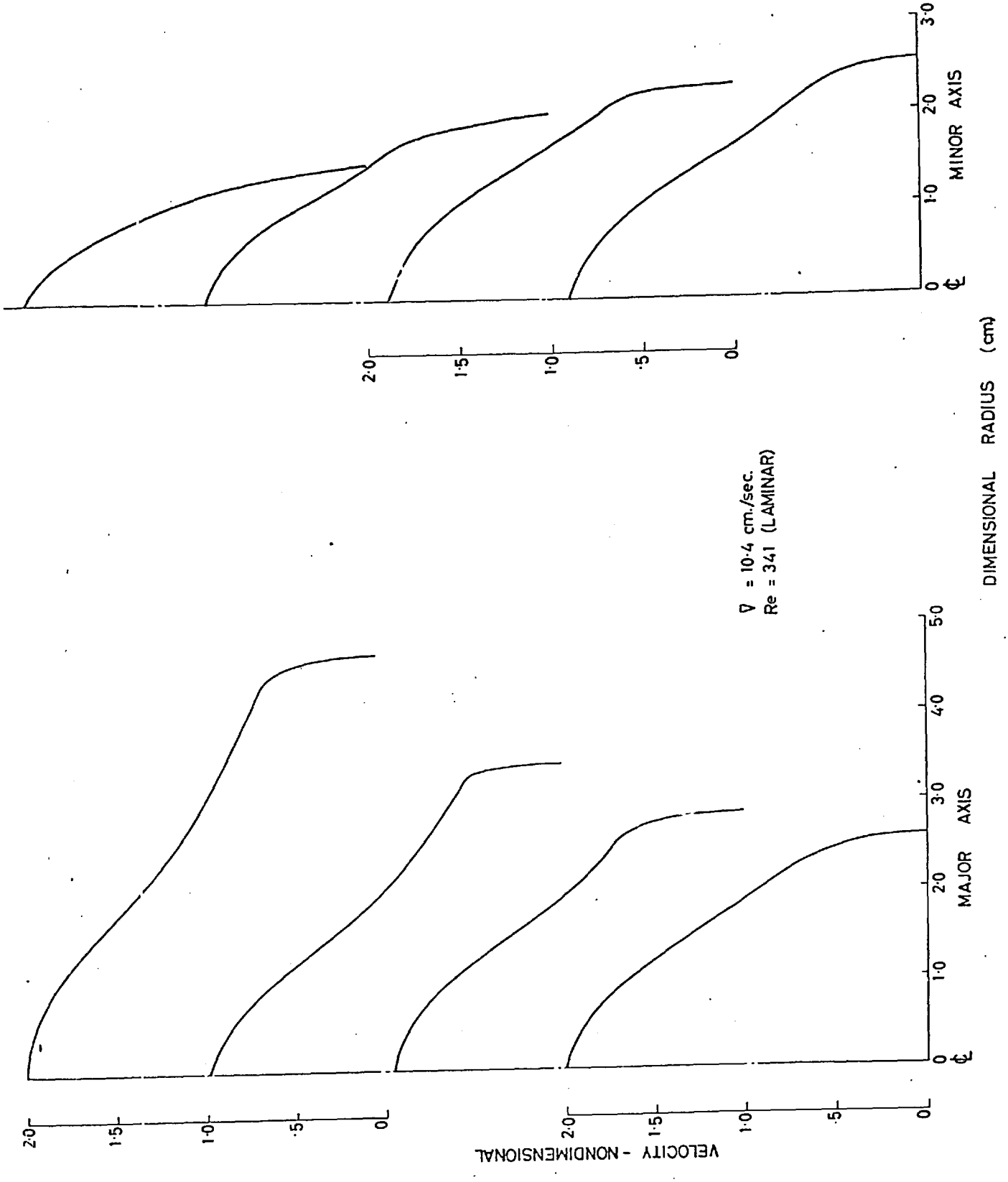


FIGURE 4.8 Primary velocity profiles along axis of tube progressively changing ellipticity. Parabolic velocity distribution at inlet.

The inflection which can be seen developing within the boundary layer on the major axis will eventually lead to separation of the flow from the wall; but as was discussed, this phenomenon was not observed within the axial length of the model used. The magnitude of the Reynolds number has a major influence on the change in the growth rate of the boundary layer at both the major and minor axes. The tendency for separation is also a function of the Reynolds number, but this relation is not simple. If we assume that the tendency for separation is expressed by the magnitude of the inflection of the velocity profile within the boundary layer, then we observe that this inflection has a maximum at a Reynolds number of about 1000, for the specific dimensions of the experimental model used. It would be expected that a direct relationship should be observed between the separation and Reynolds number, and possibly the actual onset of separation is related in such a manner. Our experimental model did not allow investigation into establishing the point of separation, since the flow into the model would not separate from the walls for all the laminar flow conditions studied.

Another prominent feature of the flow with a flat entrance profile is that, for the higher Reynolds numbers, the primary velocity within the core of the flow has only second order effects from the ellipticity. This effect becomes/

becomes more pronounced in the experiments at lower Reynolds numbers. Therefore this observation implies that the potential flow solution put forth in the first section of this chapter is probably more accurate for conditions of the higher Reynolds numbers.

Figures 4.5 to 4.8 show the primary velocity profiles measured within the test model with a parabolic inlet velocity distribution. The profiles, in general, show similar patterns of change as the experiments with flat inlet condition. With the parabolic entrance condition, the inflection of the velocity profile near the wall on the major axis becomes more pronounced than observed with the flat inlet condition. Separation was also not observed with this inlet condition.

Figures 4.9 and 4.10 display the Cartesian components of the secondary flow at three of the four axial positions. The results are shown for two of the five Reynolds numbers and both entrance conditions. The results at these two Reynolds numbers are typical of the measurements at high and low Reynolds number conditions.

In general the secondary velocities are higher (with respect to the mean velocity) for lower Reynolds numbers with a flat inlet velocity distribution. The reverse is true/

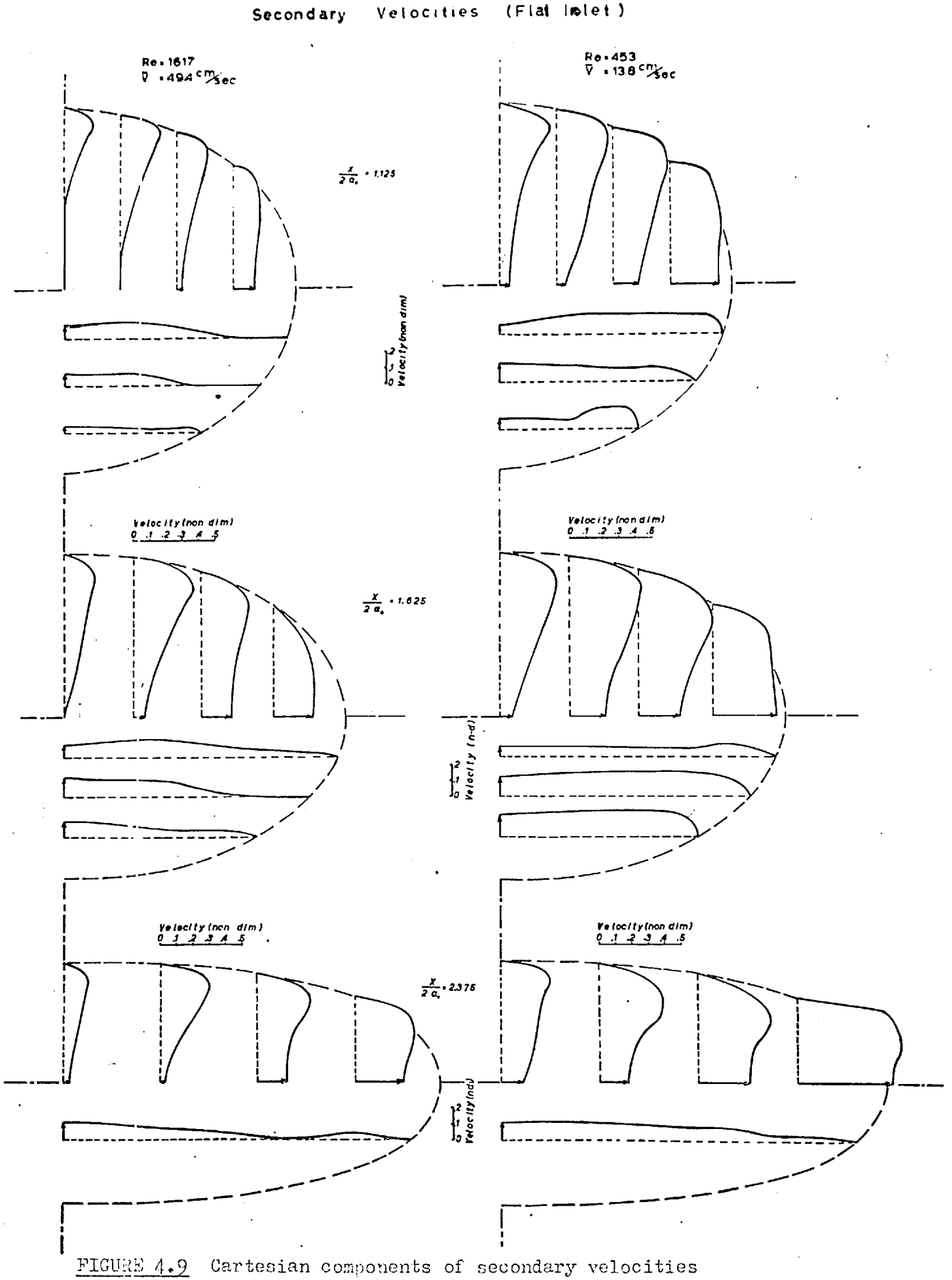


FIGURE 4.9 Cartesian components of secondary velocities within a tube progressively changing ellipticity. Half sections of elliptical tube are shown. Flat velocity distribution at inlet.

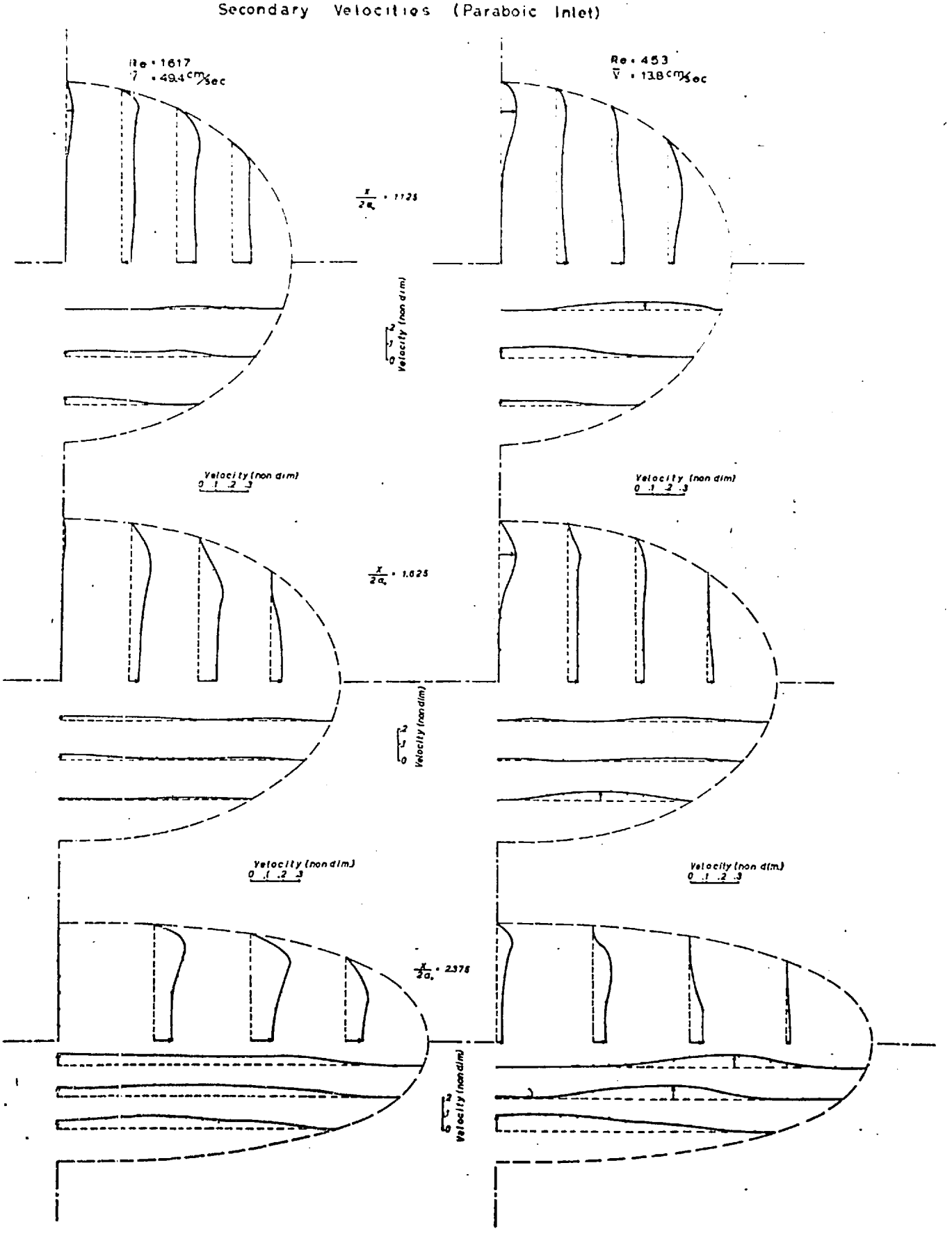


FIGURE 4.10 Cartesian components of secondary velocities within a tube progressively changing ellipticity. Half sections of elliptical tube are shown. Parabolic velocity distribution at inlet.

true for the parabolic inlet, i.e. the nondimensional secondary velocities decrease with decreasing Reynolds number. Further, the nondimensional secondary velocities are, in general, higher for the flat inlet profile than for the parabolic at all Reynolds numbers measured.

The results theoretically predicted in the first section are in fair agreement with the experiments. Comparing the potential flow solution to the experiments with a flat inlet velocity distribution, obvious discrepancies appear near the wall. The experiments imply a secondary velocity distribution which has significant influence from the developing boundary layer, hence the secondary velocity profiles are not flat, as theoretically predicted. The magnitude of the secondary velocity with respect to its position along the major or minor axis of the cross section is well accounted for by the theory. The predicted changes of secondary velocity with axial length is also in line with the experiments. The change in the magnitude of the average secondary velocity with respect to Reynolds cannot be accounted for by the inviscid theory.

The viscous theoretical solution has good comparisons to the experiments conducted with a parabolic inlet velocity distribution. The predictions of the general shape of the secondary velocity profile have good comparison with the experiments, as does the prediction of/

of a lower average secondary velocity in the viscous case than in the potential flow condition. The theory does not, however, explain the dependence of the non-dimensional magnitude of the secondary flow on the Reynolds number. This situation comes about because the parameter, $\epsilon \times$Reynolds, becomes large with some of the experimental conditions, and therefore our expansion solution becomes invalid.

In general we conclude that the theoretical solutions predict the experimental observations of the general direction of the secondary motions, the relative magnitude of the secondary velocities, and the effect of the secondary velocities on the axial velocity distribution.

Measurements of velocity gradients at the walls on the major and minor axis

Figure 4.11 displays the velocity gradient projected to wall from velocity measurements within the viscous boundary layer. In general the velocity gradients follow the changes in boundary layer thickness shown in Figures 4.3 to 4.8. This "wall shear" distribution shows similar trends at all Reynolds numbers and entrance conditions measured. The shear on the minor axis increases in an approximately linear relation with axial distance; the slope of increase related to the Reynolds number. The shear against the wall of the divergent major axis at first/

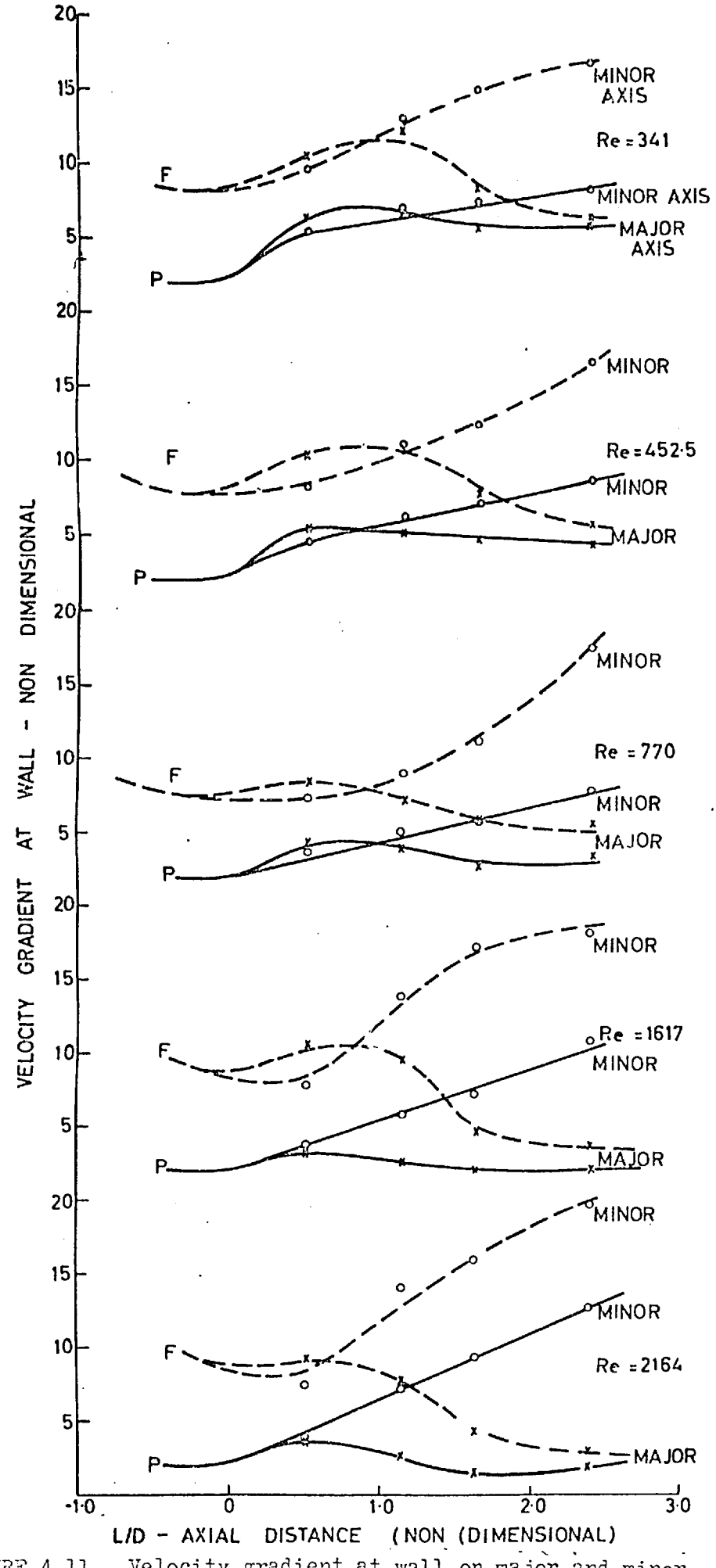


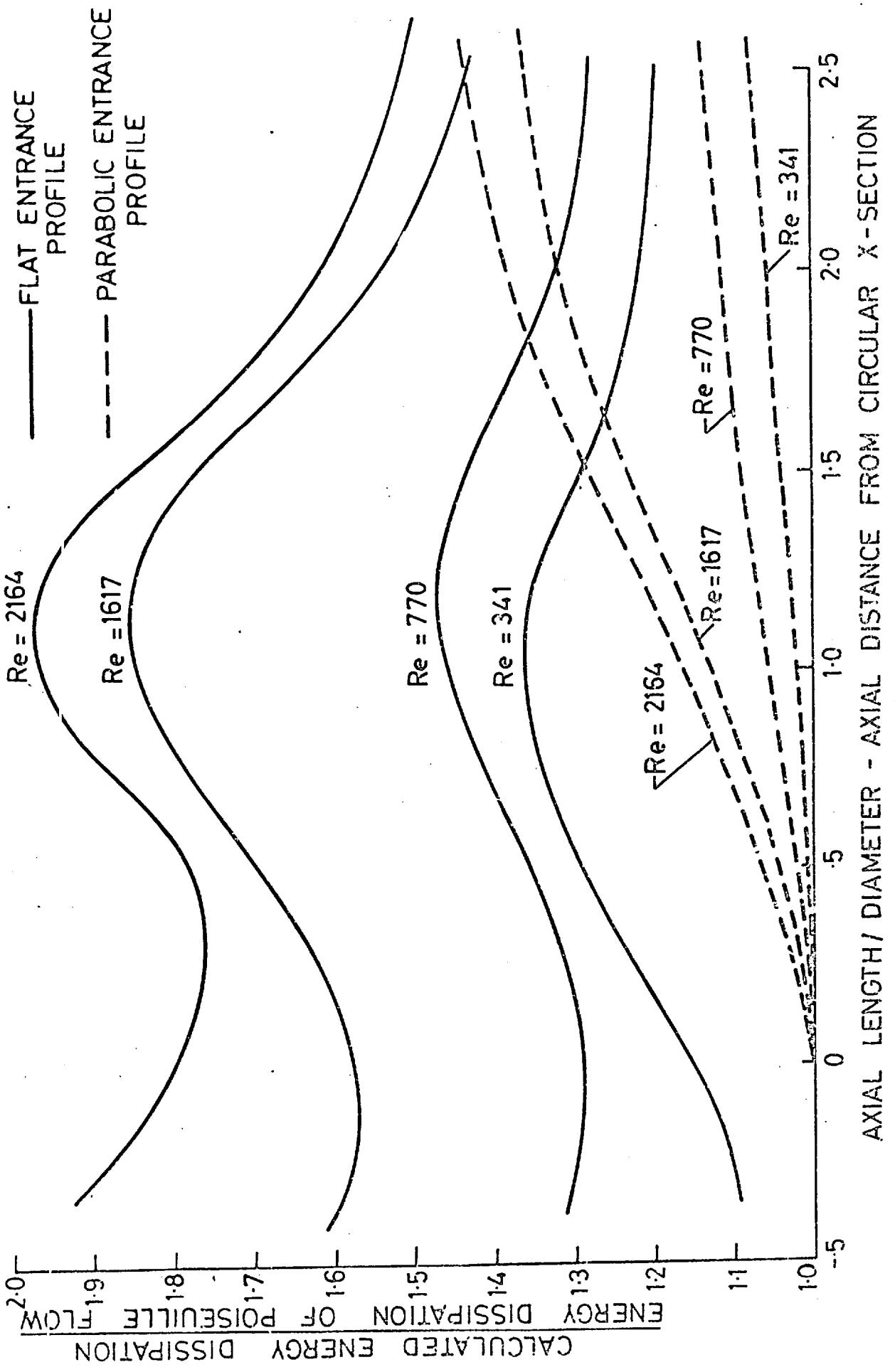
FIGURE 4.11 Velocity gradient at wall on major and minor axis. Dashed line indicates flat velocity distribution at inlet; solid line indicates parabolic velocity distribution at inlet.

first increases, then decreases sharply for the flat entrance condition. The reasons for the initial increase in shear at this location are not known; possibly the secondary currents, forcing fluid against the wall at the major axis, may cause this effect. The shear on the walls of the major axis for the parabolic condition shows a similar relation to axial distance as the flat inlet condition. The parabolic condition differs from the flat entrance condition in that after one diameter of axial distance, there is less of a decrease in shear against the outer wall.

Energy dissipation rate

The dissipation function was numerically evaluated, as discussed in Chapter 3. The calculated energy dissipation rate follows the boundary thickness (or wall shear) for the flat entrance profile condition, in that at first an increase in energy dissipation is predicted up to an axial distance of one diameter. After this location the rate of energy dissipation decreases rapidly. This rate of decrease in calculated energy dissipation after one diameter is faster than predicted for an equivalent axial position of an entrance flow into a straight circular tube. This implies that the divergent walls (at the major axis) are promoting boundary layer development at a faster rate than the convergent walls (at a minor axis) are/

FIGURE 4.12 Ratio of energy dissipation calculated from measured velocity distribution in elliptical models to energy dissipation in Poiseuille flow.



are retarding boundary layer development. The parabolic entrance condition also follows the wall shear observations, but in this case the shear on the walls of the major axis shows little change after 1.25 diameters of axial length. Therefore the energy dissipation rate increases linearly similar to the wall shear on the minor axis.

Moments of velocity distribution and kinetic energy

The moments and kinetic energy factor are shown in Table 4.2. As in the studies conducted within the curved tubes, the changes in kinetic energy are small compared to the viscous energy dissipation.

The moments are of less interest than the curved tube data. The second moment indicates the spread of the mass flow and therefore shows how rapidly the distribution of mass flow responds to the changes in tube shape; this index is, however, not a direct indication. The first moment is forced to zero from our assumption of symmetry in the flow field. The moments are included for quantitative comparison to the data in the regions of the bifurcation models, which correspond to a tube with changing ellipticity.

Conclusions

In this chapter we have theoretically and experimentally studied/

studied the three dimensional flow patterns in tubes which are originally circular and progressively become elliptical. The theoretical predictions of secondary velocities made for potential and viscous flow conditions show that the direction of secondary flow streamlines originates from the wall on the minor axis and moves toward the wall on the major axis. This pattern of streamlines, which are not closed, is a consequence of the changing cross sectional shape of the tube and occurs at all Reynolds numbers for both viscid and inviscid conditions. Experimental studies compare favourably with these predictions.

The boundary layer thickness and shape, along with the wall shear and energy dissipation rate, all show changes with axial distance which can be explained by the effects of the divergent and convergent walls on the flow, with modifications from the secondary flow.

TABLE 4.2

MOMENTS AND KINETIC ENERGY FACTOR
FOR FLOW ENTERING AN ELIPTICAL TUBE

Position	Moments of Velocity Distribution First	Second	Third	Kinetic Energy Factor	Reynolds Number	Average Velocity (cm/sec)
Flat Inlet Profile					2164 (Laminar)	66.1
L/D = 0.5	0	.654	0	1.243		
1.125		.663		1.178		
1.625		.645		1.287		
2.375		.636		1.368		
Parabolic Inlet Profile						
L/D = 0.5	0	.589	0	1.841		
1.125		.599		1.761		
1.625		.599		1.890		
2.375		.605		1.868		
Flat Inlet Profile					1617	49.4
L/D = 0.5	0	.649	0	1.274		
1.125		.659		1.202		
1.625		.644		1.305		
2.375		.634		1.384		
Parabolic Inlet Profile						
L/D = 0.5	0	.579	0	1.967		
1.125		.589		1.871		
1.625		.587		1.979		
2.375		.595		1.971		

Profile					770	23.5
L/D = 0.5	0	.638	0	1.331		
1.125		.645		1.280		
1.625		.624		1.446		
2.375		.620		1.501		
Parabolic Inlet Profile						
L/D = 0.5	0	.580	0	1.994		
1.125		.585		1.928		
1.625		.578		2.110		
2.375		.586		2.002		
Flat Inlet Profile					453	13.9
L/D = 0.5	0	.634	0	1.350		
1.125		.638		1.312		
1.625		.622		1.451		
2.375		.619		1.499		
Parabolic Inlet Profile						
L/D = 0.5	0	.598	0	1.780		
1.125		.600		1.738		
1.625		.596		1.815		
2.375		.601		1.750		
Flat Inlet Profile					341	10.4
L/D = 0.5	0	.639	0	1.305		
1.125		.645		1.257		
1.625		.630		1.382		
2.375		.626		1.435		
Parabolic Inlet Profile						
L/D = 0.5	0	.607	0	1.643		
1.125		.616		1.541		
1.625		.610		1.630		
2.375		.610		1.617		

L E G E N D

L/D is distance downstream from Tube origin.

CHAPTER 5

Flow within model bifurcations of the human pulmonary system

In this concluding chapter the three dimensional velocity field is measured in models of biological bifurcations. Information from each of the previous chapters is drawn upon. The models were constructed to mimic the biological configuration discussed in Chapter 1. The pulsed probe developed in Chapter 2 was used for the measurements. Understanding of the flow properties experimentally found in the bifurcation is promoted by comparing the results of these experiments to the results and analyses of Chapters 3 and 4.

Six model bifurcations are studied with laminar flow over a range of Reynolds numbers and with two differing entrance conditions. The models are systematically varied to incorporate the biological variation discussed in Chapter 1. It is not, however, attempted to catalogue all the intricacies of the flow properties found within the sixty differing experimental conditions. The primary purpose of the study is to understand the physical bases for the phenomena observed in the models. Therefore this chapter will present the complete set of measurements for only one experimental condition (the most typical, biologically, of the symmetrical bifurcations) and relate all/

all the other experimental conditions to this.

The results discussed in this chapter are completely experimental. No attempt is made to develop quantitative theoretical arguments, nor can any such arguments be found in the literature for the range of flow conditions of interest in the bifurcations.

We shall show that the flow properties within a bifurcation are determined from a complex interaction of the elliptical transition zone, curvature of the daughter branch, and a new boundary layer developing on the flow divider. The most prominent influence is that of the flow divider.

The pattern of secondary flow in the elliptical transition region of the bifurcation is in general similar to those found in the elliptical models of Chapter 4. Likewise the general pattern of secondary flow within the curvature of the bifurcation is at first similar to the curved tube studies of Chapter 3. The secondary flow progressively deviates from the patterns expected within curves, as the fluid moves downstream from the flow divider.

In general the primary velocity field within the first few diameters of axial length from the flow divider has the same basic distribution for all the bifurcations studied, although significant differences are found in the/

the flow stability and separation from the walls. The primary velocity distribution at distances of over two diameters downstream from the flow divider shows a dependence on curvature and bifurcation angle.

The secondary flow field also shows a basic pattern which can be observed in most of the experimental conditions. The secondary flow, however, shows less uniformity between experimental conditions than does the primary flow at axial location near the flow divider.

The energy dissipation, moments, total kinetic energy and static pressure distribution are calculated from the measured velocity fields.

Introduction

The study of flow patterns within branching systems, which attempt to mimic flow conditions within the body, has some highly interesting historical developments. Leonardo da Vinci, in about 1500, conducted experiments on branched channel flow for biological application. Da Vinci sketched (beautifully, of course) the flow patterns in his experiments which clearly show the division of the fluid stream into the two branches, an eddy formation on the surface of the flow divider, gradual disappearance of the large eddy as it moves downstream, and separation at the inner wall of curvature (which was sharp/

sharp for the experiment sketched), along with reattachment at a downstream position. This sketch, which can be found in Rouse & Ince (107), generally describes some of the principal fluid mechanic phenomena which can potentially develop at a branch point. Several other such observations concerning branch points in rivers or channels can be found in the historical literature (107). Within the past twenty years, several ad hoc studies (108, 10, 11, 12) were produced to understand the flow at a specific branch point within the cardiovascular or pulmonary system. More recently, the effects of branch points upon pressure wave reflections (33) or upon flow stability (109) has been investigated. More general investigations of the flow properties within a branched tube have recently been reported (26, 34, 110, 111, 112, 113, 114). Lew's (26) theoretical investigation neglected the inertial terms in the equations of motion to solve for the primary and secondary velocity distribution in a two dimensional channel bifurcation. The flow was thus restricted to Reynolds numbers in the range of 10^{-1} to 10^{-2}.

Naumann (113) and Zeller (114) conducted experimental studies on large scale model bifurcations with laminar flow for a range of Reynolds numbers from 400 to 1100 under steady and pulsatile conditions. Like Eustrice's original observations in curved tubes, Naumann and Zeller used coloured dye streams to describe the basic pattern of/

of flow. They found a secondary velocity component developing just downstream from the flow divider and then dying away after a few diameters. The pattern of secondary currents observed in this manner were similar in direction to fully developed curved tube flow. Separation was apparent in some of their studies. Strong components of secondary flow in the transition zone of the bifurcation was also apparent in some of the experiments. These secondary currents originated from the separated region on the inner wall of curvature at one side of the bifurcation, and moved within a tangential boundary layer, upstream and tangentially, arriving at the inner wall of curvature on the opposite side of the bifurcation. These complicated patterns of secondary flow probably resulted from the combined influence of the stagnation point at the edge of the blunt flow divider and the two areas of separation, at each inner wall of curvature (see Figure 5.1). Such highly complex flow patterns may be expected to occur when the higher pressure region around the stagnation point at the edge of the flow divider is in close proximity to the low pressure region created by separation at two inner walls of curvature. Such complex flow patterns have often been observed (109, 115) and are usually erroneously attributed to the onset of instabilities. The results of these studies point out the fact that the transition region is very important in determining the secondary flow patterns, especially if prominent stagnation and separation/

separation regions exist and are in close proximity.

The velocity field has been measured in model bifurcations by Schroter & Sudlow (110) and Schreck & Mockros (111). Schroter & Sudlow used hot wires to determine the velocity profiles in the plane of the bifurcations and normal to the plane for symmetrical bifurcations with a sharp flow divider, a total branching angle of 70° and a sharp curvature. They also used smoke streams to visualise the secondary currents; showing a secondary flow pattern downstream from the flow divider which was similar in direction to the secondary flow in fully developed curved tube flow conditions. At the inner wall of curvature they also showed separation occurring. Schreck and Mockros also used hot wires to measure the velocity profiles at each $\pi/4$ position to determine the velocity contours in a series of bifurcations. Schreck & Mockros' models were similar to the ones used by Schroter and Sudlow, but they used two symmetrical branching models with total branching angles of 42° and 80°. The occurrence of separation in their models was probable, but no mention was made of such a phenomenon occurring. The velocity distributions obtained by Schreck & Mockros were in general similar to the measurements of Schroter and Sudlow. Further, Schreck and Mockros found little change in the velocity distribution within either of the models studied.

The/

The studies of Schreck and Schroter could only give an approximation to the primary velocity distribution. This is because the components of secondary velocity cause a combined pitch and yaw on the single hot wire distorting the measurement. The experiments reported in this chapter attempt to extend these previous studies by describing each component of the three dimensional velocity field within a set of bifurcations which do not create separation at the inner wall of curvature. Further, the region of high static pressure caused by the stagnation point at the edge of the flow divider is small for the bifurcations used in our studies. Thus the patterns of secondary currents should have minimum influence from these areas of high and low pressure. This seems to be the condition in the biological system.

Experimental techniques

Experiments were carried out within bifurcations constructed from Perspex and produced by milling two half sections along a prescribed pattern. The models produced in this manner have a 2 inch diameter parent tube, and 1.5 inch diameter daughter tubes (for the symmetrical models). The transition zone within the parent tube was milled such that the cross section changed shape from circular to elliptical in the same manner as discussed in Chapter 1, and identical to the internal dimensions of the/

the first 1.75 diameters of the models used in Chapter 4. After 1.75 diameters the area increased by 13% in the same manner as found in the pulmonary airways. At the origin of the daughter tubes (the location of the flow divider) each daughter branch had a 1.5 inch diameter and was circular in cross section; this shape and diameter was maintained throughout the length of the daughter tubes. The half sections were bolted together and slots or holes were milled into the model for access of the probes.

Figure 5.1 shows the 70° symmetrical bifurcation with curvature ratio of the daughter tube equal to the mean value found in the pulmonary airways; i.e. $^{9}/_{R} = {}^{1}/_{7}$. Figure 5.2 shows the axial variation of diameter in a plane perpendicular to the plane of the bend (defined as vertical). As can be seen, this vertical length decreases within the transition region of the parent tube, as described in Chapter 1. Figure 5.3 is a view along the axis of the parent branch at the flow divider, showing that the flow divider is sharp at the plane of bifurcation and becoming more blunt near the upper and lower walls of the tube. This figure can be compared with Figure 1.9 and 1.8 of Chapter 1, which is the same view within the lung.

The positions of measurement are shown in Figure 5.1 as/

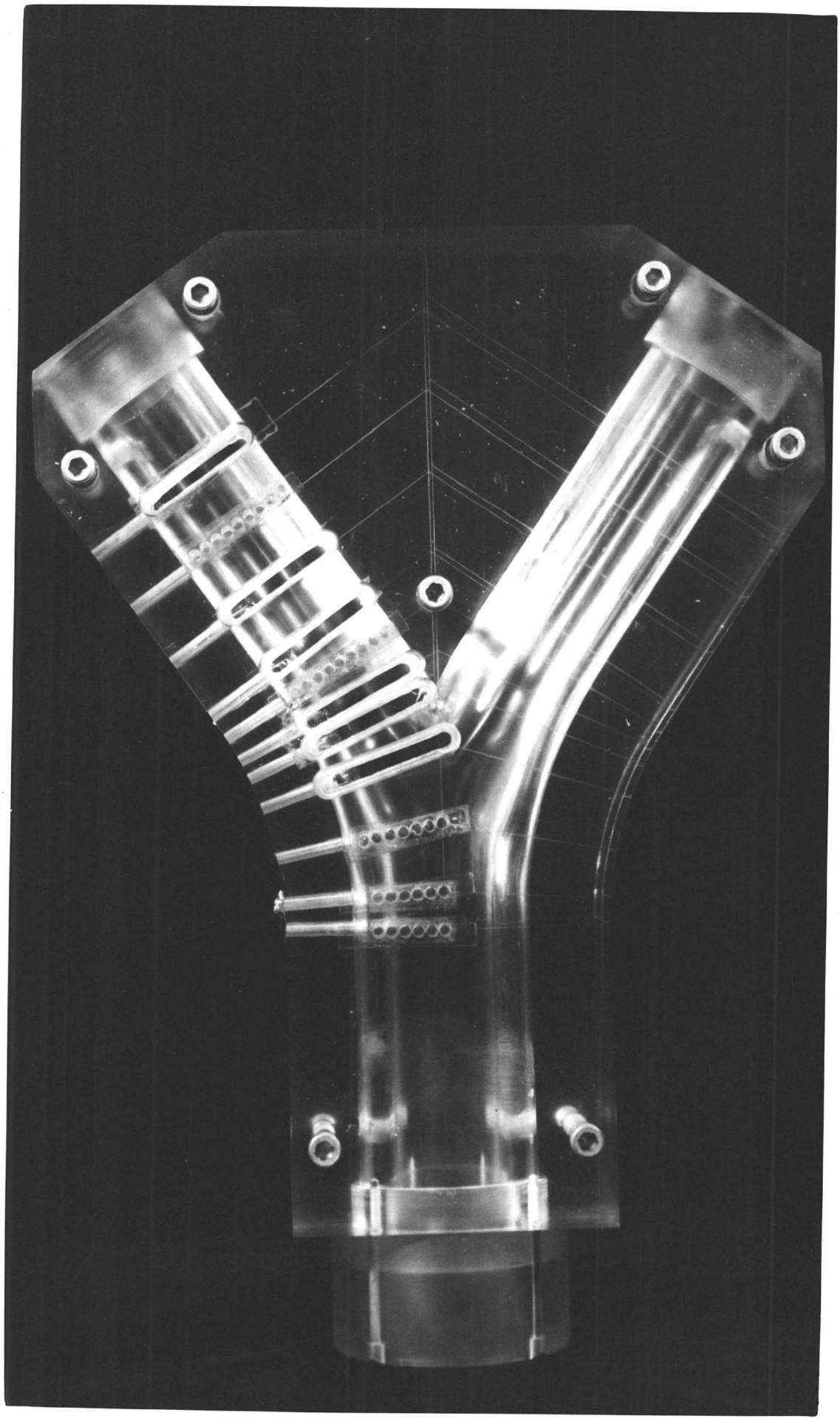


FIGURE 5.1 Bifurcation of Model 1, 70° total branching angle symmetrical daughter branches. Positions of measurement are the slats or holes in the wall of the model.

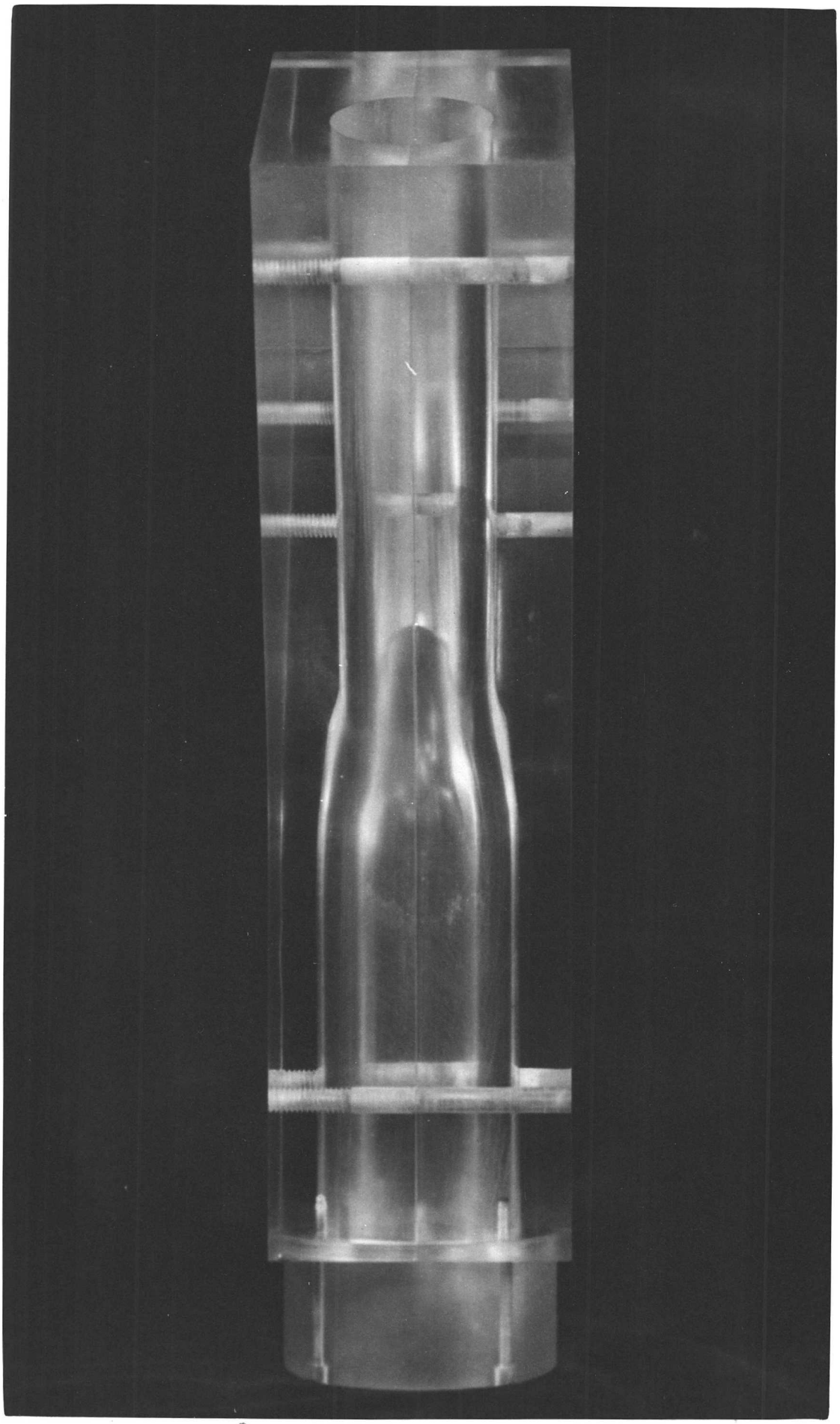


FIGURE 5.2 Axial variation of minor axis within transition zone of bifurcation.

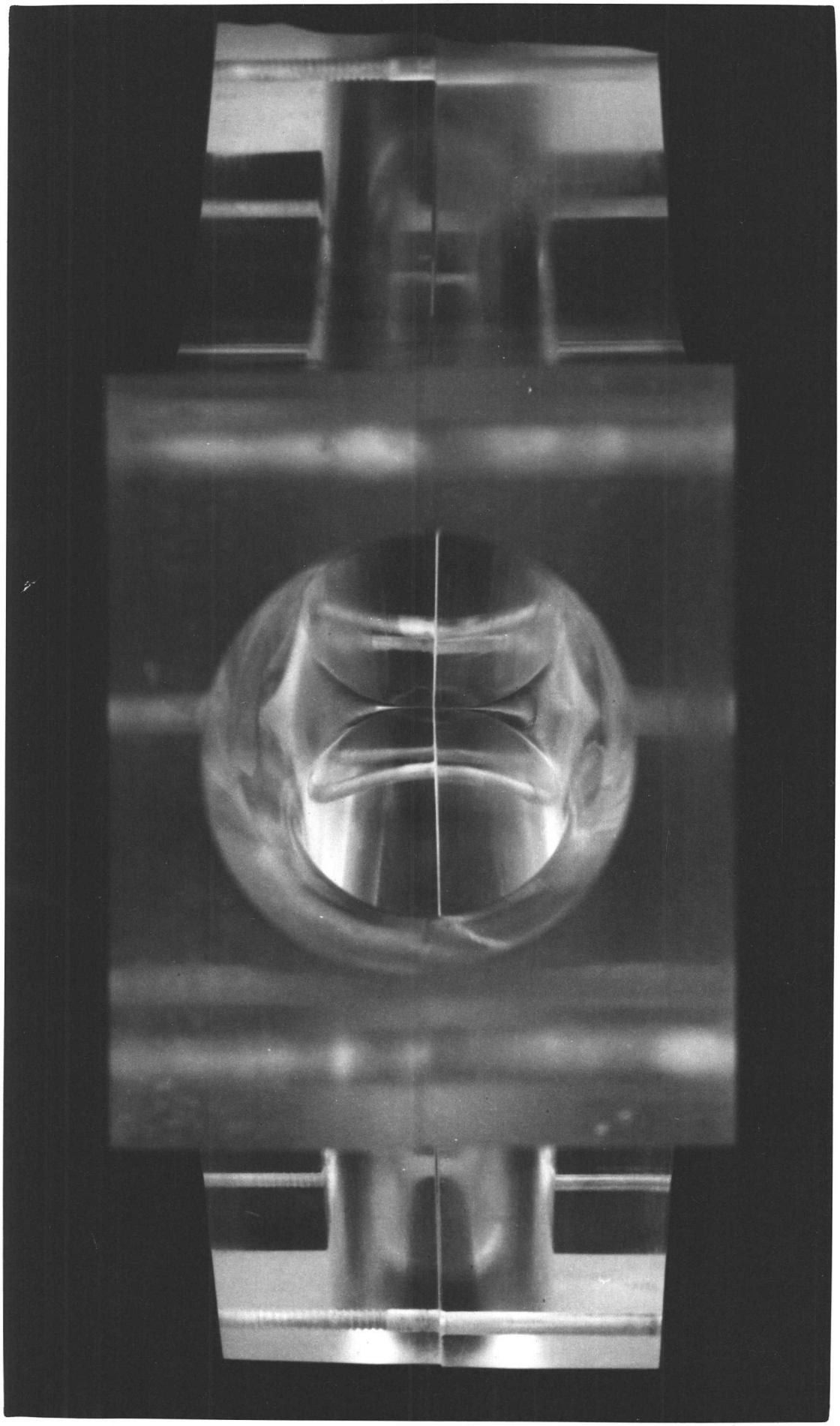


FIGURE 5.3 Shape of flow divider. This can be compared with Figure 1.9.

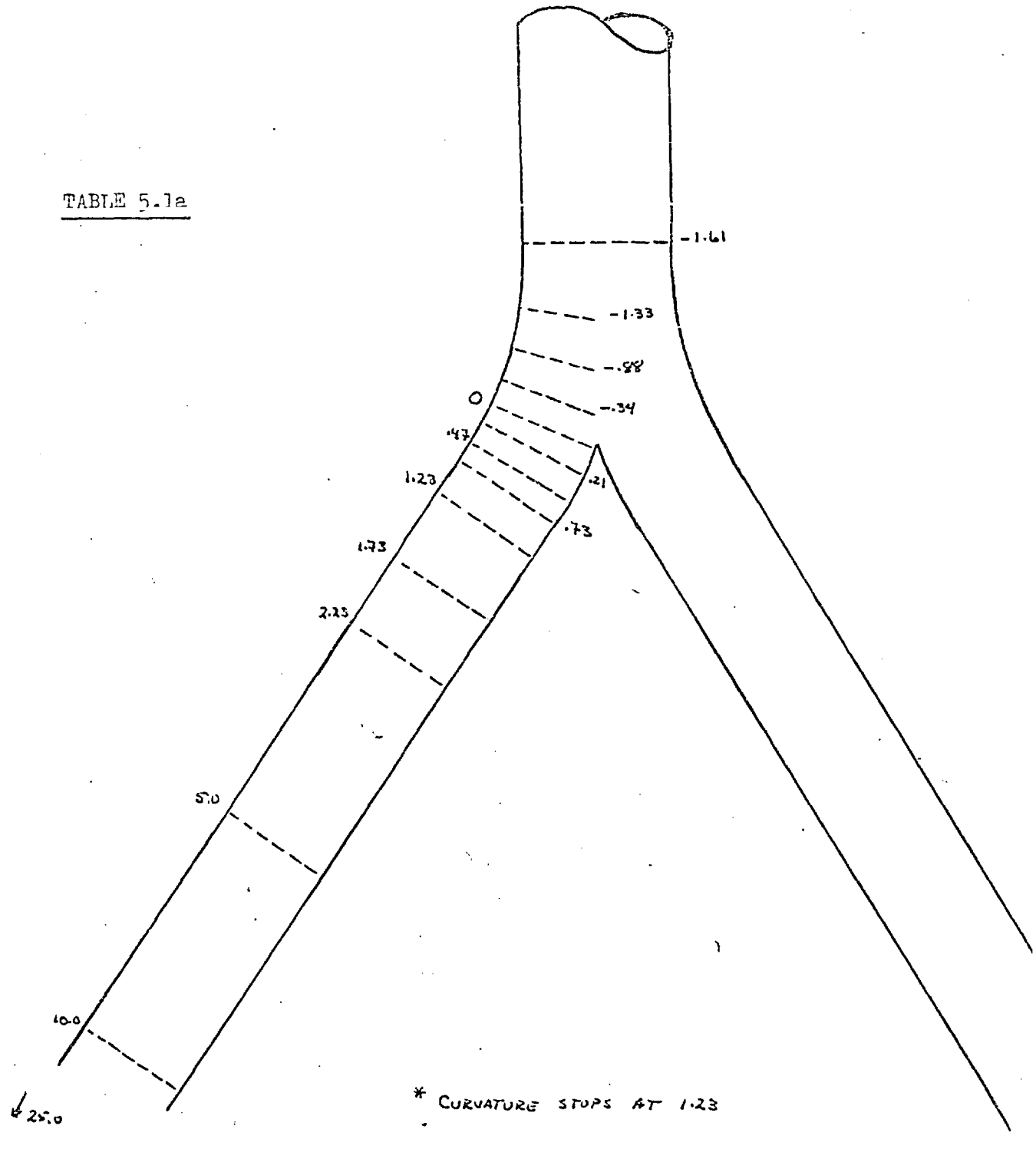
as the milled slots into the tube. Frequent measurements were taken near the location of the flow divider. Less frequent measurements were taken after two diameters downstream from the flow divider; the last measured position being 25 diameters downstream. Table 5.1a indicates the positions of measurement, relative to the axial position of the flow divider. Table 5.1b shows the Reynolds number of both parent and daughter tube along with the Dean number within the daughter tube. At each flow rate, a flat and a parabolic entrance velocity profile was produced in the same manner as for the experimental studies of Chapters 3 and 4.

The other five bifurcations used were studied under the same flow conditions but measurements were taken only at axial positions of -0.5, 0, 1.0, and 2.0 diameters from the flow divider. Each of the bifurcations varied in their geometry as shown in Table 5.1c, five of the six bifurcations had equal daughter branches; the sixth was asymmetric, as shown in Figure 1.6. Straight tubes of over 40 diameters in length were attached to the distal end of each branch. These outruns are required so that the flow splits equally into the two daughter branches of the symmetric bifurcations.

The same measurement and data handling techniques were used in the circular curved daughter branches as was used in the curved tube studies of Chapter 3. Likewise the/

TABLE 5.1a

AXIAL POSITIONS OF MEASUREMENT
L/D
-1.61
-1.33
-0.88
-0.34
0
+0.21
+0.47
+0.73
1.23*
1.73
2.23
5.0
10.0
25.0



* CURVATURE STOPS AT 1.23

TABLE 5.1b

EXPERIMENTAL FLOW CONDITIONS

Mean Velocity (Parent tube) [redacted]	Reynolds Number (Parent tube)	Mean Velocity (Daughter tube) (cm/sec)	Reynolds Number (Daughter tube)	Dean Number (Daughter tube)
66.1	2235	58.7	1495	690
49.4	1670	43.9	1115	515
41.4	1400	36.7	935	430
23.5	795	20.8	530	244
13.8	468	12.2	311	143
10.4	352	9.2	234	108

TABLE 5.1c

GEOMETRIC CONFIGURATION OF MODELS STUDIED

Model	Total Branch Angle	Diameter of Daughter tube cm.	Curvature Ratio a/R
1	70°	1.5	1/7
2	90°	1.5	1/7
3	50°	1.5	1/7
4	70°	1.5	1/14
5	90°	1.5	1/14
6 *	50° and 90°	1.25 and 1.75	1/5 and 1/16

* Asymetrical Bifurcation

the same techniques were used for the measurements and analysis in the elliptical transition zone of the parent tube as was used in the elliptical tubes of Chapter 4. Further, the same parameters are used to nondimensionalise the measurements in the bifurcations as was used in Chapters 3 and 4. Therefore the mean velocity and radius in the parent branch are used to nondimensionalise the velocities and radial lengths measured in the parent tube. Also the mean velocity and radius in the daughter tubes are used to nondimensionalise the measurements taken in these tubes. This choice of parameters to nondimensionalise the data facilitates comparison of the velocity fields measured in the bifurcation to those measured in the elliptical and curved tubes. These multiple nondimensional parameters cannot, of course, be used when displaying the energy dissipation calculations or the wall shear measurements as a function of axial position throughout the bifurcation. Therefore the radius and mean velocity in the daughter tubes were used to nondimensionalise the data for these displays.

Results/

Results

Primary velocity distribution in model 1

Figure 5.4 displays the contours of equal primary velocity at a flow condition of Reynolds = 660, with a flat entrance velocity profile. These contours are typical of the primary velocity field found in all the experiments. The basic features of the distribution are that the high velocity is toward the outer wall of curvature (or inner wall of the bifurcation), and with increasing axial distance down the daughter tube the "wing-like" features of the contours become evident. This is similar to the conditions found with a parabolic entrance profile in the experiments within curved tubes of Chapter 3.

Figure 5.5 and 5.6 show the primary velocity profile in the plane of the bifurcation for four of the five flow rates with a flat velocity profile at entrance to the parent tube. In general the profiles show similar trends for all Reynolds numbers and curvatures. The first four profiles are from the elliptical transition zone within the parent tube (Figure 5.1). The velocity distributions taken in this area of the bifurcation are not directly comparable to the velocity distributions taken within the elliptical models. This is because the plane of measurements in the elliptical models was perpendicular to/

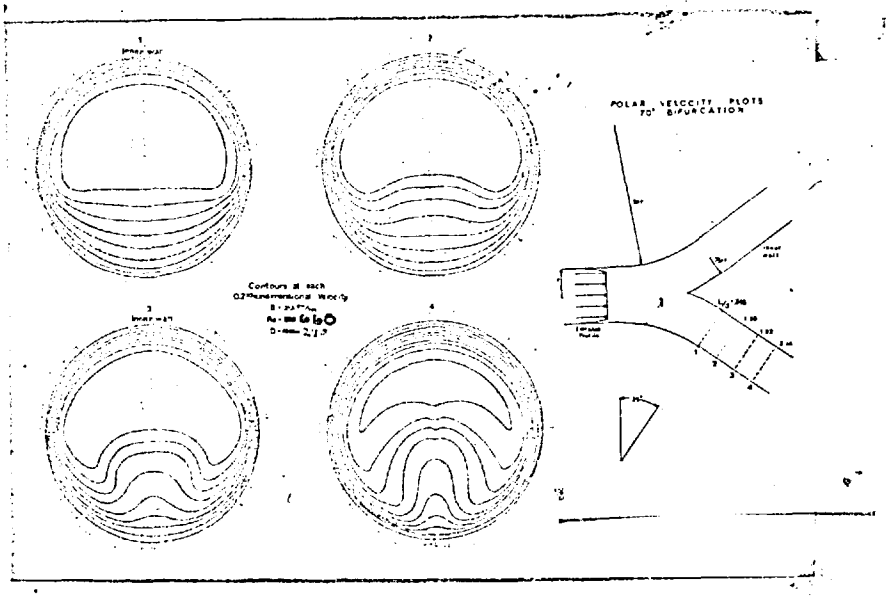


FIGURE 5.4 Velccity contours measured in Model 1 at indicated positions. Re = 660 K = 290 Each contour is at 0.2 nondimensional velocity. Flat velocity dictribution at inlet.

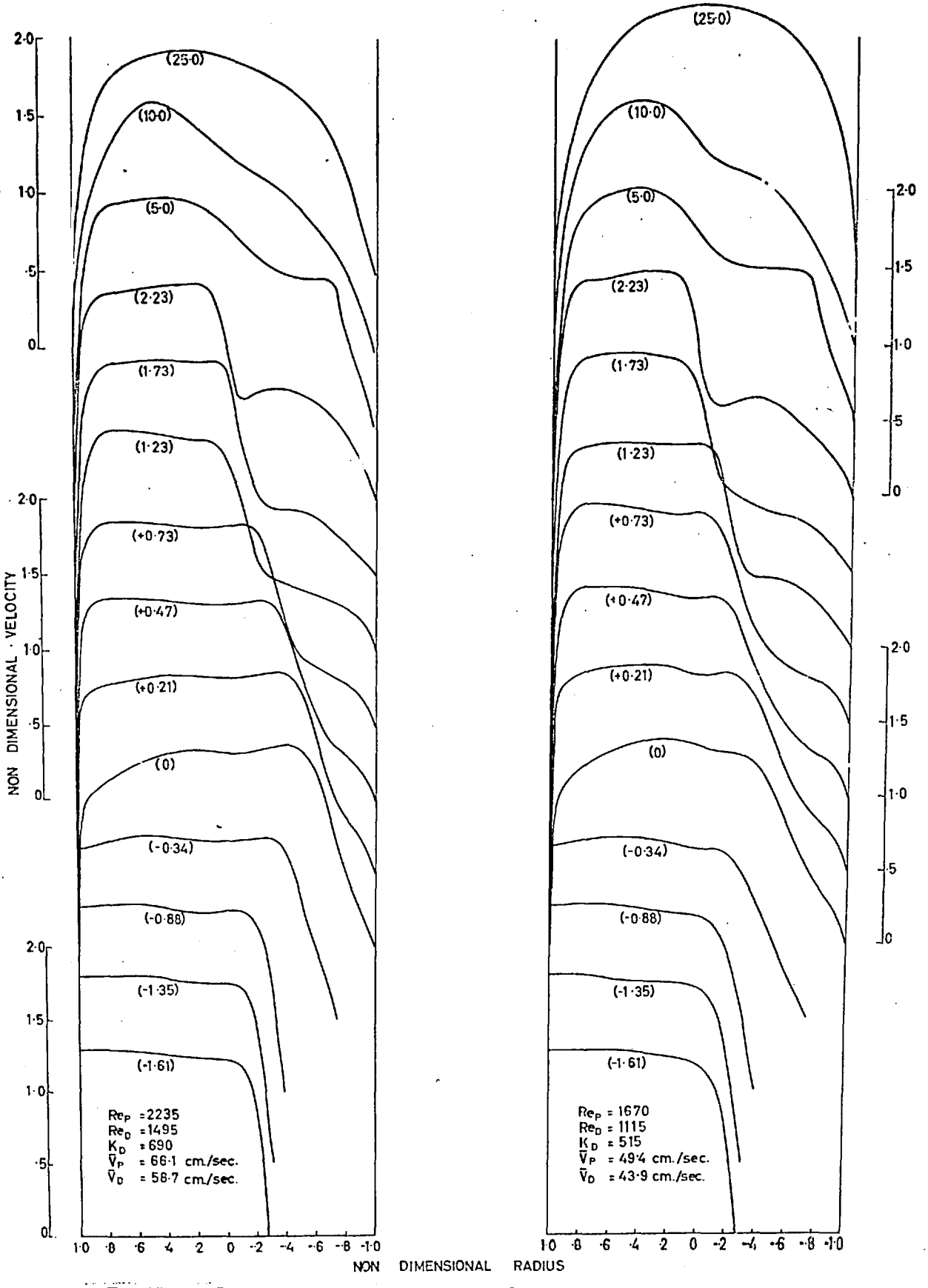
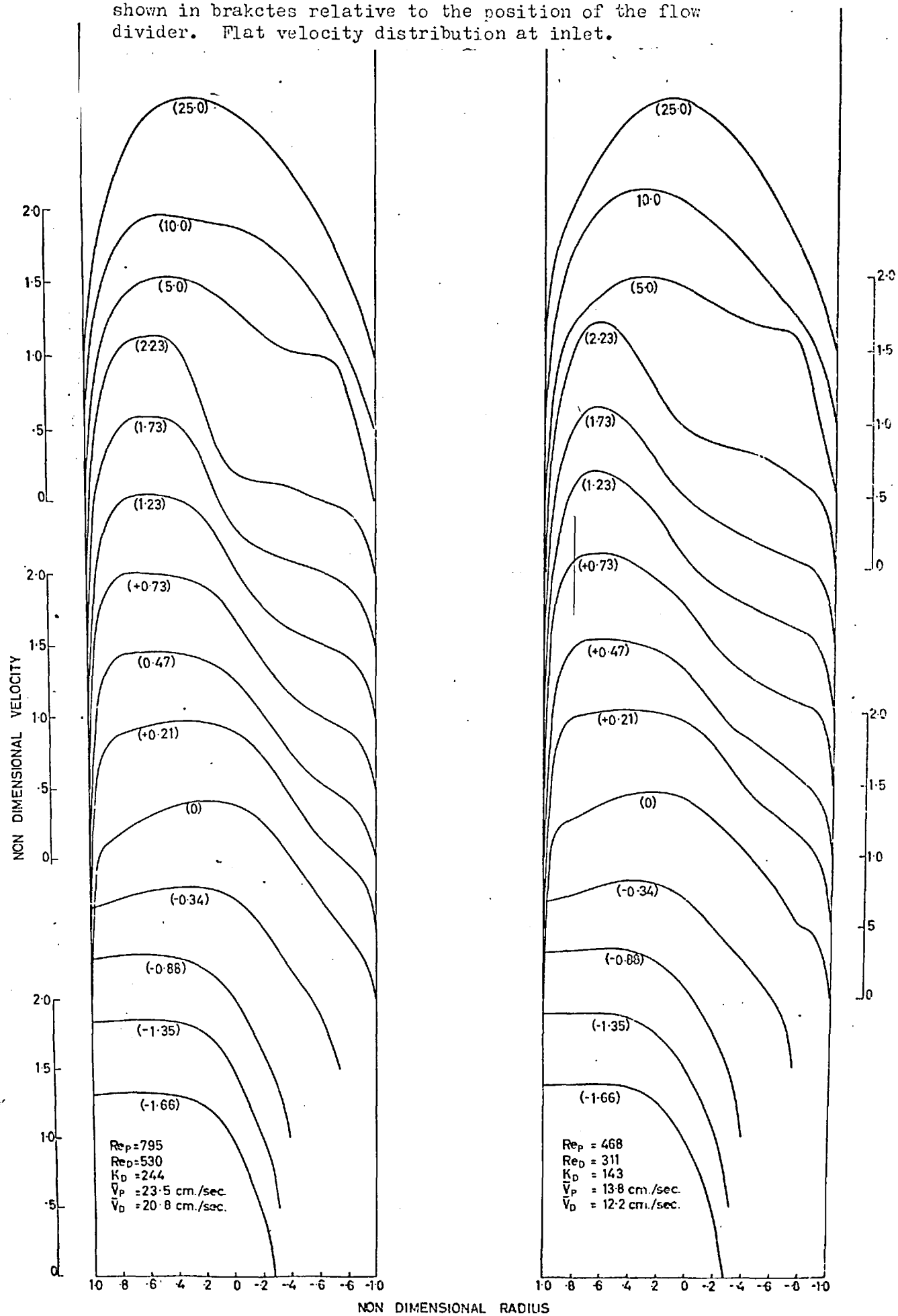


FIGURE 5.5 Primary velocity profiles within plane of bifurcation. Measured in Model 1 at axial diameters shown in brackets relative to the position of the flow divider. Flat velocity distribution at inlet.

FIGURE 5.6 Primary velocity profiles within plane of bifurcation. Measured in Model 1 at axial diameters shown in brakctes relative to the position of the flow divider. Flat velocity distribution at inlet.



to the axis of the tube, while the plane of measurement in the bifurcations was taken perpendicular to the outer wall (and thus normal to the projected axis of curvature shown in Figures 1.6 and 5.1). Comparisons between the two sets of measurements can be made for the primary velocity fields without great errors, but the compensation must be made when comparing the secondary velocity fields. As shown in the studies of Chapter 4, the boundary layer develops on the wall at the major axis at a faster rate than for a straight tube and the boundary layer development is retarded on the wall of the minor axis. The effects of viscosity in determining the boundary layer thickness and the core flow velocity distribution, rapidly become prominent at the lower Reynolds numbers in both the elliptical areas of the bifurcation and in the studies of Chapter 4. The profiles in this region show good comparison to the primary velocity distribution found within the first 1.75 diameters of axial length in the elliptical tubes studied in Chapter 4. The velocity distribution at -0.34 diameters (upstream) from the flow divider shows the effects of the upstream stagnation point at the edge of the flow divider. This effect becomes more prominent at lower Reynolds numbers (as would be expected for the flow just upstream from the stagnation point on a "bluntish" wedge).

The/

The velocity distribution entering the daughter tubes (axial length of (O)) with higher Reynolds numbers shows a potential flow skew toward the inner wall of curvature, as was noted in the curved tube experiments with higher Reynolds numbers and flat entrance conditions. The situation in the bifurcation experiments is similar for the high Reynolds numbers and a flat entrance velocity profile because the velocity distribution retains its flat shape through the elliptical area. Further, the effects of the new boundary layer development upon the flow divider are far removed from the inner wall of curvature where the skew is developed. At lower Reynolds numbers, or with a parabolic velocity distribution at entrance, the skew is not present. This is simply because the primary velocity distribution is strongly modified from the original flat shape at lower Reynolds numbers, while the distribution is never flat with a parabolic velocity distribution at inlet.

A region of low velocity fluid is developed at the inner wall of curvature downstream from the flow divider. This region shows a similar primary velocity distribution to the comparable area in the curved tube experiments. The development of a double humped appearance is an expression of the extent of the "winged shape" appearance of the velocity contours. These are developed from the large tangential components of secondary flow convecting the/

the high velocity fluid elements from the outer wall of curvature circumferentially around the tube to the inner wall of curvature. A somewhat unexpected result is that this humped shape development continues past the curvature region of the daughter tube into the straight region. This change from a curved to a straight tube takes place at the 1.23 diameter axial position within the example model used for demonstrating the flow parameters (Model 1 of Table 5.1c). At an axial length of five diameters downstream from the flow divider the flow patterns originating from the bifurcation are decaying. By 25 diameters the flow is approaching the fully developed laminar condition for Reynolds numbers in the daughter tube below 1000.

Instabilities in the flow downstream from the flow divider with laminar flow input into the models

Above Reynolds numbers of 1000 a very interesting development of instability is found. Two distinctly different types of flow instability are found. One source of instability arises from the precision symmetry of the models and occurs at low Reynolds number conditions. The other instabilities come from vortices being shed off the flow divider at high Reynolds numbers. The instability at low Reynolds numbers occurs when the resistance to flow within one arm of the bifurcation is transiently/

transiently affected by a random occurrence in the atmosphere at the termination of the long outruns or from a fluctuation in the flow input. At low Reynolds numbers the pressure drop is small within the outruns, which are 40 diameters in length. Thus significant changes in the sink pressure can affect the distribution in flow between each branch of the bifurcation. With a bifurcation which is highly symmetric, a temporal asymmetric distribution of flow caused an oscillatory condition of the flow into each branch, which is only slowly damped. Therefore extreme caution must be undertaken to preserve a uniform flow into the model with a symmetric velocity distribution at entrance and also avoiding differences in the sink pressure between each branch of the model.

The region of instabilities caused by the probable vortex shedding from the flow divider can be easily detected by the pulsed probe, which is very sensitive to temporal or direction changes of the total velocity. These instabilities are only observed within a distinctly defined space. The region of instable flow is in the shape of a cone whose axis is parallel to the axis of the tube and is about 0.8a from the centre line of the daughter tube toward the outer wall of curvature. The first observance of instabilities (the point of the cone) comes at about two diameters downstream from the flow divider

a t:/

at the highest Reynolds number conditions. The region of instabilities slowly grows with axial distance (while maintaining a distinct boundary); engulfing the entire tube at a distance between 20 and 25 diameters downstream from the flow divider, with a daughter tube Reynolds number of 1500. The onset and spread of these instabilities are delayed at lower Reynolds numbers until at daughter tube Reynolds numbers below 1000, no detectable instabilities are noted. The primary effort in this thesis was to evaluate the laminar three dimensional velocity fields, so further elucidation of this interesting phenomenon was not carried out.

Comparison of primary velocity distribution in Models 2-5 with Model 1

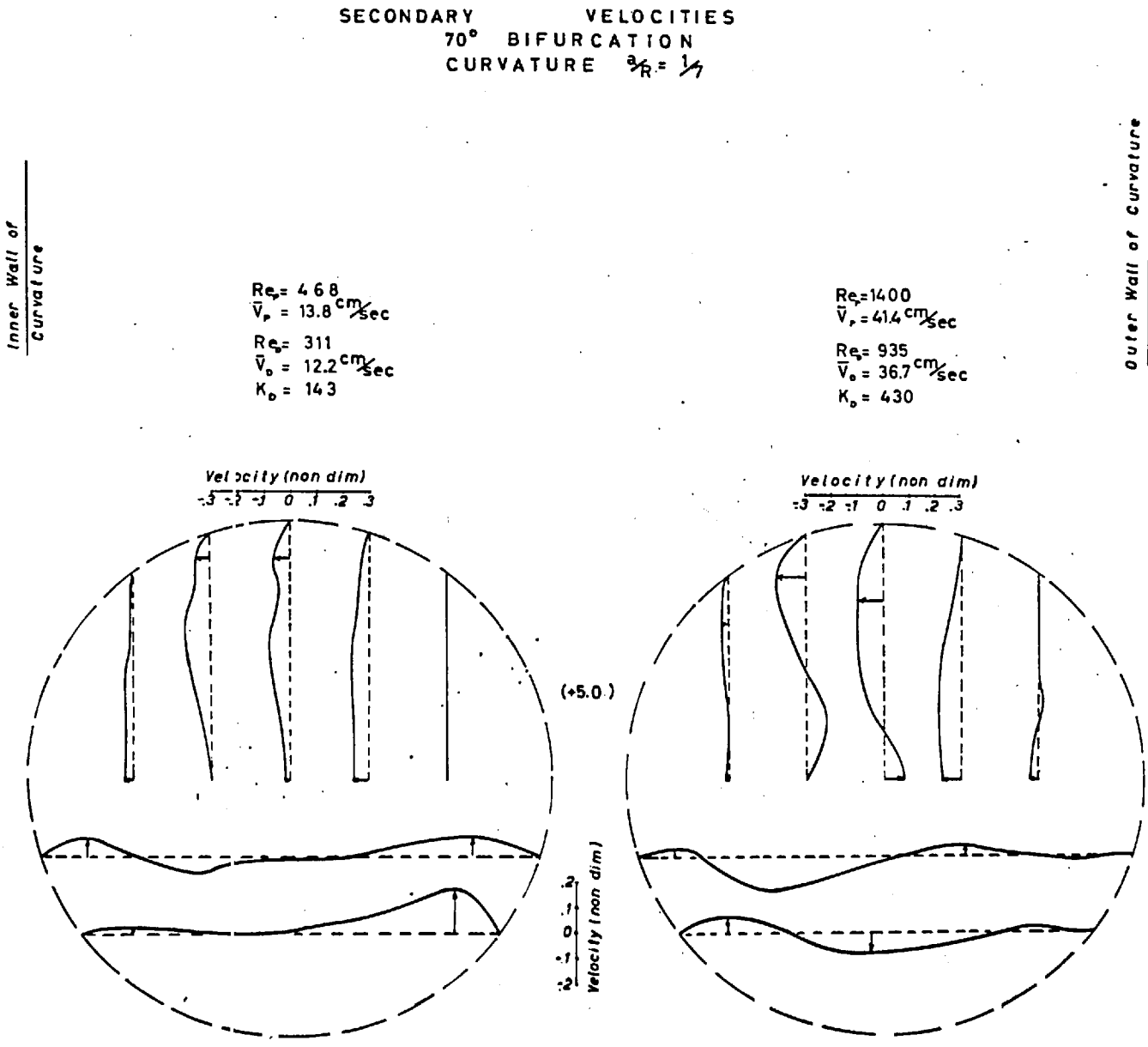
The flow within all the bifurcating models studied in this thesis showed the same general trend of primary velocity distribution with axial distance for each of the inlet velocity conditions. The higher velocity was always found near the outer wall of curvature, after one diameter of axial distance downstream from the flow divider. A region of low velocity was confined to areas near the inner wall of curvature, as shown in the experiments within Model 1. The magnitude and shape of this low velocity area was, however, dependent on the curvature ratio, being less prominent (i.e. high velocity near the inner wall) in/

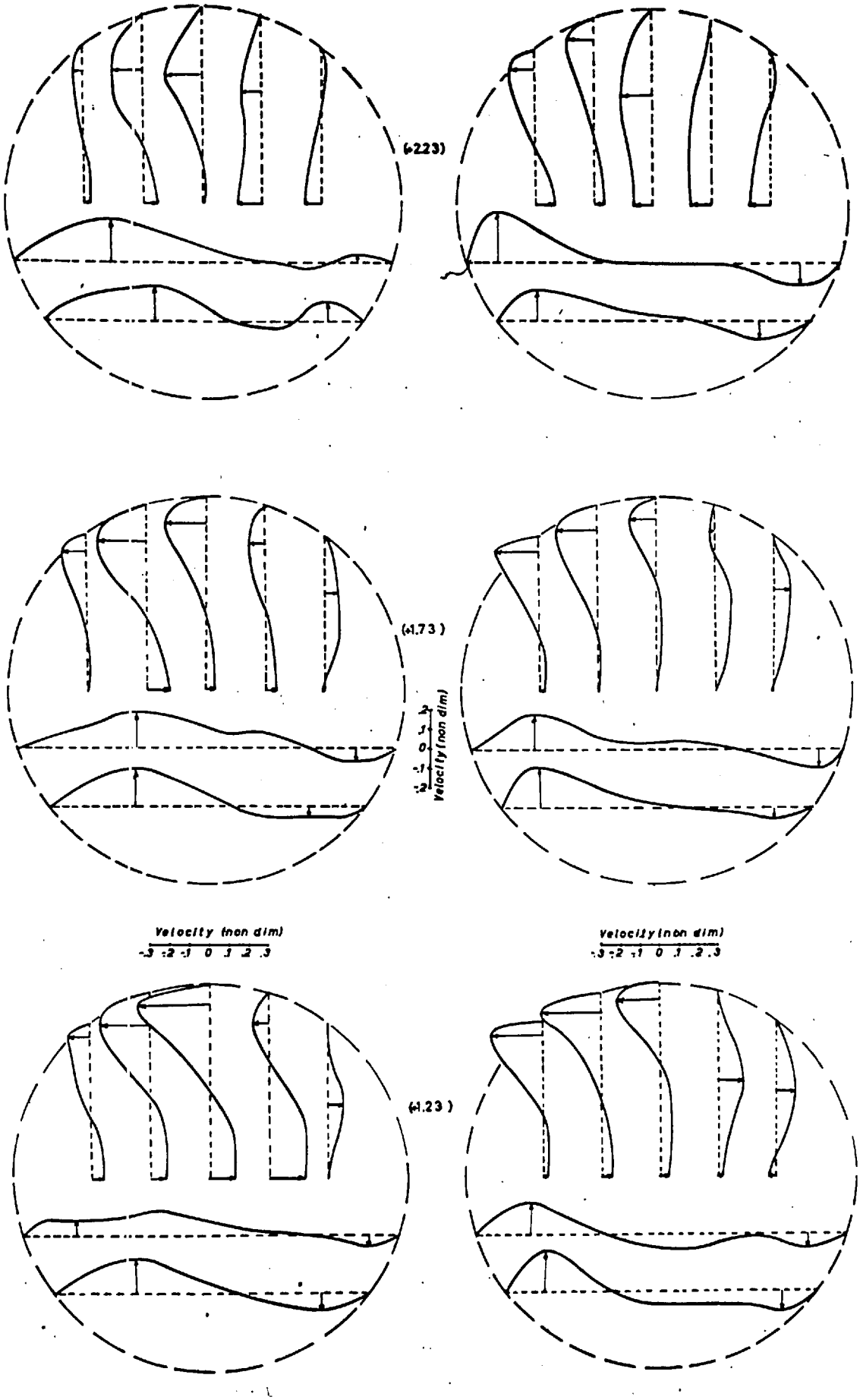
in the models with curvature ratios of 1/14. The boundary layer development on the outer wall of curvature, starting at the flow divider, was also dependent on the curvature ratio and the branching angle. This boundary layer developed at a somewhat faster rate for the models with a larger radius of curvature. The development of the boundary layer is an inverse function of the branching angle, in that with larger branching angles, the development is retarded and with small branching, the development is promoted. The difference in boundary layer thickness becomes apparent when calculating the viscous energy dissipation. The models with a higher branching angle and a smaller radius of curvature show more viscous energy loss within the first five diameters of axial length downstream from the flow divider.

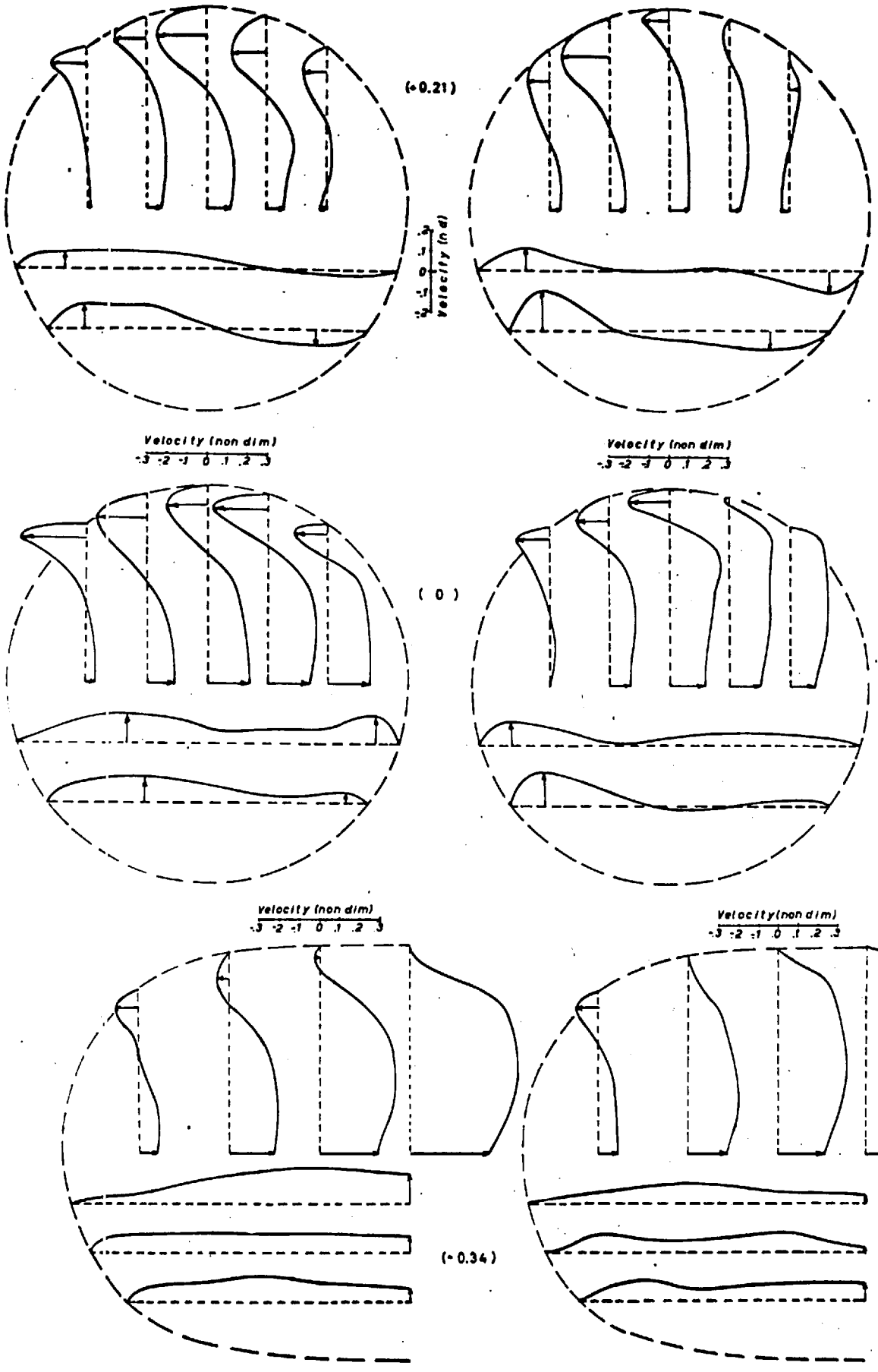
Secondary velocity field in Model 1

The secondary profiles obtained within Model 1 for two Reynolds numbers with a flat velocity distribution at the entrance to the model are shown in Figure 5.7. The profiles shown in the elliptical section of the bifurcation ($L/D = -0.34$) were measured in plane (shown in Figure 5.1) normal to the axis of the curved daughter tube, projected into the parent transition zone. This plane is positioned at an 18° angle with respect to the axis of the parent tube. Figure 5.8 is the same data but corrected for the 18° angle/

Figure 5.7 Profiles of cartesian components of secondary velocities in Model 1. Number in bracket indicates the axial position in diameters from the flow divider. Outer wall of curvature is to the right.




(+223)
(+1.73)
Velocity (non dim)
Velocity (non dim)
-3 -2 -1 0 1 2 3
Velocity (non dim)
-3 -2 -1 0 1 2 3
(+1.23)


(+0.21)
Velocity (non dim)
-.3 -.2 -.1 0 .1 .2 .3
Velocity (non dim)
-.3 -.2 -.1 0 .1 .2 .3
(0)
Velocity (non dim)
-.3 -.2 -.1 0 .1 .2 .3
Velocity (non dim)
-.3 -.2 -.1 0 .1 .2 .3
(-0.34)

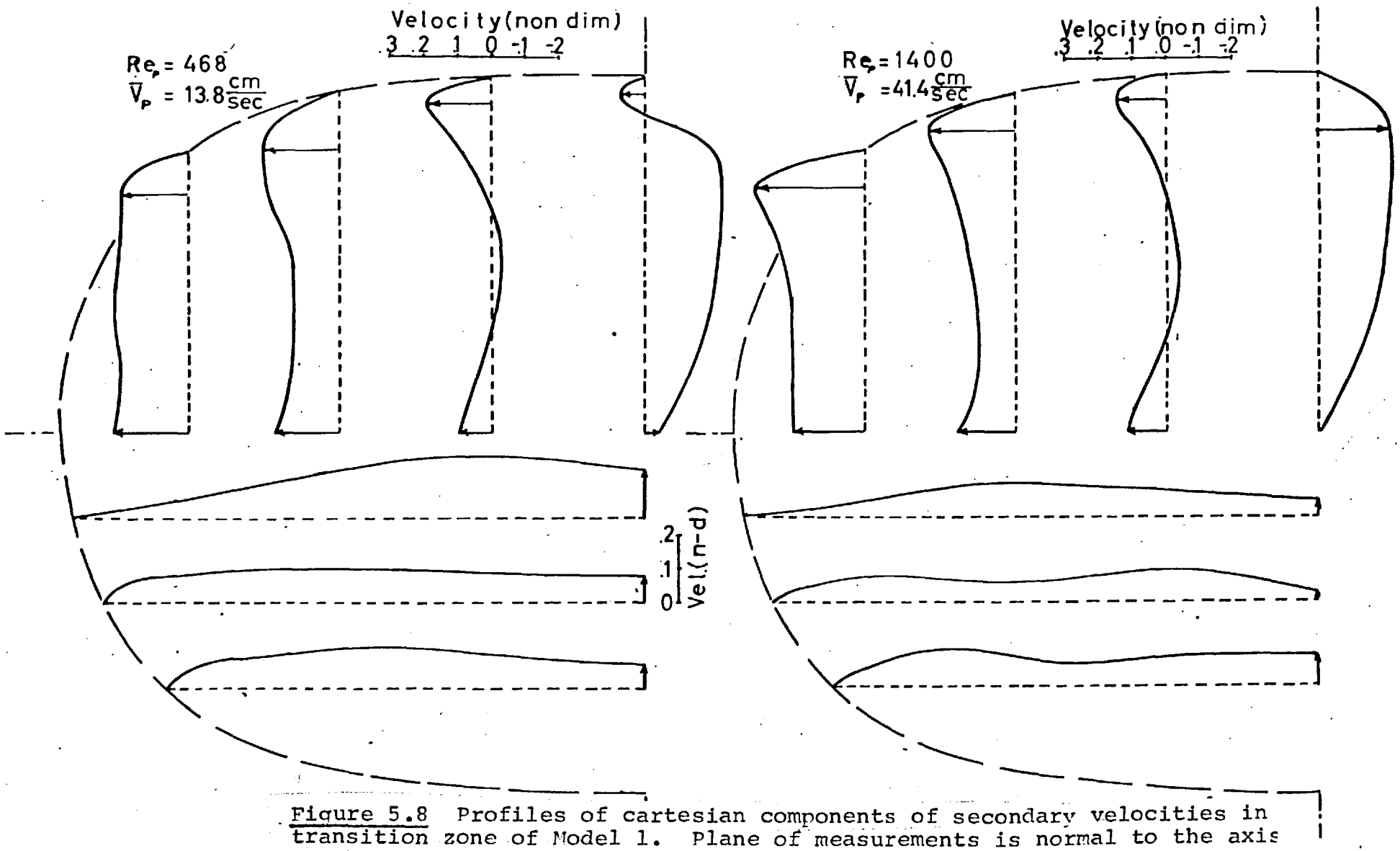


Figure 5.8 Profiles of cartesian components of secondary velocities in transition zone of Model 1. Plane of measurements is normal to the axis of the parent tube; for comparison to results of Chapter 4.

angle for comparison to the data of Chapter 4. In general the secondary velocities within the core of the flow are similar to the results of Chapter 4, except at the minor axis. The secondary velocity profiles on this vertical centreline are strongly affected by the stagnation point at the edge of the flow divider, which is 0.34 diameters (daughter tube diameters) upstream. The secondary profiles in Figure 5.7 show that the flow in the core of the tube does not follow the lines of curvature projected forward from the daughter tube. Thus the configuration within the elliptical transition zone of the parent tube does not divert the flow, so that it enters the daughter tube in a direction parallel to the axis of the tube. Instead the flow enters the daughter tube with a component of velocity toward the outer wall of curvature. This component of velocity is only strong near the region of the outer wall of curvature.

The patterns of secondary currents within the entrance of the daughter tube are in general similar to the secondary currents found within the transition bend region of a curved tube. This comparison is quite good for the experiments carried out at low Reynolds numbers, but does not compare well with the flow in the entrance of a curve near the outer wall of curvature (proximate to the flow divider) for the higher Reynolds number conditions.

At/

At these higher Reynolds numbers the flow near the outer wall of curvature shows a motion totally toward the outer wall. This is a result carried over from the secondary velocities upstream in the elliptical section. The component of secondary velocity in the horizontal plane also shows significant influence from the secondary velocity pattern carried over from the elliptical section.

The pattern of secondary flow goes through a rapid change downstream from the flow divider. The tangential component of secondary velocity increases within the tangential boundary layer from the vertical axis to the inner wall of curvature. This is similar in nature to the Squire & Winter equation depicting a linear increase in secondary flow within the initial curvature of a bent tube. The secondary velocities in the region near the developing boundary layer at the outer wall of curvature do not participate in this general pattern of secondary currents. Instead the secondary velocities within this region are quite small and directed toward the outer wall of curvature. At about one diameter downstream from the flow divider the secondary velocities diminish while maintaining the general pattern of the current. After 1.23 diameters the daughter tube becomes straight. The secondary velocities for axial positions within the straight portion of the daughter tube decrease further in magnitude while/

losing the general pattern typical of secondary currents in the initial region of a curved tube. At five diameters downstream from the flow divider the secondary velocities are primarily in a uniform pattern parallel to the plane of the bend directed toward the inner wall of curvature.

In general the secondary currents within the daughter tube of a bifurcation show good comparison to the secondary currents within the inlet region of a curved tube with a similar curvature ratio. This does not hold near the outer wall of curvature where the boundary layer development and the upstream conditions seem to have a strong influence upon the direction and magnitude of the secondary velocities. The magnitude of the secondary velocities, away from the outer wall of curvature, are in general lower than those observed within the inlet of a comparable curved tube. This can be seen best by comparing the magnitude of the core secondary velocity and tangential secondary velocity to those at a 40° position, with flat entrance, in Chapter 3. This decrease in magnitude may come about from the effects which the elliptical transition zone has on the boundary layer in the vertical plane. The transition zone will increase the vorticity in the horizontal plane while confining the vorticity in the vertical plane to a thin viscous boundary layer near the walls. Therefore the advection of the vorticity/

vorticity may be confined to within the boundary layer. The secondary velocities developed from this component of axial vorticity may thus be decreased in magnitude by the action of viscosity.

Comparison of secondary velocities in Models 2-5 to those of the example Model 1

The pattern of secondary currents is, in general, similar for all the bifurcations studied. The magnitude of the tangential secondary velocities depends upon the radius of curvature, being smaller with a curvature ratio of 1/14 than in the model used as an example, which has a value of 1/7. The bifurcations with a larger radius of curvature also show a somewhat smaller region of flow near the outer wall of curvature, which does not participate in the general pattern of secondary currents, as do the models with a smaller radius of curvature. This is because the models with a larger radius of curvature also have a longer elliptical transition zone in the parent tube. This longer transition zone creates a flow at the entrance to the daughter tubes which is more parallel to the axis of the daughter tube. The development of the magnitude of secondary currents downstream from the flow divider is dependent on the branching angle. This is similar to the development within a curved tube where the pattern of secondary velocity remains unchanged/

unchanged but the secondary velocities increase in magnitude for the first 60° of the bend. This condition was similar for the bifurcations, the largest branching angle being 45°.

The position of mass flow (the first moment)

The first moment indicates the position of the centre of mass flow. The changes in the position of the centre of mass flow give good indication of the net secondary flow. Figure 5.9 shows the position of the centre of mass flow for two Reynolds number conditions and two 70° bifurcations, with different radii of curvature. It can be seen from the figure that the net secondary flow (non dimensional) is greater at the larger Reynolds numbers. The movement of the velocity distribution is toward the wall for the first diameter of axial length downstream of the flow divider, followed by a gradual return to the centre line, accomplished at an axial length of about 25 diameters downstream. The movement of the centre of mass flow is more gradual in models with a larger radius of curvature. Furthermore, the amount of movement (or magnitude of net secondary flow) is less in these models.

A prominent feature to note is the comparison in the positions of the centre of mass flow for the bifurcation models and the curved tube models. The bifurcations/

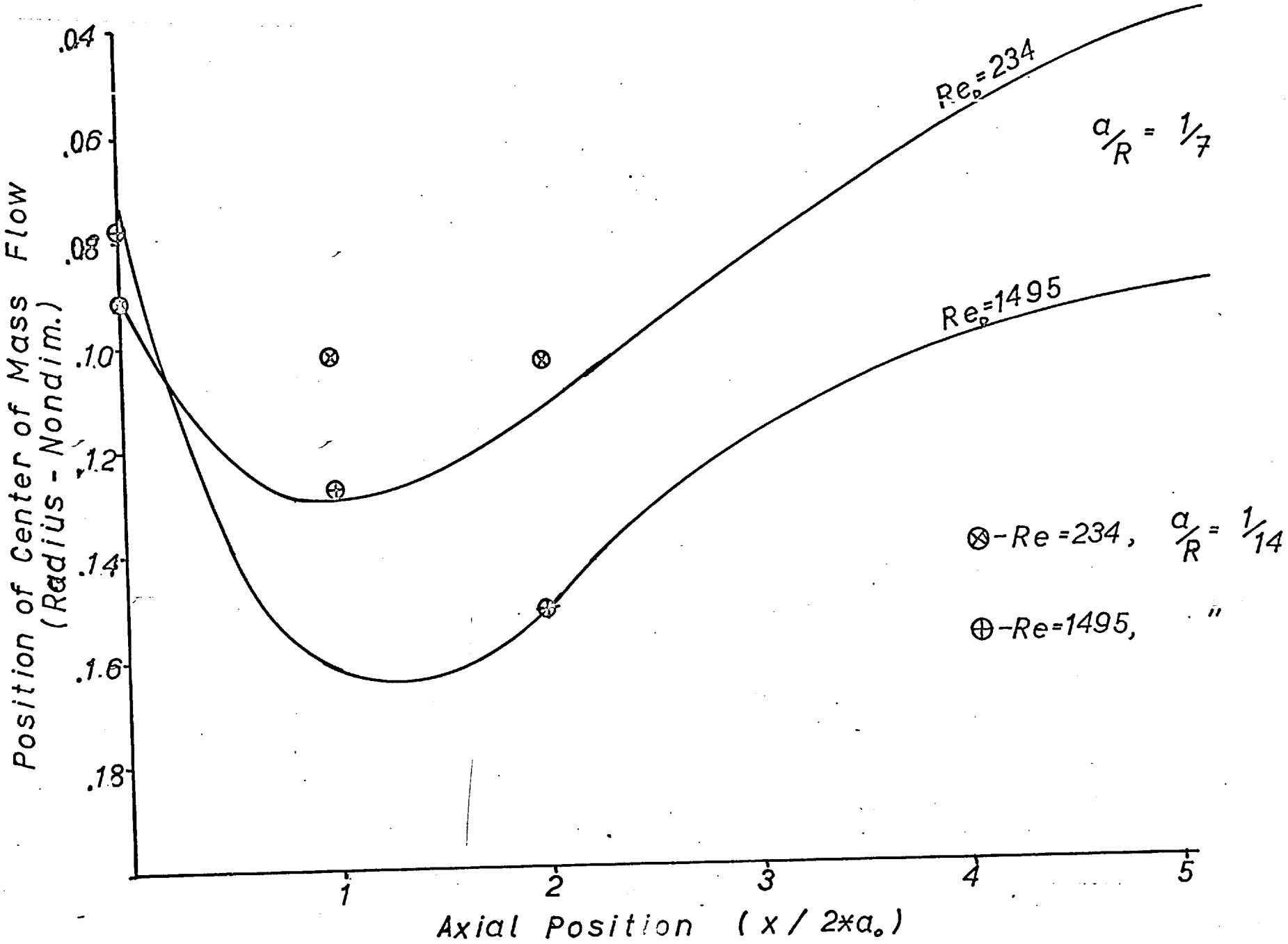


FIGURE 5.9 Position of centre of mass flow as a function of axial distance. Lines indicate data from Model 1, circles with crosses or pluses indicate 70° bifurcation with greater radius of curvature.

bifurcations show an order of magnitude of greater deviation in the position of the centre of mass flow from the tube axis than do the curved tubes. This simply indicates the strong skew in the position of the centre of mass flow at the entrance to the daughter tubes. This further indicates the influence that the entrance conditions into the daughter tube has on the development of secondary flow within the daughter tube.

Velocity gradients at the wall

Velocity gradients near the walls of the tube at the horizontal and vertical axes were measured with the same techniques discussed in Chapter 3. The results of such measurements are shown in Figure 5.10, where the mean velocity and radius of the daughter tubes are used to non-dimensionalise the data. The distribution of this wall shear is similar for all bifurcations, entrance conditions and Reynolds numbers studied. The wall shear downstream from a bifurcation shows a very high value on the outer wall of curvature (flow divider wall) and a low value at the inner wall of curvature. This wall shear distribution develops at the location of the flow divider and slowly decays with axial distance; a similar distribution still exists at 25 diameters of axial distance downstream from the flow divider.

Calculation of energy dissipation and total kinetic energy

The dissipation function and total kinetic energy

was/

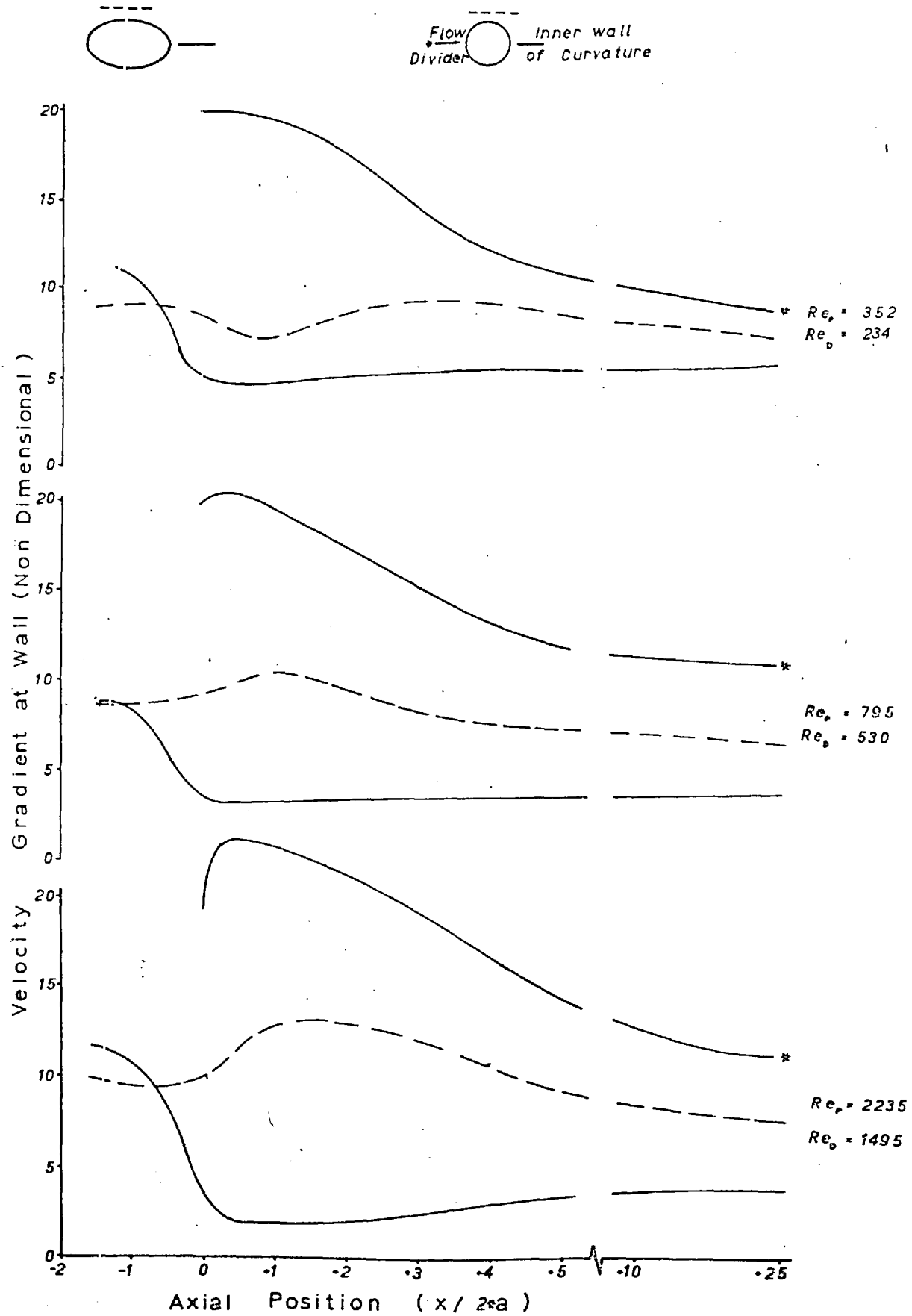


FIGURE 5.10 Velocity gradients at inner, outer and "mean" wall of curvature. Note outer wall of curvature starts at axial position of zero (the flow divider).

was calculated with the same techniques discussed in Chapter 3 and 4. The amount of energy lost via viscosity is shown in Figure 5.11. The viscous energy loss shows a characteristic pattern with axial distance, which is similar for all experimental conditions. The viscous energy loss increases by about 40% within the first diameter downstream from a bifurcation. With increasing axial distance downstream from the flow divider the energy loss per unit length slowly decreases.

The total kinetic energy shows a sharp change just before the point of bifurcation. This is due primarily to the changing cross sectional area. Figure 5.12 is a plot of the viscous pressure and kinetic pressure obtained from the above calculations; the mean static pressure obtained by requiring that the su-mation of the viscous, kinetic and static pressures be zero. In the experiments with high Reynolds numbers a significant contribution to the mean static pressure from the kinetic energy change can be predicted at the location just proximal to the flow divider. This contribution from the kinetic energy is, of course, much less with lower Reynolds number conditions. Even at these high flow conditions, the length through which a sharp change in mean static pressure is predicted is of the order of one diameter.

In Chapter 1 the assumption was made that the distention of the elastic bronchi would be uniform in shape/

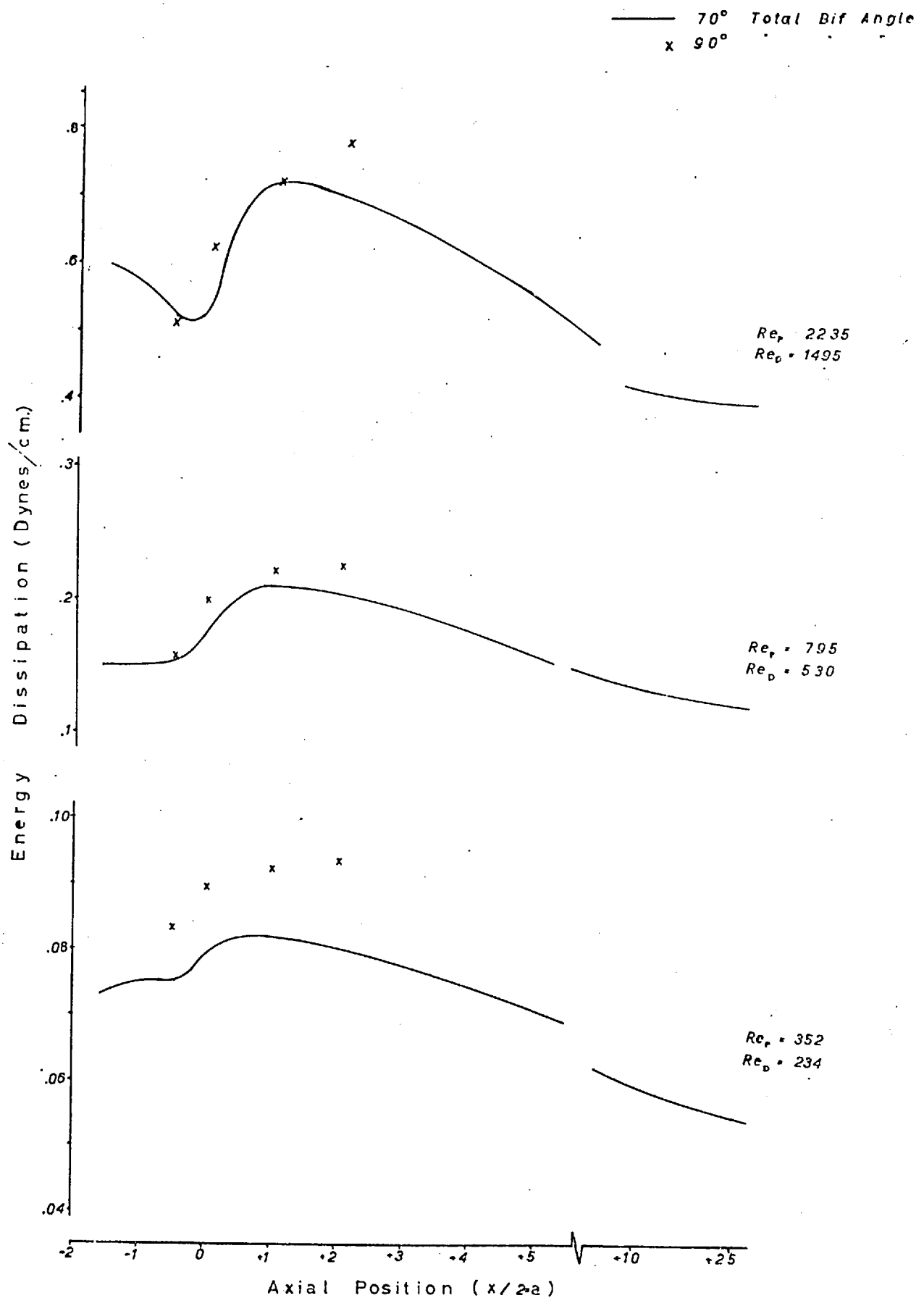


FIGURE 5.11 Energy lost per centimeter axial distance. Lined Graphs are for Model 1 and X's are from a 90° bifurcation with the same curvature.

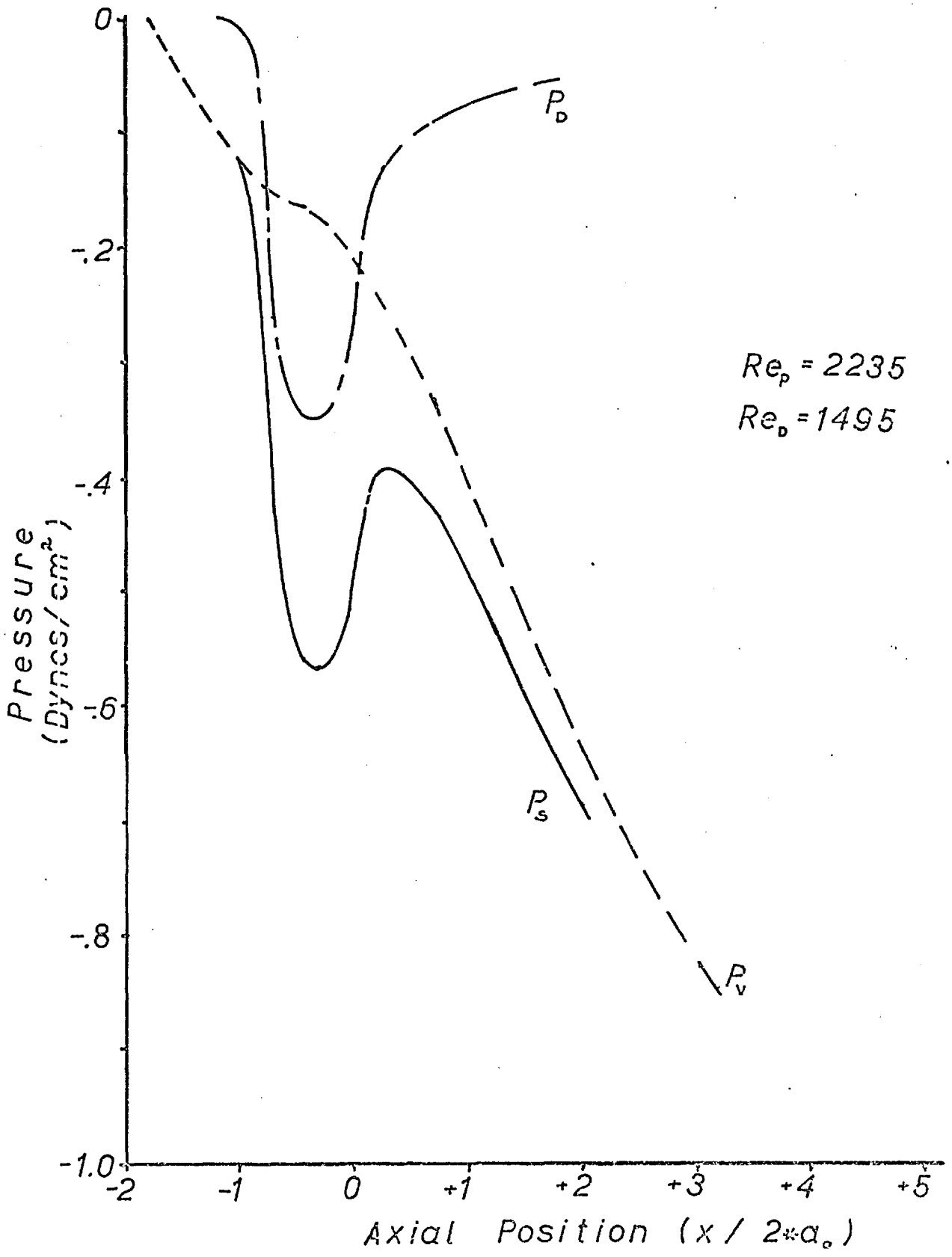


FIGURE 5.12 Viscous pressure (P_{ν}) dynamic pressure (P_D) and mean static pressure as a function of axial distance. Note influence from dynamic pressure on static pressure. Dynamic recovery is much less at lower flow rates.

shape. This assumption was only valid if static pressure changes occurred only within a length scale of 0.61 diameters or greater. The static pressure distribution of Figure 5.11 has a length scale of approximately one diameter at the position just proximal to the bifurcation. This seems to validate the previous assumption.

Conclusion

In this chapter I have attempted to evaluate the flow properties experimentally observed in six bifurcation models. I have also attempted to compare experimental results found in the bifurcations to the results of the preceding chapters.

Essentially the experimental results show general patterns in the primary velocity field, the wall shear distribution, the energy dissipation and the mean static pressure distribution with axial distance. These results can be explained by the changing elliptical shape in the transition zone, the curvature of the daughter tube and the boundary layer development on the flow divider. Changing the curvature, branch angle on the elliptical transition zone produces predictable changes in flow properties.

The/

FLOW INTO A 70° BIFURCATION WITH CURVATURE RATIO; a/R = 1/7 (FLAT INLET PROFILE)

Position	Moments of Velocity Distribution First	Second	Third	Kinetic Energy Factor	Reynolds Number	Average Velocity (cm/sec)	Dean Number	a/R
L/D = -1.61	0	.660	.003	1.200	2235	66.1		
-1.35	0	.658	.002	1.219				
-0.88	0	.658	.001	1.208				
-0.34	0	.648	.001	1.309				
0	.073	.636	.005	1.368	1495	58.7	690	1/7
0.21	.109	.636	.010	1.401				
0.47	.140	.637	.014	1.468				
0.73	.154	.643	.016	1.495				
1.23*	.158	.644	.018	1.539				
1.73	.170	.642	.023	1.612				
2.23	.134	.658	.032	1.414				
5	.093	.644	.037	1.407				
10	.096	.629	.023	1.480				
25	.059	.629	.012	1.427				
L/D= -1.61	0	.650	.004	1.259	1670	49.4		
-1.35	0	.647	.004	1.282				
-0.88	0	.645	.003	1.288				
-0.34	0	.632	.004	1.398				
0	.108	.630	.016	1.450	1115	43.9	515	1/7
0.21	.134	.633	.018	1.463				
0.47	.157	.637	.019	1.516				
0.73	.172	.631	.024	1.638				
1.23*	.169	.646	.027	1.578				
1.73	.173	.644	.022	1.629				

	5	.095	.639	.039	1.475			
	10	.106	.624	.032	1.540			
	25	.091	.612	.015	1.573			
L/D =	-1.61	0	.626	.007	1.433	795	23.5	
	-1.35	0	.626	.008	1.442			
	-0.88	0	.624	.010	1.469			
	-0.34	0	.625	.010	1.466			
	0	.104	.628	.021	1.470	530	20.8	244 1/7
	0.21	.128	.631	.028	1.479			
	0.47	.140	.634	.031	1.512			
	0.73	.155	.642	.033	1.514			
	1.23*	.149	.644	.039	1.536			
	1.73	.151	.643	.044	1.598			
	2.23	.152	.647	.049	1.601			
	5	.078	.631	.034	1.475			
	10	.080	.618	.021	1.546			
	25	.073	.604	.022	1.686			
L/D =	-1.61	0	.630	.010	1.421	468	13.8	
	-1.35	0	.627	.011	1.443			
	-0.88	0	.626	.012	1.459			
	-0.34	0	.624	.012	1.492			
	0	.110	.627	.038	1.520	311	12.2	143 1/7
	0.21	.123	.631	.046	1.522			
	0.47	.131	.632	.046	1.537			
	0.73	.147	.637	.051	1.552			
	1.23*	.142	.641	.050	1.550			
	1.73	.137	.642	.048	1.556			
	2.23	.134	.644	.049	1.539			
	5	.054	.627	.018	1.461			
	10	.081	.615	.035	1.619			
	25	.057	.604	.029	1.728			
L/D =	-1.61	0	.632	.008	1.407	352	10.4	
	-1.35	0	.634	.009	1.380			
	-0.88	0	.632	.011	1.402			
	-0.34	0	.631	.009	1.401			
	0	.092	.631	.032	1.448	234	9.2	108 1/7
	0.21	.103	.635	.039	1.449			
	0.47	.112	.633	.036	1.465			
	0.73	.132	.634	.042	1.534			
	1.23*	.124	.638	.043	1.511			
	1.73	.117	.640	.043	1.490			
	2.23	.106	.644	.041	1.438			

10	.050	.617	.028	1.558
25	.026	.606	.020	1.693

L E G E N D

Axial distance (L/D) in diameters is referred to the point of bifurcation (where L/D = 0).

* - Axial distance of 1.23 is at the end of curvature a - diameter of daughter branch; R - radius of curvature.

FLOW INTO A 90° BIFURCATION
WITH CURVATURE RATIO: a/R = 1/7
(FLAT INLET PROFILE)

Position	Moments of Velocity Distribution First	Second	Third	Kinetic Energy Factor	Reynolds Number	Average Velocity (cm/sec)	Dean Number	a/R
L/D = -0.5	0	.646	.003	1.293	2235	66.1		
0	.095	.639	.013	1.374	1495	58.7	690	1/7
1	.010	.634	.024	1.539				
2	.176	.643	.034	1.628				
L/D = -0.5	0	.633	.009	1.409	1670	49.4		
0	.119	.631	.021	1.464	1115	43.9	515	1/7
1	.159	.642	.026	1.524				
2	.179	.644	.043	1.658				
L/D = -0.5	0	.628	.009	1.429	795	23.5		
0	.115	.636	.022	1.423	530	20.8	244	1/7
1	.148	.642	.030	1.493				
2	.159	.654	.037	1.559				
L/D = -0.5	0	.627	.017	1.484	468	13.8		
0	.118	.635	.036	1.450	311	12.2	244	1/7
1	.169	.600	.060	2.166				
2	.155	.650	.047	1.553				
L/D = -0.5	0	.639	.007	1.343	352	10.4		
0	.096	.639	.028	1.373	234	9.2	108	1/7
1	.073	.613	.033	1.903				
2	.116	.653	.035	1.386				

FLOW INTO A 70° BIFURCATION
WITH CURVATURE RATIO: a/R = 1/14
(FLAT INLET PROFILE)

Position	Moments of Velocity Distribution First	Second	Third	Kinetic Energy Factor	Reynolds Number	Average Velocity (cm/sec)	Dean Number	a/R
L/D = -0.5	0	.650	.008	1.303	2235	66.1		
0	.089	.641	.007	1.359	1495	58.7	485	1/14
1	.129	.640	.015	1.423				
2	.151	.644	.030	1.519				
L/D = -0.5	0	.636	.008	1.406	1670	49.4		
0	.115	.636	.017	1.419	1115	43.9	360	1/14
1	.155	.637	.023	1.523				
2	.155	.642	.037	1.547				
L/D = -0.5	0	.638	.006	1.344	795	23.5		
0	.116	.639	.016	1.402	530	20.8	170	1/14
1	.128	.635	.022	1.476				
2	.138	.642	.044	1.496				
L/D = -0.5	0	.630	.012	1.413	468	13.8		
0	.113	.629	.036	1.424	311	12.2	100	1/14
1	.126	.634	.043	1.505				
2	.134	.641	.049	1.513				
L/D = -0.5	0	.631	.007	1.386	352	10.4		
0	.093	.642	.028	1.354	234	9.2	76	1/14
1	.103	.635	.037	1.453				
2	.104	.639	.040	1.441				

The secondary velocity field can also be qualitatively understood by comparing the results to the curved or elliptical model studies. Likewise, changes in the bifurcation geometry bring about predictable changes in the secondary velocity field. The secondary velocity field is, however, more sensitive to the geometric configuration of the bifurcation than the other flow properties analysed.

CONCLUSION

The theme of this thesis was to study flow in the human lung. I have defined the fluid mechanic problem in the lung, evaluated the flow properties in scale model studies of the airways configuration, and attempted to analyse the physics of the flow observed within the scale models. The conclusions to be drawn from these studies are that for the geometric configuration of the pulmonary airways some flow properties (such as wall shear, energy loss, kinetic energy recovery) have characteristic magnitudes and distributions for the range of geometric variability found in the normal pulmonary system. Unfortunately the flow property of primary interest, the secondary velocity field, does show considerable changes with "normal" geometric changes in the airways. This is also true, to a lesser extent, of the primary velocity field.

Although the understanding of the physiological system was the main purpose of this thesis, the analysis and experimentation within each chapter attempt to make a statement on their own.

APPENDIX TO CHAPTER 4

Details of low Reynolds number solution for flow in a tube which slowly changes ellipticity

We wish to solve the Navier-Stokes equations for the laminar flow of a fluid under the action of a uniform pressure gradient, $\hat{G}_o$, in a tube with an elliptical cross section whose major and minor axes vary in length but not in direction. We take $(\hat{x},\hat{y},\hat{z})$ as the Cartesian co-ordinates as shown in Figure 4.2A The equation for the cross section at axial position x is taken as equation (1) in the text, where a(x) and b(x) are smoothly variable functions of x. The problem in its most general form is still too difficult for a simple analysis, so we restrict a and b to be slowly varying functions of x. Then if ℓ is the axial length scale the condition

$$\epsilon = \frac{a_o}{\ell} << 1 \qquad (A.1)$$

must be satisfied. Using the same velocity components as in the text and letting the pressure be $\rho U_m^2 p$, where ρ is the density of the fluid, and U_m is a scale velocity which we choose to be the maximum axial velocity of the fluid when the pipe is circular with radius a_o, and the pressure gradient is

$$\hat{G}_o = 4\mu U_m / a_o^2 \qquad (A.2)$$

where μ is the absolute viscosity of the fluid.

We/

We also define a Reynolds number

$$Re = U_m a_o / \nu \tag{A.3}$$

where ν is the kinematic viscosity of the fluid.

We now introduce dimensionless independent variables which are slightly different than found in the text but are more convenient for the solution

$$\eta = y/\hat{a}(x) \quad , \quad \zeta = z/\hat{b}(x) \quad , \quad \xi = x/\ell \tag{A.4}$$

where y, z, a(x) and b(x) are defined in the text.

For steady flow the equations of motion become:

x-momentum equation:

$$\epsilon u\left(u_\xi - \frac{a'}{a}\eta u_\eta - \frac{b'}{b}\zeta u_\zeta\right) + \frac{v}{a}u_\eta + \frac{w}{b}u_\zeta = -\epsilon\left(p_\xi - \frac{a'}{a}\eta p_\eta - \frac{b'}{b}\zeta p_\xi\right) + \frac{1}{Re}\left(\frac{u_{\eta\eta}}{a^2} + \frac{u_{\zeta\zeta}}{b^2} + \epsilon^2 L(u)\right) \tag{A.5}$$

y-momentum equation:

$$\epsilon u\left(v_\xi - \frac{a'}{a}\eta v_\eta - \frac{b'}{b}\zeta v_\zeta\right) + \frac{v}{a}v_\eta + \frac{w}{b}v_\zeta = -\frac{1}{a}p_\eta + \frac{1}{Re}\left(\frac{v_{\eta\eta}}{a^2} + \frac{v_{\zeta\zeta}}{b^2} + \epsilon^2 L(v)\right) \tag{A.6}$$

z-momentum equation:

$$\epsilon u\left(w_\xi - \frac{a'}{a}\eta w_\eta - \frac{b'}{b}\zeta w_\zeta\right) + \frac{v}{a}w_\eta + \frac{w}{b}w_\zeta = -\frac{1}{b}p_\zeta + \frac{1}{Re}\left(\frac{w_{\eta\eta}}{a^2} + \frac{w_{\zeta\zeta}}{b^2} + \epsilon^2 L(w)\right) \tag{A.7}$$

The continuity equation is

$$\epsilon\left(u_\xi - \frac{a'}{a}\eta v_\eta - \frac{b'}{b}\zeta u_\zeta\right) + \frac{1}{a}v_\eta + \frac{1}{b}w_\zeta = 0 \tag{A.8}$$

where

$$L(\phi) = \phi_{\xi\xi} - \frac{2a'}{a}\eta\phi_{\xi\eta} - \frac{2b'}{b}\zeta\phi_{\xi\zeta} + \frac{a'^2}{a^2}\eta^2\phi_{\eta\eta} + \frac{b'^2}{b^2}\zeta^2\phi_{\zeta\zeta} + \frac{2a'b'}{ab}\eta\zeta\phi_{\eta\zeta} + \left(-\frac{a''}{a} + \frac{2a'^2}{a^2}\right)\eta\phi_\eta + \left(-\frac{b''}{b} + \frac{2b'^2}{b^2}\right)\zeta\phi_\zeta$$

and/

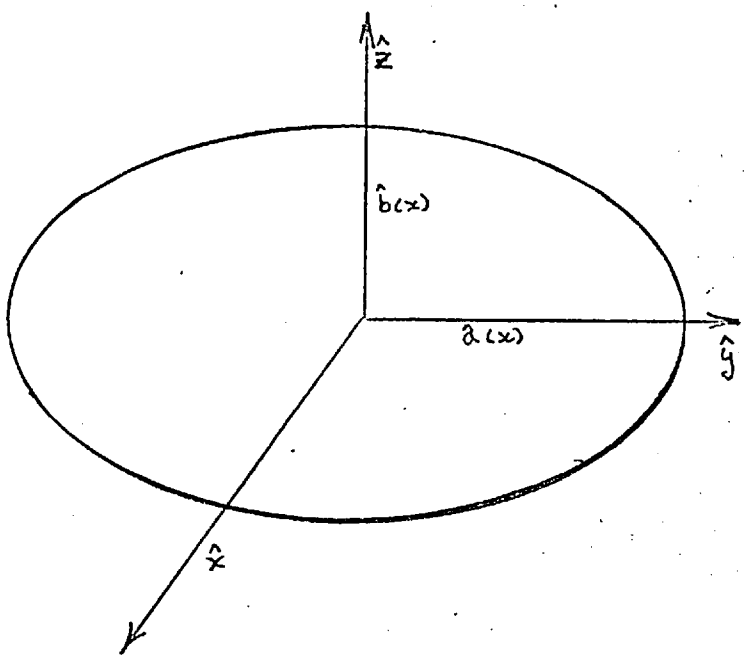


FIGURE 4.2A

$$a(\xi) = \frac{\hat{a}(x)}{a_0}, \quad b(\xi) = \frac{\hat{b}(x)}{b_0}$$

and the terms a' indicate $\frac{da}{dx}$.

The boundary conditions are that the velocities and their derivatives should be finite on the axis $\eta = \zeta = 0$, and all velocities are zero on the tube boundary,

$$u = v = w = 0 \quad \text{on} \quad \eta^2 + \zeta^2 = 1 \qquad (A.9)$$

We seek a solution in ascending powers of ϵ, and in the limit as $\epsilon \to 0$ we assume that at each x there is a quasi-parallel fully developed flow in response to the uniform pressure gradient $\hat{G}_0$. As discussed in the text, this assumption is equivalent to neglecting terms in the equations of order ϵ while retaining those of order 1/Re. In practice the theory will only hold when the Reynolds number is not too large and the axial variation slow.

The terms of higher will determine the modifications to the basic flow as the cross section varies. We shall concentrate only on the first-order terms to evaluate the direction of the secondary motions, for small ϵ, and their effect on the axial velocity profile.

The solutions of velocity components will be of the form

$$u = u_0 + \epsilon u_1 + \epsilon^2 u_2 + \cdots$$
$$v = \epsilon v_1 + \epsilon^2 v_2 + \cdots$$
$$w = \epsilon w_1 + \epsilon^2 w_2 + \cdots$$
$$p = -G_0 \xi + \epsilon p_1 + \epsilon^2 p_2 + \cdots$$

where

$$G_0 = \frac{\rho \hat{G}_0}{\rho U_m^2} = \frac{4}{\epsilon Re}$$

from/

from equations (A.1), (A.2) and (A.3). To zero order in ϵ, equation (A.5) is the only equation not trivially satisfied, and gives for u_0:

$$\frac{1}{a^2} u_{0\eta\eta} + \frac{1}{b^2} u_{0\xi\xi} = -\epsilon Re\, G_0 = -4 .$$

The solution of this equation, satisfying the boundary condition (A.9), describes fully developed flow in a uniform elliptical tube, i.e.

$$u_0 = \frac{2a^2b^2}{a^2+b^2}\left(1-\eta^2-\xi^2\right) . \qquad (A.10)$$

When a = b = 1, this reduces to Poiseuille flow in a circular tube,

$$u_0 = 1 - r^2 .$$

The first order terms in equations (A.5)-(A.8) are, respectively,

$$u_0\left(u_{0\zeta} - \frac{a'}{a}\eta u_{0\eta} - \frac{b'}{b}\xi u_{0\xi}\right) + \frac{v_1}{a} u_{0\eta} + \frac{w_1}{b} u_{0\xi} = -\left(p_{1\zeta} - \frac{a'}{a}\eta p_{1\eta} - \frac{b'}{b}\xi p_{1\xi}\right) + \frac{1}{Re}\left(\frac{1}{a^2} u_{1\eta\eta} + \frac{1}{b^2} u_{1\xi\xi}\right) \qquad (A.11)$$

$$-\frac{1}{a} p_{1\eta} + \frac{1}{Re}\left(\frac{1}{a^2} v_{1\eta\eta} + \frac{1}{b^2} v_{1\xi\xi}\right) = 0 \qquad (A.12)$$

$$-\frac{1}{b} p_{1\xi} + \frac{1}{Re}\left(\frac{1}{a^2} w_{1\eta\eta} + \frac{1}{b^2} w_{1\xi\xi}\right) = 0 \qquad (A.13)$$

$$u_{0\zeta} - \frac{a'}{a}\eta u_{0\eta} - \frac{b'}{b}\xi u_{0\xi} + \frac{1}{a} v_{1\eta} + \frac{1}{b} w_{1\xi} = 0 . \qquad (A.14)$$

In/

In order to solve the above set of equations, we first eliminate p_1, from equations (A.12) and (A.13) to give

$$\frac{1}{a} v_{1\eta\eta\zeta} + \frac{a}{b^2} v_{1\zeta\zeta\zeta} = \frac{b}{a^2} w_{1\eta\eta\eta} + \frac{1}{b} w_{1\eta\zeta\zeta} \tag{A.15}$$

The procedure is now to solve (A.14) and (A.15) for v_1, and w_1, and then to solve (A.12) or (A.13) for p_1, and finally to solve (A.11) for u_1.

If we substitute the solution (A.10) for u_0 into (A.14), that equation becomes:

$$\frac{1}{a} v_{1\eta} + \frac{1}{b} w_{1\zeta} = \frac{-4ab}{(a^2+b^2)^2} \left\{ (a^3b' + a'b^3) + (\eta^2 a^2 - \zeta^2 b^2)(a'b - ab') \right\} \tag{A.16}$$

$$= -(A + B\eta^2 + C\zeta^2)$$

defining new functions of , A, B, and C.

We were unable to find closed form solutions of (A.15) and (A.16) for general functions of a and b, but only when they are related in a particular way, as will be specified below. As was discussed in the text, this relation approximates the geometric conditions in the elliptical models used for experimentation. However, there is no reason to suppose that the actual solution in a tube which has a geometry close to satisfying this condition has a velocity distribution far removed from the solution for a tube which does satisfy the condition. We therefore assume that the solution for tubes of this particular/

particular class are expected to indicate the form of the solution for other tubes. In particular, the solution should indicate the direction of the secondary motions, and the effect on the axial velocity.

If we assume the form of the first-order secondary velocities as

$$\left.\begin{aligned} v_1 &= \alpha(\xi)\,\eta\,(1-\eta^2-\zeta^2) \\ w_1 &= \beta(\xi)\,\zeta\,(1-\eta^2-\zeta^2) \end{aligned}\right\} \qquad (A.17)$$

equation (A.15) is identically satisfied, and (A.16) gives

$$\frac{\alpha}{a}\,(1-3\eta^2-\zeta^2) + \frac{\beta}{b}\,(1-\eta^2-3\zeta^2) = -(A + B\eta^2 + C\zeta^2)$$

This is satisfied if and only if

$$\frac{\alpha}{a} + \frac{\beta}{b} = -A \quad , \quad \frac{3\alpha}{a} + \frac{\beta}{b} = B \quad , \quad \frac{\alpha}{a} + \frac{3\beta}{b} = C$$

which are self-consistent only if

$$B + C = -4A \quad , \qquad (A.18)$$

and therefore

$$\alpha = \frac{a}{8}\,(3B-C) \quad , \quad \beta = \frac{b}{8}\,(3C-B) \, .$$

In terms of a and b, the and are

$$\left.\begin{aligned} \alpha &= \frac{a^2 b\,(3a^2+b^2)}{2\,(a^2+b^2)^2}\,(a'b - ab') \\ \beta &= -\frac{ab^2\,(a^2+3b^2)}{2\,(a^2+b^2)^2}\,(a'b - ab') \end{aligned}\right\} \qquad (A.19)$$

The consistency condition (A.18) can be written as

$$3\left[ab(a^2+b^2)\right]' = 4ab(a^2+b^2)'$$

which can be solved to give

$$\frac{(ab)^3}{a^2+b^2} = \text{CONSTANT} \qquad \text{(A.20)}$$

Thus if a and b are related by (A.20) the first order secondary velocities v_1 and w_1 are given by (A.17) with α and β given by (A.19).

The first order pressure distribution, in this case, is obtained by integrating (A.12) and (A.13), to give

$$p_1 = \frac{-1}{2Re}\,\frac{(3a^2+b^2)(3b^2+a^2)}{ab(a^2+b^2)^2}(a'b-b'a)(a^2z^2-b^2y^2+\gamma) \qquad \text{(A.21)}$$

where γ is the constant of integration and must be determined by the condition that the average pressure gradient is $\hat{G}_0$, so that the first order contribution to $\hat{G}_0$ is zero, i.e.

$$\iint p_1\, dy\, dz = 0$$

where the integration is taken over the cross section of the tube. This condition eventually leads to the result that

$$\gamma = \frac{b^2-a^2}{4}$$

Finally we solve (A.11) for the first-order primary velocity, u_1, substituting from (A.10), (A.17) and (A.21) for u_0, v_1, w_1, and p_1. The final solution for u_1 is

$$u_1 = (1-\eta^2-\zeta^2)(\alpha_1+\alpha_2\eta^2+\alpha_3\zeta^2+\alpha_4\eta^4+\alpha_5\eta^2\zeta^2+\alpha_6\zeta^4) \quad (A.22)$$

where the coefficients α_n and functions of ξ and are given by the mating equation

$$\underset{\sim}{A}\ \underset{\sim}{\alpha} = \underset{\sim}{\beta}$$

The $\underset{\sim}{\alpha}$ is the column vector of the α_n, $\underset{\sim}{A}$ is the b x b matrix

$$\underset{\sim}{A} = \begin{pmatrix} \frac{1}{a^2}+\frac{1}{b^2} & -\frac{1}{a^2} & -\frac{1}{b^2} & 0 & 0 & 0 \\ 0 & \frac{6}{a^2}+\frac{1}{b^2} & \frac{1}{b^2} & -\frac{6}{a^2} & -\frac{1}{b^2} & 0 \\ 0 & \frac{1}{a^2} & \frac{1}{a^2}+\frac{1}{b^2} & 0 & -\frac{1}{a^2} & -\frac{6}{b^2} \\ 0 & 0 & 0 & \frac{15}{a^2}+\frac{1}{b^2} & \frac{1}{b^2} & 0 \\ 0 & 0 & 0 & \frac{1}{a^2} & \frac{1}{a^2}+\frac{1}{b^2} & \frac{1}{b^2} \\ 0 & 0 & 0 & 0 & \frac{1}{b^2} & \frac{1}{a^2}+\frac{15}{b^2} \end{pmatrix}$$

and $\underset{\sim}{\beta}$ is the column vector whose transpose is

$$\underset{\sim}{\beta}^T = -\frac{1}{2}\,(A_1,\ B_1,\ C_1,\ D_1,\ D_1/3,\ D_1)$$

where /

where

$$A_1 = F'/8Re$$

$$B_1 = -\frac{1}{2Re}\left\{\frac{a^2F'}{a^2-b^2} - \frac{2Fab(a'b-b'a)}{(a^2-b^2)^2}\right\}$$

$$C_1 = \frac{1}{2Re}\left\{\frac{b^2F'}{a^2-b^2} - \frac{2Fab(a'b-b'a)}{(a^2+b^2)^2}\right\}$$

$$D_1 = \frac{-4a^3b^3}{(a^2+b^2)^2}(a'b-b'a)$$

$$F = \frac{(3a^2+b^2)(a^2+3b^2)}{ab(a^2+b^2)^2}(a^2-b^2)(a'b-b'a).$$

Equation (A.17) and (A.19) are the equations (9) and (10) of the text and examples of these velocities are shown in Figure 4.2b.

Recently, Manton (116) has produced a similar asymptotic series solution for low Reynolds number flow through an axisymmetric tube whose radius varies slowly in the axial direction. Manton developed the expansions for the stream function and vorticity in the general case up to second order.

REFERENCES

1. Macklem, P.T. (1971) Airway obstruction and collateral ventilation. Physiol. Reviews, Vol.51, n.2: 368-436.

2. Atabek, H.B. (1968) Wave propagation through a viscous fluid contained in a tethered, initially stressed, orthotropic elastic tube. Biophys. J. 8: 626-649.

2a. Pickett, G.F. (1968) Incompressible viscous flow in a curved pipe. Ph.D. Thesis, Imperial College.

3. Weibel, E.R. (1963) Morphometry of the Human Lung. Berlin, Springer: 139.

4. Horsfield, K., G. Dart, D.E. Olson, G.F. Filley & G. Cumming (1971) Models of the human bronchial tree. J. Appl. Physiol. 31, no.2: 207-217.

5. Olson, D.E., G. Dart & G.F. Filley (1970) Pressure drop and fluid flow regime of air inspired into the human lung. J. App. Physiol. 28, no.4: 482-494.

6. Horton, R.E. (1945) Erosional development of streams and their drainage basins: hydrophysical approach to quantitative morphology. Bull. Geol. Soc. Am. 56: 275-370.

7. Strahler, A.H. (1950) Equilibrium theory of erosional shapes approached by frequency distribution analysis. Am. J. Sci. 248: 673-696.

8. Murray, C.D. (1927) Branching angle of trees. J. Gen. Physiol. 10: 725-729.

9. Woldenberg, M.J., G. Cumming, K. Harding, K. Horsfield, K. Prowse & Shiam Singhal (1970) Law and order in the human lung. Harvard papers in Theoretical Geography, "Geography and the Properties of Surfaces" series.

10. Dekker, E. (1961) Transition between laminar and turbulent flow in human trachea. J. Appl. Physiol. 16: 1060-1064.

11. West, J.B. & P. Hugh-Jones (1959) Patterns of gas flow in the upper bronchial tree. J. Appl. Physiol. 14: 753-759.

12. Olson, D.E., K. Horsfield & G.F. Filley (1969) Investigation of flow patterns in the upper airways during mouth breathing. In: Aspen Emphysema Conference 12th.

13. Olson, D.E. (1968) Flow in the upper airways. Fed. of Exp. Biolog. Conference, Atlantic City.

14. Olson, D.E., L.D. Iliff & M.F. Sudlow (1971) Some aspects of the physics of flow in the central airways. Symposium on Models in Ventilatory Mechanics, Paris, in print.

15. Sekihara, T., D.E. Olson & G.F. Filley (1968) Airflow regimes and geometrical factors in the human airways. In: Current Res. Chronic Respiratory Disease, Proc. Emphysema Conf. 11th: 103-114.

16. Wilson, T.A. & K-H Lin (1967) Convection and diffusion in the airways and the design of the bronchial tree. Satellite Symposium to XI Inter-Physiological Congress, Haverford, Penn.

17. Cumming, G., J. Crank, K. Horsfield & I. Parker (1966) Gaseous diffusion in the airways of the human lung. Respir. Physiol. 1: 58-74.

18. Cumming, G., K. Horsfield & S.B. Preston (1971) Diffusion equilibrium in the lungs examined by nodal analysis. Respir. Physiol. 12: 329-345.

19. Stibitz, G.R. (1969) Calculating diffusion in biological systems by random walks with special reference to gaseous diffusion in the lung. Respir. Physiol. 7: 230-262.

20. Taylor, Sir G.I. (1953) Dispersion of soluble matter in solvent flowing slowly through a tube. Proc. Roy. Soc. A, 219: 186.

21. Aris, R. (1956) On the dispersion of a solute in a fluid flowing through a tube. Proc. Roy. Soc. A, 235: 67.

22. Lighthill, M.J. (1966) Initial development of diffusion in Poiseuille flow. J. Inst. Maths. Applics. 2: 97-108.

23. Chatwin, P.C. (1971) The approach to normality of the concentration distribution of a solute in a solvent flowing along a straight pipe. J. Fluid Mech., submitted.

24. Dean, W.R. (1928) The streamline motion of fluid in a curved pipe. Phil. Mag. S.7, Vol.5, No.30: 673-695.

25. Lew, H.S. & Y.C. Fung (1970) Entry flow into blood vessels at arbitrary Reynolds numbers. J. of Biomechanics 2: 105-117.

26. Lew, H.S. (1971) Low Reynolds equi-bifurcation flow in a two dimensional channel. J. Biomechanics 3: 23-28.

27. Richardson, E.G. & E. Tyler (1929) The transverse velocity gradient near the mouths of pipes in which an alternating or continuous flow of air is established. Proc. Phys. Soc. 42: 1-15.

28. Sexl, T. (1930) Uber den von E.G. Richardson entdeckten Annulareffekt. Zeitschrift für Physik 61: 349.

29. Womersley, J.R. (1957) An elastic tube theory of pulse transmission and oscillating flow in mammalian arteries. WADC Technical Report TR 56-614, Wright Air Development Center.

30. Morgan, G.W. & J.P. Kiely (1954) Wave propagation in a viscous liquid contained in a flexible tube. J. of Acoustical Soc. Am. 26: 323.

31. Morgan, G.W. & W.R. Ferrante (1955) Wave propagation in an elastic tube filled with streamlined liquid. J. of Acoustical Soc. Am. 27: 715.

32. Atabek, H.B. & H.S. Lew (1966) Wave propagation through a viscous incompressible fluid contained in an initially stressed elastic tube. Biographical J. 6: 481.

33. McDonald, D.A. Blood Flow in Arteries. London, Edward Arnold Publishers Ltd., 1960.

34. Pedley, T.J., R.C. Schroter & M.F. Sudlow (1971) Flow and pressure drop in systems of repeatedly branching tubes. J. Fluid Mech. 46, pt.2: 365-383.

35. Atabek, H.B. & C.C. Chang (1961) Oscillatory flow near the entry of a circular tube. Z.A.M.P. XII: 185.

36. Kuchar, N.R. & S. Ostrach (1967) Unsteady entrance flows in elastic tubes with application to the vascular system. Report FTAS/TR-67-25 of the Division of Fluid, Thermal & Aerospace Sciences, Case Western Reserve University, Cleveland, Ohio.

37. Lyne, W.H. (1970) Unsteady viscous flow in a curved pipe. J. Fluid Mech. 45, pt.1: 13-31.

38. Hughes, J.M.B., F.G. Hoppin, Jr. & J. Mead (1971) Effect of lung inflation on bronchial length and diameter in excised lungs. J. Appl. Physiol, in print.

39. Hyatt, R.E. & R. Flath (1966) Influence of lung parenchyma on pressure-diameter behaviour of dog bronchi. J. Appl. Physiol. 21: 1448-1452.

40. Mead, J., T. Takishmia & D. Leith (1970) Stress distribution in lungs: a model of pulmonary elasticity. J. Appl. Physiol. 28: 596-608.

41. West, J.B. & F. Mathews (1971) Stress and strain in the lung due to its own weight. J. Appl. Physiol., in print.

42. Timoshenko, S. (1940) Theory of Plates and Shells. Chapter XI, McGraw-Hill.

43. Morgan, G.W. (1952) On the steady laminar flow of a viscous incompressible fluid in an elastic tube. Bull. of Math. Biophys. 14: 19.

44. Kuchar, N.R. & S. Ostrach (1966) Flows in the entrance regions of circular elastic tubes. Proc. ASME Symp. on Biomedical Fluid Mech., Denver, Colorado.

45. Bauer, A.G. (1965) Direct measurement of velocity by hot-wire anemometry. AIAA Journal, Vol.3, No.6: 1189-1191.

46. Sato, H. Non-linearity and inversion effects of hot-wire anemometer on the mean and fluctuating-velocity measurements at low wind-speed. Prept. Inst. Sci. Technol. Univ. Tokyo 11: 73 (1957).

47. Kovasznay, L.S.G. (1948) Hot-wire investigation of the wake behind cylinders at low Reynolds numbers. Proc. Roy. Soc. Lond. A, 198: 174.

48. Bradbury, L.J.S. & I.P. Castro (1971) A pulsed wire technique for velocity measurements in highly turbulent flows. J. Fluid Mech., in print.

49. Tombash, I.H. (1969) Velocity measurements with a new probe in inhomogeneous turbulent jets. Ph.D. Thesis, Calif. Institute of Tech.

50. Davies, C.N. (1961) A formalised anatomy of the human respiratory tract. Inhaled Particles & Vapours Symposium.

51. Bournia, A., J. Coull & G. Houghton (1961) Dispersion of gases in laminar flow through a circular tube. Proc. Roy. Soc. A, 261: 227.

52. Bailey, H.R., & W.B. Gogarty (1962) Numerical and experimental results on the dispersion of a solute in a fluid in laminar flow through a tube. Proc. Roy. Soc. A, 259: 352.

53. Ananthakrishnan, V., W.N. Gill & A.J. Bardulry (1965) Laminar dispersion in capillaries: Part 1. Mathematical analysis. A.I.Ch.E. Journal, Vol.11, No.6: 106.

54. Erdogan, M.E. & P.C. Chatwin (1967) The effects of curvature and buoyancy on the laminar dispersion of solute in a horizontal tube. J. Fluid Mech. 29, pt.3: 465-484.

55. Crank, J. Mathematics of diffusion. London, Oxford University Press (1964).

56. Fujita, H. (1952) Formal solution of diffusion, equation with variable diffusivity. Text. Res. Journ. 22: 757 & 823.

57. Carslaw, H.S. & J.C. Jaeger (1959) Conduction of heat in solids. London, Oxford University Press.

58. Weast, R.C., ed. (1966) Handbook of Chemistry and Physics, 47th edition. The Chemical Rubber Co., Cleveland, Ohio.

59. Kaye, G.W.C. & T.H. Laby (1966) Tables of physical and chemical constants, 3rd edition. London, Longman, Green & Co.

60. Goldsmith, A., T.E. Waterman & H.J. Hirschham (1961) Handbook of Thermophysical Properties of Solid Materials, Vol.1 - Elements. London, Pergamon Press.

61. Collis, D.C. & N.J. Williams (1959) Two-dimensional convection from heated wires at low Reynolds numbers. J. Fluid Mech. 6: 357.

62. Bradbury, L.J.S. & I.P. Castro (1971) Some comments on heat transfer laws for fine wires. (To be submitted)

63. Yih, C-S. (1953) Free convection due to boundary surfaces. In: Fluid Models in Geophysics. Proceedings of the First Symposium on the Use of Models in Geophysical Fluid Dynamics, U.S. Government Printing Office, Washington 25 D.C.: 117-133.

64. Yih, C-S. (1952) Laminar free convection due to a live source of heat. Trans. A.G.U. 33, No.5: 689-672.

65. Cebeci, T. & T.Y. Na (1970) Skin-friction characteristics of laminar power-low fluids on a slender circular cylinder. J. Appl. Mech. Trans. ASME, V.37, Ser.E1: 230-232.

66. Cole, J. & A. Roshko (1954) Heat transfer from wires at Reynolds numbers in the Oseen range. Proc. Heat Transfer and Fluid Mechanics Inst., Univ. of Calif., Berkeley, Calif. Stanford Univ. Press: 13-21.

67. Kassoy, D.R. (1967) Heat transfer from circular cylinders at low Reynolds numbers, I. Theory for variable property flow. Phys. Fluids 10, No.5: 938-946.

68. Mahoney, J.J. (1956) Heat transfer at small Grashof numbers. Proc. Roy. Soc. A 238: 412-423.

69. Hodnett, D.F. (1968) Slow compressible flow past a circular cylinder. Physics of Fluids 11, No.8: 1636-1647.

70. Collis, D.C. (1956) Forced convection of heat from cylinders at low Reynolds numbers. J. Aero. Sci. 23: 697-698.

71. Owen, E. & R.C. Pankhurst (1966) The measurement of air flow, 4th edition. London, Pergamon Press.

72. Kaplun, S. (1957) Low Reynolds number flow past a circular cylinder. J. Math. & Mech. 6: 595.

73. Lagerstrom, P.L. & J.D. Cole (1955) Examples illustrating expansion procedures for the Navier-Stokes equations. Journ. of Rational Mechanics & Analysis 4: 817.

74. Proudman, I. & J.R.A. Pearson (1957) Expansion at small Reynolds numbers for flow past spheres and circular cylinders. J. Fluid Mech. 2: 237.

75. Chang, I-Dee (1965) Slow motion of a sphere in a compressible viscous fluid. Z. Agnew Math. Phys. 16: 449-470.

76. Aihara, Y., D.R. Kassoy & P.A. Libby (1967) Heat transfer from circular cylinders at low Reynolds numbers, II. Experimental results and comparison with theory. Phys. of Fluids, Vol.10, No.5: 947-952.

77. King, L.V. (1914) On the convection of heat from small cylinders in a stream of fluid. Determination of convection constants of small platinum wires with application to hot-wire anemometry. Phil. Trans. A. 214: 373-432.

78. Hilpert, R. (1933) Wärmeabgabe von geheizten Drähten und Rohren im Luftstrom. Forsch. Arb. Ing. Wes. 4: 214-224.

79. Davies, P.O.A.L. & M.J. Fisher (1964) Heat transfer from electrically heated cylinders. Proc. Roy. Soc. A 280: 486-527.

80. Nikuradse, J. (1957) In: Applied Hydro and Aeromechanics by L. Prandtl & O.G. Tietjens, Dover Public. New York: 27.

81. Langhaar, H.L. (1942) Steady flow in the transition length of a straight tube. J. of Appl. Mech. Trans. ASME, Vol.64: A55-58.

82. Schiller, L. (1922) Die Entwicklung der Laminaren Geschwindigkeitsverteilung und ihre Bedeutung für Zahigkeitsmessungen. Zeitschrift für angewandte Mathematik und Mechanik, Band 2, Heft 2: 96-106.

83. Schlichting, H. (1955) Boundary Layer Theory. McGraw-Hill, New York.

84. Zanker, K.J. & T.E. Brock (1967) A review of the literature on fluid flow through closed conduit bends. The British Hydromechanics Research Association, TN 901.

85. Thompson, J. (1876) On the origin of windings of rivers in alluvial plains, with remarks on the flow of water round bends in pipes. Proc. Roy. Soc. (London), 28: 5-8.

86. Hawthorne, W.R. (1961) Flow in bent pipes. Proc. of Seminar in Aero. Sciences, pp.305-333. Nat. Aero. Lab., Bangalore.

87. Squire, H.B. (1954) Note on secondary flow in a curved circular pipe. ARC Rep. No. 16, 601.

88. Akiyama, M. & K.C. Cheng (1971) Boundary vorticity method for laminar forced convection heat transfer in curved pipes. Int. J. Heat Mass Transfer 14: 1659-1675.

89. Barva, S.N. (1963) On secondary flow in stationary curved pipes. Quart. Journ. Mech. & Applied Math. Vol.XVI, Pt.1: 61-77.

90. Dean, W.R. & J.M. Hurst (1959) Note on the motion of fluid in a curved pipe. Mathematika 6: 77-85.

91. Ito, H. (1969) Laminar flow in curved pipes. ZAMM 49: 653-663.

92. McConalogue, D.J. & R.S. Srivastava (1968) Motion of a fluid in a curved tube. Proc. Roy. Soc. A, 307: 37-53.

93. Mori, Y. & W. Nakayama (1965) Study on forced convective heat transfer in curved pipes (1st report, Laminar Region). Int. J. Heat Mass Transfer 8: 67-82.

94a. Rowe,M. (1970) Measurements and computations of flow in pipe bends. J. Fluid Mech. 43, Pt.4: 771-783.

94b. Rowe, M. (1966) Some secondary flow problems in fluid dynamics. Ph.D. Thesis, University of Cambridge.

95. Squire, H.B. & K.G. Winter (1951) The secondary flow in a cascade of airfoils in a non-uniform stream. J. Aero. Sci. 18: 271-277.

96. Detra, R.W. (1953) The secondary flow in curved pipes. Mitt. a.d. Inst. f. Aerodynamik, No.20, ETH, Zurich.

97. Hawthorne (1951) Secondary circulation in fluid flow. Proc. Roy. Soc. (London) A, 206: 374-387.

98. Eichenberger, H.P. (1951) Shear flow in bends. M.Sc. Thesis, M.I.T.

99. Goldstein, S. (1965) Modern Developments in Fluid Dynamics, Vol.I. Dover Publ. Inc., New York.

100. Bansod, P. & P. Bradshaw (1971) The flow in S-shaped ducts. Imperial College Aero Report 71-10.

101. Eustrice, J. (1911) Experiments on stream-line motion in curved pipes. Proc. Roy. Soc. A., 85: 119-131.

102. Dean, W.R. (1927) Note on the motion of fluid in a curved pipe. Phil. Mag. S.7, Vol.4, No.2: 208-223.

103. Cuming, H.G. (1952) The secondary flow in curved pipes. A.R.C., R and M, No.2880.

104. Adler, M. (1934) Strömung in gekrümmten Rohren. ZAMM 14: 257-275.

105. Caro, C.G., J.M. Fitz-Gerald & R.C. Schroter (1971) Atheroma and arterial wall shear: Observation, correlation and proposal of a shear dependent mass transfer mechanism for atherogenesis. Proc. Roy. Soc. (London) B, 177: 109-159.

106. Joy, W. (1950) Thesis, M.I.T.

107. Rouse, H. & S. Ince (1957) History of hydraulics. Iowa Inst. of Hydraulics Res., State University of Iowa.

108. Barnett, C.H. & W. Cochrane (1956) Flow of viscous liquids in branches tubes. Nature 177: 740-742.

109. Krovetz, L.J. (1965) The effect of vessel branching on haemodynamic stability. Phys. in Med. & Bio. 10, No.3: 417-427.

110. Schroter, R.C. & M.F. Sudlow (1969) Flow patterns in models of the human bronchial airways. Resp. Physiol. 7: 341-355.

111. Schreck, R.M. & L.F. Mockros (1970) Fluid dynamics in the upper pulmonary airways. AIAA 3rd Fluid and Plasma Dynamics Conf., Los Angeles, Calif.

112. Gutstein, W.H. & D.J. Schneck (1967) In vitro boundary layer studies of blood flow in branches tubes. J. Atheroscler. Res. 7: 295-299.

113. Naumann, A. (1970) Strömungsfragen der Medizin. In: Arbeitsgemeinschaft für Forschung des Landes Nordrhein-Westfalen, Heft 203.

114. Zeller, H., N. Talukder & J. Loreny (1970) Model studies of pulsating flow in arterial branches and wave propagation in blood vessels. AGARD Conf. Proc. No.65, Paper 15.

115. Attinger, E.O. (1964) Pulsatile Blood Flow, p.179. McGraw-Hill, New York.

116. Manton, M.J. (1971) Low Reynolds number flow in slowly varying axisymmetric tubes. J. Fluid Mech. 49, Pt.3: 451-459.

117. Olson, David Edward (1969) Tchebycheff approximate solutions to nonlinear differential equations. Ph.D. Thesis, Univ. of Utah.